

UC San Diego

UC San Diego Electronic Theses and Dissertations

Title

Peptide Brush Polymers as Control Elements in Soft Materials and Liquid Crystals

Permalink

<https://escholarship.org/uc/item/7cb2341d>

Author

Adamiak, Lisa

Publication Date

2016

Peer reviewed|Thesis/dissertation

UNIVERSITY OF CALIFORNIA, SAN DIEGO

Peptide Brush Polymers as Control Elements in Soft Materials and Liquid Crystals

A thesis submitted in partial satisfaction of the requirements for the degree Doctor of
Philosophy

in

Chemistry

by

Lisa Adamiak

Committee in Charge:

Professor Nathan Gianneschi, Chair
Professor Thomas Hermann
Professor Elizabeth A. Komives
Professor Robert F. Mattrey
Professor Yitzhak Tor

2016

Copyright

Lisa Adamiak, 2016

All rights reserved.

The dissertation of Lisa Adamiak is approved, and it is acceptable in quality and form for publication on microfilm and electronically:

Chair

University of California, San Diego

2016

DEDICATION

I dedicate this thesis to my family.

EPIGRAPH

"Now I understand," said the last man.

Arthur C. Clarke, Childhood's End

TABLE OF CONTENTS

SIGNATURE PAGE	iii
DEDICATION	iv
EPIGRAPH.....	v
TABLE OF CONTENTS.....	vi
LIST OF ABBREVIATIONS.....	x
LIST OF FIGURES	xiv
LIST OF TABLES.....	xxii
LIST OF SCHEMES.....	xxiii
ACKNOWLEDGEMENTS.....	xxiv
VITA.....	xxix
ABSTRACT OF THE DISSERTATION	xxx
Chapter 1: Introduction.....	1
1.1 Introduction.....	1
1.1.1 Assembly across length scales	1
1.1.2 Strategies towards the assembly of synthetic polymers	3
1.1.3 Enzyme-responsive materials as emerging dynamic systems.....	4
1.2 Biosynthetic polymers as functional materials	7
1.2.1 Introduction to biosynthetic polymers	7
1.2.2 Architecture control: primary sequence	10
1.2.3 Tacticity control	13
1.2.4 Grafting control.....	15
1.2.5 Stimuli for directed assembly of biosynthetic polymer materials.....	18
1.3 Signal transduction using liquid crystals	21
1.3.1 Liquid crystal materials.....	21
1.3.2 Liquid crystal emulsion droplets as a sensing platform	23
1.3.3 Detecting molecular events at liquid crystal interfaces.....	24
1.4 Obstacles for the use of nanomaterials in biomedical applications	27
1.4.1 Nanomaterials at biological interfaces	27
1.4.2 Mitigating recognition by macrophages and enhancing NP targeting	31

1.5	Acknowledgements.....	36
1.6	References.....	36
Chapter 2: Enzyme-Responsive Soft Materials Prepared by <i>Graft-Through</i> Ring Opening		
	Metathesis Polymerization of Peptides.....	52
2.1	Introduction.....	52
2.2	<i>Graft-through</i> polymerization of peptides using Ring Opening Metathesis Polymerization (ROMP).....	54
2.2.1	Formulation of nanoparticles from PPAs.....	58
2.2.2	Demonstrating enzyme-responsiveness of NPs and soluble polymers	60
2.3	Proteolysis of peptide polymers prepared by incorporation of canonical amino acids <i>via graft-through</i> ROMP	62
2.3.1	<i>Graft-through</i> polymerization of complex peptides	62
2.3.2	Enzymatic activity of peptide brush polymers.....	63
2.4	Improving the solubility of peptide polymers by incorporating permanent cations	65
2.4.1	Synthesis of <i>exo-7</i> -oxanorbornyl cations and betaines and their polymerization in DMF	68
2.5	Enzyme-directed assembly of peptide brush polymers.....	72
2.5.1	Polymerization of peptide derivatives containing quaternary amines	73
2.5.2	Polymerization kinetics of peptide brush polymers bearing quaternary amines	75
2.5.3	Enzyme kinetics of peptide brush polymers and nanoparticles	78
2.5.4	Enzyme-triggered assembly of PBPs.....	83
2.5.5	<i>In vivo</i> biodistribution of enzyme-responsive PBPs	85
2.6	Peptide brush polymers as enzyme-responsive MRI contrast agents	91
2.6.1	Relaxivity properties of enzyme-responsive polymers	93
2.7	Conclusions and future outlook	103
2.8	Acknowledgements.....	105
2.9	Methods	106
2.9.1	Peptide synthesis.....	107
2.9.2	RP-HPLC analysis of proteolytic studies.....	108
2.9.3	Standard curves for quantifying enzyme cleavage.....	109
2.9.4	Polymerizations.....	110
2.9.5	Representative polymerization and purification of Gd-DOTA-containing peptide brush polymers	113
2.9.6	Formulation and characterization of fluorogenic nanoparticles.....	114
2.9.7	Transmission Electron Microscopy (TEM)	115
2.9.8	Standard curve for Gd(III) determination	115
2.9.9	Procedure for Gd(III) concentration determination of polymers	115
2.9.10	MRI procedures	116

2.9.11	Analysis of T1 data	116
2.9.12	<i>In vivo</i> protocols.....	117
2.9.13	<i>Ex vivo</i> biodistribution	118
2.9.14	¹ H NMRD Profiles	121
2.10	References.....	122
Chapter 3: Peptide Brush Polymers and Nanoparticles for Activating and Evading		
Macrophage Uptake		129
3.1	Introduction.....	129
3.2	Synthesis of peptide brush polymers and formulation of polymeric NPs.....	131
3.3	Cellular internalization of peptide brush polymers and polymeric NPs by RAW 264.7 cells	139
3.3.1	Mechanism of cellular uptake	144
3.3.2	Serum-dependent cellular uptake	145
3.4	Enzyme-activated uptake of polymeric NPs	148
3.5	Conclusions and future outlook	153
3.6	Acknowledgements.....	156
3.7	Methods	156
3.7.1	Transmission electron microscopy.....	156
3.7.2	Peptide synthesis	157
3.7.3	Polymerizations.....	159
3.7.4	Formulation of polymeric nanoparticles	165
3.7.5	Concentration determination of polymeric nanoparticles	166
3.7.6	Cell culture.....	167
3.7.7	Analysis of cellular uptake in RAW264.7 cells by flow cytometry.....	168
3.7.8	Mechanistic studies by flow cytometry	169
3.7.9	Live cell confocal microscopy	170
3.7.10	Enzyme-treatment of materials prior to cell incubation.....	170
3.7.11	Cell viability assay	175
3.8	References.....	178
Chapter 4: Programming Liquid Crystal Interfaces with Enzyme-Responsive Polymers and		
Surfactants		183
4.1	Introduction.....	183
4.2	Strategy for triggering liquid crystal ordering transitions using peptide polymer amphiphiles and surfactants	184
4.3	Surface activities of PPA-decorated LC microdroplets	186
4.4	Characterization of liquid crystal microdroplets in the presence of surfactants by polarized light microscopy.....	190

4.5	<i>In situ</i> detection of proteolytic degradation of peptide polymer amphiphile-coated liquid crystal microdroplets	192
4.6	Conclusion and future outlook.....	193
4.7	Acknowledgements.....	194
4.8	Methods	194
4.8.1	General methods	194
4.8.2	Estimation of charge densities	196
4.8.3	Response of LC microdroplets to Thermolysin	196
4.8.4	Peptide synthesis and purification.....	197
4.8.5	Synthesis of biphenyl monomer.....	199
4.8.6	Polymer synthesis and purification	201
4.8.7	Preparation of LC emulsions.....	204
4.8.8	Thermolysin treatment of PPA-laden 5CB droplets	205
4.8.9	Amphiphilic development with surfactants	207
4.8.10	LC droplet characterization with microscopy	207
4.8.11	Surface pressure-area isotherms.....	208
4.9	References.....	208
Chapter 5: Design of Triggerable Amphiphiles with Mesogenic Side Chains for Multi-Scale Responses with Liquid Crystals..... 211		
5.1	Introduction.....	211
5.2	Identifying LC configurations of polymer-decorated LC droplet emulsions by flow cytometry	217
5.3	Studying the effects of polymer side chain structure on polymer-LC interactions	219
5.4	Copolymer composition and architecture on LC ordering.....	226
5.5	The organization of copolymers at the air–water interface.....	229
5.6	Enzyme-responsive copolymer-decorated LC droplets	231
	233	
5.7	Conclusion and future outlook.....	233
5.8	Acknowledgements.....	235
5.9	Methods	235
5.9.1	Materials	235
5.9.2	General Methods.....	236
5.9.3	Characterization of LC droplets with optical microscopy	237
5.9.4	Surface-pressure area isotherm measurements	237
5.9.5	Representative homopolymer procedure	239
5.9.6	Representative block copolymer procedure	240
5.9.7	Representative random copolymer procedure with PEG12 monomer	240
5.9.8	Representative random copolymer procedure using peptide monomer	240
5.10	References.....	286

LIST OF ABBREVIATIONS

Å	Angstrom (0.1 nm)
A.U.	arbitrary units
Au	gold
AFM	atomic force microscopy
Ar	aryl
ATP	adenosine triphosphate
ATRP	atom transfer radical polymerization
B	bilayer
- <i>b</i> -	block, in block copolymer
br	broad
°C	degrees Celsius
C	cylinder
¹³ C	carbon
CA	contrast agent
5CB	4-cyano-4'-pentylbiphenyl
CL	cylinder length
CPP	cell penetrating peptide
CT	computed tomography
CTA	chain transfer agent
δ	chemical shift
d	doublet, days, deuterated
dd	doublet of doublet
DabcyI	4-((4-(dimethylamino)phenyl)azo)benzoic acid
DCM	dichloromethane
DIPEA	N,N-Diisopropylethylamine
DLS	dynamic light scattering
DMEM	Dulbecco's minimum essential medium
DMF	dimethylformamide
DMSO	dimethylsulfoxide
dn/dc	change in refractive index with respect to change in concentration
DNA	deoxyribonucleic acid
DOTA	1,4,7,10-tetraazacyclododecane-1,4,7,10-tetraacetic acid
DP	degree of polymerization
DPBS	Dulbecco's phosphate buffered saline
Ebes	Peg ₂ -succinamic acid
Edans	5-(2-aminoethylamino)-1-naphthalenesulfonic acid
EDTA	ethylenediaminetetraacetic acid
EI-MS	electron ionization mass spectrometry
EPR	enhanced permeation and retention effect
equiv	equivalents
ESI	electrospray ionization
EtOAc	ethyl acetate
eV	electron volts
EVE	ethyl vinyl ether
FACS	fluorescence-activated cell sorting
FDA	food and drug administration
Fmoc	fluorenylmethoxycarbonyl chloride

FSC	forward scatter
g	grams
Gd	gadolinium
h	hours, Hill coefficient
¹ H	proton
HATU	(1-[Bis(dimethylamino)methylene]-1H-1,2,3-triazolo[4,5-b]pyridinium 3-oxid hexafluorophosphate)
HCl	hydrochloric acid
H-F	hand-foot syndrome
H ₂ O	water
HPLC	high performance liquid chromatography
HPMA	N-(2-Hydroxypropyl)methacrylamide
HNO ₃	nitric acid
HRMS	High Resolution Mass Spectrometry
Hz	Hertz (s ⁻¹)
ICP-OES	inductively coupled plasma optical emission spectrometry
igG	immunoglobulin G
J	NMR coupling constant
K	degrees Kelvin
kDa	kilodalton
kcal	kilocalories
k _{cat}	turnover number
K _m	the substrate concentration at which the reaction rate is at half-maximum
λ _{abs}	absorbance wavelength
λ _{em}	emission wavelength
λ _{ex}	excitation wavelength
L	liters
LC	liquid crystal
LCST	lower critical solution temperature
L-DLPC	l-alpha-dilauroyl phasphatidyl choline
LRMS	low resolution mass spectrometry
m	meter, multiplet
M	molar
MALDI-TOF	matrix-assisted laser desorption ionization-time of flight
MALS	multi-angle light scattering
Me	methyl (CH ₃)
MeOH	methanol (CH ₃ OH)
Mes	mesityl, 2,4,6-trimethylphenyl (2,4,6-Me ₃ C ₆ H ₂)
MgSO ₄	magnesium sulfate
mg	milligram
MI	myocardial infarction
min	minutes
mL	milliliters
MMP	matrix metalloproteinase
Mn	number average molecular weight
mol	moles
MPS	mononuclear phagocyte system
MRI	magnetic resonance imaging
MS	mass spectrometry

Mtt	methyltrityl
Mw	weight average molecular weight
Mn	number average molecular weight
MWCO	molecular weight cut-off
<i>n</i>	director
NaHCO ₃	sodium bicarbonate
NaOH	sodium hydroxide
NHS	<i>N</i> -hydroxysuccinimide
nm	nanometer (10 Å)
NMP	nitroxide-mediated radical polymerization
NMR	Nuclear Magnetic Resonance
NMRD	Nuclear Magnetic Relaxation Dispersion
NP	nanoparticle
N _w ^{agg}	aggregation number
OEG	oligoethylene glycol
OPG	osteoprotegerin
π	pi
Π-A	surface pressure-area
PAMAM	poly(amidoamine)
PBP	peptide brush polymer
PBS	phosphoate buffered saline
pCB	poly(carboxybetaine)
Pd	palladium
PEG	poly(ethylene glycol)
PEI	poly(ethyleneimine)
Ph	phenyl
PLL	poly(L-lysine)
PPA	peptide polymer amphiphile
ppm	parts per million
PNA	peptide nucleic acid
PS	polystyrene
PVP	poly(vinylpyrrolidone)
PVA	poly(vinyl alcohol)
q	quartet, number of bound water molecules in the inner coordination sphere
r ₁	relaxivity, 1/T ₁ , (L/mmol · s ⁻¹)
R	organic group, alkyl group
RAFT	reversible addition-fragmentation chain-transfer
RDRP	reversible-deactivation radical polymerization
RES	reticuloendothelial system
RI	refractive index
RNA	ribonucleic acid
ROP	ring-opening polymerization
ROMP	ring-opening metathesis polymerization
RP	reverse-phase
r.t.	room temperature
σ	sigma
s	singlet, seconds
SDS	sodium dodecyl sulfate
SEC	size-exclusion chromatography

SLS	static light scattering
SPPS	solid phase peptide synthesis
SSC	side scatter
t	triplet
$t_{1/2}$	half-life
τ_m	mean residency time of bound water molecules
τ_r	rotational correlation time of the contrast agent
T_1	longitudinal proton relaxation time
T	Tesla
T.A.	termination agent
TEM	transmission electron microscopy
Temp	temperature
TFA	trifluoroacetic acid
TFE	2,2,2-trifluoroethanol
T_g	glass transition temperature
THF	tetrahydrofuran
TIPS	triisopropylsilane
TLC	thin layer chromatography
tma	trimethylammonium chloride
Tris	tris(hydroxymethyl)aminomethane
UV	ultraviolet
μm	micrometer
μM	micromolar
V	volts
V_{max}	maximum velocity
X	halide, peptide sequence

LIST OF FIGURES

Figure 1.1 Various architectures of functional biosynthetic polymers <i>via</i> the conjugation of natural and synthetic moieties	7
Figure 1.2 Various grafting strategies used for the preparation of biosynthetic polymers	9
Figure 1.3 Strategy for the polymerization of unstrained macrocycles	13
Figure 1.4 IEG-inspired iterative synthesis of sequence and stereocontrolled polymers	15
Figure 1.5 Enzyme-responsive peptide–polymer amphiphiles.....	19
Figure 1.6 Thermotropic liquid crystals exhibit temperature-dependent phase behaviors	23
Figure 1.7 A change in LC orientation is induced by binding of a surfactant to the LC surface.....	25
Figure 1.8 The interactions between nanoparticles and a cell at the cell-NP interface.....	28
Figure 1.9 Examples of alternative surface modifications to PEGylation	33
Figure 2.1 The chemical functional group diversity afforded by the 20 canonical amino acid	53
Figure 2.2 Polymerization of a model peptide, GVPAFLI, with PEG to confer solubility	57
Figure 2.3 Characterization of PPAs formulated into NPs	59
Figure 2.4 Characterization of PPA 4 formulated into NPs.....	60
Figure 2.5 RP-HPLC chromatograms of homopolymer prepared from monomer 4	61
Figure 2.6 Trypsin activity on lysine-containing peptide monomers 9 and 10 and the corresponding polymers 9 ₂₁ and 10 ₁₉	64
Figure 2.7 SEC-MALS chromatograms of peptide homopolymers	66
Figure 2.8 Degradation of the purified NorGPLGLAG-Ebes peptide monomer.....	67
Figure 2.9 Monitoring the polymerization of the benzyl bromide quaternary amine monomer.....	70
Figure 2.10 Copolymerization of cationic benzyl monomer 3 with an aliphatic peptide	71
Figure 2.11 Enzyme-driven assembly for peptide brush polymers (PBPs)	73
Figure 2.12 Solid phase peptide synthesis (SPPS) of monomers consisting of NorAha.	75
Figure 2.13 Polymerization kinetics of <i>N</i> -terminus conjugated peptide monomers	76
Figure 2.14 Plots comparing the number-average molecular weight (M_n) as a function of monomer to initiator feed ratio ($[M]_0/[I]_0$).....	77

Figure 2.15 Percent conversion of 1 mM substrate by 1 μ M thermolysin at 37 $^{\circ}$ C	79
Figure 2.16 Schematic of a fluorogenic peptide	81
Figure 2.17 Characterization of the nanoparticles prepared from the fluorogenic block copolymer.....	81
Figure 2.18 Michaelis-Menten plots.....	82
Figure 2.19 Enzyme kinetics of the fluorogenic monomer with thermolysin.....	83
Figure 2.20 (A) Dry-state TEM micrograph and (B) cryo-EM of the enzymatic reaction	84
Figure 2.21 Dry-state TEM images and RP-HPLC chromatograms of NPBP1 controls	84
Figure 2.22 Enzyme-triggered assemblies of N-terminus conjugated PBPs	85
Figure 2.23 <i>Ex vivo</i> biodistribution (measured by ICP-OES of Gd) analysis in a syngeneic 4T1 tumor model	87
Figure 2.24 Metabolic experiments to determine the manner and duration of clearance of NPBP3	88
Figure 2.25 Recognition sites for chymotrypsin.....	90
Figure 2.26 RP-HPLC chromatograms of NPBP3 treated with nonspecific proteases	91
Figure 2.27 Enzyme-triggered assembly of peptide brush polymers bearing a Gadolinium (III) complex	92
Figure 2.28 Enzyme-triggered aggregation of PBPs bearing a Gd-DOTA complex.....	95
Figure 2.29 T_1 relaxation time using a 7T MRI at 298 K measured as a function of Gd(III)	96
Figure 2.30 Nuclear magnetic resonance dispersion (NMRD) profiles	97
Figure 2.31 Time progression of the contrast enhancement shown in axial T_1 -weighted MR images of the metastatic tumor lung.....	98
Figure 2.32 Multiple regions of interest were sampled from MR axial scans	99
Figure 2.33 Comparison of thermolysin recognition on responsive (L polymer) and non-responsive control (D polymer) Gd-DOTA containing peptide brush polymers (PBPs).....	100
Figure 2.34 <i>Ex vivo</i> biodistribution (measured by ICP-OES of Gd) analysis of balb/c mice	101
Figure 2.35 Blood circulation time of balb/c mice with and without metastatic 4T1 tumor	102
Figure 2.36 Proposed chemical structure of a Gd-DOTA analogue for future study	105
Figure 2.37 Standard curve of the synthesized, authentic N1 peptide cleavage fragment.....	109

Figure 2.38 Standard curve of the synthesized, authentic C1 peptide cleavage fragment.....	109
Figure 2.39 Peptides displayed on particle 2 (derived from PPA 2) are not cleaved by the protease MMP-2	110
Figure 2.40 SEC-MALS characterization of the fluorogenic (A) homopolymer	111
Figure 2.41 SEC-MALS chromatograms of (A) NorAhaFPGPLGLAGK(tma) and (B) tmaGPLGLAGFPK(NorAha).....	111
Figure 2.42 Verifying the “livingness” of the polymerization of NorAhaFPGPLGLAGK(tma) and tmaGPLGLAGFPK(NorAha).....	112
Figure 2.43 Calibration curve generated for the colorimetric Arsenazo III assay	114
Figure 2.44 Tumor volume measured by calipers or mass	119
Figure 2.45 Blood circulation time and <i>ex vivo</i> biodistribution experiments of healthy (non-immune compromised) C57/bl/6 mice	120
Figure 2.46 Complete data for <i>ex vivo</i> biodistribution (complement to Figure 2.23).....	120
Figure 2.47 <i>Ex vivo</i> biodistribution (measured by ICP-OES of Gd) analysis in a syngeneic 4T1 tumor model.....	121
Figure 3.1 Examining size and charge effects of water-soluble peptide brush polymers and polymeric nanoparticles.....	131
Figure 3.2 Proteolysis of <i>N</i> - and <i>C</i> -terminus peptide substrates displayed as brush polymers.....	132
Figure 3.3 Polymerization schemes for the preparation of peptide-containing homopolymers and block copolymers.	134
Figure 3.4 Chemical structures of random copolymers comprised of two different hydrophobic groups (phenyl and C7 linear aliphatic) and the Nzw peptide.....	135
Figure 3.5 Transmission electron microscopy (TEM) images of spherical NPs	137
Figure 3.6 TEM images of the random copolymers	138
Figure 3.7 Percent viability of materials used for RAW 264.7 uptake experiments	140
Figure 3.8 Cellular uptake by RAW264.7 cells quantified as normalized mean fluorescence	141

Figure 3.9 Cellular uptake of spherical NPs formulated from Nzw peptide-containing random copolymers.	142
Figure 3.10 Merged bright field and epifluorescence channels from Z-stack live-cell confocal analysis of RAW 264.7 cells.	143
Figure 3.11 Batch variation of spherical NPs on RAW 264.7 cell uptake	144
Figure 3.12 Mechanism of cellular uptake of <i>N</i> - and <i>C</i> -terminus NPs of various charge	145
Figure 3.13 Comparing the effect of serum on the cellular uptake of <i>N</i> - and <i>C</i> -terminus NPs	146
Figure 3.14 Comparing the effect of serum on the cellular uptake of <i>N</i> - and <i>C</i> -terminus homopolymers (DP 25)	147
Figure 3.15 Transmission electron microscopy (TEM) images.....	149
Figure 3.16 Cellular uptake of spherical NPs of various charges before and after treatment with 0.3 μ M thermolysin	149
Figure 3.17 Live cell confocal microscopy of RAW 264.7 cells incubated with Ccat and Czw NPs before and after thermolysin treatment	150
Figure 3.18 Cellular uptake of hydrophilic polymers of various charges after treatment with 0.3 μ M thermolysin	151
Figure 3.19 Dry-state TEM images of hydrophilic peptide brush polymers	152
Figure 3.20 Percent viability of enzyme-treated materials	153
Figure 3.21 Dry-state TEM image of Czw NPs.....	157
Figure 3.22 Solid phase synthesis of (A) Nzw and (B) Czw monomers using an orthogonal methyltrityl (Mtt) deprotection strategy.	158
Figure 3.23 Peptide homopolymers of theoretical (i) DP 25 and (ii) DP 100 characterized by SEC-MALS	161
Figure 3.24 Peptide block copolymers characterized by SEC-MALS.....	162
Figure 3.25 Polymerization kinetics of norbornene peptide (Nzw) and hydrophobic monomers measured by $^1\text{H-NMR}$	162
Figure 3.26 Random copolymers, synthesized with the N-zwitterionic peptide monomer	163

Figure 3.27 Intensity correlation curves (i) from which DLS data (ii) are derived of the DP 25 homopolymers in DPBS	164
Figure 3.28 Intensity correlation curves (i) from which DLS data (ii) are derived of DP 100 homopolymers in DPBS	165
Figure 3.29 Standard curves generated by measuring absorbance at 260 nm for spherical NPs formulated from block copolymers.....	166
Figure 3.30 Dynamic light scattering (DLS) plots of block copolymers formulated into nanoparticles (NPs) in DPBS.....	167
Figure 3.31 Representative gating for spherical NPs formulated from random copolymers.....	169
Figure 3.32 Standard curve of the synthesized, authentic <i>N</i> -cationic (Ncat) peptide cleavage fragment (LAGK(R ₁)).....	171
Figure 3.33 Standard curve of the synthesized, authentic <i>C</i> -cationic peptide cleavage fragments (R ₁ -GPL, 1, and R ₁ -GPLG, 2).....	171
Figure 3.34 Standard curve of the synthesized, authentic <i>C</i> -zwitterionic peptide cleavage fragment (R ₁ -EGPLG).	172
Figure 3.35 Representative RP-HPLC traces of materials prior to thermolysin treatment.....	173
Figure 3.36 Example histograms from flow cytometry analysis	174
Figure 3.37 Merged bright field and epifluorescence channels	175
Figure 3.38 Optimization of RAW 264.7 cell plating density	176
Figure 3.39 ¹ H and ¹³ C NMR Spectrum of C7 Monomer.....	177
Figure 4.1 Response of PPA-programmed LC microdroplet to enzymatic reactions	185
Figure 4.2 Block copolymer synthesis of PPA 1, 2, and 3 <i>via</i> ROMP.	186
Figure 4.3 Surface pressure (Π) –area isotherms of the PPAs.....	187
Figure 4.4 Representative optical micrographs of PPA3-decorated LC microdroplets	190
Figure 4.5 Optical response of LC microdroplets triggered by enzymatic processing	193
Figure 4.6 Purification of peptide monomer (I).....	198
Figure 4.7 Purification of peptide monomer (II)	198

Figure 4.8 Purification of peptide monomer (III)	199
Figure 4.9 ¹ H NMR spectrum of Nor-biphenyl.	200
Figure 4.10 ¹³ C NMR spectrum of Nor-biphenyl.	201
Figure 4.11 Characterization of Nor-biphenyl homopolymer <i>via</i> ¹ H NMR and SEC-MALS.	202
Figure 4.12 Characterization of PPA 1 block copolymer <i>via</i> ¹ H NMR and SEC-MALS.....	203
Figure 4.13 Characterization of PPA 2 block copolymer <i>via</i> ¹ H NMR and SEC-MALS.....	203
Figure 4.14 Characterization of PPA 3 block copolymer <i>via</i> ¹ H NMR and SEC-MALS.....	204
Figure 4.15 Analysis of Thermolysin-treated PPA 1-laden 5CB droplets.....	206
Figure 4.16 Analysis of Thermolysin-incubated PPA 2-laden 5CB droplets	207
Figure 5.1 Examples of amphiphilic copolymers reported in previous studies	213
Figure 5.2 The catalogue of homopolymers utilized	217
Figure 5.3 Liquid crystal droplets of 5CB exhibit different droplet configurations	218
Figure 5.4 (A) Scatter plots generated from flow cytometry of LC droplets.....	220
Figure 5.5 Percentage of radial configuration generated from LC droplets decorated with homopolymers 1₁₈ , 5₂₀ , 3₂₁ , and 6₁₆	222
Figure 5.6 Percentage of radial configuration generated from LC droplets decorated with homopolymers 7₁₆ , 1₁₈ , 2₁₈ , and 8₁₆	224
Figure 5.7 Percentage of radial configuration generated from LC droplets decorated with homopolymers 1₁₈ , 9₁₆ , 2₁₈ , and 10₁₉	225
Figure 5.8 Chemical structures of copolymers synthesized by ROMP used in this study.....	226
Figure 5.9 The percentage of radial droplets generated for (A) block copolymer-decorated LC droplets and (B) random copolymer-decorated LC droplets	228
Figure 5.10 Comparison of the random and block copolymer architectures	229
Figure 5.11 Langmuir surface pressure-area isotherms.....	231
Figure 5.12 Peptide polymer amphiphiles (PPAs), synthesized as random copolymers	233
Figure 5.14 Langmuir isotherms for block copolymers	238
Figure 5.15 Langmuir isotherms for 1₁₇-<i>b</i>-PEG12₂₉ at various compression rates	239

Figure 5.16 Polymerization and characterization of 1 ₁₉	241
Figure 5.17 Polymerization and characterization of 2 ₁₈	241
Figure 5.18 Polymerization and characterization of 3 ₂₁	242
Figure 5.19 Polymerization and characterization of 4 ₁₅	242
Figure 5.20 Polymerization and characterization of 5 ₂₀	243
Figure 5.21 Polymerization and characterization of 6 ₁₆	243
Figure 5.22 P Polymerization and characterization of 7 ₁₆	243
Figure 5.23 Polymerization and characterization of 8 ₁₆	244
Figure 5.24 P Polymerization and characterization of 9 ₁₆	244
Figure 5.25 Polymerization and characterization of 10 ₁₉	244
Figure 5.26 Polymerization and characterization of 1 ₁₉ - <i>b</i> -PEG 12 ₅	245
Figure 5.27 Polymerization and characterization of 2 ₁₈ - <i>b</i> -PEG 12 ₁₂	245
Figure 5.28 Polymerization and characterization of 1 ₂₁ - <i>b</i> -peptide ₁₀	245
Figure 5.29 Polymerization and characterization of 1 ₂₆ - <i>b</i> -PEG 12 ₁₆	246
Figure 5.30 Polymerization and characterization of 1 ₃₀ - <i>b</i> -PEG 12 ₂₆	246
Figure 5.31 Polymerization and characterization of 1 ₁₇ - <i>b</i> -PEG 12 ₂₉	246
Figure 5.32 Polymerization and characterization of 1 ₄₇ - <i>b</i> -PEG 12 ₁₅	247
Figure 5.33 Polymerization and characterization of 1 ₁₄ - <i>ran</i> -PEG 12 ₁₇	247
Figure 5.34 Polymerization and characterization of 1 ₁₂ - <i>ran</i> -PEG 12 ₂₀	247
Figure 5.35 Polymerization and characterization of 1 ₂₆ - <i>ran</i> -PEG 12 ₁₉	248
Figure 5.36 Polymerization and characterization of 1 ₃₃ - <i>ran</i> -PEG 12 ₁₇	248
Figure 5.37 Polymerization and characterization of 1 ₂₂ - <i>ran</i> -peptide ₅	248
Figure 5.38 Polymerization and characterization of 1 ₂₀ - <i>ran</i> -peptide ₇	249
Figure 5.39 ¹ H-NMR and ¹³ C-NMR spectra of 1	266
Figure 5.40 ¹ H-NMR and ¹³ C-NMR spectra of 2	267
Figure 5.41 ¹ H-NMR and ¹³ C-NMR spectra of 3	268
Figure 5.42 ¹ H-NMR spectrum of 4	269

Figure 5.43 $^1\text{H-NMR}$ and $^{13}\text{C-NMR}$ spectra of 5	270
Figure 5.44 $^1\text{H-NMR}$ and $^{13}\text{C-NMR}$ spectra of 6	271
Figure 5.45 $^1\text{H-NMR}$ and $^{13}\text{C-NMR}$ spectra of 7	272
Figure 5.46 $^1\text{H-NMR}$ and $^{13}\text{C-NMR}$ spectra of 8	273
Figure 5.47 $^1\text{H-NMR}$ and $^{13}\text{C-NMR}$ spectra of 9	274
Figure 5.48 $^1\text{H-NMR}$ and $^{13}\text{C-NMR}$ spectra of 10	275
Figure 5.49 $^1\text{H-NMR}$ and $^{13}\text{C-NMR}$ spectra of S3	276
Figure 5.50 $^1\text{H-NMR}$ and $^{13}\text{C-NMR}$ spectra of S4	277
Figure 5.51 $^1\text{H-NMR}$ and $^{13}\text{C-NMR}$ spectra of S5	278
Figure 5.52 $^1\text{H-NMR}$ and $^{13}\text{C-NMR}$ spectra of S6	279
Figure 5.53 $^1\text{H-NMR}$ and $^{13}\text{C-NMR}$ spectra of S7	280
Figure 5.54 $^1\text{H-NMR}$ and $^{13}\text{C-NMR}$ spectra of S8	281
Figure 5.55 $^1\text{H-NMR}$ and $^{13}\text{C-NMR}$ spectra of S9	282
Figure 5.56 $^1\text{H-NMR}$ and $^{13}\text{C-NMR}$ spectra of S10	283
Figure 5.57 $^1\text{H-NMR}$ and $^{13}\text{C-NMR}$ spectra of S11	284
Figure 5.58 $^1\text{H-NMR}$ and $^{13}\text{C-NMR}$ spectra of S13	285

LIST OF TABLES

Table 2.1 SEC-MALS characterization providing molecular weight and dispersities of PPAs and nanoparticles.....	58
Table 2.2 SEC-MALS characterization of peptide homopolymers bearing polar residues	66
Table 2.3 Summary of molecular characterization and kinetic values for homopolymers	77
Table 2.4 Summary of molecular characterization and kinetic values for homopolymers	78
Table 2.5 Magnetic relaxivity properties of several commercially available small molecule and macromolecular contrast agents	94
Table 2.6 Summary of relaxivity values calculated from plots in Figure 2.29	96
Table 2.7 Summary of blood circulation times of peptide brush polymers	102
Table 2.8 Summary of RP-HPLC, ESI Analyses of Authentic Peptide Cleavage Fragments	109
Table 2.9 SEC-MALS characterization of NorAhaFPGPLGLAGK(tma) and tmaGPLGLAGFPK(NorAha) peptide homopolymers.	112
Table 2.10 Relaxivity (r_1) of polymers prior to and after enzymatic cleavage	117
Table 3.1 Peptide sequences used to synthesize homopolymers and NPs of various charge.....	134
Table 3.2 Dynamic Light Scattering and zeta potential measurements of spherical NPs	137
Table 3.3 Characterization of spherical NPs formulated from amphiphilic random copolymers	138
Table 3.4 Summary of SEC-MALS characterization of water-soluble homopolymers and amphiphilic block copolymers.....	160
Table 3.5 SEC-MALS characterization of amphiphilic block copolymers (batch 2)	161
Table 3.6 Summary of SEC-MALS characterization and kinetic values for homopolymers	163
Table 3.7 SEC-MALS characterization of random copolymers	163
Table 3.8 Summary of RP-HPLC and ESI characterization	172
Table 3.9 Characterization of peptide cleavage fragments	173
Table 4.1 ζ -potentials (mV) of PPA-laden 5CB droplets at various PPA concentrations.....	188
Table 4.2 ζ -potentials (mV) of bare and PPA-laden 5CB droplets	189
Table 5.1 Copolymer library for examining copolymer-LC interactions	227

LIST OF SCHEMES

Scheme 2.1 Synthesis of peptide-polymer amphiphiles (PPAs)	55
Scheme 2.2 Synthesis of <i>exo</i> -7-oxanorbornene monomers.....	69
Scheme 2.3 Synthesis of hydrophilic peptide brush polymers (PBPs) and block copolymers	74
Scheme 5.1 Synthesis of homopolymers, block and random copolymers using ROMP	216
Scheme 5.2 Synthesis of norbornene monomers 1, 2, 5, 7, 9, and 10	249
Scheme 5.3 Synthesis of norbornene monomer 3	258
Scheme 5.4 Synthesis of norbornene monomer 4	260
Scheme 5.5 Synthesis of norbornene monomer 8	261
Scheme 5.6 Synthesis of norbornene monomer 6	263

ACKNOWLEDGEMENTS

I would like to start by first acknowledging my advisor, Professor Nathan Gianneschi, who, from my perspective, is best defined by his genuine optimism in any situation and unswerving belief in his students. Nathan's persistence and enthusiasm for conducting research on the cutting edge of materials science is remarkable, and is something that I will carry with me to remind myself when confronted with obstacles.

I would also like to thank my committee members for their guidance and support during these past five years; Professor Yitzhak Tor (an incredibly thoughtful organic chemist who has great insight into scientific scholarship); Professor Robert Mattrey (who recognizes the applied side of materials science well and has given me a lot of practical advice); Professor Thomas Hermann (an incredible RNA biochemist and possibly the most patient advisor I know); and Professor Betsy Komives (who shares her enthusiasm openly and has been wonderfully supportive during my thesis work as well as the making of the departmental Christmas video).

I would also like to acknowledge Professor Haim Weizman (who has set an extraordinary standard for excellence in teaching and laboratory safety at UCSD and is always available to talk); and Professor Stacey Brydges (who has not only contributed greatly to increasing the presence of women and underrepresented minorities in STEM, but is incredibly passionate about student learning).

Robyn Swanland needs an acknowledgement for everything she does and with such a cool attitude. The staff in the chemistry department (Jeanine Sun, Jeff Rances, Erica Lennard, Melanie Fernandez) all deserve a special thanks along with Shelley Weisel, the former funding coordinator.

I would also like to thank the former and current members of the Gianneschi group: Nia Bell, Angela Blum, Alex Caldwell, Cassi Callmann, Andrea Carlini, Miao-Ping Chen,

Wonmin Choi, Naneki Collins-McCallum, Dustin Crystal, Treffly Ditri, Michael Hahn, Ziyang Hu, Yuran Huan, Carrie James, Lizanne Koch, Ti-Hsuan Ku, Kevin Luo, Julia Michaelis, Ben Monson, Lucas Parent, Billy Pistel, Maria Proetto, Lyndsay Randolph, Alexander Roloff, Anthony Rush, Alfred Tam, Kate Veccharelli, Zhao Wang, Daniel Wright, Xiujun Yue, and Nanzhi Zang. A special nod is given to newer lab members, Joo Hee Lee and Kelsey Alexander, for putting up with me while I wrote this thesis, and Mollie Touve, who was a wonderful travel companion in Boston. Matt Thompson deserves special recognition for all that he does, which includes: fixing any instrument provided he has tinkered with it long enough; planning backpacking trips for twenty clueless people; offering great advice; opening difficult solvent drums; ordering chemicals and supplies; managing safety for the entire lab; training new lab members; and most importantly, he does all of this with a smile. Without him the lab would, quite literally, explode.

I would like to especially acknowledge my closest friends in the lab. Sarah Barnhill, who, when she becomes an astronaut, will grant me the pleasure of knowing an astronaut. Professor Steven (Pudgy) Nguyen, who is never afraid to reveal his true character to the world, though we might not be ready for it. Clare LeGuyader, who is the most fiercely independent person I know and who I have also shared many life conversations with. Swagat Sahu, who is loud and makes friends with everyone, and enjoys Game of Thrones as much as I do. Jacquelin Kammeyer, who has many mutual opinions on academic culture. Andrea Luthi, who is a great listener and is always willing to help. Further, I would like to acknowledge Sara Beck Pancer, who was an REU student that was so amazing, we persuaded her to stay in the lab until her recent acceptance in an anatomy program in Boulder, CO.

There are a number of colleagues and friends at UCSD that I would also like to acknowledge for their support and kinship. The Tor lab (both past and present members): Andro Rios, Lisa McCoy, Kristina Hamill, Ryan Weiss, Andrea Fin, Yao Li, Kaivin Hadidi,

and in particular, Patrycja Hopkins, who has been in the trenches with me from day one, and hosts the best Polish Easter brunches. The Yang lab (both former and current members) including Kevin Cao, Dan Sheik, Jessica Cifelli, and Leibniz Hang. Members of SWIGS who I have gotten to know over the years: Alissa Sasayama, Melissa Clark, Katherine Nadler, Jessie Peters, Faith Katz, Gwen Merlen, Walter Frauman, Jessie Moreton, Katia Charov, and Yanice Benitez. There are many others, including the Godula lab (particularly Mia Huang and Taryn Lucas). Whitney Bryks, a fellow graduate student who has also been a good friend since our undergraduate career at UC Santa Cruz.

I would also like to acknowledge Anthony Mrse (the NMR guru of the Chemistry department), Miriam Scadeng, Bob Bussell, Professor Dennis Carson, Tomoko Hayashi, and Brian Crain for their assistance in all the MRI and animal-related work.

My partner in crime and closest friends outside of the lab deserve a special place for all of their emotional support. First, Alex Rovira, my rock, who is also the sentimental one and the ghostwriter of all of my greeting cards. I simply could not imagine going through this process without him. Ember and Chris Tota, our second family, who enjoy beer as much as we do and whom we strive to spend all of our free time with. Laura Miller, who I miss driving with and listening to David Bowie. Ewa Ulatowska, my best friend, who understands me. And of course, Paige Shapiro, who is a kindred spirit.

Last, but not least, I would like to thank my family. None of this would be possible without the support from my mom, Ania, who shows me that persistence and hard work can overcome anything; my dad, Kris, who is adventurous and has an amazing ability to recall historical details; my brother, Krzysio (little Chris), who finds the humor in everything.

Chapter 1 is adapted, in part, from Andrea S. Carlini, Lisa Adamiak, and Nathan C. Gianneschi. "Biosynthetic Polymers as Functional Materials." *Macromolecules*, 2016, 49, 4379-4394. Copyright 2016 American Chemical Society. Permission to use copyrighted

images and text in the manuscript was also obtained from Andrea S. Carlini and Nathan C. Gianneschi. The dissertation author was the second author on this manuscript.

Chapter 2 is adapted, in part, from Michael E. Hahn, Lyndsay M. Randolph, Lisa Adamiak, Matthew P. Thompson, and Nathan C. Gianneschi. "Polymerization of a Peptide-based Enzyme Substrate." *Chem. Comm.*, 2013, 49, 2873-2875. Copyright 2013 Royal Society of Chemistry. Permission to use copyrighted images and data in the manuscript was also obtained from Michael E. Hahn, Lyndsay M. Randolph, Matthew P. Thompson, and Nathan C. Gianneschi. The dissertation author was the third author on this manuscript.

Chapter 2 is adapted, in part, from Jacquelin K. Kammeyer, Angela P. Blum, Lisa Adamiak, Michael E. Hahn, and Nathan C. Gianneschi. "Polymerization of Protecting-Group Free Peptides via ROMP." *Polym. Chem.*, 2013, 4, 3929-3933. Copyright 2013 Royal Society of Chemistry. Permission to use copyrighted images and data in the manuscript was also obtained from Jacquelin K. Kammeyer, Angela P. Blum, Michael E. Hahn, and Nathan C. Gianneschi. The dissertation author was the third author on this manuscript.

Chapter 2 also contains material that is currently being prepared for submission for publication: "Enzyme-triggered Assembly of Peptide Brush Polymers" Lisa Adamiak, Andrea J. Luthi, Clare M. LeGuyader, Michael E. Hahn, Miriam Scadeng, Tomoko Hayashi, Dennis Carson, and Nathan C. Gianneschi. The dissertation author was the first author of this pending manuscript.

Chapter 3 contains material that is currently being prepared for submission for publication: "Peptide Brush Polymers and Nanoparticles for Evading and Activating Macrophage Uptake" Lisa Adamiak and Nathan C. Gianneschi. The dissertation author was the primary author of this pending manuscript.

Chapter 4 is adapted from C. Derek Ma, Lisa Adamiak, Daniel S. Miller, Xiaoguang Wang, Nathan C. Gianneschi, and Nicholas L. Abbott. "Liquid Crystal Interfaces

Programmed with Enzyme-Responsive Polymers and Surfactants.” *Small*, 2015, 11, 5747-5751. Copyright 2015 Wiley. Permission to use copyrighted images and data in the manuscript was also obtained from C. Derek Ma, Daniel S. Miller, Xiaoguang Wang, Nathan C. Gianneschi and Nicholas L. Abbott. The dissertation author was the co-first author on this manuscript.

Chapter 5 contains material that is currently being prepared for submission for publication: "Design of Triggerable Amphiphiles with Mesogenic Side-Chains for Multi-Scale Responses with Liquid Crystals," Joel Pendery, Lisa Adamiak, Jiawei Sun, Nathan C. Gianneschi, and Nicholas L. Abbott. The dissertation author was the co-first author on this pending manuscript.

VITA

2010	Bachelor of Science, Chemistry University of California, Santa Cruz
2013	Master of Science, Chemistry University of California, San Diego
2016	Doctor of Philosophy, Chemistry University of California, San Diego

PUBLICATIONS

Lisa Adamiak, Andrea J. Luthi, Clare M. LeGuyader, Sara Beck Pancer, Michael E. Hahn, Miriam Scadeng, Tomoko Hayashi, Dennis Carson, Nathan C. Gianneschi. “Enzyme-triggered Assembly of Peptide Brush Polymers.” (In preparation).

Lisa Adamiak, Nathan C. Gianneschi. “Peptide Brush Polymers and Nanoparticles for Evading and Activating Macrophage Uptake.” (In preparation.)

Joel S. Pendery, [†] Lisa Adamiak, [†] Jiawei Sun, Nathan C. Gianneschi, Nicholas L. Abbott. “Design of Triggerable Amphiphiles with Mesogenic Side Chains for Multiscale Responses in Liquid Crystals.” (In preparation).

Andrea S. Carlini, Lisa Adamiak, Nathan C. Gianneschi. “Biosynthetic Polymers as Functional Materials.” *Macromolecules* **49**, 4379–4394 (2016).*

Derek C. Ma, [†] Lisa Adamiak, [†] Daniel S. Miller, Xiaoguang Wang, Nathan C. Gianneschi, Nicholas L. Abbott. “Liquid Crystal Interfaces Programmed with Enzyme-Responsive Polymers and Surfactants.” *Small* **11**, 5747–5751 (2015).*

Carrie R. James, Anthony M. Rush, Thomas Insley, Lela Vuković, Lisa Adamiak, Peter Král, Nathan C. Gianneschi. “Poly(oligonucleotide).” *J. Am. Chem. Soc.* **136**, 11216–11219 (2014).

Jacquelin K. Kammeyer, Angela P. Blum, Lisa Adamiak, Michael E. Hahn, Nathan C. Gianneschi. “Polymerization of Protecting-Group-Free Peptides via ROMP.” *Polym. Chem.* **4**, 3929–3933 (2013).*

Michael E. Hahn, Lyndsay M. Randolph, Lisa Adamiak, Matthew P. Thompson, Nathan C. Gianneschi. “Polymerization of a Peptide-Based Enzyme Substrate.” *Chem. Commun.* **49**, 2873–2875 (2013).

([†]equal contribution, *cover article).

ABSTRACT OF THE DISSERTATION

**PEPTIDE BRUSH POLYMERS AS CONTROL ELEMENTS IN SOFT
MATERIALS AND LIQUID CRYSTALS**

by

Lisa Adamiak

Doctor of Philosophy in Chemistry

University of California, San Diego 2016

Professor Nathan Gianneschi, Chair

Recognition and cellular uptake by macrophages and ensuing clearance by the mononuclear phagocyte system (MPS) stands as a significant biological barrier for nanoparticle (NP) therapeutics. Here, we report a readily deployable method to prepare peptide brush polymers (PBPs) by ROMP, which are used to examine the effects of charge, size, and composition on macrophage uptake using RAW 264.7 cells. In our long-standing interest of developing enzyme-responsive systems, the polymers were encoded with multiple copies of a peptide substrate (GPLGLAG) for proteolytic enzymes specific to diseased or inflamed tissues. The incorporation of a permanent cation (quaternary amine) into the peptide

sequence further permitted water-solubility for homopolymers and facilitated formulation of discrete, uniform NPs formulated from block copolymers, which were also investigated. An enzyme-activatable cell uptake strategy is also reported by way of a zwitterionic-to-cationic charge switch using a model system.

Similarly, enzyme hydrolysis of *N*-terminus conjugated peptide brush polymers (NPBPs) was shown to promote the assembly of discrete, nanoscale cylindrical micelles, upon exposure of carboxylates on the polymer after proteolytic cleavage. In contrast, *C*-terminus conjugated PBPs (CPBPs), which are structural isomers of NPBPs and expose protonated amines when subjected to proteolysis, remain as fully dispersed polymers, as indicated by TEM. As an initial assessment of their behavior *in vivo*, intravenous (IV) and intratumoral (IT) injections of *N*- and CPBP analogues were performed in a metastatic and solid tumor model known to have elevated levels of matrix metalloproteases capable of cleaving peptide substrates on NPBP and CPBP. These systems incorporated a Gd-DOTA label for tracking as well as assessment of relaxivity properties by MRI.

In a separate application, peptide polymer amphiphiles (PPAs) were used to decorate liquid crystal (LC) microdroplets comprised of the nematic 5CB, in order to provide the basis for multi-length scale response systems. The PPAs were designed with biphenyl, mesogen-like side-chains to promote assembly at the LC microdroplet interfaces and peptidic moieties (GPLGLAG) capable of enzymatic processing by thermolysin. Enzymatic cleavage of the PPAs was shown to trigger changes in PPA-surfactant complexes formed at the interface of the LC, thus giving rise to an easily measured optical response. To improve the design of PPAs for triggering LC interfaces, a library of norbornyl mesogens was synthesized to study the nature of homopolymer and copolymer anchoring at the LC/aqueous interface. From these collective experiments, a set of design principles emerged that was then used to design an optimized PPA copolymer.

Chapter 1

Introduction

1.1 Introduction

1.1.1 Assembly across length scales

Multi-component assembly transcends many domains and length scales in nature.¹ One example is the virion, which varies in dimension from 10 to 10^2 nm, and consists of ordered structural arrangements of proteins, nucleic acids, and lipid membranes.² Supramolecular organization of these components is sufficient to build many copies of stable, symmetric virus particles, which are evolutionarily adapted to protect the viral genome and infect host cells. A eukaryotic cell exquisitely integrates these same biological components, and assembles them to give rise to a metabolically active machine ~ 10 μm in scale. Many natural systems also use self-assembly as a means to propagate molecular signals, resulting in unique macroscale responses.^{2,3} In the host defense mechanism of *Mimosa pudica*, or the “touch-me-not” plant, physical contact of the plant stimulates a rapid action potential cascade arranged by specialized motor organs (pulvini), which then provokes leaflet curling in a matter of minutes.^{4,5} This process is also reversible, leading to a recovery of turgor pressure as the flux of water and ions is directed back into pulvinar cells.⁶

By reducing down multiplex, dynamic systems, such as a cell or plant tissue, into a series of chemical reactions, self-assembly is the essential link for concerting processes across many length scales, from Ångström to meter length scale dimensions. Note that we broadly refer to “self-assembly” as a term borrowed from the field of supramolecular

chemistry, which defines the spontaneous organization of molecular components without outside interference.^{7,8} From a philosophical standpoint, and as a justification for its marked presence across disciplines such as molecular biology and organic chemistry, it may be reasoned that our ability to induce and direct self-assembly, especially of soft, non-crystalline materials, is the gap to our understanding life. The concept of self-assembly and its essential role in producing functional multi-component, natural systems has certainly motivated researchers to utilize assembly to develop fully synthetic or semi-synthetic mimics. As such, two kinds of self-assembly processes are studied: static and dynamic.⁷ Static assembly describes stable, non-energy dispelling systems that are at global or local equilibrium; while systems that fall under dynamic assembly are ones that dissipate energy to form well-ordered structures and patterns. In the latter case, such as a eukaryotic cell, the flux of energy must be sustained in the system to conserve steady-state populations of structures. The practical difficulty of achieving this in the laboratory has hindered progress for dynamic assembly; thus, static assembly is more broadly investigated. Nevertheless, recognizing the potential differences in structural ordering between assembly at thermodynamic equilibrium and non-equilibrium, researchers are increasingly striving to implement strategies such as kinetic control into their repository.⁹ As the more available form, static assembly has reported progress in a range of fields, such as electronic microfabrication,¹⁰ nanotechnology,^{11,12} auxetic protein arrays,¹³ molecular recognition,¹⁴⁻¹⁷ magnetic storage devices,¹⁸ colloid interfaces,¹⁹⁻²² zeolites and clay chemistry,²³⁻²⁶ scanning probe microscopy,^{27,28} and liquid crystals;^{29,30} among them a few intriguing accounts describe advancements towards rudimentary dynamic systems that, at present, are restricted to translational or rotational motors^{31,32} or oscillating chemical reactions.^{33,34}

1.1.2 Strategies towards the assembly of synthetic polymers

The most common fabrication method for the synthesis of structures on the nanoscale is utilizing thermodynamic control, in other words, relying on the total gain in entropy due to the hydrophobic effect.³⁵ A so-called “bottom-up” approach is used in this case to generate stable structures, which occupy thermodynamic minima. In contrast, a “top-down” approach relies on utilizing techniques such as lithography (used for the fabrication of microelectronic devices), which can be employed to reproduce nanostructures of various sizes (especially in the micrometer range) with narrow dispersity.^{10,36} Directed self-assembly of macromolecules by the former typically relies on the phase separation of amphiphilic block copolymers to form discrete nanostructures usually in the 10-100 nm range.³⁷⁻³⁹ Further, continuous hierarchical structures can be designed by increasing the number of blocks in copolymer architectures⁴⁰⁻⁴² or through chemical reduction post-polymerization.⁴³ The main strategy for preparing high molecular weight molecules of this type is through covalent polymerization, which, for reasons that will be discussed in a later section (see section 1.2 on biosynthetic polymers), are mostly limited to producing materials with limited control over polymer sequence and architecture. Nonetheless, compared to small amphiphilic molecules, block copolymers prepared by this method can organize into sophisticated assemblies and offer versatility in terms of their synthesis (molecular weight, composition, hydrophobic: hydrophilic ratio, and block sequences).^{39,44,45}

A number of studies utilizing theoretical models and empirically determined phase diagrams relating a given morphology to block copolymer composition has enabled some predictive power over the construction of different shape and size nanomaterials;^{46,47} though this is still a challenge, especially in the context of kinetically controlled assemblies.^{48,49} Aside from the most widely generated and studied morphology, the spherical micelle, the fabrication of nanomaterials displaying exotic morphologies such as vesicles,⁵⁰ toroids,⁵¹

fibers,⁵² and other assemblies⁵³ have also been reported.⁴⁹ In regards to their use in biological systems, most of these nanostructures are incompatible as delivery vehicles for therapeutic or targeted agents, for reasons that will be discussed in section 1.4.

A second class of methods used towards the assembly of synthetic systems, coined by Whitesides, is “self-organizing syntheses,” which relies on weak and less directional bonds, such as ionic, hydrogen bonding, and van der Waals interactions, to organize molecules into higher-order structures.³ Examples of these include liquid crystals,⁵⁴ colloids,⁵⁵ micelles,⁴⁴ emulsions,^{56,57} Langmuir Blodgett films,^{58,59} and assembled monolayers.^{59–62} These systems have been used for a multitude of applications but the ones that will be the focus of this chapter are liquid crystalline materials (described further in section 1.3), which offer opportunities specifically towards the development of multi-scale response systems. In this regard, integrating amphiphilic polymers with liquid crystals may enable progress towards dynamic systems fueled by molecular changes at liquid crystal interfaces.

1.1.3 Enzyme-responsive materials as emerging dynamic systems

Recognizing the tightly regulated spatial and temporal control afforded by natural systems to regulate assembly, researchers are continually seeking to develop laboratory-based approaches, which can enable reproducible bottom-up syntheses of nanostructures. One motivating concept consists of the exploitation of biological catalysts such as enzymes to control assembly.⁶³ To this end, the investigation of enzyme-driven gelation provides a straightforward and observable process that can be analyzed for the occurrence of topological defects.³⁴ For example, by modifying reaction conditions, specifically enzyme concentrations, Ulijn and coworkers demonstrated that the formation of assemblies can be kinetically

directed to form structurally distinct supramolecular products occupying thermodynamic minima.⁶⁴

Proteases have been used to direct the assembly of *N*-(fluorenyl-9-methoxycarbonyl) (Fmoc)-protected dipeptides through hydrolysis⁶⁵ or condensation⁶⁶ of amide bonds. Though proteolytic cleavage can be an irreversible process; biological systems reconcile the need for reversing biochemical pathways by employing the same enzyme as both protease and ligase through control of substrate concentrations, or at times by using a pair of enzymes with opposed functions such as phosphatases (dephosphorylation) and kinases (phosphorylation in the presence of ATP).³ Utilizing this concept, imaging intracellular⁶⁷ or extracellular⁶⁸ assembly processes in live cells was demonstrated using enzyme-triggered hydrogelation of small molecule precursors. For example, Xu and coworkers induced supramolecular assembly from the dephosphorylation of Fmoc-protected tyrosine residues.⁶⁵ Moreover, the combination of phosphorylation and proteolysis can provide dual-handles to which control over nanoparticle morphology (i.e. shape) is enabled.⁶⁹

Overall, the concept of enzyme-driven assembly not only advances the discovery of peptide-based nanofabrication approaches but also provides a method for amplifying molecular events that can be transduced over macroscopic length scales. Enzyme-triggered supramolecular gelation from simple, non-gelating constituents is but one category that serves these objectives. Given the structural complexity and functional group versatility offered by synthetic polymers, a more intriguing, albeit difficult, approach is to direct the assembly of polymeric precursors.⁶³ To the best of our knowledge, there are only three examples demonstrating this concept either with abiotic polymers,⁷⁰ caged peptide-polymer conjugates,⁷¹ or with water-soluble block copolymers.⁷² Related to the previous discussion of static nanostructure assembly, the underutilization of polymers in this context arises from the difficulty in controlling polymer architecture as well as predicting the structural dynamics of

their assemblies.⁷³ Nevertheless, the design of any number of diverse polymeric constructs offers an untapped potential for realizing dynamic systems, which can interface with biological systems in more purposeful ways than previously documented. In section 1.2, the status of functional biosynthetic polymers is described, along with a discussion of innovative strategies reported within the past five years that have made great strides in overcoming the aforementioned barriers.

1.2 Biosynthetic polymers as functional materials

1.2.1 Introduction to biosynthetic polymers

The structure and function of biopolymers found in nature has evolved over the past few billion years to form the underpinnings of life. Biosynthetic polymeric materials exemplify the diversity accessible through synthesis and semi-synthesis that is inspired by and utilizes biopolymers (Figure 1.1a).

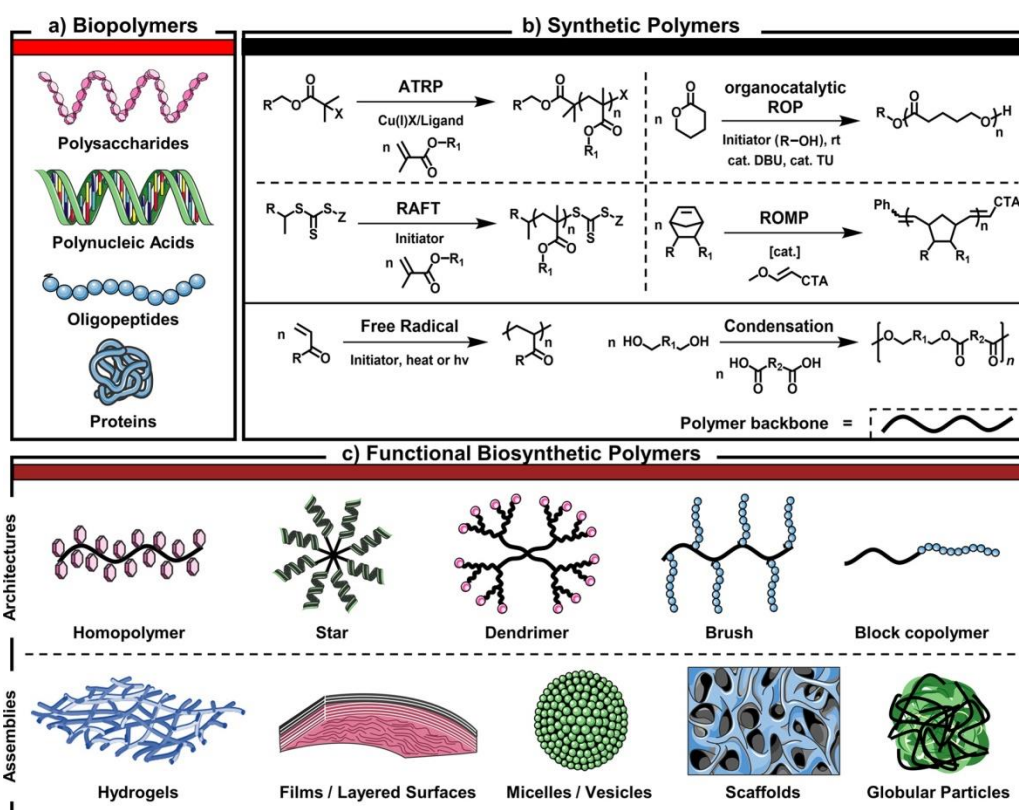


Figure 1.1 Various architectures of functional biosynthetic polymers *via* the conjugation of natural and synthetic moieties. (a) Biopolymers (polysaccharides, polynucleic acids, oligopeptides, and proteins) and their building blocks (nucleotides, monosaccharides, and amino acids) may be combined with (b) synthetic polymers (black) *via* a variety of polymerization methods. Representative controlled chain growth polymerization methods are depicted above uncontrolled versions. (c) The resulting functional biosynthetic polymers may act as an unstructured conjugate with various architectures or conjugate assemblies.

Hancock and Ludersdorf prepared the first artificial polymer in 1840, through treatment of natural rubber with sulfur to create a tough and elastic material.⁷⁴ It was another century before significant advances in polymer chemistry would enable the production of totally synthetic and complex polymeric materials. Within the past few decades, biologically compatible synthetic materials have emerged as one of the most exciting and prolific fields in polymer chemistry due to the widespread adoption of living and controlled polymerization methods (Figure 1.1b). These materials, herein referred to as biosynthetic polymers, are now used for a multitude of applications such as novel biomolecule stabilizers, drug-delivery vehicles, therapeutics, biosensors, biomedical adhesives, antifouling materials, and biomimetic scaffolds.⁷⁵⁻⁷⁸

Biosynthetic polymers are materials that combine synthetic components with biopolymers or moieties prepared as mimics of those found in nature (Figure 1.1c).⁷⁹ These materials consist of (a) synthetically modified biopolymers, such as functionalized hyaluronic acid derivatives⁸⁰ or labeled proteins via cellinstruction.⁸¹ In the prior case concerning biopolymers such as polysaccharides or proteins, wherein reactive sites (amine, hydroxyl, thiol, carboxylic acid) are conventionally present as multiple copies, site-specific conjugation (*graft-to*) and subsequent purification are typically difficult (Figure 1.2). Other categories of biosynthetic polymers that enable more precise control over advanced architectures, functionalization, and subsequently dynamic function are (b) biomolecules conjugated to synthetic polymers produced by various grafting strategies (i.e. *graft-to*, *graft-through*, and *graft-from*) (Figure 1.2);^{82,83} or (c) bioinspired or fully synthetic polymers that act as biopolymer surrogates, which execute similar functions and occasionally exceed the performance of biopolymers.⁸⁴ Considerable effort has been directed toward increasing the precision by which biomolecules are incorporated into polymers - in other words, expanding the so-called “bioconjugate toolbox.”⁸⁵⁻⁸⁷ With the advent of “click”-type chemistries, that is,

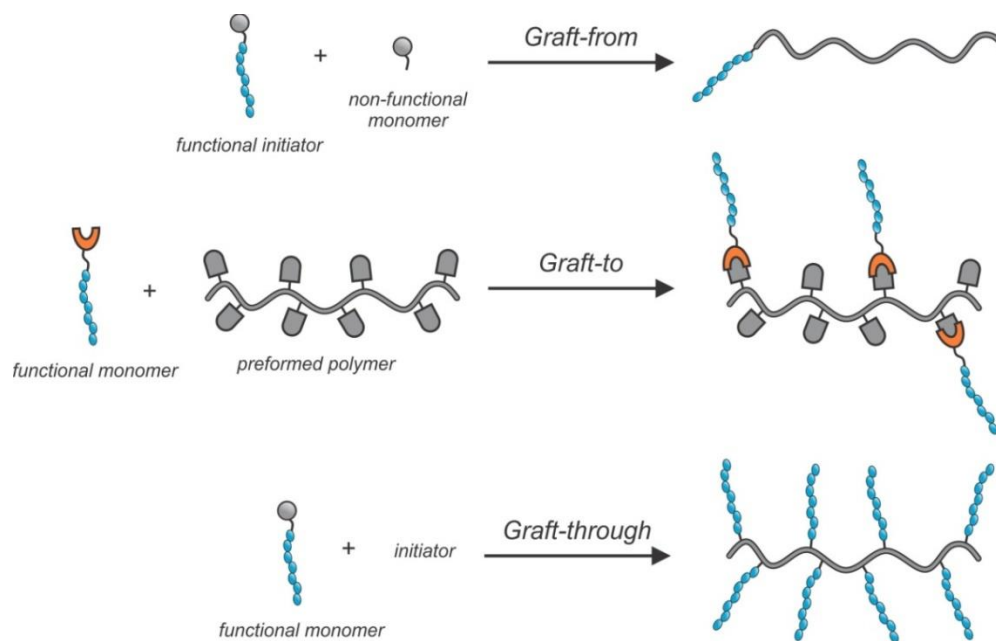


Figure 1.2 Various grafting strategies used for the preparation of biosynthetic polymers. In this schematic, a biopolymer such as a peptide is denoted by the blue oligomer while the synthetic constructs are shown in grey. The orange component represents a “clickable” moiety to enable post-polymerization conjugation of a biopolymer to a preformed synthetic polymer.

oxime,^{88,89} Staudinger ligation,^{90,91} thiol-ene,⁹² copper-catalyzed azide-alkyne cycloaddition (CuAAC),⁹³ and strain-promoted azide/alkyne click (SPAAC),⁹⁴ among others,⁹⁵⁻⁹⁷ biomolecule-polymer conjugates are not only readily attainable but achieve high fidelity. There are many reports that document interesting advancements in this regard but what is highlighted in this subsection are paradigm shifts in the development of functional biosynthetic polymers.

Recent works that will be discussed address two of the most significant problems, which still hinder progress in the field of functional biosynthetic polymers: (1) architecture control of synthetic components and (2) structural dynamics of polymer assemblies. The third prevalent problem in this context is the biostabilization (storage, release, and bioresistance) of therapeutic cargos; though this issue will not be discussed here. Most systems utilize

controlled polymerization methods for addressing previously unmet challenges in architecture control and functional complexity, with some exceptions in which uncontrolled polymerization methods are necessary for simplicity and expense mitigation. The first subsection will discuss fundamental advances in polymer chemistry toward controlling primary sequence, tacticity, and functionality *via* grafting, which are paramount for the execution of complex biological functions, as demonstrated by the precise stereoregularity of biopolymers (i.e., proteins and DNA). The next two subsections highlight significant progress made in advanced bulk functionality of unstructured and/or assembled biosynthetic polymers.

Provided the number of articles that detail incremental advances in functionalization methods using various stimuli-responsive moieties, a comprehensive discussion is not included here but provided are several published reviews on these topics.^{85,98,99} Throughout section 1.2, the merits of simple formulations for designing highly functional biosynthetic polymers are discussed. The conclusion gives a projected outlook on further progress in the field that hinges on the ability to overcome recurring limitations. In this context, our creative efforts to equate to what evolution has perfected are just beginning. In the foreseeable future, further advancements may no longer rely on copying nature for solutions but rather emerge from the limits of our own imagination.

1.2.2 Architecture control: primary sequence

The basic informational biopolymers from which all life on earth is built are carbohydrates, nucleic acids, and proteins,¹⁰⁰ with noninformational biogenic polymers such as melanins making tremendous functional contributions.¹⁰¹ Biological organisms are capable of producing biopolymers with extreme complexity and high fidelity and accuracy, while using robust machinery and only a handful of simple monomers including saccharides, nucleotides, amino acids (and their derivatives), other metabolites, and fatty acids.^{2,100}

Naturally, our current knowledge and abilities in the field of polymer chemistry pale in comparison to that achieved by billions of years of evolution. Nonetheless, researchers have devoted substantial efforts to synthesize polymers using libraries of novel monomers possessing different physical and chemical properties with diversities far beyond those prevalent in biological systems. Furthermore, strategic organization of these polymeric monomers can enhance the polymer complexity and overall mode of action.^{102,103} In this way, semisynthetic or fully synthetic materials may be tailored to mimic the highly versatile and functional properties of biopolymers. The following discussion focuses on current efforts to increase the control of polymer architecture as well as microstructure such as the specific arrangement of monomer sequence and stereoisomers.

Controlled polymerizations may be iterative, step growth, or chain growth in mechanism. In contrast to the others, chain growth strategies generally lack control over primary sequence despite controlled polymerization techniques. The discovery of living polymerizations by Michael Szwarc in 1956 was the first breakthrough in chain growth methods, whereby growth of a polymer chain proceeds at a constant rate, affording polymers with narrow molecular weight distributions or low dispersity.¹⁰⁴ For the synthesis of precisely controlled polymers, the majority of suitable methods encompass reversible-deactivation radical polymerization (RDRP), including (a) Atom Transfer Radical Polymerization (ATRP), Single-Electron Transfer Living Radical Polymerization (SET LRP)^{105,106} or Supplemental Activator and Reducing Agent (SARA),^{107,108} Activators Regenerated by Electron Transfer (ARGET),^{109–111} Electrochemically mediated ATRP (eATRP),^{112,113} photoinduced ATRP (Photo-ATRP),^{114,115} and Metal-free Photoinduced Electron Transfer ATRP (PET-ATRP),¹¹⁶ and (b) Reversible Addition–Fragmentation Chain Transfer (RAFT) Polymerization, with alternatives such as PET-RAFT,^{117,118} (c) Iniferter Polymerization,¹¹⁹ and (d) Nitroxide Mediated Polymerization (NMP).^{120–123} Other well-characterized methods

include Ring-opening Polymerization (ROP), with common variants including organocatalyzed,¹²⁴ anionic,^{125–127} coordination–insertion,¹²⁸ enzymatic,^{129,130} *N*-carboxyanhydride Polymerization,^{131,132} and Ring-opening Metathesis Polymerization (ROMP),¹³³ with alternatives such as alternating ROMP (AROMP)^{134–136} and metal-free ROMP.¹³⁷

With uncontrolled polymerization methods, one is restricted by limited primary sequence and architecture control. Despite the expansive inventory of controlled polymerization methods available, there is still no equivalent to the kind of sequence control afforded by solid phase synthesis first pioneered by R. B. Merrifield, even with the foremost controlled polymerization methods.¹³⁸ Manual or automated iterative strategies have been used to synthesize sequence-controlled polymers;¹³⁹ however, these approaches are impractical as they incur the expenses of unsustainable methods and time. Regardless, stepwise approaches are still the only known process for developing sequence-controlled polymers for tuning properties such as single-chain morphologies.¹⁴⁰ Meanwhile, efforts to develop streamlined chemistries are imperative; as such, there have been some recent achievements toward the ability to control primary sequence. For example, Hawker and co-workers reported a new strategy for ROMP of sequence-controlled polymers using a macrocyclic monomer containing distinct ABCDE-type moieties.¹⁴¹ Prior to this work, efforts to synthesize sequence-controlled polymers via multisubstituted cyclooctadienes using ROMP have been limited in number and types of incorporated functionalities.^{142,143} During chain extension, the growing polymer sequence obtained ordered repeats of ABCDE units along a polyester backbone. To achieve this, the authors used a small molecule polymerization trigger derived from saccharin to synthesize an unstrained macrocycle. Close proximity of the macrocycle olefin to a terminal alkyne enabled fast intramolecular

cyclization and subsequent rapid ROMP with Grubbs third generation catalyst (G3) (Figure 1.3).

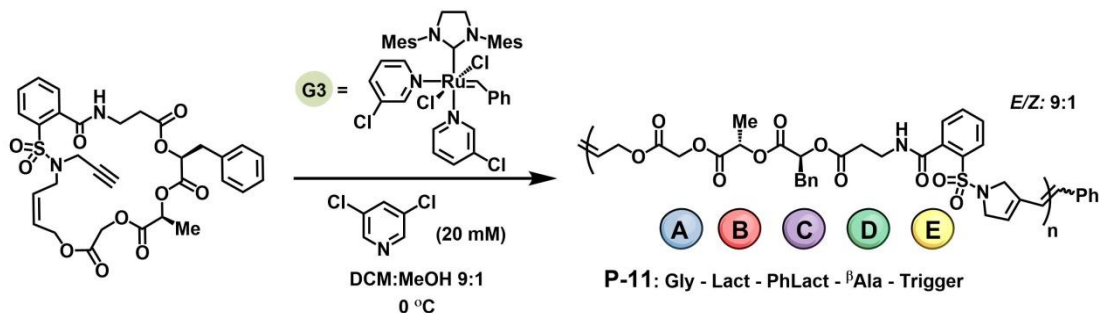


Figure 1.3 Strategy for the polymerization of unstrained macrocycles enabling primary sequence control. Monomers are composed of a ROMP polymerization trigger attached to a series of glycolate (Gly), (S)-lactate (Lact), (S)-phenyllactate (PhLact), and β-alanine (β Ala).

This work demonstrates a general synthetic strategy for ROMP of diverse repeat units such as ester, sulfonamide, heterocyclic, etc., incorporated within the polymer backbone. The strategy also provides one of the few known methods for synthesizing fully biodegradable ROMP polymers,¹⁴⁴ a recurring challenge with highly functionalized biosynthetic polymers. Improvements in the AROMP method were also reported recently. Several examples describe iterative monomer addition by Ru-promoted isomerization of bicyclo[4.2.0]oct-7-ene-7-carboxamides¹³⁶ or *via* living copolymerization of 1,1-disubstituted cyclopropenes with low-strain cyclic olefins.¹³⁵ Though there is a great need for further improvement, especially in the context of tailoring these methods toward increased chemical diversity and demonstrated biofunctionality, these approaches chronicle an exciting movement toward efforts to control the primary sequence of copolymers.

1.2.3 Tacticity control

Biopolymers containing tertiary and quaternary structures mediate a wide array of complex biological processes due to the preservation of their stereochemistry. It is known

that the relative stereochemistry of individual units of polymers, or tacticity, can significantly impact the physical and chemical properties of synthetic polymers.¹⁴⁵ Even so, stereoregulation remains a barrier for precise control of polymer structure. In a recent example by the Johnson group, an iterative exponential growth (IEG)-inspired approach was demonstrated for the economically scalable synthesis of sequence- and stereocontrolled unimolecular polymers.¹⁴⁶ In this IEG plus side chain functionality strategy, 1R and 1S epoxy alkynes were either subjected to azide substitution followed by functionalization or to deprotection in order to afford species that were coupled efficiently by CuAAC “click” chemistry, generating four different epoxy–alkyne diastereomers (Figure 1.4). These “dimers” were then matched appropriately to synthesize macromolecules with the desired tacticity through multiple cycles of azide-instructed epoxide opening, alkyne deprotection, and subsequent CuAAC click conjugation. Comparison of thermogravimetric analysis data for isotactic and syndiotactic hexadecamers revealed subtle differences in thermal properties, namely the glass transition temperatures (T_g), suggesting that differences in intermolecular polymer interactions were at play. This method demonstrated the scalable synthesis of a 6300 Da syndiotactic polymer; however, the final product was recovered in approximately 1 week. In order to minimize the length of time required, semiautomated synthesis by Flow-IEG offers a favorable application of this method toward primary sequence and architecture control.¹⁴⁷

With the increasing interest in tacticity control in mind, polymer chemists are actively pursuing advances in conventional chain growth methods. By improving control over primary structure and tacticity, more detailed analyses can be made to understand the correlation between these parameters and macromolecular assembly and function, thus bringing synthetic capabilities closer to the complexity afforded by nature.

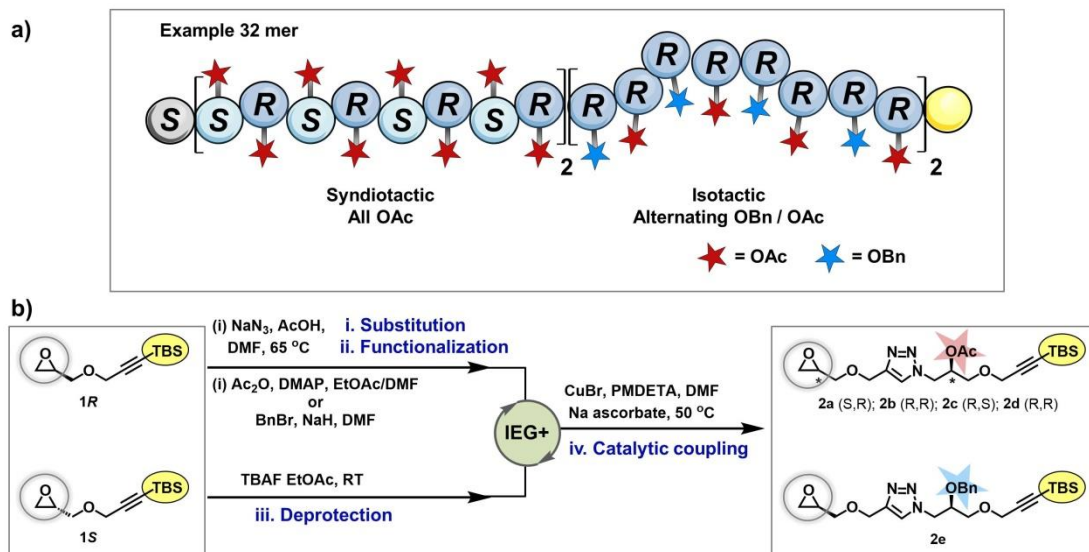


Figure 1.4 IEG-inspired iterative synthesis of sequence and stereocontrolled polymers. (a) Example of a 32-mer prepared by (b) orthogonal azidification, functionalization and silyl deprotection of two chiral monomers (1S, 1R) followed by CuAAC “click” of key stereoisomeric intermediates to generate polymers with precise sequences and stereochemistry.

1.2.4 Grafting control

While researchers are investigating novel methods for finely tuning polymer primary sequence, controlled polymerization strategies enable the incorporation of complex biomolecules that, in themselves, possess absolute sequence control. Therefore, by gaining excellent control over biomolecule graft polymers, materials are generated with 2-dimensional architectural control, including the polymer backbone and side chains as a biologically interactive system. In this subsection, we highlight the impact of 2-dimensional architectures on biological mode of action.

Efforts have been directed at the expansion of *graft-through* methodologies with ROMP in order to avoid the large kinetic barrier implicit in post-polymerization conjugation of macromolecules. Successful conjugation of macromolecules is limited by steric hindrance, which often results in variable degrees of grafting, difficult purification and low

reproducibility of polymer bioconjugates. As such, considerable effort in our group has been devoted toward the direct polymerization of complex peptides,¹⁴⁸ nucleobases,¹⁴⁹ bioderived polyesters,¹⁵⁰ imaging agents,¹⁵¹ and therapeutic drugs.¹⁵² These biosynthetic polymers possess extreme complexity with rigorous control over polymer assembly and in some cases biofunctionality as tumor targeting¹⁵³ and protease resistant materials.¹⁵⁴ In particular, protected and/or deprotected peptide-based monomers, which range in size from 5 to 30 amino acids, can be polymerized into dense brushes as homopolymers¹⁵⁵ or amphiphilic block copolymers that self-assemble into micellar nanoparticles.¹⁵⁶ This modular approach allows very large peptides of any given sequence to be polymerized in the presence of the bipyridyl modified, Grubbs second generation catalyst. Attachment of 6-aminohexanoyl spacers to separate the polymerizable norbornene subunit from the peptide sequence further enhances polymerization rates, maintains low dispersity, and enables higher degrees of polymerization of biomacromonomers. Other strategies that incorporate complex functionality may rely on a *grafting from* approach, such as the preparation of high-chain density cylindrical copolypeptide brushes, *via* two rounds of *N*-carboxyanhydride polymerization in a one-pot procedure, with controlled segment lengths.¹⁵⁷ Accompanying the unmistakable advantage that *graft-through* and some *graft-from* strategies present for generating highly dense peptide polymers,¹⁵⁸ unique modes of action may be accessed, such as restricted proteolytic degradation.¹⁵⁴

Regardless of which strategy is utilized, varying polymer architecture *via* grafting has the potential to modulate biological function. For instance, Sumerlin and co-workers used *graft-to* polymer bioconjugates in order to improve the therapeutic function of osteoprotegerin (OPG), which is a protein that restricts osteoclast formation and subsequently bone resorption in accelerated bone loss disorders.¹⁵⁹ Specifically, the role of side chain grafting density was examined for OPG-polymer bioconjugates using linear, loosely

branched, and densely branched poly(ethylene glycol) (PEG) architectures. Modest restoration of bone mineral density was achieved for the loosely branched conjugate/analogue in comparison to the other architectures. In another example, Tew and co-workers synthesized bioinspired protein transduction domain mimics with varying degrees of hydrophilic guanidine and hydrophobic phenyl group segregation.¹⁶⁰ Three types of polymers were analyzed for their membrane affinity and cellular internalization characteristics: non-segregated homopolymers, intermediately segregated gradient copolymers, and strongly segregated block copolymers. Gradient copolymers with intermediate segregation displayed the highest activity and solubility with low cytotoxicity. Insight from this structure–activity survey was used for efficient siRNA delivery and gene knockdown in human T cells.¹⁶¹ Thus, architecture control *via* selective grafting strategies can potentially improve efficacy of biosynthetic polymers, depending on the function required.

Researchers are becoming increasingly aware of the importance of architecture^{39,99,162} and tacticity¹⁶³ in multi-component assembly. Precise control over both stereo- and regiochemistry may accelerate opportunities for regulating geometries such as polymer tertiary and quaternary structures. Just as nature employs DNA and RNA sequences to encode biological information, and harnesses protein tertiary and quaternary structures to confer specialized activities, so too can researchers aspire to use semisynthetic or fully synthetic polymers for the preparation of artificial viruses or enzymes, or cofactors in cascade pathways. Further, the ability to directly polymerize large biomolecules has the advantage of loading dense arrays of information. This contrasts with previous synthetic efforts of post-polymerization modification, which have little sequence control, lower grafting densities, and are often difficult to characterize. Achieving complex sequences using simple synthetic methods is paramount; continued efforts in this regard will undoubtedly surpass practically tenuous methods in the movement toward synthetic biological mimics.

1.2.5 Stimuli for directed assembly of biosynthetic polymer materials

Complexing biosynthetic polymers into assemblies can increase their versatility and function. For example, nano- and micrometer scale particles, vesicles, films, and hydrogels have been developed using self-assembled polymers.¹⁶⁴⁻¹⁶⁶ Polymeric assemblies encompassing these architectures have been developed for various functions including stabilizing internal cargos, slowing clearance within biological systems, performing as supportive scaffolds, and/or serving as vehicles for signaling and detection. Many research groups have sought to develop assemblies with environmentally adaptive characteristics and therefore have devoted efforts to develop stimuli-responsive biomaterials for triggered signaling,¹⁶⁷ drug release,⁷⁸ and/or degradation.⁹⁵ Motivations for this aim arise from the desire to mimic natural behaviors like blood clotting and wound healing. However, controlling structurally dynamic behaviors within these assemblies is still difficult. Success along this avenue can advance previously unrealized opportunities for functionally diverse materials that surpass the limited utility of structurally inert designs. A notable example in this regard is the enhanced therapeutic efficacy of assemblies with active targeting capabilities compared to ones with passive abilities at low doses.¹⁶⁸ Nonetheless, in the interest of translating these systems for use in biological systems, increasing functional complexity without forfeiting synthetic simplicity is necessary.

The clinical relevance of shape-changing biosynthetic polymers has been demonstrated in both a myocardial infarction (MI) and a fibrosarcoma tumor model.^{152,153,156,169} In post-MI treatment specifically, developing systems capable of noninvasive delivery and heart retention for periods longer than 1 week is currently a significant challenge. By utilizing discrete fluorescent nanoparticles that can enzymatically assemble into aggregated scaffolds, researchers observed a signal enhancement for the targeted diseased tissues relative to healthy tissue (Figure 1.5). Matrix metalloproteinases

(MMPs), which are overexpressed in areas of severe inflammation, cleave the peptides displayed on the nanoparticle surface. A shift in the polymer amphiphilicity, a consequence of proteolytic cleavage of hydrophilic peptide fragments, then causes nanoparticle reassembly into micron-scale aggregates in the infarct tissue.

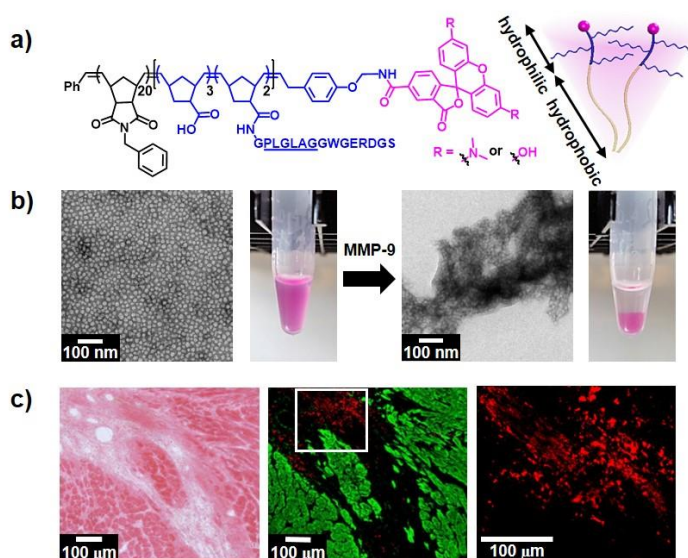


Figure 1.5 Enzyme-responsive peptide–polymer amphiphiles change shape in response to biological stimulus. (a) Diagram of a dye-labeled brush peptide–polymer amphiphile (PPA) bearing an MMP-9 specific recognition sequence, shown underlined. PPAs self-assemble into nanoparticles through hydrophobic–hydrophilic interactions when dialyzed into aqueous buffer. (b) Responsive nanoparticles aggregate in response to enzymatic cleavage by TEM. (c) Injection of particles into an infarcted heart (left) result in infarct-specific aggregation and retention over healthy tissue by fluorescence (middle and right). Scale bar: 100 μm.

These enlarged aggregates are slow to clear, which prolongs their tissue retention and enhances diagnostic ability by way of the colocalization of fluorogenic material with the site of damage. Retention of these materials within infarcted tissue up to 28 days was observed, which greatly exceeds insufficient retention times of hours to days observed with other active-targeting nanoparticle formulations.^{170,171} A similar shape-changing system demonstrated active cargo release of bound drugs at the site of scaffold assembly in a fibrosarcoma tumor model.¹⁵² These proof-of-concept works demonstrate exceptional utility

achieved by the dynamic morphological response of enzyme-responsive micellar assemblies in two ways: first as a discrete vehicle for noninvasive intravenous delivery and second as a stationary scaffold for diagnostics and localized drug release.

Alternative stimuli, such as temperature or pH, have been shown to provoke changes in peptide-based particle assemblies. In one example, researchers developed a “nanopeptifier” system, which relies on thermally triggered assembly of elastin-like polypeptide amphiphiles containing a cell-penetrating peptide (CPP) domain on the hydrophilic block.¹⁷² Once assembled into micelles, the high density CPP surface array enhances cellular uptake. To assess therapeutic payload delivery, a proapoptotic peptide was attached to the hydrophobic domain; the resulting nanopeptifier acts as a dynamic switch, inducing apoptosis only in micellar form above the lower critical solution temperature (LCST). In another example by Savin and co-workers, poly(L-lysine)-b-poly(propylene oxide)-b-poly(L-lysine) triblock copolymers containing different lysine fractions were found to adopt distinct morphological transitions, either spherical micelle to vesicle or spherical micelle to disk micelle structures, as a function of pH.¹⁷³ Dynamic morphologies like this may have the capacity to alter *in vivo* biodistribution and shape-change induced drug release or targeting.

Despite increasing efforts for instilling stimuli-responsiveness in polymeric assemblies, some basic questions governing the spatial organization of these assemblies still remain. Specifically, how does conformational fluidity of a biofunctional polymer assembly impact its interaction at biological interfaces, in contrast to inert analogues? For example, amphiphilic block copolymers are promising in their use as artificial biological membranes, which are known to stabilize membrane proteins.¹⁷⁴ An interesting observation emerged from this study by Meier and co-workers, which determined that high flexibility of poly-(dimethylsiloxane)-containing block copolymers may be responsible for successful integration of model membrane proteins despite mismatches in their hydrophobic domain

sizes. As such, the identity of block copolymers within an assembly must be carefully considered when designing biomimetic membranes and analogous systems.

Within the past several decades, interest in dynamic biosynthetic polymers has expanded and with it so have new approaches to develop materials that encompass both the complex functions intrinsic to natural biomolecules and tunable capabilities like stimuli responsiveness built into synthetic polymers. By introducing dynamic complexity into polymeric assemblies such as nanoparticles discussed herein, or even hydrogels, elastomers, adhesives, and foams, we may build a better understanding of biological processes that govern tissue assembly and preservation. Ideally, these mimetic polymeric scaffolds could emulate the physical properties of natural, soft and hard tissues to afford wound healing, tissue regeneration, and load-bearing support; or offer opportunities towards systems that propagate information across length scales in sensing applications.

1.3 Signal transduction using liquid crystals

1.3.1 Liquid crystal materials

Liquid crystals (LCs) are a state of matter that is contingent upon non-covalent interactions between molecules for directing orientations within condensed phases (Figure 1.6).¹⁷⁵ LCs are widely recognized for their use in liquid crystal displays, which is arguably the most successfully applied technology that utilizes a responsive, soft material. In this case, an applied electric field is able to change the molecular orientation of the bulk LC, thus causing a change in its optical appearance. Contributing to their unique properties, LC phases consist of principal, rod-like molecules, called mesogens, that are capable of long-range orientational ordering (Figure 1.6B).¹⁷⁶ The crystalline-like behavior and high mobility of LCs enable this and many unifying characteristics (described further in this subsection) despite the large chemical diversity of their mesogenic constituents.

Liquid crystals are classified according to their phase behavior. For example, liquid crystals are characterized as thermotropic when the temperature of the system directs the phase behavior.¹⁷⁷ Alternatively, the phase behavior of lyotropic (and as a subset, chromonic) liquid crystals depends on the nature of solvent added. Though other types of phases have emerged from within these two categories of liquid crystals,^{178–180} the greatest progress has been achieved in studies of liquid crystals in the nematic phase. Herein, the discussion is limited to nematic LCs.

The thermotropic liquid crystal, pentyl cyanobiphenyl (5CB) (Figure 1.6B), consists of a high weight-percent of aromatic rings, which imparts the bulk LC with crystalline-like behavior, contributing to anisotropic and dielectric mechanical properties as well as optical birefringence.¹⁷⁷ Owing to the linear aliphatic component of the 5CB structure, mesogens within the LC are also able to diffuse *via* rotational or translational motion and rapidly reorganize (Figure 1.6B). The combination of these two characteristics enables 5CB to adopt a director (\mathbf{n}), in other words, an average orientation, in the nematic LC phase that spans several orders of magnitude larger than dimensions on the molecular scale.¹⁷⁷ Since the intermolecular forces that underscore the formation and organization of LCs are easily perturbed and can be coupled to an optical output, LCs are increasingly explored as the basis of chemical and biological sensors.^{175–177} Further, in the interest of developing materials capable of propagating information across length scales, many researchers have focused their efforts on designing interfaces that can bind to specific stimuli and lead to surface-actuated changes, propagating reorganization throughout the bulk LC material.

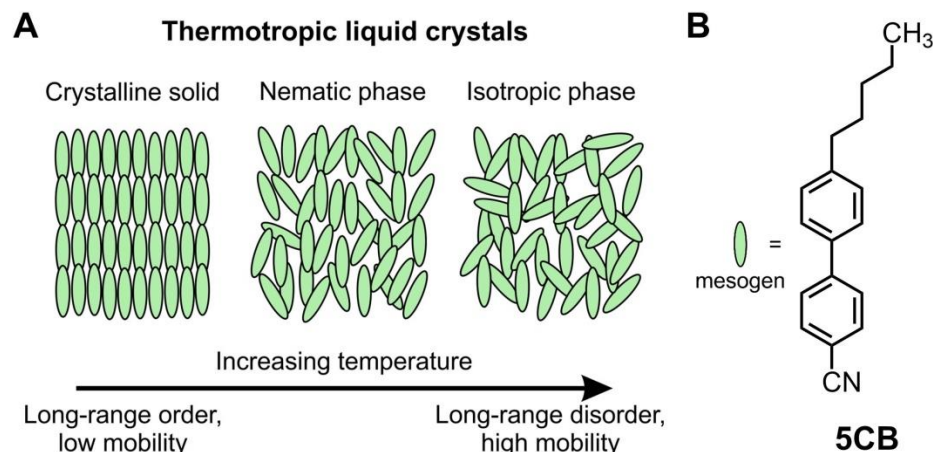


Figure 1.6 Thermotropic liquid crystals exhibit temperature-dependent phase behaviors. (A) Illustration of the various LC phases such as crystalline, nematic, and isotropic as a function of increasing temperature. (B) Chemical structure of a thermotropic liquid crystal, pentyl cyanobiphenyl, (5CB), which forms a nematic phase at room temperature (the phase transition temperature for 5CB is 22 °C from crystalline to nematic and 35 °C from nematic to isotropic).

1.3.2 Liquid crystal emulsion droplets as a sensing platform

Many examples of LC-based optical platforms have been developed to identify the presence of biomolecules, such as DNA,¹⁸¹⁻¹⁸³ oligopeptides,^{184,185} proteins,¹⁸⁶ viruses¹⁸⁷ and phospholipids,¹⁸⁸ and even support and analyze the growth of cells.¹⁸⁹ Many of these sensors are confined to planar films on the order of 1- to 20- micrometers in thickness, and are suited for studying the response of LCs to chemically-functionalized solids. These LC-solid interfaces, when compared to LC-aqueous interfaces, such as those found in LC droplet in aqueous emulsions, are disadvantageous for biomolecule sensing for several reasons. First, LC-aqueous interfaces are more deformable than LC-solid interfaces.¹⁷⁶ The greater motility of mesogens at the LC-aqueous interface is thus able to better accommodate lateral reorientation of biomolecules upon binding to LC surfaces. Second, water is a required solvent for proper biomolecule folding and function, and also enables the transport of biological analytes to the LC-aqueous interfaces. Third, the initial director configuration of

LC emulsion droplets is dictated by the chemistry of the LC interface and not by surface treatments required for planar LC films.¹⁹⁰ Fourth, the elastic strain energy of LCs can affect the assembly of amphiphilic molecules at the LC-aqueous interface, leading to interfacial phases not observed for LC-solid interfaces.¹⁹¹ Fifth, tailoring the response of LC emulsions (director configuration) to the presence of specific analytes can be achieved by modifying the size of the droplet (which affects the elastic strain of the LC).¹⁹² Finally, suspensions of LC emulsions can be readily handled and analyzed using microfluidic devices.¹⁹³ For these reasons, LC-in-water emulsions are rapidly emerging as a biomolecule-sensing platform and have been used to report the presence of a variety of analytes such as surfactants,^{194,195} lipids,^{194,196} proteins,¹⁹⁷ gram-negative bacteria,¹⁹⁸ and positively charged dendrimers.¹⁹⁹ The responses of water-dispersed LC droplets to a variety of molecular species has defined a new set of opportunities available for the design of active materials based on LCs.

1.3.3 Detecting molecular events at liquid crystal interfaces

LCs confined within spherical droplets in water will arrange themselves to minimize the free energy of the system from three principal considerations: (i) surface anchoring, (ii) elastic strain in the bulk, and (iii) topological defects.¹⁹² Related to the discussion in the previous section, these energetic contributions differ substantially between LCs confined in planar films and spherical droplets, enabling improved opportunities for biomolecule sensing using LC emulsions.¹⁷⁷

In the presence of water, the LC in the nematic phase aligns tangential (or planar) to the droplet interface and exhibits a configuration known as bipolar (Figure 1.7).¹⁷⁵ In the bipolar orientation, two diametrically opposed point defects (termed boojums) form at the poles of the droplet (Figure 1.7B). When surfactants adsorb to the LC surface, a bipolar-to-

radial geometry transition occurs; in other words, the LC reorients perpendicular (or homeotropic) to the droplet interface (Figure 1.7B).

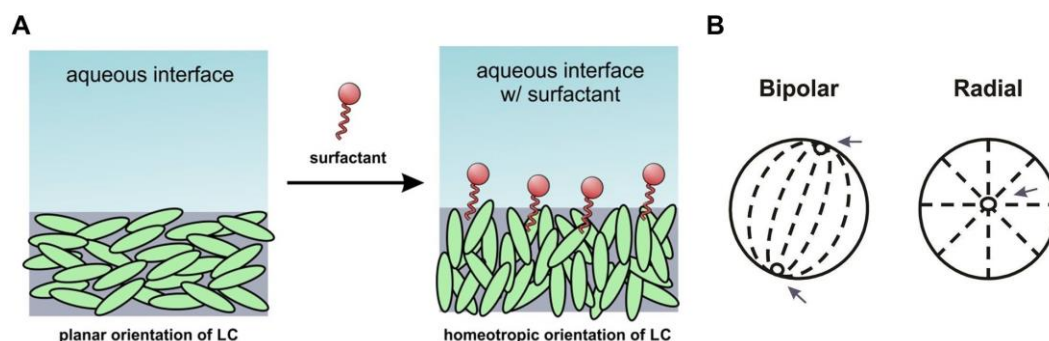


Figure 1.7 A change in LC orientation is induced by binding of a surfactant to the LC surface. (A) Illustration depicting the orientation of mesogens (parallel or planar orientation) at the LC-aqueous interface in water (left) and their reorganization (homeotropic or perpendicular orientation) in the presence of an adsorbate (right). (B) Schematic showing bipolar (left) and radial (right) configurations of micrometer-sized droplets of a nematic liquid crystal. Arrows indicate the point defects located at the poles of the droplet (for bipolar) and at the center of the droplet (for radial). The director (\mathbf{n}) for each configuration are also indicated (dotted lines) depicting the planar orientation of the LC (for bipolar) and perpendicular orientation of the LC (for radial).

The interactions between adsorbents and LC interfaces are largely dictated by the sterics of the hydrophobic portion of the adsorbent and the LC. Ordering transitions resulting from these interactions can be visualized using optical microscopy. Due to their birefringent nature (exhibiting two different refractive indices), nematic LCs can rotate plane polarized light and appear as a bright signal when viewed under crossed polarizers in an optical microscope.¹⁷⁷ Though conventional surface-driven changes in the orientational ordering of LCs is widely studied; another possible mechanism for triggering changes in LC geometries involves the assembly of amphiphilic surfactants at nanoscopic point defects.¹⁹⁶ Intriguingly, Abbott and coworkers found that picomolar concentrations of endotoxin were able to perturb LC ordering, and that in general, transitions in LC configuration were dependent on lipid

architecture.²⁰⁰ Studies of amphiphile structure-based selective ordering at LC interfaces provides a collection of principles with which to design new responsive materials.

LC droplets confined within spherical droplets in the optimal size range for sensing (1 to 10 μm) can be readily prepared *via* a variety of methods, the most common being ultrasonification.²⁰¹ Emulsification in the presence of a synthetic or biological amphiphile can lead to the spontaneous formation of decorated LC droplets capable of reporting on the presence of analytes in solution. For example, Gupta and coworkers demonstrated that 5CB droplets decorated with the phospholipid L-DLPC can undergo enzymatic cleavage reactions with phospholipase A₂, facilitating desorption of the enzymatically-processed lipid from the LC interface and causing a radial-to-bipolar ordering transition.¹⁹⁴ Researchers have also demonstrated that functionalization of poly(ethyleneimine)-coated LC droplets with glutaraldehyde followed by conjugation to the antibody immunoglobulin G (igG) provided an immunoassay platform in which to visualize fluorescent anti-igG binding to igG.¹⁹⁷ In this example, the surfactant, Tween 20, was used in the treatments and provoked radial-to-bipolar ordering transition upon anti-igG binding, potentially due to Tween 20 rearrangement at the LC-aqueous interface.¹⁹⁴

In the context of biological sensors, it remains difficult to predict and characterize the molecular-level interactions occurring at these types of complex interfaces. In contrast to biologically-responsive systems, chemically-responsive LC sensors such as those used in gas sensing surfaces and technologies, are well characterized.²⁰²⁻²⁰⁴ Though these previous studies have highlighted opportunities for the utility of LCs in biosensing applications, the first challenge in this field is to ascertain the rules for organizing molecules at LC interfaces. The second challenge is utilizing these assemblies for triggering changes in LC orientational ordering in a controlled manner.

1.4 Obstacles for the use of nanomaterials in biomedical applications

1.4.1 Nanomaterials at biological interfaces

Injectable nanomaterials have gained considerable interest in the last two decades in the field of medicine due to their versatility as therapeutic carriers and favorable pharmacokinetic properties. Established since the 1980s from studies of polymer-drug conjugates and proposed as the reason for the success of the first tested liposomal carriers; the “enhanced permeability and retention” (EPR) effect is the principal hypothesis given to the observed phenomenon that macromolecules extravagate and accumulate in solid tumors to a greater extent than in normal tissue, notably observed in subcutaneous xenograft small rodent models of the human disease state.^{205–207} The physiology of tumor tissue differs substantially from that of normal tissue; for example, tumor tissue can be highly vascularized and in certain models can consist of poor vascular architecture and defective lymphatic drainage. It is primarily these characteristics that are thought to enable the EPR effect for nanomaterials, at least in the case of model systems *in vivo*. A highly debated topic, the EPR effect is, nevertheless, universally invoked as the mechanism of action for both passive and active targeting systems, despite modest improvements in therapeutic index routinely observed in practice.²⁰⁸

The advent of new strategies for nanoparticle (NP) preparation, principally using controlled syntheses of biosynthetic polymers, have led to an enormous expansion of opportunities towards improving NP delivery.²⁰⁹ Much of this progress has been realized in the development of stimuli-responsive materials for active targeting.⁸⁵ However, the interactions moderating the biological passage of nanomaterials throughout a living system remain largely indefinite and nanomaterial-dependent, which necessitates continued

investigations into NP-specific structure-function relationships (Figure 1.8).^{210,211} That is, active targeting or retention within tissues has largely been the focus, with many of these strategies failing because of unfavorable interactions with blood proteins and phagocytic cells before targeting can occur. A good example showcasing the realistic threat that nanomaterials impose on human health rests with the widespread use of asbestos as building insulators in the 1940s, which led to a growth in cases of lung disease caused by the accumulation of respirable needle-like fibers.²¹² Nevertheless, nanotechnology is perceived as part of the future in medical diagnosis and treatment. However, understanding the molecular basis for NP-biological interactions is crucial to its success and it is precisely our understanding of that interface that remains poorly understood and generally underappreciated.

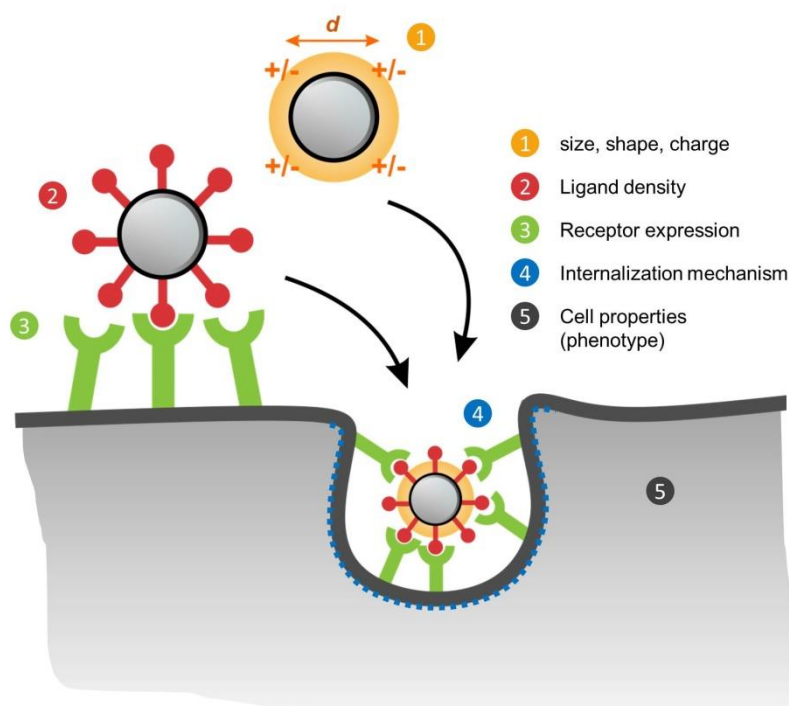


Figure 1.8 The interactions between nanoparticles and a cell at the cell-NP interface. Shown is a list of nanomaterial properties that can influence these interactions. Figure is adapted from Chan and coworkers.²¹³

There are three key problems which prevent the use of most nanomaterial constructs in the clinic: (i) opsonization, the process by which proteins recognize and bind to a nanomaterial surface, blocking any active targeting ligands, changing surface charge and defining the pharmacokinetic profile beyond what may have been initially intended;²¹⁴ (ii) immune activation by inciting the complement system (also related to the first problem);²¹⁴⁻²¹⁶ and (iii) premature removal by the mononuclear phagocytic system (MPS).^{214,217-219} The intimate relationship between these processes have made it extremely difficult to elucidate specific factors contributing to one without the other. For example, the complement system, which is central to the host immune response (i.e. attenuating inflammatory responses and identifying the presence of pathogens), is thought to play a determining role in the activation of acute allergic reactions after the administration of nanomedicines.²¹⁶ Clinical evidence from studies of liposomal-based vehicles involving animal models (dogs and pigs) as well as human trials have established indicators of acute immune reactions such as haemodynamic responses (hyper- or hypotension)^{220,221}, respiratory issues.²²² or hand-foot (H-F) syndrome.²²³

Within the complement system, three pathways (classical, alternative, or lectin) generate distinct mechanisms that are responsible for activating specific complement proteins, the central one being C3.^{224,225} When the complement system elicits an immune reaction, the protein C3 is cleaved into its corresponding fragments, C3b and iC3b, which are immediately opsonized to the nanomaterial surface.²¹⁶ Once bound to the surface, these constituent proteins then undergo a conformational change to active forms which illicit recognition by phagocytes bearing complement receptors such as monocytes or macrophages from hepatic (Kupfer cells), or splenic marginal zone and red-pulp regions.^{216,226} This process aids in identification of foreign material and subsequent removal from circulation.²¹⁴ An additional mechanism of phagocytic recognition involves non-specific binding to opsonins associating with hydrophobic domains on the NP surface.^{214,227} These types of opsonins

consist of complement factors such as C4, C5, immunoglobulin, as well as blood components such as fibronectin, albumin, type I collagen, and others.²²⁸ Considering that the key aim of nanomedicine is to widen the therapeutic index *via* targeted delivery, uncontrolled immune activation by the complement system can actually aggravate the pathology of nanomaterial target sites.²²⁹ For example, the C5a complement protein enhances tumor growth by suppressing the CD8⁺ T-cell anti-tumor response.²³⁰ Overall, the intricate composition of opsonins coating NP surfaces, the so called “protein-corona,” has complicated the current understanding of cell-NP interactions.²³¹

For polymeric NPs that are above the renal clearance threshold (~10 nm diameter), general accumulation of NPs in MPS organs occurs *via* endocytosis by phagocytes.²³² Following endocytosis, oxidative degradation proceeds in endosomes by secretion of superoxide, nitric oxide, and hydrogen peroxide.^{214,233} This process can be particularly ineffective for non-biodegradable systems, resulting in long-term storage in MPS organs. As such, many chronic symptoms of NP retention emerge such as inflammation, dysfunctional phagocytosis or the development of mesothelioma are reported for inorganic NPs.^{234–236} The physiochemical properties of polymers (degree of polymerization, architecture, hydrophobicity, and chemical functionality) and nanomaterials (morphology, hydrodynamic diameter, surface topology and chemistry) are important for regulating activation by the complement, avoiding opsonization, and macrophage evasion; though each of these features may incite activation *via* different pathways. This, in turn, requires decoupling the material properties for investigating their individual effects. Often, this is practically difficult to achieve with the current methods available for polymer and nanomaterial preparations (see section 1.1 and 1.2 for description of methods used to prepare nanostructures and biosynthetic polymers, respectively). Since opsonization and subsequent phagocytosis can occur on the time scale of seconds to hours following systemic infusion,²¹⁴ most research in the area

involving NP vehicle development for drug delivery focuses on mitigating these two issues. From these surveys, a number of parameters have been correlated with opsonization and macrophage uptake such as NP size,^{237,238} NP shape,^{239,240} flow dynamics of hard materials,²⁴¹ and NP surface functionalization;^{226,237} though, many of these studies employ gold NPs,^{226,227,242–247} which may differ in their biological responses compared to those of organic-based nanomaterials.²⁴⁸

1.4.2 Mitigating recognition by macrophages and enhancing NP targeting

Among the physiochemical considerations described above, the most widely adopted for the inhibition of opsonization and production of long-circulating nanomaterials is *grafting to* or adsorbing poly(ethylene glycol) to a nanomaterial surface, processes collectively known as PEGylation.²¹⁴ For example, DOXIL® is the first FDA-approved nanomaterial, is a PEGylated liposomal formulation encapsulating doxorubicin, to be used for the treatment of cancer.^{249–251} While effective, it is known to cause acute hypersensitivity reactions upon first exposure.²⁵² The non-pegylated form Myocet® was developed in response to this issue, which exhibited a similar therapeutic index as DOXIL® but presented reduced side effects.²⁵³ Nevertheless, PEG is perceived as the standard in stealth-promoting modifications, despite additional evidence that points to its conflicting benefits for reasons that will be discussed later.

Due to the possibility of unprotected surface coverage from the desorption of PEG molecules (in the adsorption strategy), the more common approach is to covalently bind PEG to the surface.^{214,254} It has been shown that surface density and chain length of PEG affect its shielding capability.²⁵⁵ To elaborate, the mechanism by which PEG was initially thought to prevent opsonization was through PEG chain compression caused by the influx of opsonins attempting to associate with the NP surface. This PEG compression then promotes steric

strain, preventing opsonin binding. It is now speculated that PEG derives its non-fouling (protein-resistance) characteristics through multivalent hydrogen bonds formed between its ether functional groups and water molecules.²⁵⁶ This in turn causes PEG to adopt a balloon-type conformation, which prevents protein access through an impenetrable water barrier. Theoretical calculations for the free energy as a function of PEG chain length and density indicate that long chain lengths and high density are optimal for protein resistance, with PEG density being a larger contributing factor.²⁵⁵ This finding is corroborated by empirical studies, which demonstrate that chain length correlates with productive shielding and circulation time; as well as surface coverage on the effect of PEG conformation-dependent stealth.²⁵⁷ PEG is typically grafted alone but Feng and coworkers demonstrated that when used synergistically with another stealth-like polymer such as water-soluble chitosan,²⁵⁸ PEG was able to reduce macrophage sequestration and improve circulation time *in vivo*; specifically, resulting in measured circulation half-lives ($t_{1/2}$) of 63.5 h and 1.1 h for the combinatorial and control materials, respectively.

Despite the consistency in its utilization as a stealth-promoter, PEGylation is highly controversial, with arising concerns of its correlation with chronic hypersensitivity.²⁵⁹ Furthermore, in the interest of developing materials with biological-responsiveness, the protein-resistant property of PEG may in fact be detrimental to bioactivity. For example, Keefe and Jiang demonstrated that a model protein (α -chymotrypsin (α CT)) conjugated to PEG exhibited lower substrate affinities (measured as the Michaelis constant, K_m) as a function of α CT concentration.²⁶⁰ Comparatively, conjugation of α CT to a zwitterionic polymer, poly(carboxybetaine) (pCB), preserved bioactivity and stabilized α CT to a greater extent than the PEG conjugate counterpart after 8 h incubation in urea. Indeed, efforts to navigate away from PEG are becoming more common;²⁶¹ although these alternatives may also face uncertainties such as the immunotoxicity detected for NPs coated with pCB.²⁶²

Nonetheless, the exploration of other functionalities such as trehalose, a nonreducing disaccharide, has led to its discovery as an extremely effective protein- and poly(nucleic acid)-stabilizing expient.^{263,264} Additional examples warrant further investigation, such as charged betaine-type polymers²⁶⁵ or non-ionic polymers such as poly(vinyl alcohol),²⁶⁶ polysaccharides,^{263,264,266,267} poly(*N*-vinyl-2-pyrrolidone),²⁶⁸ poly(*N*-(2-hydroxypropyl)methacrylamide) (HPMA),^{269,270} or poly(oxazoline),^{271–273} (Figure 1.9).

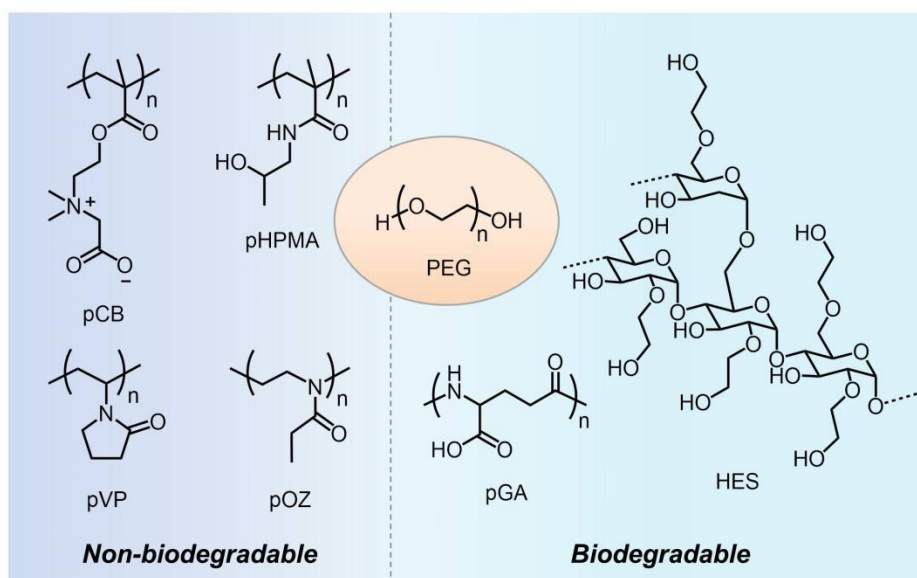


Figure 1.9 Examples of alternative surface modifications to PEGylation. Non-biodegradable versions are shown: poly(carboxybetaine) (pCB); poly(*N*-(2-hydroxypropyl)methacrylamide) (HPMA); poly(vinyl alcohol) (pVP); and poly(oxazoline) (pOZ). Biodegradable versions are depicted: polysaccharides such as hydroxyethyl starch (HES) and poly(glutamic acid) (pGA).

In the last several decades, consensus in the field dictated that opsonization was overall a detrimental process towards NP circulation *in vivo*. This concept permeated rapidly across different strategies required for protein-resistant materials, exemplified by the use of PEG. However, a recent study by Wurm and coworkers revealed that opsonization of specific proteins was actually a requirement for stealth.²⁷⁴ For example, when used to modify polystyrene-based nanoparticles, PEG was able to affect the composition of opsonins bound

to the NP surface, namely through the recruitment of clusterin proteins, which then prevented non-specific cellular uptake. To examine this further, the PEG-modified NPs were incubated with clusterin proteins and subjected to treatment with macrophage cells. The results demonstrated that a “pre-coating” stealth layer was formed, preventing binding by non-productive opsonins and cellular internalization. Other groups have examined whether pre-coating NPs with different types of opsonins could be used to direct protein corona formation and non-specific cellular uptake. Interestingly, pre-coating NPs with immunoglobulins and complement proteins, which are known ligands that bind to macrophage receptors to provoke phagocytosis, did not increase NP uptake by macrophage cells.²⁷⁵ Immunolabeling experiments further indicated that competitive interactions between other opsonins within the protein corona obstructed binding to macrophage receptors. These studies have challenged the current understanding of opsonization and how it relates to the biological fate of nanomaterials.^{231,276}

Other strategies for avoiding macrophage recognition have emerged that bypass the manipulation of protein corona or conjugation to hydrophilic polymers. One such strategy is the incorporation of “self-peptides” based on the CD47 membrane protein, which avoids macrophage uptake by signaling the phagocyte receptor CD172a.²⁷⁷ Another unique method by Zhang and coworkers utilized a top-down approach to coat polymeric NPs with natural erythrocyte membranes, enabling long-circulation following injection.²⁷⁸ Inspiration has also been taken from the ability of pathogenic organisms, such as *Pseudomonas aeruginosa*, to prevent immune recognition by virtue of their hydrophilic or densely-packed glycosylated membrane surfaces.^{279,280} As a major component, sialic acid glycans can interact with the regulatory protein factor H, which then prevents activation of the alternative pathway in the complement system.²⁸¹ Phage-displayed libraries of peptides that bind to factor H also represent an effective strategy for identifying possible peptide-based candidates for

improving the biocompatibility of nanomaterials.²⁸² Through this technique, the cyclic tridecapeptide, Compstatin®, was discovered as a highly potent inhibitor of the complement protein C3 and is now being tested in clinical trials for the treatment of macular degeneration.²⁸³ These strategies chronicle an intriguing possibility to label foreign materials with “indicators of self” *via* the incorporation of natural motifs.

The promise of nanotechnology in medicine continues to push the discovery of novel strategies to mitigate the aforementioned biological barriers (complement activation, opsonization, and non-specific cellular uptake), which have prevented the viability of nanomaterial usage in the clinic. Despite significant advancements to mitigate these issues, a provocative, recent study by Chan and coworkers concluded that of all the collected data from the last decade, only 0.7 % of an administered NP dose (median efficiency) is able to reach a solid tumor.²⁸⁴ This is considerably lower than the proposed 1-10 % figure proposed previously. Even more astonishing is the finding that active targeting systems contribute to a meager 0.3 % increase in NP delivery compared with passive analogues. Indeed, these findings have initiated a serious dialogue within the scientific community about the potential ineffectiveness of NP delivery approaches.²⁸⁵ As one example, many protocols used by researchers to determine toxicity or stability of a nanomaterial in serum are not standardized, leading to incomparable results across different laboratories.²⁸⁶ Consider also the immunotoxicity of PEG that some groups have reported while others have not, as previously mentioned.²⁵⁹ Nevertheless, this discussion provides an important opportunity to specify the ways nanomaterials should be evaluated. Indeed, similar controversies have arisen over small molecule drugs and the fact that they too are difficult to predict, prepare and deploy despite many years of development and the stature of traditional medicinal chemistry as a mature field. Living systems are exceptionally complex, and we simply do not have a precise handle to which the interface between tissues and synthetic materials are studied. The key is to

remain inspired by the possibilities and maintain an attitude that multidisciplinary approaches and collaborations with neighboring fields will open doors for the field itself and for biomedicine alike.

1.5 Acknowledgements

Chapter 1 is adapted, in part, from Andrea S. Carlini, Lisa Adamiak, and Nathan C. Gianneschi. "Biosynthetic Polymers as Functional Materials." *Macromolecules*, 2016, 49, 4379-4394. Copyright 2016 American Chemical Society. Permission to use copyrighted images and text in the manuscript was also obtained from Andrea S. Carlini and Nathan C. Gianneschi. The dissertation author was the second author on this manuscript.

1.6 References

- (1) Mann, S. *Biomineralization: principles and concepts in bioinorganic materials chemistry*; Oxford University Press, 2001.
- (2) Voet, D.; Voet, J. G. *Biochemistry*, 3rd ed.; John Wiley & Sons, 2004.
- (3) Alberts, B.; Johnson, A.; Lewis, J.; Raff, M.; Roberts, K.; Walter, P. *Molecular Biology of the Cell*, 4th ed.; Garland Science: New York, 2002.
- (4) Monshausen, G. B.; Gilroy, S. *Trends Cell Biol.* **2009**, *19* (5), 228.
- (5) Wilson, M. E.; Makshev, G.; Haswell, E. S. *Biochemistry* **2013**, *52* (34), 5708.
- (6) Naismith, J. H.; Booth, I. R. *Annu. Rev. Biophys.* **2012**, *41*, 157.
- (7) Whitesides, G. M.; Grzybowski, B. *Science* **2002**, *295* (5564), 2418.
- (8) Ariga, K.; Hill, J. P.; Lee, M. V.; Vinu, A.; Charvet, R.; Acharya, S. *Sci. Technol. Adv. Mater.* **2008**, *9* (1), 14109.
- (9) Moore, J. S.; Kraft, M. L. *Science* **2008**, *320* (5876), 620.
- (10) Ruiz, R.; Kang, H.; Detcheverry, F. A.; Dobisz, E.; Kercher, D. S.; Albrecht, T. R.; de Pablo, J. J.; Nealey, P. F. *Science* **2008**, *321* (5891), 936.
- (11) Meng, F.; Zhong, Z.; Feijen, J. *Biomacromolecules* **2009**, *10* (2), 197.

- (12) Mastroianni, S. E.; Epps, T. H. *Langmuir* **2013**, *29* (12), 3864.
- (13) Suzuki, Y.; Cardone, G.; Restrepo, D.; Zavattieri, P. D.; Baker, T. S.; Tezcan, F. A. *Nature* **2016**, *533* (7603), 369.
- (14) So, C. R.; Liu, J.; Fears, K. P.; Leary, D. H.; Golden, J. P.; Wahl, K. J. *ACS Nano* **2015**, *9* (6), 5782.
- (15) Manzanera, M.; Frankel, D. J.; Li, H.; Zhou, D.; Bruckbauer, A.; Kreutzmann, P.; Blackburn, J. M.; Abell, C.; Rayment, T.; Klenerman, D.; Barker, P. D. *Nano Lett.* **2006**, *6* (3), 365.
- (16) Crowley, J. D.; Goshe, A. J.; Bosnich, B. *Chem. Commun.* **2003**, *100* (22), 2824.
- (17) Drechsler, U.; Erdogan, B.; Rotello, V. M. *Chem. - A Eur. J.* **2004**, *10* (22), 5570.
- (18) Whittell, G. R.; Manners, I. *Adv. Mater.* **2007**, *19* (21), 3439.
- (19) Park, B. J.; Lee, D. *Small* **2015**, *11* (35), 4560.
- (20) Kozina, A.; Ramos, S.; Díaz-Leyva, P.; Castillo, R. *J. Phys. Chem. C* **2016**, *120* (30), 16879.
- (21) Bradley, L. C.; Stebe, K. J.; Lee, D. *J. Am. Chem. Soc.* **2016**, *138* (36), 11437.
- (22) Lotito, V.; Zambelli, T. *Langmuir* **2016**, *32* (37), 9582.
- (23) Bergaya, F.; Jaber, M.; Lambert, J.-F. In *Rubber-Clay Nanocomposites*; John Wiley & Sons, Inc.: Hoboken, NJ, USA, 2011; pp 1–44.
- (24) Huang, L.; Wang, Z.; Sun, J.; Miao, L.; Li, Q.; Yan, Y.; Zhao, D. *J. Am. Chem. Soc.* **2000**, *122* (14), 3530.
- (25) Corma, A.; Rey, F.; Rius, J.; Sabater, M. J.; Valencia, S. *Nature* **2004**, *431* (7006), 287.
- (26) Lin, J.-J.; Chen, Y.-M.; Tsai, W.-C.; Chiu, C.-W. *J. Phys. Chem. C* **2008**, *112* (26), 9637.
- (27) Barker, E. C.; Goh, C. Y.; Jones, F.; Mocerino, M.; Skelton, B. W.; Becker, T.; Ogden, M. I. *Chem. Sci.* **2015**, *6* (11), 6133.
- (28) Sumpter, B. G.; Liang, L.; Nicolai, A.; Meunier, V. *Acc. Chem. Res.* **2014**, *47* (11), 3395.
- (29) Park, J. H.; Kim, K. H.; Park, Y. W.; Lagerwall, J. P. F.; Scalia, G. *Langmuir* **2015**, *31* (34), 9432.

- (30) Bellini, T.; Zanchetta, G.; Fraccia, T. P.; Cerbino, R.; Tsai, E.; Smith, G. P.; Moran, M. J.; Walba, D. M.; Clark, N. A. *Proc. Natl. Acad. Sci.* **2012**, *109* (4), 1110.
- (31) Davies Wykes, M. S.; Palacci, J.; Adachi, T.; Ristroph, L.; Zhong, X.; Ward, M. D.; Zhang, J.; Shelley, M. J. *Soft Matter* **2016**, *12* (20), 4584.
- (32) Li, J.; Rozen, I.; Wang, J. *ACS Nano* **2016**, *10* (6), 5619.
- (33) Zhou, H.; Liang, E.; Ding, X.; Zheng, Z.; Peng, Y. *Chem. Commun.* **2012**, *48* (85), 10553.
- (34) Epstein, I. R.; Xu, B. *Nat. Nanotechnol.* **2016**, *11* (4), 312.
- (35) Whitesides, G. M.; Mathias, J. P.; Seto, C. T. *Science* **1991**, *254* (5036), 1312.
- (36) Venkataraman, S.; Hedrick, J. L.; Ong, Z. Y.; Yang, C.; Ee, P. L. R.; Hammond, P. T.; Yang, Y. Y. *Adv. Drug Deliv. Rev.* **2011**, *63* (14–15), 1228.
- (37) *Complex Macromolecular Architectures*; Hadjichristidis, N., Hirao, A., Tezuka, Y., Du Prez, F., Eds.; John Wiley & Sons (Asia) Pte Ltd: Singapore, 2011.
- (38) Bates, F. S.; Fredrickson, G. H. *Phys. Today* **1999**, *52* (2), 32.
- (39) Bates, F. S.; Hillmyer, M. A.; Lodge, T. P.; Bates, C. M.; Delaney, K. T.; Fredrickson, G. H. *Science* **2012**, *336* (6080), 434.
- (40) Chatterjee, J.; Jain, S.; Bates, F. S. *Macromolecules* **2007**, *40* (8), 2882.
- (41) Liu, H.-H.; Huang, C.-I.; Shi, A.-C. *Macromolecules* **2015**, *48* (17), 6214.
- (42) Meuler, A. J.; Hillmyer, M. A.; Bates, F. S. *Macromolecules* **2009**, *42* (19), 7221.
- (43) Tureau, M. S.; Epps, T. H. *Macromolecules* **2012**, *45* (20), 8347.
- (44) Halperin, A. J. *Macromol. Sci. Part C Polym. Rev.* **2006**, *46* (2), 173.
- (45) Patterson, J. P.; Robin, M. P.; Chassenieux, C.; Colombani, O.; O'Reilly, R. K. *Chem. Soc. Rev.* **2014**, *43* (8), 2412.
- (46) Won, Y.-Y.; Brannan, A. K.; Davis, H. T.; Bates, F. S. *J. Phys. Chem. B* **2002**, *106* (13), 3354.
- (47) Jain, S.; Bates, F. S. *Science* **2003**, *300* (5618), 460.
- (48) Barnhill, S. A.; Bell, N. C.; Patterson, J. P.; Olds, D. P.; Gianneschi, N. C. *Macromolecules* **2015**, *48* (4), 1152.
- (49) Lodge, T. P. *Macromol. Chem. Phys.* **2003**, *204* (2), 265.

- (50) Discher, D. E.; Eisenberg, A. *Science* **2002**, 297 (5583), 967.
- (51) Pochan, D. J.; Chen, Z.; Cui, H.; Hales, K.; Qi, K.; Wooley, K. L. *Science* **2004**, 306 (5693), 94.
- (52) Qian, J.; Zhang, M.; Manners, I.; Winnik, M. A. *Trends Biotechnol.* **2010**, 28 (2), 84.
- (53) Zhang, L.; Eisenberg, A. *Science* **1995**, 268 (5218), 1728.
- (54) Tschierske, C. *Angew. Chemie Int. Ed.* **2013**, 52 (34), 8828.
- (55) Hiemenz, P. C.; Rajagopalan, R. *Principles of colloid and surface chemistry.*; Marcel Dekker, 1997.
- (56) Morikawa, M.; Yoshihara, M.; Endo, T.; Kimizuka, N. *Chem. - A Eur. J.* **2005**, 11 (5), 1574.
- (57) Bai, S.; Pappas, C.; Debnath, S.; Frederix, P. W. J. M.; Leckie, J.; Fleming, S.; Ulijn, R. V. *ACS Nano* **2014**, 8 (7), 7005.
- (58) Ungar, G.; Tschierske, C.; Abetz, V.; Holyst, R.; Bates, M. A.; Liu, F.; Prehm, M.; Kieffer, R.; Zeng, X.; Walker, M.; Glettner, B.; Zywockinski, A. *Adv. Funct. Mater.* **2011**, 21 (7), 1296.
- (59) Shao, J.-J.; Lv, W.; Yang, Q.-H. *Adv. Mater.* **2014**, 26 (32), 5586.
- (60) Badia, A.; Lennox, B.R.; Reven, L. *Acc. Chem. Res.* **2000**, 33 (7) 475.
- (61) Ulman, A. *Chem. Rev.* **1996**, 96 (4), 1533.
- (62) Prime, K.; Whitesides, G. *Science* **1991**, 252 (5009) 1164.
- (63) Hahn, M. E.; Gianneschi, N. C. *Chem. Commun.* **2011**, 47 (43), 11814.
- (64) Hirst, A. R.; Roy, S.; Arora, M.; Das, A. K.; Hodson, N.; Murray, P.; Marshall, S.; Javid, N.; Sefcik, J.; Boekhoven, J.; van Esch, J. H.; Santabarbara, S.; Hunt, N. T.; Ulijn, R. V. *Nat. Chem.* **2010**, 2 (12), 1089.
- (65) Yang, Z.; Gu, H.; Fu, D.; Gao, P.; Lam, J. K.; Xu, B. *Adv. Mater.* **2004**, 16 (16), 1440.
- (66) Toledano, S.; Williams, R. J.; Jayawarna, V.; Ulijn, R. V. *J. Am. Chem. Soc.* **2006**, 128 (4), 1070.
- (67) Gao, Y.; Shi, J.; Yuan, D.; Xu, B. *Nat. Commun.* **2012**, 3, 1033.
- (68) Zhou, J.; Du, X.; Berciu, C.; He, H.; Shi, J.; Nicastro, D.; Xu, B. *Chem* **2016**, 1 (2), 246.

- (69) Ku, T.-H.; Chien, M.-P.; Thompson, M. P.; Sinkovits, R. S.; Olson, N. H.; Baker, T. S.; Gianneschi, N. C. *J. Am. Chem. Soc.* **2011**, *133* (22), 8392.
- (70) Rao, J.; Hottinger, C.; Khan, A. *J. Am. Chem. Soc.* **2014**, *136* (16), 5872.
- (71) Kühnle, H.; Börner, H. G. *Angew. Chemie Int. Ed.* **2009**, *48* (35), 6431.
- (72) Amir, R. J.; Zhong, S.; Pochan, D. J.; Hawker, C. J. *J. Am. Chem. Soc.* **2009**, *131* (39), 13949.
- (73) Carlini, A. S.; Adamiak, L.; Gianneschi, N. C. *Macromolecules* **2016**, *49* (12), 4379.
- (74) Günay, K. A.; Theato, P.; Klok, H.-A. In *Functional Polymers by Post-Polymerization Modification*; Wiley-VCH Verlag GmbH & Co. KGaA: Weinheim, Germany, 2013; pp 1–44.
- (75) Khan, F.; Tanaka, M.; Ahmad, S. R. *J. Mater. Chem. B* **2015**, *3* (42), 8224.
- (76) Theato, P.; Sumerlin, B. S.; O'Reilly, R. K.; Epps, III, T. H. *Chem. Soc. Rev.* **2013**, *42* (17), 7055.
- (77) Muskovich, M.; Bettinger, C. J. *Adv. Healthc. Mater.* **2012**, *1* (3), 248.
- (78) Blum, A. P.; Kammeyer, J. K.; Rush, A. M.; Callmann, C. E.; Hahn, M. E.; Gianneschi, N. C. *J. Am. Chem. Soc.* **2015**, *137* (6), 2140.
- (79) Poole-Warren, L. A.; Patton, A. J. In *Biosynthetic Polymers for Medical Applications*; 2016; pp 3–31.
- (80) Vasi, A.-M.; Popa, M. I.; Butnaru, M.; Dodi, G.; Verestiuc, L. *Mater. Sci. Eng. C* **2014**, *38*, 177.
- (81) Ngo, J. T.; Schuman, E. M.; Tirrell, D. A. *Proc. Natl. Acad. Sci.* **2013**, *110* (13), 4992.
- (82) Liu, K.; Zheng, L.; Liu, Q.; de Vries, J. W.; Gerasimov, J. Y.; Herrmann, A. *J. Am. Chem. Soc.* **2014**, *136* (40), 14255.
- (83) Rowland, M. J.; Atgie, M.; Hoogland, D.; Scherman, O. A. *Biomacromolecules* **2015**, *16* (8), 2436.
- (84) Bapat, A. P.; Roy, D.; Ray, J. G.; Savin, D. A.; Sumerlin, B. S. *J. Am. Chem. Soc.* **2011**, *133* (49), 19832.
- (85) Cobo, I.; Li, M.; Sumerlin, B. S.; Perrier, S. *Nat. Mater.* **2014**, *14* (2), 143.
- (86) Espeel, P.; Du Prez, F. E. *Macromolecules* **2015**, *48* (1), 2.
- (87) Patterson, D. M.; Nazarova, L. A.; Prescher, J. A. *ACS Chem. Biol.* **2014**, *9* (3), 592.

- (88) Alconcel, S. N. S.; Kim, S. H.; Tao, L.; Maynard, H. D. *Macromol. Rapid Commun.* **2013**, *34* (12), 983.
- (89) Mukherjee, S.; Hill, M. R.; Sumerlin, B. S. *Soft Matter* **2015**, *11* (30), 6152.
- (90) Sletten, E. M.; Bertozzi, C. R. *Acc. Chem. Res.* **2011**, *44* (9), 666.
- (91) Liu, S.; Edgar, K. J. *Biomacromolecules* **2015**, *16* (9), 2556.
- (92) Stamenović, M. M.; Espeel, P.; Camp, W. Van; Du Prez, F. E. *Macromolecules* **2011**, *44* (14), 5619.
- (93) Canalle, L. A.; van der Knaap, M.; Overhand, M.; van Hest, J. C. M. *Macromol. Rapid Commun.* **2011**, *32* (2), 203.
- (94) van Oers, M. C. M.; Rutjes, F. P. J. T.; van Hest, J. C. M. *J. Am. Chem. Soc.* **2013**, *135* (44), 16308.
- (95) Kharkar, P. M.; Kloxin, A. M.; Kiick, K. L. *J. Mater. Chem. B* **2014**, *2* (34), 5511.
- (96) Shih, H.-W.; Prescher, J. A. *J. Am. Chem. Soc.* **2015**, *137* (32), 10036.
- (97) McKay, C. S.; Finn, M. G. *Chem. Biol.* **2014**, *21* (9), 1075.
- (98) Klok, H.-A. *Macromolecules* **2009**, *42* (21), 7990.
- (99) Romulus, J.; Henssler, J. T.; Weck, M. *Macromolecules* **2014**, *47* (16), 5437.
- (100) Reece, J. B.; Urry, L. A.; Cain, M. L.; Wasserman, S. A.; Minorsky, P. V.; Jackson, R.; Campbell, N. A. *Campbell Biology (10th Edition)*; 2014.
- (101) García-Borrón, J. C.; Olivares Sánchez, M. C. In *Melanins and Melanosomes*; Wiley-VCH Verlag GmbH & Co. KGaA: Weinheim, Germany, 2011; pp 87–116.
- (102) Lutz, J.-F.; Sumerlin, B.; Matyjaszewski, K. *Macromol. Rapid Commun.* **2014**, *35* (4), 377.
- (103) Noel, A.; Borguet, Y. P.; Raymond, J. E.; Wooley, K. L. *Macromolecules* **2014**, *47* (20), 7109.
- (104) Szwarc, M. *Nature* **1956**, *178* (4543), 1168.
- (105) Zhang, Q.; Collins, J.; Anastasaki, A.; Wallis, R.; Mitchell, D. A.; Becer, C. R.; Haddleton, D. M. *Angew. Chemie Int. Ed.* **2013**, *52* (16), 4435.
- (106) Samanta, S. R.; Anastasaki, A.; Waldron, C.; Haddleton, D. M.; Percec, V. *Polym. Chem.* **2013**, *4* (22), 5555.

- (107) Costa, J. R. C.; Mendonça, P. V.; Maximiano, P.; Serra, A. C.; Guliashvili, T.; Coelho, J. F. J. *Macromolecules* **2015**, *48* (19), 6810.
- (108) Konkolewicz, D.; Krys, P.; Góis, J. R.; Mendonça, P. V.; Zhong, M.; Wang, Y.; Gennaro, A.; Isse, A. A.; Fantin, M.; Matyjaszewski, K. *Macromolecules* **2014**, *47* (2), 560.
- (109) Mackenzie, M. C.; Shrivats, A. R.; Konkolewicz, D.; Averick, S. E.; McDermott, M. C.; Hollinger, J. O.; Matyjaszewski, K. *Biomacromolecules* **2015**, *16* (1), 236.
- (110) Mendonça, P. V.; Averick, S. E.; Konkolewicz, D.; Serra, A. C.; Popov, A. V.; Guliashvili, T.; Matyjaszewski, K.; Coelho, J. F. J. *Macromolecules* **2014**, *47* (14), 4615.
- (111) Simakova, A.; Averick, S. E.; Konkolewicz, D.; Matyjaszewski, K. *Macromolecules* **2012**, *45* (16), 6371.
- (112) Shida, N.; Koizumi, Y.; Nishiyama, H.; Tomita, I.; Inagi, S. *Angew. Chemie Int. Ed.* **2015**, *54* (13), 3922.
- (113) Magenau, A. J. D.; Bortolamei, N.; Frick, E.; Park, S.; Gennaro, A.; Matyjaszewski, K. *Macromolecules* **2013**, *46* (11), 4346.
- (114) Ribelli, T. G.; Konkolewicz, D.; Pan, X.; Matyjaszewski, K. *Macromolecules* **2014**, *47* (18), 6316.
- (115) Ribelli, T. G.; Konkolewicz, D.; Bernhard, S.; Matyjaszewski, K. *J. Am. Chem. Soc.* **2014**, *136* (38), 13303.
- (116) Liu, X.; Zhang, L.; Cheng, Z.; Zhu, X. *Polym. Chem.* **2016**, *7* (3), 689.
- (117) Shanmugam, S.; Boyer, C. *J. Am. Chem. Soc.* **2015**, *137* (31), 9988.
- (118) Xu, J.; Shanmugam, S.; Boyer, C. *ACS Macro Lett.* **2015**, *4* (9), 926.
- (119) Otsu, T. *J. Polym. Sci. Part A Polym. Chem.* **2000**, *38* (12), 2121.
- (120) Tesch, M.; Hepperle, J. A. M.; Klaasen, H.; Letzel, M.; Studer, A. *Angew. Chemie Int. Ed.* **2015**, *54* (17), 5054.
- (121) Guégain, E.; Guillaneuf, Y.; Nicolas, J. *Macromol. Rapid Commun.* **2015**, *36* (13), 1227.
- (122) García-Valdez, O.; Champagne-Hartley, R.; Saldívar-Guerra, E.; Champagne, P.; Cunningham, M. F. *Polym. Chem.* **2015**, *6* (15), 2827.
- (123) Delplace, V.; Harrison, S.; Ho, H. T.; Tardy, A.; Guillaneuf, Y.; Pascual, S.; Fontaine, L.; Nicolas, J. *Macromolecules* **2015**, *48* (7), 2087.

- (124) Kamber, N. E.; Jeong, W.; Waymouth, R. M.; Pratt, R. C.; Lohmeijer, B. G. G.; Hedrick, J. L. *Chem. Rev.* **2007**, *107* (12), 5813.
- (125) McGrath, A. J.; Shi, W.; Rodriguez, C. G.; Kramer, E. J.; Hawker, C. J.; Lynd, N. A. *Polym. Chem.* **2015**, *6* (9), 1465.
- (126) Ito, S.; Ishizone, T.; Hirao, A. *Macromolecules* **2015**, *48* (22), 8307.
- (127) Hirao, A.; Goseki, R.; Ishizone, T. *Macromolecules* **2014**, *47* (6), 1883.
- (128) Crawford, K. E.; Sita, L. R. *J. Am. Chem. Soc.* **2013**, *135* (24), 8778.
- (129) Kundu, S.; Bhangale, A. S.; Wallace, W. E.; Flynn, K. M.; Guttman, C. M.; Gross, R. A.; Beers, K. L. *J. Am. Chem. Soc.* **2011**, *133* (15), 6006.
- (130) Castano, M.; Zheng, J.; Puskas, J. E.; Becker, M. L. *Polym. Chem.* **2014**, *5* (6), 1891.
- (131) Deming, T. J. *Chem. Rev.* **2016**, *116* (3), 786.
- (132) Cao, J.; Hu, P.; Lu, L.; Chan, B. A.; Luo, B.-H.; Zhang, D. *Polym. Chem.* **2015**, *6* (8), 1226.
- (133) Chatterjee, A. K.; Toste, F. D.; Choi, T.-L.; Grubbs, R. H. *Adv. Synth. Catal.* **2002**, *344* (6–7), 634.
- (134) Romulus, J.; Tan, L.; Weck, M.; Sampson, N. S. *ACS Macro Lett.* **2013**, *2* (8), 749.
- (135) Elling, B. R.; Xia, Y. *J. Am. Chem. Soc.* **2015**, *137* (31), 9922.
- (136) Tan, L.; Li, G.; Parker, K. A.; Sampson, N. S. *Macromolecules* **2015**, *48* (14), 4793.
- (137) Ogawa, K. A.; Goetz, A. E.; Boydston, A. J. *J. Am. Chem. Soc.* **2015**, *137* (4), 1400.
- (138) Merrifield, R. B. *J. Am. Chem. Soc.* **1963**, *85* (14), 2149.
- (139) Ouahabi, A. Al; Kotera, M.; Charles, L.; Lutz, J.-F. *ACS Macro Lett.* **2015**, *4* (10), 1077.
- (140) Roy, R. K.; Lutz, J.-F. *J. Am. Chem. Soc.* **2014**, *136* (37), 12888.
- (141) Gutekunst, W. R.; Hawker, C. J. *J. Am. Chem. Soc.* **2015**, *137* (25), 8038.
- (142) Zhang, J.; Matta, M. E.; Hillmyer, M. A. *ACS Macro Lett.* **2012**, *1* (12), 1383.
- (143) Thomas, R. M.; Grubbs, R. H. *Macromolecules* **2010**, *43* (8), 3705.
- (144) Fishman, J. M.; Kiessling, L. L. *Angew. Chem. Int. Ed. Engl.* **2013**, *52* (19), 5061.

- (145) Cameron, D. J. A.; Shaver, M. P. *J. Polym. Sci. Part A Polym. Chem.* **2012**, *50* (8), 1477.
- (146) Barnes, J. C.; Ehrlich, D. J. C.; Gao, A. X.; Leibfarth, F. A.; Jiang, Y.; Zhou, E.; Jamison, T. F.; Johnson, J. A. *Nat. Chem.* **2015**, *7* (10), 810.
- (147) Leibfarth, F. A.; Johnson, J. A.; Jamison, T. F. *Proc. Natl. Acad. Sci.* **2015**, *112* (34), 10617.
- (148) Hahn, M. E.; Randolph, L. M.; Adamiak, L.; Thompson, M. P.; Gianneschi, N. C. *Chem. Commun.* **2013**, *49* (28), 2873.
- (149) James, C. R.; Rush, A. M.; Insley, T.; Vuković, L.; Adamiak, L.; Král, P.; Gianneschi, N. C. *J. Am. Chem. Soc.* **2014**, *136* (32), 11216.
- (150) Veccharelli, K. M.; Tong, V. K.; Young, J. L.; Yang, J.; Gianneschi, N. C. *Chem. Commun.* **2016**, *52* (3), 567.
- (151) Thompson, M. P.; Randolph, L. M.; James, C. R.; Davalos, A. N.; Hahn, M. E.; Gianneschi, N. C. *Polym. Chem.* **2014**, *5* (6), 1954.
- (152) Callmann, C. E.; Barback, C. V.; Thompson, M. P.; Hall, D. J.; Mattrey, R. F.; Gianneschi, N. C. *Adv. Mater.* **2015**, *27* (31), 4611.
- (153) Chien, M.-P.; Thompson, M. P.; Barback, C. V.; Ku, T.-H.; Hall, D. J.; Gianneschi, N. C. *Adv. Mater.* **2013**, *25* (26), 3599.
- (154) Blum, A. P.; Kammeyer, J. K.; Yin, J.; Crystal, D. T.; Rush, A. M.; Gilson, M. K.; Gianneschi, N. C. *J. Am. Chem. Soc.* **2014**, *136* (43), 15422.
- (155) Kammeyer, J. K.; Blum, A. P.; Adamiak, L.; Hahn, M. E.; Gianneschi, N. C. *Polym. Chem.* **2013**, *4* (14), 3929.
- (156) Chien, M.-P.; Carlini, A. S.; Hu, D.; Barback, C. V.; Rush, A. M.; Hall, D. J.; Orr, G.; Gianneschi, N. C. *J. Am. Chem. Soc.* **2013**, *135* (50), 18710.
- (157) Rhodes, A. J.; Deming, T. J. *J. Am. Chem. Soc.* **2012**, *134* (47), 19463.
- (158) Lin, E.-W.; Maynard, H. D. *Macromolecules* **2015**, *48* (16), 5640.
- (159) Tucker, B. S.; Stewart, J. D.; Aguirre, J. I.; Holliday, L. S.; Figg, C. A.; Messer, J. G.; Sumerlin, B. S. *Biomacromolecules* **2015**, *16* (8), 2374.
- (160) Sgolastra, F.; Minter, L. M.; Osborne, B. A.; Tew, G. N. *Biomacromolecules* **2014**, *15* (3), 812.
- (161) deRonde, B. M.; Torres, J. A.; Minter, L. M.; Tew, G. N. *Biomacromolecules* **2015**, *16* (10), 3172.

- (162) Wright, D. B.; Patterson, J. P.; Pitto-Barry, A.; Lu, A.; Kirby, N.; Gianneschi, N. C.; Chassenieux, C.; Colombani, O.; O'Reilly, R. K. *Macromolecules* **2015**, *48* (18), 6516.
- (163) Ren, J. M.; Satoh, K.; Goh, T. K.; Blencowe, A.; Nagai, K.; Ishitake, K.; Christofferson, A. J.; Yiapanis, G.; Yarovsky, I.; Kamigaito, M.; Qiao, G. G. *Angew. Chemie Int. Ed.* **2014**, *53* (2), 459.
- (164) Mai, Y.; Eisenberg, A. *Acc. Chem. Res.* **2012**, *45* (10), 1657.
- (165) De Koker, S.; De Cock, L. J.; Rivera-Gil, P.; Parak, W. J.; Auzély Velty, R.; Vervaet, C.; Remon, J. P.; Grooten, J.; De Geest, B. G. *Adv. Drug Deliv. Rev.* **2011**, *63* (9), 748.
- (166) Buwalda, S. J.; Boere, K. W. M.; Dijkstra, P. J.; Feijen, J.; Vermonden, T.; Hennink, W. E. *J. Control. Release* **2014**, *190*, 254.
- (167) Kramer, J. R.; Deming, T. J. *J. Am. Chem. Soc.* **2014**, *136* (15), 5547.
- (168) Singh, R.; Norret, M.; House, M. J.; Galabura, Y.; Bradshaw, M.; Ho, D.; Woodward, R. C.; Pierre, T. G. St.; Luzinov, I.; Smith, N. M.; Lim, L. Y.; Iyer, K. S. *Small* **2016**, *12* (3), 351.
- (169) Nguyen, M. M.; Carlini, A. S.; Chien, M.-P.; Sonnenberg, S.; Luo, C.; Braden, R. L.; Osborn, K. G.; Li, Y.; Gianneschi, N. C.; Christman, K. L. *Adv. Mater.* **2015**, *27* (37), 5547.
- (170) Dvir, T.; Bauer, M.; Schroeder, A.; Tsui, J. H.; Anderson, D. G.; Langer, R.; Liao, R.; Kohane, D. S. *Nano Lett.* **2011**, *11* (10), 4411.
- (171) Wang, Y.; Lin, T.; Zhang, W.; Jiang, Y.; Jin, H.; He, H.; Yang, V. C.; Chen, Y.; Huang, Y. *Theranostics* **2015**, *5* (8), 787.
- (172) MacEwan, S. R.; Chilkoti, A. *Nano Lett.* **2014**, *14* (4), 2058.
- (173) Ray, J. G.; Naik, S. S.; Hoff, E. A.; Johnson, A. J.; Ly, J. T.; Easterling, C. P.; Patton, D. L.; Savin, D. A. *Macromol. Rapid Commun.* **2012**, *33* (9), 819.
- (174) Itel, F.; Najer, A.; Palivan, C. G.; Meier, W. *Nano Lett.* **2015**, *15* (6), 3871.
- (175) Lowe, A. M.; Abbott, N. L. *Chem. Mater.* **2012**, *24* (5), 746.
- (176) Carlton, R. J.; Hunter, J. T.; Miller, D. S.; Abbasi, R.; Mushenheim, P. C.; Tan, L. N.; Abbott, N. L. *Liq. Cryst. Rev.* **2013**, *1* (1), 29.
- (177) Bukusoglu, E.; Bedolla Pantoja, M.; Mushenheim, P. C.; Wang, X.; Abbott, N. L. *Annu. Rev. Chem. Biomol. Eng.* **2016**, *7* (1), 163.

- (178) Otani, T.; Araoka, F.; Ishikawa, K.; Takezoe, H. *J. Am. Chem. Soc.* **2009**, *131* (34), 12368.
- (179) Hough, L. E.; Jung, H. T.; Kriuerke, D.; Heberling, M. S.; Nakata, M.; Jones, C. D.; Chen, D.; Link, D. R.; Zasadzinski, J.; Heppke, G.; Rabe, J. P.; Stocker, W.; Körblova, E.; Walba, D. M.; Glaser, M. A.; Clark, N. A. *Science* **2009**, *325* (5939), 456.
- (180) Chen, D.; Nakata, M.; Shao, R.; Tuchband, M. R.; Shuai, M.; Baumeister, U.; Weissflog, W.; Walba, D. M.; Glaser, M. A.; MacLennan, J. E.; Clark, N. A. *Phys. Rev. E* **2014**, *89* (2), 22506.
- (181) Price, A. D.; Schwartz, D. K. *J. Am. Chem. Soc.* **2008**, *130* (26), 8188.
- (182) Malone, S. M.; Schwartz, D. K. *Langmuir* **2011**, *27* (19), 11767.
- (183) Noonan, P. S.; Roberts, R. H.; Schwartz, D. K. *J. Am. Chem. Soc.* **2013**, *135* (13), 5183.
- (184) Clare, B. H.; Guzmán, O.; de Pablo, J.; Abbott, N. L. *Langmuir* **2006**, *22* (18), 7776.
- (185) Bai, Y.; Abbott, N. L. *J. Am. Chem. Soc.* **2012**, *134* (1), 548.
- (186) Gupta, V. K.; Skaife, J. J.; Dubrovsky, T. B.; Abbott, N. L. *Science* (80-.). **1998**, *279* (5359), 285.
- (187) Jang, C.-H.; Cheng, L.-L.; Olsen, C. W.; Abbott, N. L. *Nano Lett.* **2006**, *6* (5), 1053.
- (188) Brake, J. M.; Daschner, M. K.; Luk, Y.-Y.; Abbott, N. L. *Science* **2003**, *302* (5653), 2094.
- (189) Lockwood, N. A.; Mohr, J. C.; Ji, L.; Murphy, C. J.; Palecek, S. P.; de Pablo, J. J.; Abbott, N. L. *Adv. Funct. Mater.* **2006**, *16* (5), 618.
- (190) Kinsinger, M. I.; Buck, M. E.; Abbott, N. L.; Lynn, D. M. *Langmuir* **2010**, *26* (12), 10234.
- (191) Gupta, J. K.; Meli, M.-V.; Teren, S.; Abbott, N. L. *Phys. Rev. Lett.* **2008**, *100* (4), 48301.
- (192) Miller, D. S.; Abbott, N. L. *Soft Matter* **2013**, *9* (2), 374.
- (193) Khan, W.; Choi, J. H.; Kim, G. M.; Park, S.-Y. Y. *Lab Chip* **2011**, *11* (20), 3493.
- (194) Gupta, J. K.; Zimmerman, J. S.; de Pablo, J. J.; Caruso, F.; Abbott, N. L. *Langmuir* **2009**, *25* (16), 9016.
- (195) Tjipto, E.; Cadwell, K. D.; Quinn, J. F.; Johnston, A. P. R.; Abbott, N. L.; Caruso, F. *Nano Lett.* **2006**, *6* (10), 2243.

- (196) Lin, I.-H.; Miller, D. S.; Bertics, P. J.; Murphy, C. J.; de Pablo, J. J.; Abbott, N. L. *Science* **2011**, *332* (6035), 1297.
- (197) Aliño, V. J.; Pang, J.; Yang, K.-L. *Langmuir* **2011**, *27* (19), 11784.
- (198) Sivakumar, S.; Wark, K. L.; Gupta, J. K.; Abbott, N. L.; Caruso, F. *Adv. Funct. Mater.* **2009**, *19* (14), 2260.
- (199) Bera, T.; Fang, J. *J. Mater. Chem.* **2012**, *22* (14), 6807.
- (200) Carter, M. C. D.; Miller, D. S.; Jennings, J.; Wang, X.; Mahanthappa, M. K.; Abbott, N. L.; Lynn, D. M. *Langmuir* **2015**, *31* (47), 12850.
- (201) Tixier, T.; Heppenstall-Butler, M.; Terentjev, E. M. *Langmuir* **2006**, *22* (5), 2365.
- (202) Xu, H.; Bi, X.; Ngo, X.; Yang, K.-L. *Analyst* **2009**, *134* (5), 911.
- (203) Shah, R. R.; Abbott, N. L. *Science* **2001**, *293* (5533), 1296.
- (204) Cadwell, K. D.; Alf, M. E.; Abbott, N. L. *J. Phys. Chem. B* **2006**, *110* (51), 26081.
- (205) Matsumura, Y.; Maeda, H. *Cancer Res.* **1986**, *46* (12 Pt 1), 6387.
- (206) Fang, J.; Nakamura, H.; Maeda, H. *Adv. Drug Deliv. Rev.* **2011**, *63* (3), 136.
- (207) Maeda, H.; Wu, J.; Sawa, T.; Matsumura, Y.; Hori, K. *J. Control. Release* **2000**, *65* (1), 271.
- (208) Nakamura, Y.; Mochida, A.; Choyke, P. L.; Kobayashi, H. *Bioconjug. Chem.* **2016**, DOI: 10.1021/acs.bioconjchem.6b00437.
- (209) Suh, W. H.; Suslick, K. S.; Stucky, G. D.; Suh, Y.-H. *Prog. Neurobiol.* **2009**, *87* (3), 133.
- (210) Seaton, A.; Donaldson, K. *The Lancet*. 2005, pp 923–924.
- (211) Kagan, V. E.; Bayir, H.; Shvedova, A. A. *Nanomedicine Nanotechnology, Biol. Med.* **2005**, *1* (4), 313.
- (212) Donaldson, K.; Tran, C. L. *Mutat. Res. Mol. Mech. Mutagen.* **2004**, *553* (1), 5.
- (213) Albanese, A.; Tang, P. S.; Chan, W. C. W. *Annu. Rev. Biomed. Eng.* **2012**, *14*, 1.
- (214) Owens Iii, D. E.; Peppas, N. A. *Int. J. Pharm.* **2006**, *307* (1), 93.
- (215) Merkel, O. M.; Urbanics, R.; Bedöcs, P.; Rozsnyay, Z.; Rosivall, L.; Toth, M.; Kissel, T.; Szebeni, J. *Biomaterials* **2011**, *32* (21), 4936.

- (216) Moghimi, S. M.; Andersen, A. J.; Ahmadvand, D.; Wibroe, P. P.; Andresen, T. L.; Hunter, A. C. *Adv. Drug Deliv. Rev.* **2011**, *63* (12), 1000.
- (217) Gustafson, H. H.; Holt-Casper, D.; Grainger, D. W.; Ghandehari, H. *Nano Today* **2015**, *10* (4), 487.
- (218) Storm, G.; Belliot, S. O.; Daemen, T.; Lasic, D. D. *Adv. Drug Deliv. Rev.* **1995**, *17* (1), 31.
- (219) Moghimi, S. M.; Hunter, A. C.; Murray, J. C. *Pharmacol. Rev.* **2001**, *53* (2), 283.
- (220) Green, A. E.; Rose, P. G. *Int. J. Nanomedicine* **2006**, *1* (3), 229.
- (221) Szebeni, J.; Alving, C. R.; Rosivall, L.; Bünger, R.; Baranyi, L.; Bedöcs, P.; Tóth, M.; Barenholz, Y. *J. Liposome Res.* **2007**, *17* (2), 107.
- (222) Szebeni, J.; Baranyi, L.; Sávyay, S.; Bodó, M.; Milosevits, J.; Alving, C. R.; Bünger, R. *Am. J. Physiol. Heart Circ. Physiol.* **2006**, *290* (3), H1050.
- (223) Uziely, B.; Jeffers, S.; Isacson, R.; Kutsch, K.; Wei-Tsao, D.; Yehoshua, Z.; Libson, E.; Muggia, F. M.; Gabizon, A. *J. Clin. Oncol.* **1995**, *13* (7), 1777.
- (224) Mackay, I. R.; Rosen, F. S.; Walport, M. J. *N. Engl. J. Med.* **2001**, *344* (14), 1058.
- (225) Mackay, I. R.; Rosen, F. S.; Walport, M. J. *N. Engl. J. Med.* **2001**, *344* (15), 1140.
- (226) Elci, S. G.; Jiang, Y.; Yan, B.; Kim, S. T.; Saha, K.; Moyano, D. F.; Yesilbag Tonga, G.; Jackson, L. C.; Rotello, V. M.; Vachet, R. W. *ACS Nano* **2016**, *10* (5), 5536.
- (227) Cheng, X.; Tian, X.; Wu, A.; Li, J.; Tian, J.; Chong, Y.; Chai, Z.; Zhao, Y.; Chen, C.; Ge, C. *ACS Appl. Mater. Interfaces* **2015**, *7* (37), 20568.
- (228) Frank, M. M.; Fries, L. F. *Immunol. Today* **1991**, *12* (9), 322.
- (229) Moghimi, S. M.; Andresen, T. L. *Molecular Immunology*. 2009, pp 1571–1572.
- (230) Markiewski, M. M.; DeAngelis, R. A.; Benencia, F.; Ricklin-Lichtsteiner, S. K.; Koutoulaki, A.; Gerard, C.; Coukos, G.; Lambris, J. D. *Nat. Immunol.* **2008**, *9* (11), 1225.
- (231) Schöttler, S.; Landfester, K.; Mailänder, V. *Angew. Chemie Int. Ed.* **2016**, *55* (31), 8806.
- (232) He, C.; Hu, Y.; Yin, L.; Tang, C.; Yin, C. *Biomaterials* **2010**, *31* (13), 3657.
- (233) Jeong, Y. S.; Oh, W.-K.; Kim, S.; Jang, J. *Biomaterials* **2011**, *32* (29), 7217.
- (234) Peracchia, M. .; Fattal, E.; Desmaële, D.; Besnard, M.; Noël, J. .; Gomis, J. .; Appel, M.; d'Angelo, J.; Couvreur, P. *J. Control. Release* **1999**, *60* (1), 121.

- (235) Sharifi, S.; Behzadi, S.; Laurent, S.; Forrest, M. L.; Stroeve, P.; Mahmoudi, M. *Chem. Soc. Rev.* **2012**, *41* (6), 2323.
- (236) Zhao, F.; Zhao, Y.; Liu, Y.; Chang, X.; Chen, C.; Zhao, Y. *Small* **2011**, *7* (10), 1322.
- (237) Townson, J. L.; Lin, Y.-S.; Agola, J. O.; Carnes, E. C.; Leong, H. S.; Lewis, J. D.; Haynes, C. L.; Brinker, C. J. *J. Am. Chem. Soc.* **2013**, *135* (43), 16030.
- (238) Pedersen, M. B.; Zhou, X.; Larsen, E. K. U.; Sorensen, U. S.; Kjems, J.; Nygaard, J. V.; Nyengaard, J. R.; Meyer, R. L.; Boesen, T.; Vorup-Jensen, T. *J. Immunol.* **2010**, *184* (4), 1931.
- (239) Champion, J. A.; Mitragotri, S. *Proc. Natl. Acad. Sci.* **2006**, *103* (13), 4930.
- (240) Geng, Y.; Dalhaimer, P.; Cai, S.; Tsai, R.; Tewari, M.; Minko, T.; Discher, D. E. *Nat. Nanotechnol.* **2007**, *2* (4), 249.
- (241) Tsoi, K. M.; MacParland, S. A.; Ma, X.-Z.; Spetzler, V. N.; Echeverri, J.; Ouyang, B.; Fadel, S. M.; Sykes, E. A.; Goldaracena, N.; Kathis, J. M.; Conneely, J. B.; Alman, B. A.; Selzner, M.; Ostrowski, M. A.; Adeyi, O. A.; Zilman, A.; McGilvray, I. D.; Chan, W. C. W. *Nat. Mater.* **2016**.
- (242) Khlebtsov, N.; Dykman, L. *Chem. Soc. Rev.* **2011**, *40* (3), 1647.
- (243) Ernsting, M. J.; Murakami, M.; Roy, A.; Li, S.-D. *J. Control. Release* **2013**, *172* (3), 782.
- (244) Wong, A. C.; Wright, D. W. *Small* **2016**.
- (245) Larson, T. A.; Joshi, P. P.; Sokolov, K. *ACS Nano* **2012**, *6* (10), 9182.
- (246) Jiang, Y.; Huo, S.; Mizuhara, T.; Das, R.; Lee, Y.-W.; Hou, S.; Moyano, D. F.; Duncan, B.; Liang, X.-J.; Rotello, V. M. *ACS Nano* **2015**, *9* (10), 9986.
- (247) Walkey, C. D.; Olsen, J. B.; Guo, H.; Emili, A.; Chan, W. C. W. *J. Am. Chem. Soc.* **2011**, *134* (4), 2139.
- (248) Bai, Y.; Xing, H.; Wu, P.; Feng, X.; Hwang, K.; Lee, J. M.; Phang, X. Y.; Lu, Y.; Zimmerman, S. C. *ACS Nano* **2015**, *9* (10), 10227.
- (249) Tacar, O.; Sriamornsak, P.; Dass, C. R. *J. Pharm. Pharmacol.* **2013**, *65* (2), 157.
- (250) Papahadjopoulos, D.; Allen, T. M.; Gabizon, A.; Mayhew, E.; Matthay, K.; Huang, S. K.; Lee, K. D.; Woodle, M. C.; Lasic, D. D.; Redemann, C. *Proc. Natl. Acad. Sci. U. S. A.* **1991**, *88* (24), 11460.
- (251) Barenholz, Y. (Chezy). *J. Control. Release* **2012**, *160* (2), 117.

- (252) Chanan-Khan, A.; Szebeni, J.; Savay, S.; Liebes, L.; Rafique, N. M.; Alving, C. R.; Muggia, F. M. *Ann. Oncol.* **2003**, *14* (9), 1430.
- (253) Mrozek, E.; Rhoades, C. A.; Allen, J.; Hade, E. M.; Shapiro, C. L. *Ann. Oncol.* **2005**, *16* (7), 1087.
- (254) Vonarbourg, A.; Passirani, C.; Saulnier, P.; Benoit, J.-P. *Biomaterials* **2006**, *27* (24), 4356.
- (255) Jeon, S. .; Lee, J. .; Andrade, J. .; De Gennes, P. . *J. Colloid Interface Sci.* **1991**, *142* (1), 149.
- (256) Szleifer, I. *Curr. Opin. Solid State Mater. Sci.* **1997**, *2* (3), 337.
- (257) Zahr, A. S.; Davis, C. A.; Pishko, M. V. *Langmuir* **2006**, *22* (19), 8178.
- (258) Sheng, Y.; Liu, C.; Yuan, Y.; Tao, X.; Yang, F.; Shan, X.; Zhou, H.; Xu, F. *Biomaterials* **2009**, *30* (12), 2340.
- (259) Knop, K.; Hoogenboom, R.; Fischer, D.; Schubert, U. S. *Angew. Chem. Int. Ed. Engl.* **2010**, *49* (36), 6288.
- (260) Keefe, A. J.; Jiang, S. *Nat Chem* **2012**, *4* (1), 59.
- (261) Pelegri-O'Day, E. M.; Lin, E.-W.; Maynard, H. D. *J. Am. Chem. Soc.* **2014**, *136* (41), 14323.
- (262) Elsabahy, M.; Li, A.; Zhang, F.; Sultan, D.; Liu, Y.; Wooley, K. L. *J. Control. Release* **2013**, *172* (3), 641.
- (263) O'Shea, T. M.; Webber, M. J.; Aimetti, A. A.; Langer, R. *Adv. Healthc. Mater.* **2015**, *4* (12), 1802.
- (264) Lee, J.; Ko, J. H.; Lin, E.-W.; Wallace, P.; Ruch, F.; Maynard, H. D. *Polym. Chem.* **2015**, *6* (18), 3443.
- (265) Parrott, M. C.; DeSimone, J. M. *Nat. Chem.* **2012**, *4* (1), 13.
- (266) Rafique, A.; Mahmood Zia, K.; Zuber, M.; Tabasum, S.; Rehman, S. *Int. J. Biol. Macromol.* **2016**, *87*, 141.
- (267) Bat, E.; Lee, J.; Lau, U. Y.; Maynard, H. D. *Nat. Commun.* **2015**, *6*, 6654.
- (268) Pound, G.; McKenzie, J. M.; Lange, R. F. M.; Klumperman, B. *Chem. Commun.* **2008**, *10* (27), 3193.
- (269) Ulbrich, K.; Šubr, V.; Strohalm, J.; Plocová, D.; Jelínková, M.; Říhová, B. *J. Control. Release* **2000**, *64* (1), 63.

- (270) Borgman, M. P.; Ray, A.; Kolhatkar, R. B.; Sausville, E. A.; Burger, A. M.; Ghandehari, H. *Pharm. Res.* **2009**, *26* (6), 1407.
- (271) Zalipsky, S.; Hansen, C. B.; Oaks, J. M.; Allen, T. M. *J. Pharm. Sci.* **1996**, *85* (2), 133.
- (272) Luxenhofer, R.; Sahay, G.; Schulz, A.; Alakhova, D.; Bronich, T. K.; Jordan, R.; Kabanov, A. V. *J. Control. Release* **2011**, *153* (1), 73.
- (273) Luxenhofer, R.; Han, Y.; Schulz, A.; Tong, J.; He, Z.; Kabanov, A. V.; Jordan, R. *Macromol. Rapid Commun.* **2012**, *33* (19), 1613.
- (274) Schöttler, S.; Becker, G.; Winzen, S.; Steinbach, T.; Mohr, K.; Landfester, K.; Mailänder, V.; Wurm, F. R. *Nat. Nanotechnol.* **2016**, *11* (4), 372.
- (275) Mirshafiee, V.; Kim, R.; Park, S.; Mahmoudi, M.; Kraft, M. L. *Biomaterials* **2016**, *75*, 295.
- (276) Butcher, N. J.; Mortimer, G. M.; Minchin, R. F. *Nat. Nanotechnol.* **2016**, *11* (4), 310.
- (277) Rodriguez, P. L.; Harada, T.; Christian, D. A.; Pantano, D. A.; Tsai, R. K.; Discher, D. E. *Science* **2013**, *339* (6122), 971.
- (278) Hu, C.-M. J.; Zhang, L.; Aryal, S.; Cheung, C.; Fang, R. H.; Zhang, L. *Proc. Natl. Acad. Sci.* **2011**, *108* (27), 10980.
- (279) Cabral, D. A.; Loh, B. A.; Speert, D. P. *Pediatr. Res.* **1987**, *22* (4), 429.
- (280) Reitter, J. N.; Means, R. E.; Desrosiers, R. C. *Nat. Med.* **1998**, *4* (6), 679.
- (281) Blaum, B. S.; Hannan, J. P.; Herbert, A. P.; Kavanagh, D.; Uhrin, D.; Stehle, T. *Nat. Chem. Biol.* **2014**, *11* (1), 77.
- (282) Wu, Y.-Q.; Qu, H.; Sfyroera, G.; Tzekou, A.; Kay, B. K.; Nilsson, B.; Nilsson Ekdahl, K.; Ricklin, D.; Lambris, J. D. *J. Immunol.* **2011**, *186* (7), 4269.
- (283) Ricklin, D.; Lambris, J. D. *Adv. Exp. Med. Biol.* **2008**, *632*, 273.
- (284) Wilhelm, S.; Tavares, A. J.; Dai, Q.; Ohta, S.; Audet, J.; Dvorak, H. F.; Chan, W. C. W. *Nat. Rev. Mater.* **2016**, *1* (5), 16014.
- (285) Torrice, M. *ACS Cent. Sci.* **2016**, *2* (7), 434.
- (286) Yang, W.; Zhang, L.; Wang, S.; White, A. D.; Jiang, S. *Biomaterials* **2009**, *30* (29), 5617.

Chapter 2

Enzyme-Responsive Soft Materials Prepared by *Graft-through* Ring Opening Metathesis

Polymerization of Peptides

2.1 Introduction

The synthesis of nanomaterials from soft, or organic-based, molecules has become increasingly robust in the last twenty years due to the widespread interest in their potential in the biomedical sciences.^{1,2} Biohybrid nanoparticles (NPs) that bear both natural and non-natural components are particularly motivating in this context.³ With the advent of methods available for preparing biosynthetic polymers (as described in section 1.2), from which soft, nanoscale structures are formulated by self-organization (bottom-up approach), new opportunities for interfacing nanomaterials with biological systems have emerged.^{4,5} Furthermore, given the large chemical diversity of amino acid side chains (Figure 2.1), the ability to incorporate biomolecules such as peptides into an amphiphilic block copolymers enables an enormous palette from which to construct nanoscale structures.

The most common synthetic strategy for preparing polymers that incorporate biomolecules utilizes post-polymerization modification, in other words, a *graft-to* approach.⁶ *Graft-to* techniques employed to date have inherent limitations, despite the explosion of “click” chemistries pioneered in the last decade.⁷ Further, where material purity and

reproducibility are a concern for biomedical applications, biohybrid polymers prepared by *graft-to* techniques are inherently heterogeneous and must be purified following each conjugation step, which can lead to laborious and low yielding syntheses. Lastly, the type of bioconjugate strategy implemented may severely modulate biological function such as the effect of grafting density on osteoclast formation of osteoprotegerin (OPG)-polymer conjugates⁸ or proteolytic degradation of peptidyl nanoparticles.⁹ The *graft-from* approach offers the potential to form well-defined bioconjugates *via* incorporation of an initiator to the biomolecule followed by polymer chain extension from the site of initiation.^{10,11} General advantages to this strategy include fewer and facile purification steps. Nevertheless, the requirement of a macroinitiator precludes the use of this technique for biomolecules containing many reactive functional groups such as polysaccharides (hydroxyl, amine)¹² or proteins (cysteine residues).¹³ For applications where multiple copies of a biomolecule may be advantageous, for example high wt. % loading of a peptide therapeutic,¹⁴ the *graft-from* strategy is limited due to the equivalent proportion of biomolecule and polymer.¹⁵

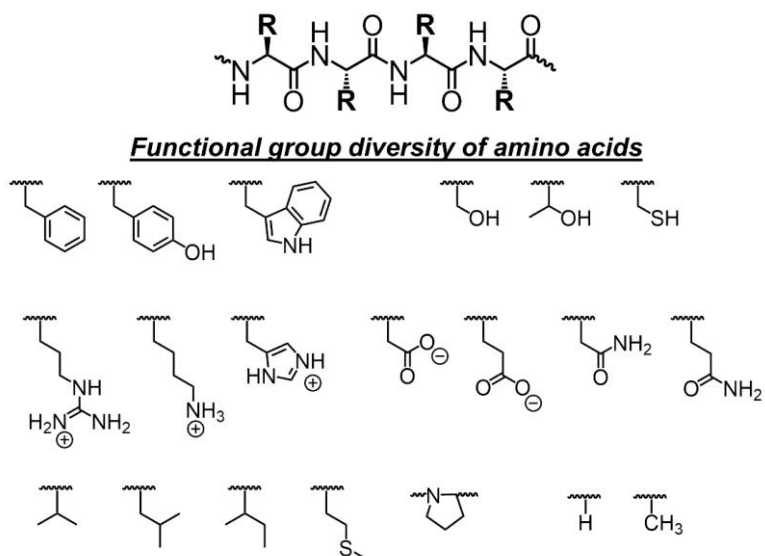


Figure 2.1 The chemical functional group diversity afforded by the 20 canonical amino acid side chains.

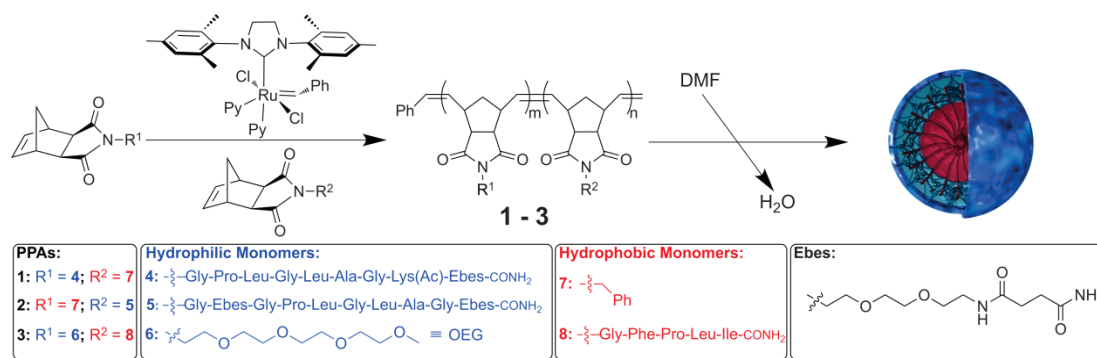
As an alternative method, we hypothesized that the direct incorporation of peptides, or *graft-through* approach, would allow for a one-pot synthesis of complex biohybrid brush polymers with reduced heterogeneity, as well as high wt. % loading of a biomolecule. To this end, a synthetic polymerization technique that is functional group tolerant and proceeds under mild conditions is optimal for maintaining the integrity of the incorporated biomolecules.

2.2 *Graft-through* polymerization of peptides using Ring Opening Metathesis Polymerization (ROMP)

In this work, we have deployed Ring Opening Metathesis Polymerization (ROMP) using the pyridyl modified Grubbs' catalyst, $((\text{H}_2\text{IMES})(\text{pyr})_2(\text{Cl})_2\text{Ru}=\text{CHPh})$, herein abbreviated [Ru], which, as a living polymerization method, allows exquisite control over polymer structure. For example, ROMP has been used for the *graft-through* polymerization of large, complex macromonomers containing camptothecin and doxorubicin to generate brush and bottle-brush polymers.^{16,17} Nonetheless, there have been limited examples demonstrating the polymerization of monomers bearing pendant amino acids. Studies utilizing the initiator, $\text{Ru}=\text{CHPh}(\text{Cl})_2(\text{PCy}_3)_2$, proved inefficient and generally resulted in polymers of high dispersity (\mathfrak{D}).^{18,19} In earlier work, the Gianneschi lab used ROMP to generate peptide-bearing polymers, though these were prepared by a post-polymerization reaction between NHS activated esters on the polymer side chains and primary terminal amines on the peptide.^{20,21} This conjugation strategy is not only laborious but rather disadvantageous for the preparation of biosynthetic polymers in terms of reproducibility and control over density.

In the work presented in this Chapter, we demonstrated that peptides can be directly incorporated by ROMP using [Ru] to form water-soluble homopolymers and block

copolymer amphiphiles capable of being formulated into core-shell, biohybrid nanoparticles (Scheme 2.1). Following standard protocols for solid-phase peptide synthesis (SPPS) of these peptides, we then prepared peptide-containing block copolymers or peptide-polymer amphiphiles (PPAs), wherein the peptide is incorporated as either the hydrophobic or the hydrophilic block (Scheme 2.1). Combinations of hydrophilic monomers **4–6** and hydrophobic monomers **7** and **8** afforded the resulting PPAs **1–3** (Figure 2.2). Monomers **4** and **5** contain peptide sequences, GPLGLAGK(Ac)-Ebes and G-Ebes-GPLGLAG-Ebes respectively, that are known substrates of the disease-associated enzymes matrix metalloproteinases-2 and -9, (MMP-2 and -9),²² with a hydrophilic moiety (Ebes) included in the sequences to promote phase separation of the ensuing block copolymers. Monomer **8** comprises of a hydrophobic peptide sequence, GFPLI, which was chosen to demonstrate generality of the approach toward the formation of nanoparticles with peptides buried within the hydrophobic core.



Scheme 2.1 Synthesis of peptide-polymer amphiphiles (PPAs) and formulation into nanoparticles. Hydrophobic components of the PPAs are color-coded in red. Hydrophilic components of the PPAs are color-coded in blue.

We first set out to determine if peptides of this class can be efficiently polymerized by ROMP. To this end, a monomer analogue of **4** (NorGPLGLAG-Ebes) was polymerized using [Ru] at room temperature. NMR spectroscopy demonstrated that the polymerization

reaction was complete as evidenced by the conversion of the norbornenyl olefinic protons to polynorbornenyl olefinic protons. Size-exclusion chromatography coupled with multi-angle light scattering (SEC-MALS) demonstrated that both high degree of polymerization ($DP = 131$) and low dispersity ($\mathcal{D} = 1.012$) were achieved using this method. Importantly, we found that optimized conditions, including the use of an air-free dinitrogen atmosphere, were required for optimal results with either dimethylformamide (DMF) or dichloromethane–methanol (DCM, MeOH) mixtures performing as effective solvents. This second finding was important, as it demonstrated that the polar aprotic solvent (DMF), ideally suited for solubilizing peptides, could also function as an appropriate solvent for their polymerization. Earlier work on the effects of solvent choice for ROMP concluded that solvents such as alcohols had a detrimental effect on the catalytic activity,²³ and the choice in solvent could generally affect the formation of the ruthenium-carbene active species, thereby altering the tacticity of the polymer.^{24,25}

Next, we set out to determine if *graft-through* ROMP of peptides could be used to prepare PPAs of low-polydispersity that could be formulated into NPs. The one-pot synthesis of PPA **1** was accomplished upon the addition of [Ru] (Scheme 2.1) to a solution of hydrophilic peptidyl monomer **4** followed by the addition of the hydrophobic monomer **7**. In addition, PPA **2** was prepared *via* the reverse order of addition, that is, polymerization of the hydrophobic monomer **7** followed by the hydrophilic norbornenyl peptide monomer **5**, demonstrating generality in the polymerization process with respect to order of addition (Scheme 1). Furthermore, we set out to determine if hydrophobic peptide-containing norbornenyl monomer **8**, once polymerized, could be utilized to form the hydrophobic block of a well-defined polymer, PPA **3**, which is not a specific enzyme substrate, but is structurally related to previously published systems for comparison (Scheme 2.1).^{19,26} This arrangement could also provide protection of the pendant moieties (i.e. peptides) by encapsulation and

Table 2.1 SEC-MALS characterization providing molecular weight and dispersities of PPAs and nanoparticles

PPA	M_n (Da) ^a	(M_w/M_n) ^b	DP_m ^c	DP_n ^d	D_h ^e (nm)	PDI ^f
1	44,630	1.20	13	106	28	0.062
2	24,860	1.06	74	6	124	0.020
3	28,130	1.05	59	11	282	0.053
4	27,220	1.04	49	14	250	-

^a M_n denotes number-average molecular weight. ^b M_w denotes weight-average molecular weight. ^c DP_m denotes degree of polymerization of the first block. ^d DP_n denotes degree of polymerization of the second block. ^e D_h denotes hydrodynamic diameter of the nanoparticles formulated from each PPA. ^f PDI denotes polydispersity index of the nanoparticles.

2.2.1 Formulation of nanoparticles from PPAs

To formulate PPAs into NPs, each polymer was dissolved separately in DMF followed by the slow addition of water to a final concentration of 50% by volume.²⁸ The incipient NP suspensions were then dialyzed against water to remove DMF. Dynamic light scattering (DLS) in water was employed to determine the hydrodynamic diameter of the NPs derived from PPAs **1–3** (Figure 2.3). Statistical analysis of the DLS data demonstrated that the size distribution of the nanoparticles was narrow (Table 2.1). Transmission electron microscopy (TEM) of the nanoparticles validated the DLS data showing the presence of spherical particles (Figure 2.3). Interestingly, NPs formulated from PPA **3** exhibited a bicontinuous micelle morphology (Figure 2.3D), resembling assemblies formulated from structurally-similar systems.¹⁹

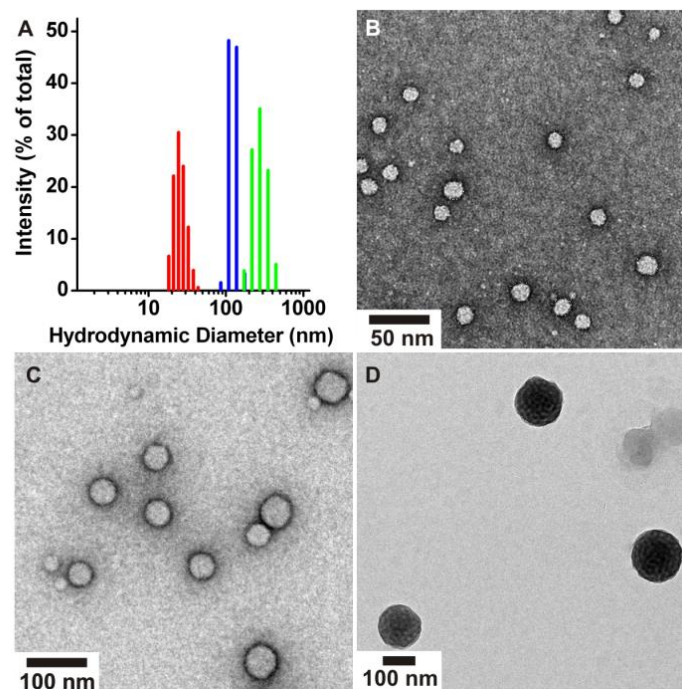


Figure 2.3 Characterization of PPAs formulated into NPs. (A) DLS size intensity distribution of NPs derived from PPA 1 (red), PPA 2 (blue), and PPA 3 (green). TEM of NPs derived from (A) PPA 1; (B) PPA 2; and (C) PPA 3.

Further, these types of assemblies appear to be particular to the identity of the peptide. PPA 4 prepared from PEG and GPFLI, which is an analogue of the peptide used in PPA 3 (GFPLI) except for the exchange of residues in positions X_2 and X_3 , also displayed bicontinuous micellar morphologies (Figure 2.4, Table 2.1).

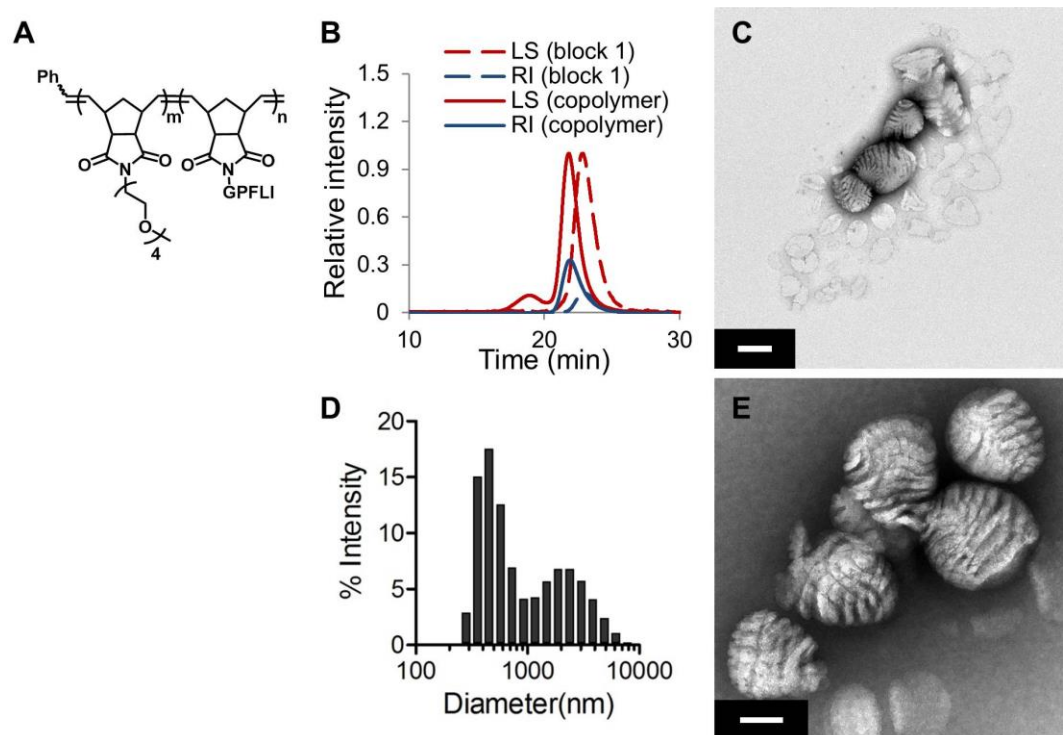


Figure 2.4 Characterization of PPA **4** formulated into NPs. (A) Chemical structure and (B) SEC-MALS chromatogram of PPA **4**. (C) TEM micrograph (dry-state) of NPs prepared from PPA **4**. Scale bar is 0.2 μm . (D) DLS size intensity distribution of NPs derived from PPA **4**. (E) TEM micrograph (dry-state) at higher magnification. Scale bar is 100 nm. These bicontinuous structures are reminiscent of those published yet also unique, which deserves further investigation.¹⁹

2.2.2 Demonstrating enzyme-responsiveness of NPs and soluble polymers

Given the high spatial density of peptides displayed on the resultant polymers, a preliminary experiment was conducted to determine if the peptides arrayed covalently on the polymer backbone would retain the ability to function as enzyme substrates. For these studies, water-soluble homopolymers prepared from monomer **4** were compared to well-defined spherical micellar NPs formed from PPA **1** (Figure 2.3B). Following incubation of the water-soluble polymer prepared from monomer **4** with MMP-2, RP-HPLC revealed the appearance of the proteolysis product $\text{NH}_2\text{-LAGK(Ac)-Ebes-CONH}_2$ (Figure 2.4, iv). Proteolysis did not occur when MMP-2 was heat denatured prior to incubation with the

peptide polymer (Figure 2.5, ii) and proteolysis was markedly blunted when carried out in the presence of EDTA (Figure 2.5, iii), which is known to inhibit the enzyme *via* chelation of the catalytic Zn^{2+} ion. This demonstrated that the enzyme was indeed responsible for proteolysis of the water-soluble peptide-homopolymer prepared by *graft-through* polymerization of the substrate.

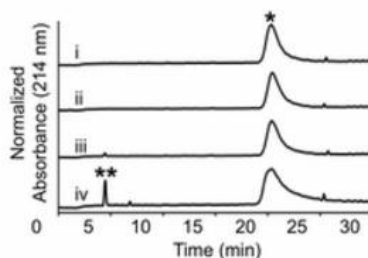


Figure 2.5 RP-HPLC chromatograms of homopolymer prepared from monomer 4 alone (i) as well as following incubation with heat-treated MMP-2 (ii), EDTA-treated MMP-2 (iii), and active MMP-2 (iv). Peak due to peptide-based brush copolymer (*); peak due to peptide cleavage product NH_2 -LAGK(Ac)-Ebes-CONH $_2$ (**).

Finally, micellar NPs derived from PPA **1** were incubated with active MMP-2 and no proteolysis product could be identified by RP-HPLC under the same conditions used for processing homopolymers. This suggests that the peptide substrates arrayed on the particle are protected from protease-mediated cleavage. Given similar enzymatic resistance observed for densely packed DNA-shell forming NPs to endonucleases,²⁹ we hypothesize that this phenomenon is due to the steric crowding of the displayed peptides on the NP scaffold, preventing the enzyme from accessing the scissile peptide bond within the displayed peptides. This is in contrast to the high activity we have observed for related systems that are responsive to MMP catalyzed cleavage when prepared *via* post-polymerization modification of polymers with peptides.²⁰ Notably, these earlier systems were characterized by a lower density of peptides displayed, due to low conjugation efficiency inherent to post-

polymerization reactions. These results hint at the possibility of arranging peptides to capitalize on resistance to proteolytic degradation, which has since been documented in our laboratory for the preparation of cell penetrating peptide polymers.³⁰ Nevertheless, optimizing conditions to amplify activity and responsiveness may be a more difficult task for such systems. In the next section, the relationships between substrate spatial density, sequence identity and enzymatic activity were investigated.

2.3 Proteolysis of peptide polymers prepared by incorporation of canonical amino acids *via graft-through* ROMP

2.3.1 *Graft-through* polymerization of complex peptides

Following the demonstrated success of *graft-through* polymerization of simple aliphatic peptides *via* ROMP, the generality of the approach was examined by our laboratory with more problematic peptide sequences. To this end, pentapeptide-modified norbornene monomers were prepared with the general structure, norbornyl-GX₂PLX₅. Residues at positions X₂ and X₅ were modified with the 17 remaining canonical amino acids, not including glycine (G), proline (P), and leucine (L) already present in the sequence.³¹ In these studies, ¹H NMR was used to follow the course of the polymerization, by monitoring the disappearance of the monomeric olefin protons ($\delta = 6.33$ ppm) and the appearance of the polymer norbornyl olefin protons ($\delta = 5.6$ and 5.8 ppm). SEC-MALS under the standard set of conditions was used to characterize molecular weight and dispersity of the resulting polymers. From the 31 peptide monomer library generated, and an exploration of a set of two reaction conditions, where the monomer:initiator ratio (M:I) = 20:1 and 200:1, several key findings were described. First, peptides containing cysteine residues exhibited less than 25 % conversion when M:I = 20:1 and no significant polymerization was observed when M:I =

200:1. Second, at M:I = 200:1, the residues R, K, and M (arginine, lysine and methionine, respectively), exhibited reduced conversions, the lowest being 76 % for methionine. Third, characterization of peptide polymers bearing carboxylic acid-containing residues (D, E, i.e. aspartic acid and glutamic acid, respectively) by SEC-MALS proved difficult, possibly due to their propensity to aggregate in DMF and potentially interact with the size exclusion column.

Several strategies were established to restore the polymerization of complex peptide sequences. For example, spacing the peptide away from the norbornene reactive site with a five carbon spacer, derived from norbornene hexanoic acid as previously published,³² was shown to enable the polymerization of unprotected lysine-containing sequences. The polymerization of peptides with side-chain protecting groups further improved polymerization rates, exhibiting a 4.5-fold increase compared to the unprotected variant. With these combined strategies in hand, enzymatic studies were conducted with lysine-containing sequences in order to probe the effect of substrate special density on proteolysis.

2.3.2 Enzymatic activity of peptide brush polymers

Peptide monomers, **9** and **10**, were prepared with a key lysine residue within the sequence that renders them substrates of the model protease, trypsin, which is known to cleave at the C-terminal side of lysine residues. Trypsin was chosen as a case study because its substrates consist of amino acids generally regarded as difficult to polymerize in a *graft-through* manner.³³ Note that these peptides also contain a distribution of serine and glutamine residues to impart the polymers with solubility in aqueous solution (Figure 2.6). Two sequences were prepared to examine the effect of substrate position on enzymatic activity. Specifically, Monomer **9** contains a lysine residue adjacent to the norbornene unit (position X₂), and monomer **10** includes a lysine closer to the C-terminus (position X₆ in these sequences). Monomers **9** and **10** were successfully polymerized to generate **9**₂₁ and **10**₁₉.

Enzymatic reactions were monitored *via* RP-HPLC to calculate percent cleavage as compared with standard curves of the authentic cleavage products. ESI-MS confirmed the identity of the predicted cleaved fragments analyzed from isolated peaks. Both monomers behaved as expected, undergoing complete consumption by trypsin within 90 minutes (Figure 2.6). On the contrary, polymers **9**₂₁ and **10**₁₉ exhibited variable activity depending on the location of the scissile bond. A meager ~10 % conversion was detected when the substrate was positioned near the backbone (**9**₂₁), while **10**₁₉ exhibited near quantitative consumption.

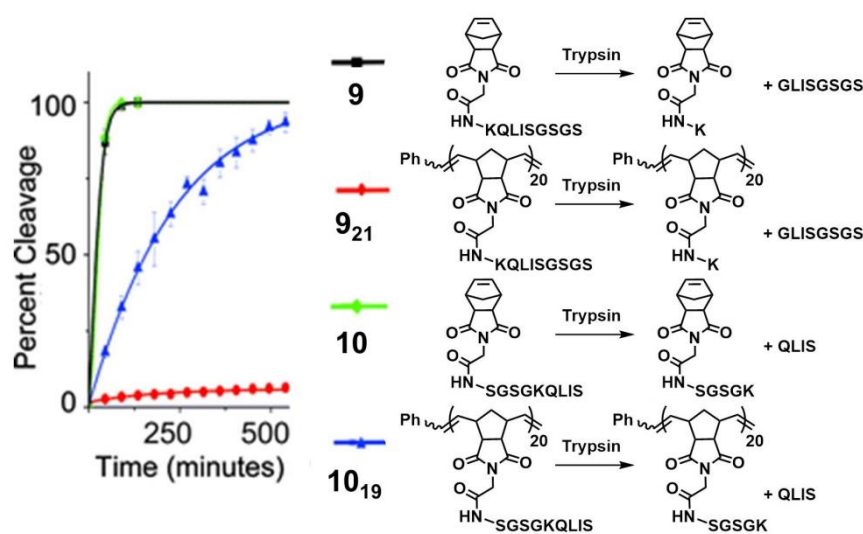


Figure 2.6 Trypsin activity on lysine-containing peptide monomers **9** and **10** and the corresponding polymers **9**₂₁ and **10**₁₉.

The collection of studies in this section describes a robust method for the preparation of *graft-through* peptides *via* ROMP. Specifically, a set of principles defining the polymerization of difficult peptide sequences and modulation of proteolytic activity is now established. The 31 pentapeptide library overall serves as a representative set of sequences reflective of the tolerance of [Ru] to peptide-based side chains. The work described in the

following section seeks to investigate related systems that can enhance bioactivity and investigate whether such systems can be triggered by enzymes to form discrete assemblies.

2.4 Improving the solubility of peptide polymers by incorporating permanent cations

Despite the high spatial density of peptides displayed on polymers prepared by *graft-through* ROMP, peptides of a given sequence arrayed covalently on the polymer backbone still retained the ability to function as enzyme substrates. This ability is of critical importance for the installation of peptide-based substrates in nanoparticle scaffolds that, when enzymatically processed, lead to dramatic morphology change of the nanoparticle.^{21,34} As described in section 2.2, soluble peptide polymers can exhibit higher proteolytic susceptibility than NPs, which may be applied towards developing bioactive systems. In the systems described previously, hydrophilicity was imparted to the polymers either by conjugation of Ebes (containing a short oligo(ethylene glycol) (OEG) chain) to the peptide³⁵ or incorporation a grouping of serine and glutamine residues.³¹ However, these insertions are not ideal since every conjugation step in SPPS limits the overall peptide yield, with increasing probability of truncated peptides that form unproductive sequences.³⁶ With formerly established strategies, namely incorporation of a C5 alkyl spacer derived from conjugation to norbornene hexanoic acid, several sequences were investigated to determine whether protecting-group-free polymerization *via* ROMP could be achieved. These sequences incorporate the MMP-2 and -9 recognition sequences as previously used (GPLGLAG) and contained an array of polar residues, **X** (Figure 2.7).

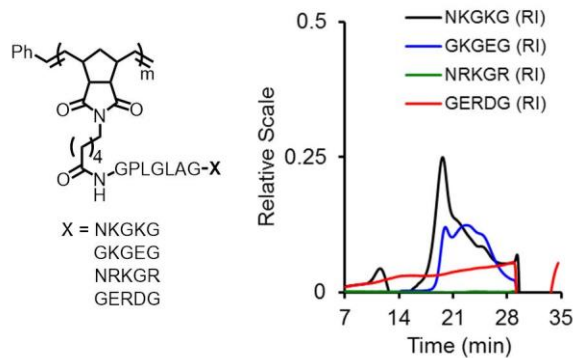


Figure 2.7 SEC-MALS chromatograms of peptide homopolymers consisting of an assortment of polar residues for imparting solubility. RI indicates refractive index.

Following polymerization of these monomers, SEC-MALS analysis was found to be problematic for all peptide polymers. Note that polymers containing NRKGR and GERDG as part of their peptide sidechains could not be characterized due to the absence of eluted peaks by SEC-MALS. The poor performance of these polymers was presumed to be due to aggregation, despite one of the sequences containing no carboxylic acid residues (Table 2.2). These results suggest that protecting-group-free polymerization of peptidyl monomers by ROMP may be challenging and that polymerization reactions yielding low \bar{D} values may be peptide-dependent.

Table 2.2 SEC-MALS characterization of peptide homopolymers bearing polar residues

X	M_n (g/mol)^a	\bar{D}^b	DP (m)^c
NKGKG	202,800	1.625	153 (10)
GKGEg	186,700	1.122	147 (10)
NRKGR	n/a	n/a	n/a (10)
GERDG	n/a	n/a	n/a (10)

^a M_n denotes number-average molecular weight. ^b \bar{D} denotes dispersity ^c DP (m) denotes degree of polymerization. (m) denotes theoretical DP.

Although conjugation of the hydrophilic Ebes moiety may alleviate the necessity for multiple amino acid incorporations; it was found that peptides containing Ebes degrade

rapidly (Figure 2.8). As determined by the relative peak heights on RP-HPLC, nearly 30 % of NorGPLGLAG-Ebes degraded at room temperature after 48 h (Figure 2.8C). This precludes the use of Ebes-conjugated peptides for long-term storage and use.

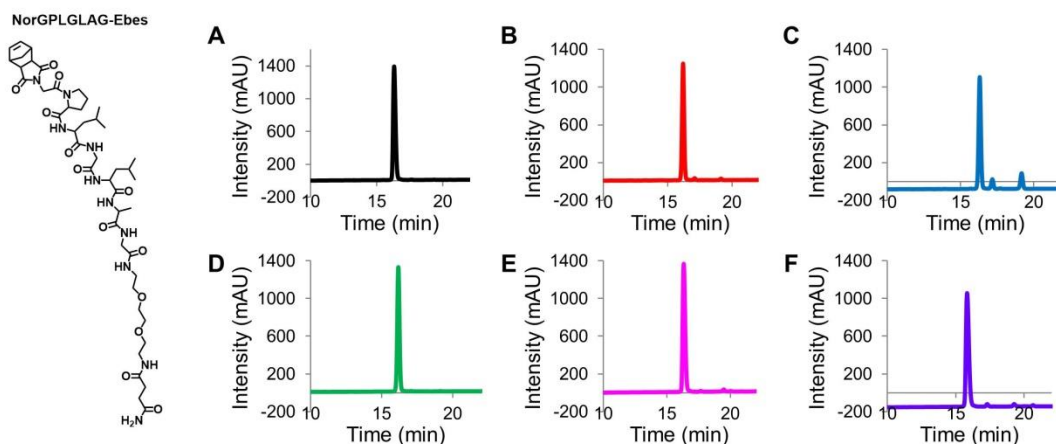


Figure 2.8 Degradation of the purified NorGPLGLAG-Ebes peptide monomer (A) when subjected to various conditions as monitored by RP-HPLC: (B) 4 °C for 48 h; (C) rt for 48 h; (D) -5 °C for 48 h; (E) 37 °C for 1 h; (F) 70 °C for 1 h.

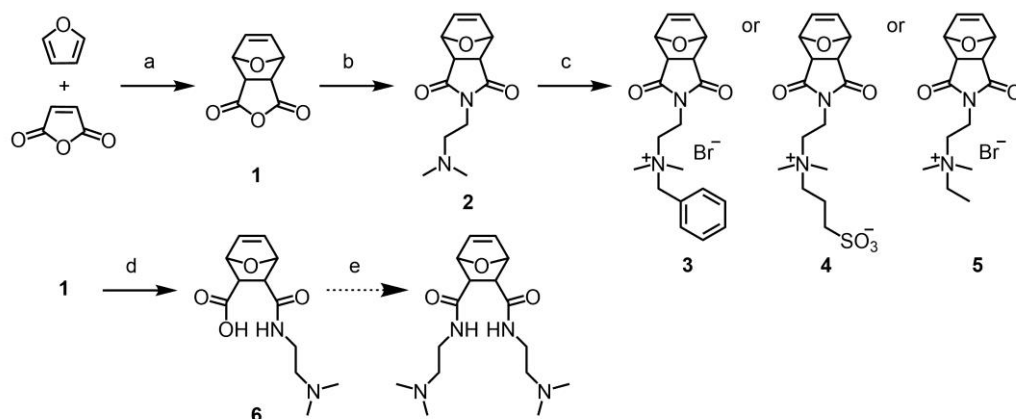
In the interest of developing polymeric NPs characterized with low heterogeneity, it is hypothesized that formulating them from amphiphilic polymers with low dispersity is crucial. This concept was realized in earlier work showing that when peptide-bearing amphiphilic block copolymers (characterized by high dispersity), were formulated into self-assembled NPs, the resultant NPs were heterogeneous as demonstrated by electron tomography.¹⁹ This is in contrast to the systems described in section 2.2, in which nanoparticles formulated from relatively simple peptide polymer amphiphiles (PPAs) showed both exceptionally low unimer polydispersity (due to a high degree of synthetic control) and low polydispersity of the nanoparticles. Presumably, these homogenous systems were acquired due to the high quality of the amphiphilic constituents used in the particle formulation. Nevertheless, there is still a need for developing reproducible synthetic

strategies, which enable predictability towards the construction of supramolecular systems from peptide-containing polymers. Further, there is a long-standing interest in developing water-soluble polymers as bioactive systems. In this context, soluble polymers bearing multiple copies of ionic groups (polyelectrolytes or polyzwitterions) are well-studied, for reasons that will be described later. The next section describes the incorporation of permanent cations (to generate polyelectrolytes or polyzwitterions) as a general strategy for conveying water-solubility to ROMP polymers.

2.4.1 Synthesis of *exo*-7-oxanorbornyl cations and betaines and their polymerization in DMF

Lowe and coworkers have previously demonstrated the polymerization of water-soluble, cationic ammonium *exo*-7-oxanorbornene derivatives using Grubbs first generation initiator, $\text{RuCl}_2(\text{PCy}_3)_2\text{CHPh}$, in TFE/methylene chloride solvent mixture *via* ROMP.³⁷ This study surveyed an array of permanently cationic and betaine (consisting of both cationic and anionic moieties) *exo*-norbornene monomers, since it has been well documented that *exo*-norbornenes polymerize more readily than *endo*-derivatives.^{38,39} Following procedures by Tew and coworkers, the preparation of monomers of this type proceeds with a Diels-Alder cycloaddition reaction using furan as the diene and maleic anhydride as the dienophile to afford *exo*-3,6-epoxy-1,2,3,6-tetrahydrophthalic anhydride, **1** (Scheme 2.2).⁴⁰ The tertiary amine imide intermediate, **2**, was then synthesized from a reaction between **1** and *N,N*-dimethylethylene diamine. This common precursor was then functionalized with several alkyl and aromatic halides *via* a Menshutkin reaction, to yield the desired oxanorbornene monomeric compounds, **3-5** (Scheme 2.2). Further, compound **1** was functionalized with *N,N*-dimethylethylene diamine to afford compound **6** with a single dimethyl amino group. While a Mitsunobu reaction was attempted with precursor **6** to afford the dual-dimethyl

amino-functionalized monomer, the product could not be isolated.⁴⁰ Following these synthetic procedures, the cationic benzyl monomer **3** was polymerized with [Ru] in DMF, a solvent for which polymerization of peptides is easily accomplished. ¹H NMR was used to monitor the course of the polymerization and determine whether the reaction proceeded in a living manner.



(a) Toluene, rt, 48 h, 66 %. (b) N,N'-Dimethylethylenediamine, 1:1 THF/MeOH, 50 °C, 48 h, 81 %. (c) (3) benzyl bromide, THF, 50 °C, 12 h, 89 %; (4) propanesultone, THF, 50 °C, 12 h, 21 %; (5) bromoethane, THF, 50 °C, 12 h, 67 %. (d) dimethylethanolamine, acetone, rt, 1 h, 64 %. (e) dimethylethanolamine, DIAD, PPh₃, THF, rt, 12 h.

Scheme 2.2 Synthesis of *exo*-7-oxanorbornene monomers.

Polymerization of **3** reached completion fairly rapidly, reaching full conversion in 60 min (Figure 2.9B). A log plot of the polymerization indicates a linear fit, demonstrating that **3** polymerizes in a living fashion (Figure 2.9C). Attempts were made to polymerize monomers **4** and **5** in DMF but their partial solubility at millimolar concentrations prevented further investigations into their use. As such, monomer **3** was used in the copolymerization of other monomers to identify the extent of its utility as a solubilizing moiety. **3** was copolymerized with a model aliphatic peptide (FPGPLG) to determine whether it could assist with solubility in the resultant copolymer (Figure 2.10). The appearance of a bimodal distribution on SEC-MALs suggested that copolymerization of **3** with a peptide was uncontrolled, causing

unproductive chain extension reactions (Figure 2.10B). Nevertheless, the resultant copolymer was dialyzed into Tris buffer at pH 7.4 from trifluoroethanol (TFE) to determine whether phase separation occurred in aqueous solution to form discrete assemblies. The absence of discrete nanostructures by TEM suggested that the copolymer was indeed hydrophilic and that **3** could, in principle, be used to solubilize other moieties (Figure 2.10C). For example, it has been used to promote the solubility of peptide nucleic acid (PNA)-based polymers.⁴¹

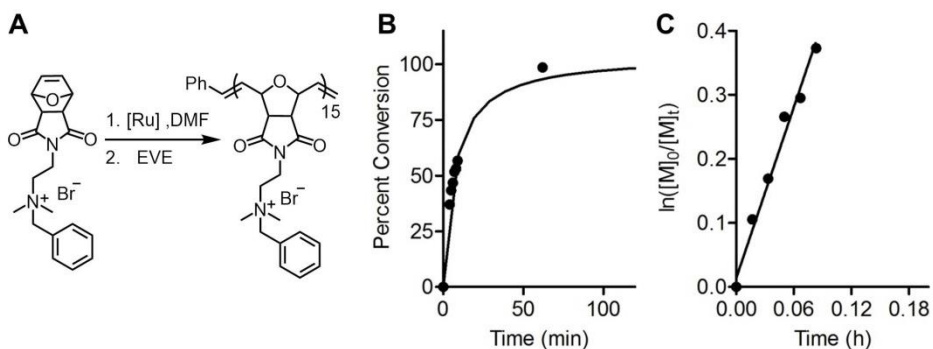


Figure 2.9 Monitoring the polymerization of the benzyl bromide quaternary amine monomer. (A) Polymerization of **3** catalyzed by [Ru] in DMF. (B) Following the polymerization by ¹H NMR and plotting percent conversion of the monomeric olefin (6.33 ppm) as a function of time. (C) Pseudo-first kinetics of the polymerization. The rate constant ($k_{\text{obs}} = 4.45 \text{ h}^{-1}$).

Encouraged by the solubilizing properties of permanent cations, we then aimed to incorporate them directly into norbornyl peptide monomers. To reiterate, we were interested in developing a practical method of synthesizing water-soluble peptide polymers without the incorporation of PEG-like moieties (which may alter bioactivity) or a cluster of polar amino acids (which results in poor SEC-MALS performance and lowers the peptide yield). Further, the biocompatibility of betaines and ionic polymers is well documented, as described in chapter 1, which is a desirable feature for bioactive systems that lend themselves to *in vivo* applications. The next section describes a simple SPPS procedure using a pseudo-orthogonal deprotection strategy that enables the direct incorporation of a quaternary ammonium group

in a peptide sequence. Several model sequences were prepared as water-soluble peptide brush polymers (PBPs), which contain a single permanent cation per peptide side chain. PBPs were prepared either as polyelectrolytes (consisting of a single charge of cationic nature in this case) or as polyzwitterions (consisting of both cationic and anionic charge, imparted by a glutamate residue).

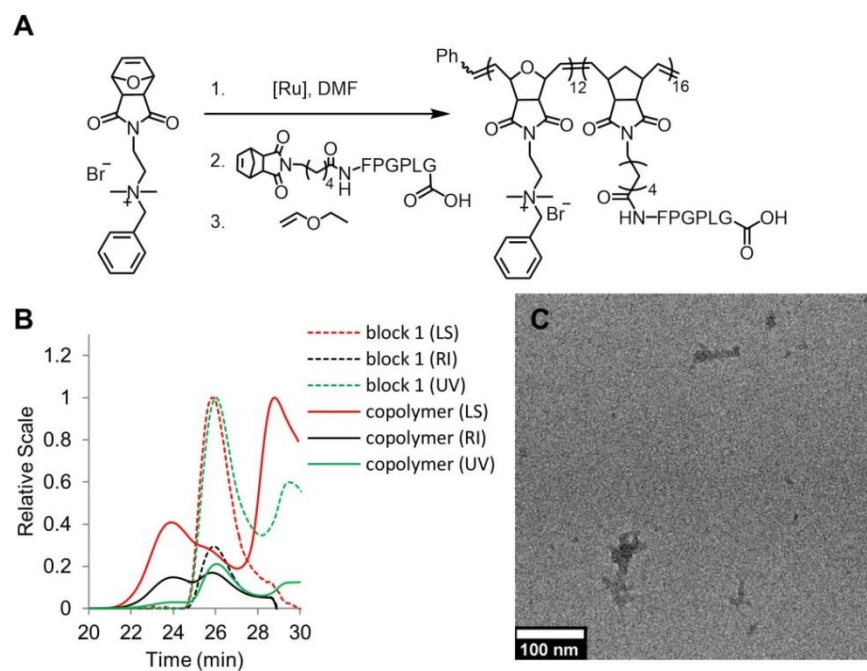


Figure 2.10 Copolymerization of cationic benzyl monomer **3** with an aliphatic peptide. (A) ROMP of **3** with norbornyl-FPGPLG. (B) SEC-MALS characterization of copolymer. (C) dry-state TEM image of **3-b-FPGPLG** copolymer in tris pH 7.4 buffer. The absence of discrete assemblies on the TEM grid suggested that the copolymer was soluble in aqueous solution. Poor performance by DLS further corroborated this observation (data not shown).

We hypothesized that PBPs of polyelectrolyte and polyzwitterionic character would readily undergo proteolytic cleavage with an appropriate enzyme, though their activities may vary due to their conformational behaviors in the presence of small molecular weight salts (buffered solution), described later. Intriguingly, discrete cylindrical micelles were formed upon proteolytic cleavage of peptide side chains of several model PBPs. This enzyme-

directed behavior is described further, along with its implications towards the development of disease-targeted polymeric systems. Finally, enzyme-responsive Gadolinium (Gd)-labeled PBPs were prepared and studied *in vivo*, to discern their clearance and biodistribution profiles in a murine tumor model. The inclusion of a heavy metal, paramagnetic agent (Gd) onto the polymer renders it as a polymeric magnetic resonance imaging (MRI) contrast agent (CA). Properties relating to its performance as a polymeric CA were also investigated.

2.5 Enzyme-directed assembly of peptide brush polymers

Stimuli-responsive polymers are a growing class of materials capable of undergoing unique changes in properties, resulting in the *in situ* generation of complex nanoscale structures.⁴² Various approaches to produce “smart” polymers that can respond to environmental triggers that are inherently present in a natural system stem from a collective interest in biomimicry.⁴³ Natural macromolecules or biopolymers continuously undergo conformational changes and participate in multi-component assembly processes for directing stimulus-triggered responses, such as those examples described in chapter 1. Frequently, stimuli including changes in pH, temperature, electrolyte concentration or UV light are harnessed to provoke transitions despite their general lack of specificity or impracticality in terms of translation to biological systems.⁴⁶ Alternatives include small molecule triggered polymers and nanoscale polymeric materials,^{45,46} protein recognition systems⁴⁷ and DNA-driven sense-response systems.^{48,49} Among stimuli, enzymes are unique in terms of both selectivity and specificity for their substrates, and their intrinsic capacity to act as molecular amplifiers, turning over their substrates in a catalytic manner. Enzymes operate under a range of mild, ambient solution conditions *in vitro*, and of course physiological conditions, which is a feature that is desirable for biological applications.⁴⁴ Despite these advantages, the extent to which enzymatic reactions have been utilized in this manner is generally limited to examples

demonstrating morphological changes of polymeric nanoparticles^{9,20} or nanoparticle disassembly.⁵⁰⁻⁵² At present, there are only three reported strategies for directing assembly processes of non-assembled polymeric substrates using enzymes.⁵³⁻⁵⁵ With the goal to expand the existing toolbox for these types of transformations, and exploring these materials as *in vivo* delivery systems, we exploited electrostatic interactions as the driving force for nanoscale assembly, driven by enzymatic hydrolysis (Figure 2.11).

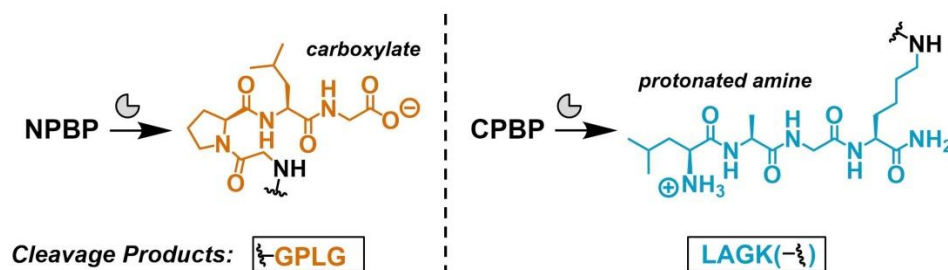
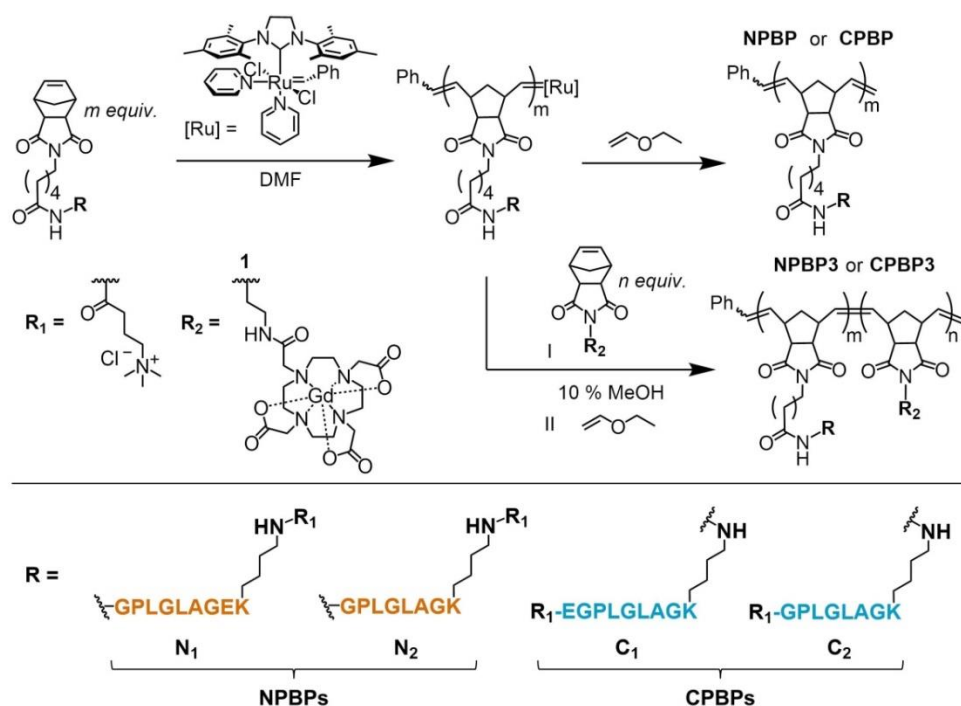


Figure 2.11 Enzyme-driven assembly for peptide brush polymers (PBPs) is dependent upon the identity of the charged moieties remaining on the polymer; carboxylates for N-terminal linked PBP (NPBP) or protonated amines for C-terminal linked PBP (CPBP) after proteolytic degradation.

2.5.1 Polymerization of peptide derivatives containing quaternary amines

Herein, we designed peptide brush polymers (PBPs) to be susceptible to cleavage by matrix metalloproteinase-9 (MMP-9), which is a gelatinase responsible for extracellular matrix remodeling and is a known disease biomarker.²² We selected the amino acid sequence (GPLGLAG) because it is an optimized recognition sequence for MMP-9 and conserved this motif across PBP analogues.⁵⁶ Further, we used thermolysin, a highly active bacterial zinc protease, as an *in vitro* proxy for MMP-9 because it is easily available, robust, and can cleave at sites adjacent to nonpolar residues in position P1', which results in discriminate consumption of the peptide.⁵⁷ Using this responsive amino acid sequence, four peptides were designed (Scheme 2.3). To test whether enzymatically exposed anionic or cationic groups

PBPs demonstrated different assembly characteristics, peptides were prepared bearing a polymerizable moiety connected to the *N*-terminus (N1/N2) or *C*-terminus (C1/C2), respectively (Scheme 2.3). Additionally, the impact of charge neutral vs charged PBPs was assessed by the incorporation (N1/C1) or omission (N2/C2) of an anionic glutamate in the amino acid sequence to create polyzwitterionic and polyelectrolyte PBPs, respectively, following enzyme cleavage.



Scheme 2.3 Synthesis of hydrophilic peptide brush polymers (PBPs) and block copolymers using graft-through Ring Opening Metathesis Polymerization (ROMP)

First, peptide monomers were synthesized by solid-phase peptide synthesis (SPPS) using standard fluorenylme-thyloxycarbonyl (Fmoc) chemistry. On-resin amide coupling of norbornene-(*N*-hexanoic acid) and (3-carboxypropyl)-trimethyl-ammonium chloride to the *N*-terminus and the ϵ -amino group of a *C*-terminal lysine residue afforded structural isomers (Figure 2.12). These monomers were then used to synthesize N- and CPBPs *via* ROMP using

the pyridyl modified Grubbs' initiator (Scheme 2.3). Given the tolerance of this catalyst to functionally complex amino acids,³¹ PBPs can be readily prepared using a graft-through approach, enabling high incorporations of functional peptide as well as metal-based complexes useful for imaging purposes, such as Gadolinium (Gd)-based chelates.⁵⁸ The fast initiation and slow propagation kinetics afforded by the catalyst, permits a "living" polymerization; that is, the absence of chain termination events permitting low dispersity and precise control over degree of polymerization (DP).^{59,60} Finally, ionic monomers can be polymerized by ROMP, as previously demonstrated by Lowe and coworkers in mixed solvent (TFE/chloroform) conditions.³⁷

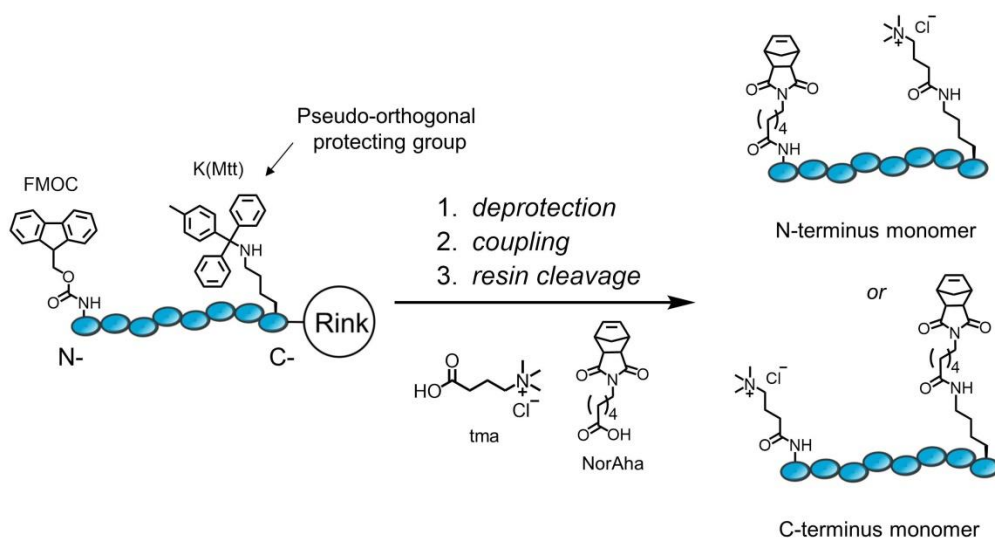


Figure 2.12 Solid phase peptide synthesis (SPPS) of monomers consisting of NorAha conjugated to the *N*- or the *C*-terminus of the peptide. Subsequent conjugation of (3-carboxypropyl)trimethylammonium chloride (tma) affords the final peptide monomers. The pseudo-orthogonal protecting group on the ε-amino group of the *C*-terminal lysine residue enables conjugation of NorAha and tma in these two manners.

2.5.2 Polymerization kinetics of peptide brush polymers bearing quaternary amines

Ionic Polymers bearing multiple copies of ionic groups (polyelectrolytes or polyzwitterions) are interesting for several reasons, not limited to their biocompatibility and

anti-microbial properties.^{61–63} Since peptide monomers bearing quaternary amine moieties have been previously explored in limited contexts,⁶⁴ it was first important to confirm that they could be polymerized in a living fashion in DMF, a solvent used previously by our laboratory for the *graft-through* polymerization of peptides.³¹ To investigate this, ¹H-NMR spectroscopy was used to verify pseudo-first order kinetics of these monomeric substrates (Figure 2.13). Both N1 and N2 monomers reached complete conversion within 1.5 h. A plot of the number-average molecular weight (M_n) as a function of monomer: initiator ratio ($[M]_0/[I]_0$) obeyed a linear fit, which is indicative of a living polymerization (Figure 2.13B, Table 2.3). As an additional method of verification, N- and CPBP analogues were polymerized to specific DPs by varying the monomer to initiator ratio ($[M]_0/[I]_0$) and determining the resulting molecular weights by size exclusion chromatography multi-angle light scattering (SEC-MALS) (Figure 2.14). Linear plots were consistent with the theoretical values for the expected molecular weights of the homopolymers. Lastly, from the SEC-MALS chromatograms, measured dispersities (\mathcal{D}) were small, further consistent with the living nature of these polymerizations (Table 2.4). Other peptide derivatives comprised of the aromatic residue-containing sequence (FPGPLGLAG) were also verified by these methods.

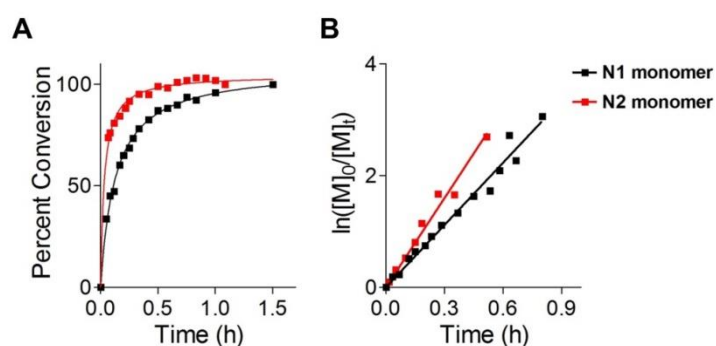


Figure 2.13 Polymerization kinetics of *N*-terminus conjugated peptide monomers measured by ¹H-NMR. (A) Percent conversion measured as a function of time and (B) pseudo-first order kinetic plots. The following slopes were determined by least-squares fitting: 3.718 hr⁻¹ and 5.327 hr⁻¹ for N1 and N2 monomers, respectively.

Table 2.3 Summary of molecular characterization and kinetic values for homopolymers ^a

Monomer	$[M]_0/[I]_0$	M_n (Da) ^b	\bar{D} ^c	DP ^d	k_p (L/(mol s)) ^e	Completion time ^f
N2	25	18,190	1.042	17	1.519	40
N1	25	42,910	1.016	35	0.995	90

^a Characterization for homopolymers shown in Figure 2.13. ^b M_n denotes number-average molecular weight. ^c \bar{D} denotes dispersity ^d DP denotes degree of polymerization. ^e Rate constant of propagation assuming [Ru] is constant (pseudo-first order kinetics). ^f Time required to reach 100% conversion of the monomer.

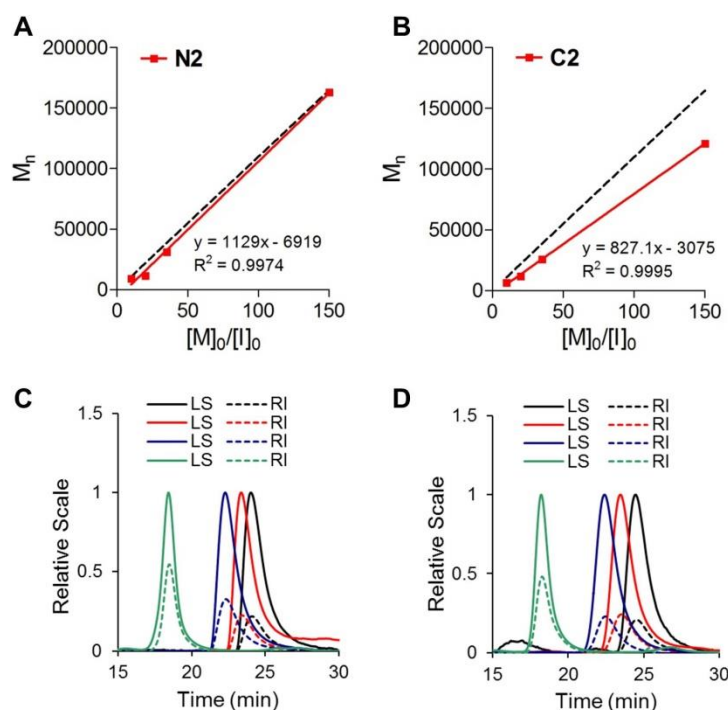
**Figure 2.14** Plots comparing the number-average molecular weight (M_n) as a function of monomer to initiator feed ratio ($[M]_0/[I]_0$) for the polymerization of (A) N2 and (B) C2. Note that an equation of the best-fit line for each is reported and is consistent with a living polymerization. Theoretical values for expected molecular weights are also indicated (black dotted line). SEC-MALS traces for the NPBP2 and CPBP2 homopolymers are shown in (C) and (D), respectively.

Table 2.4 Summary of molecular characterization and kinetic values for homopolymers ^a

Monomer	[M] ₀ /[I] ₀	Theor M _n (Da) ^b	M _n (Da) ^b	Đ ^b	DP ^b
N2	10	10,977	9,204	1.010	8
N2	20	21,953	11,640	1.002	11
N2	35	38,418	31,230	1.001	27
N2	150	164,651	162,900	1.057	148
C2	10	10,977	6,556	1.014	6
C2	20	21,953	11,990	1.001	11
C2	35	38,418	25,890	1.001	24
C2	150	164,651	121,100	1.046	110

^a Characterization for homopolymers shown in Figure 2.14. ^b Determined by SEC-MALS, 0.5 M LiBr in DMF ; dn/dc = 0.179.

2.5.3 Enzyme kinetics of peptide brush polymers and nanoparticles

In order to utilize proteolysis as a mechanism for self-assembly of PBPs, we first sought to examine how proteolytic consumption of PBPs by thermolysin varies with peptide composition and polymer degree of polymerization (DP). Previous work has shown that peptides displayed in a high density brush polymer exhibit resistance to proteolytic degradation.³⁰ However, we postulated that conjugation of a quaternary amine moiety to the peptide would enable PBPs to adopt an extended conformation in buffered solution, leading to increased solubility and greater access to enzymes. Notably, chain extension has been well documented for polyelectrolyte systems, such as polyampholytes and polybetaines, and is known as the antipolyelectrolyte effect.⁶⁵ The opposite solution behavior, known as the polyelectrolyte effect, occurs for strong poly-acids and bases when subjected to low molecular weight salts. This leads to Debye-Hückel shielding, causing polyelectrolytes to adopt a more entropically favored, globule-like conformation in salt solution.⁶⁶ Attempts to detect this phenomenon using batch-mode, bulk static light scattering (SLS) methods were met with unreliable results. Nonetheless, to determine whether these properties may enhance

or restrict enzymatic activity, N- and C- monomers and PBPs of either polyelectrolyte or polyzwitterionic character were incubated with thermolysin at 37 °C in 50 mM Tris pH 7.8 buffer containing 150 mM NaCl, 5 mM CaCl₂ and 1 mM ZnCl₂, which were required for proper protein folding. At various time points, these solutions were then quenched with 10% v/v 0.5 mM EDTA and analyzed by RP-HPLC to compare product peak areas with standard curves of the authentic cleavage products. From this, the amount of converted product over time was quantified (Figure 2.15).

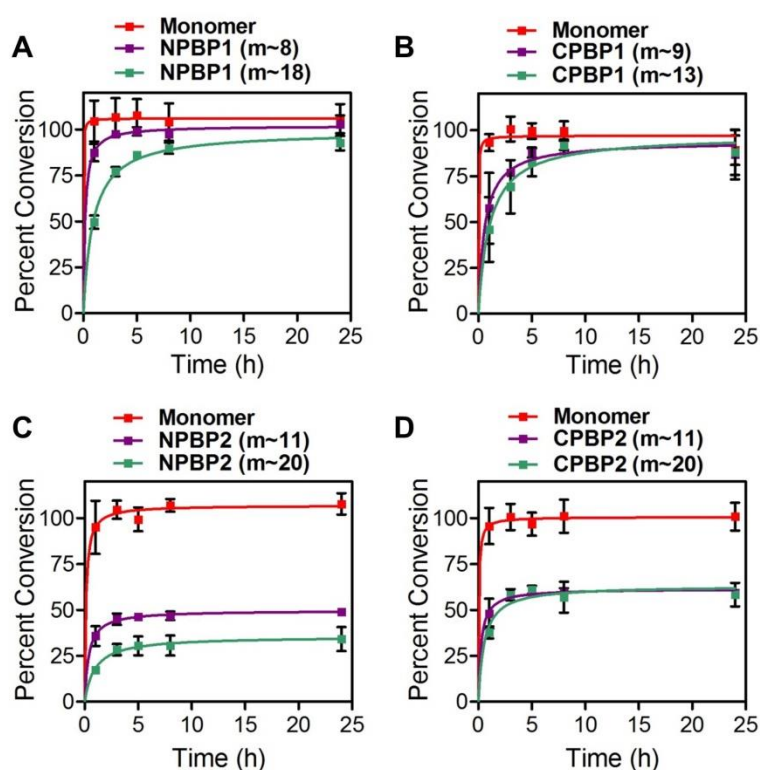


Figure 2.15 Percent conversion of 1 mM substrate by 1 μM thermolysin at 37 °C determined by RP-HPLC analysis. Polyzwitterionic substrates, (A) N- and (B) C- monomers and PBPs, as well as polyelectrolyte substrates, (C) N- and (D) C- monomers and PBPs of varying DPs are depicted. Error bars represent SD of 3 trials.

In all polyzwitterionic systems (NPBP1 and CPBP1), at least 84% of the substrate was consumed in 24 h. For polyelectrolyte systems (NPBP2 and CPBP2, m~11), only 49% and 59% of the substrate was converted in 24 h, respectively. These results are somewhat

surprising considering that positively charged substrates have been shown to attract enzymes bearing a net negative charge under physiological conditions.⁶⁷ Thermolysin, which has an isoelectric point of 4.45, should in principle exhibit strong electrostatic interactions with cationic substrates, therefore leading to higher rates of hydrolysis for NPBP2 and CPBP2 substrates than for NPBP1 and CPBP1 substrates.⁵⁷ Nevertheless, this difference in enzyme-responsiveness may be attributed to the preferred conformational states of the ionic polymers in buffered solution. In addition, a reduction in reaction rate seemed to correlate with an increase in DP for both polyzwitterionic and polyelectrolyte NPBPs (NPBP1 and NPBP2, respectively) (Figure 2.15A and C). Interestingly, CPBP analogues maintained similar conversion rates between polymers of similar varying DPs. This difference may be due to a greater distance separating the norbornyl polymer backbone from the peptide recognition sequence, minimizing steric interactions (Scheme 2.3).

We further sought to obtain detailed kinetic information of the enzyme processing of PBPs by preparing the peptide sequence as a fluorogenic substrate, consisting of a donor (Edans) and quencher (Dabcyl) pair (Figure 2.16). We expected that the fluorogenic PBP would be more resistant to proteolysis than the fluorogenic monomer constituent, which has been shown as a general feature for high density brush polymers.³⁰ However, we note that zwitterionic PBPs described here (N1/C1) demonstrate relatively similar enzymatic activity to their monomeric counterparts. Further, complete abolishment of activity is not observed for N2/C2 substrates, suggesting that PBPs can function as macromolecular enzyme substrates.

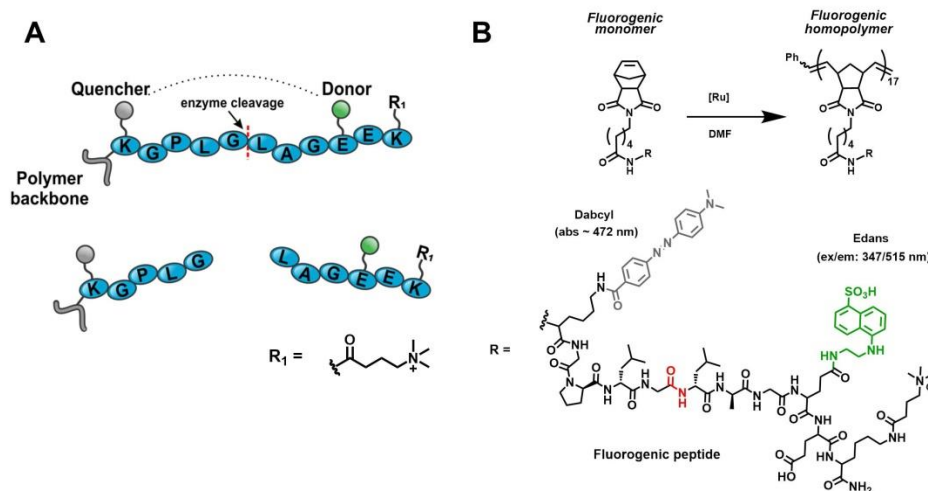


Figure 2.16 Schematic of a fluorogenic peptide bearing a donor molecule (Edans) and a quencher molecule (DabcyI). (A) Proteolysis of the peptide substrate liberates the peptide fragment bearing the donor from the polymer, reviving fluorescence. (B) Chemical structure of the fluorogenic peptide monomer, which was polymerized using [Ru] in DMF to prepare the fluorogenic homopolymer. The amide bond (shown in red) is the cut site for the protease MMP-9.

To underscore the potential utility of PBPs, we also prepared an amphiphilic block copolymer consisting of a hydrophilic block of fluorogenic peptides, which could self-assemble in aqueous solution to form spherical micellar nanoparticles (Figure 2.17).

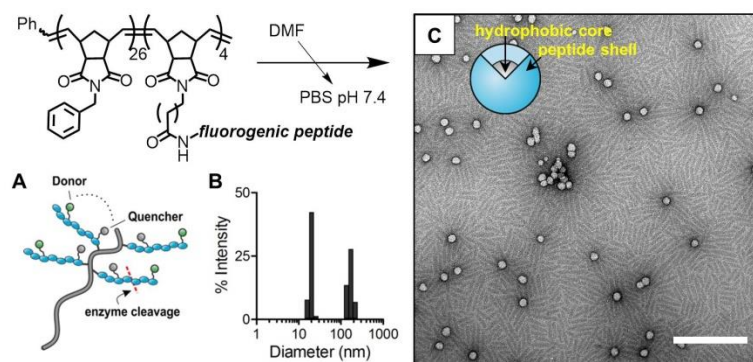


Figure 2.17 Characterization of the nanoparticles prepared from the fluorogenic block copolymer. (A) Dialysis of the fluorogenic block copolymer from DMF into PBS at pH 7.4 affords spherical nanoparticles approx. 20 nm in diameter that display peptides on the shell. (B) DLS and (C) dry-state TEM characterization of the particles. Scale bar is 200 nm.

Our reasoning is that in order to be able to harness enzymes to synthetically reproduce multicomponent assemblies in nature, PBPs (as homopolymers) are better suited than nanoparticle assemblies as enzyme substrates, since some micellar assemblies formulated from brush polymers, especially with higher degrees of polymerization, can be resistant to nucleases or to proteases.^{29,35} In kinetic assays, the fluorogenic monomer was readily cleaved by MMP-9 (Figure 2.18A) and thermolysin (Figure 2.18, 2.19). Kinetic data from thermolysin cleavage exhibited a sigmoidal curve, suggesting positive cooperativity between the enzyme and substrate (Hill coefficient, $h > 1$). As such, the fluorogenic homopolymer (DP = 17) was not explored further with thermolysin.

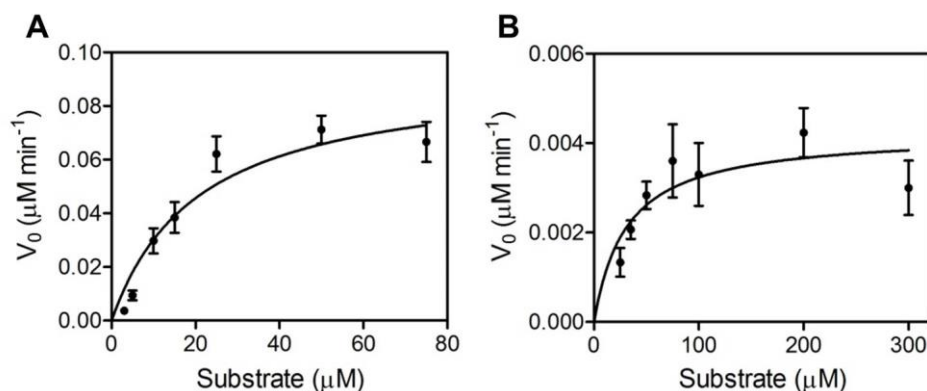


Figure 2.18 Michaelis-Menten plots. Proteolysis of (A) fluorogenic monomer, where $k_{\text{cat}} = 0.047 \text{ s}^{-1}$, $K_m = 20.7 \text{ } \mu\text{M}$ and $k_{\text{cat}}/K_m = 2.27 \text{ s}^{-1}\text{M}^{-1}$; and (B) fluorogenic homopolymer, where $k_{\text{cat}} = 0.0021 \text{ s}^{-1}$, $K_m = 30.9 \text{ } \mu\text{M}$ and $k_{\text{cat}}/K_m = 0.068 \text{ s}^{-1}\text{M}^{-1}$. There was minimal change in fluorescence for the fluorogenic nanoparticle; therefore, Michaelis-Menten plots could not be generated (data not shown). Standard deviation is plotted from $n = 3$ measurements.

The fluorogenic homopolymer exhibits some cleavage upon treatment with MMP-9, lending a specificity constant (k_{cat}/K_m) that was approximately 33-fold lower than that of the fluorogenic monomer. Nevertheless, no fluorescence was detected for the fluorogenic particle; where by up to 300 μM substrate concentration was assayed. Limited solubility of the nanoparticle prevented further analysis at higher concentrations. Overall, these results

suggest that PBPs can be recognized and cleaved by enzymes in a manner that may permit their use for enzyme-triggered assembly.

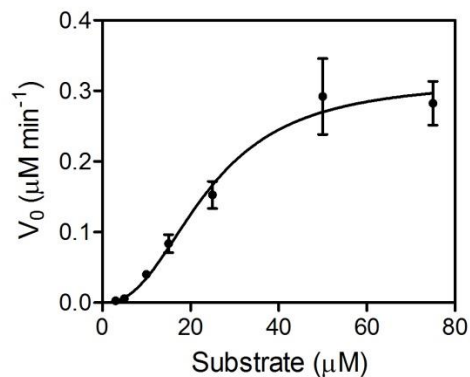


Figure 2.19 Enzyme kinetics of the fluorogenic monomer with thermolysin. An allosteric sigmoidal fit to the curve gives rise to constants, $V_{\max} = 0.3155 \mu\text{M min}^{-1}$, $h = 2.405$, $R^2 = 0.96$, where h is the Hill coefficient. Error bars represent SD of 4 trials.

2.5.4 Enzyme-triggered assembly of PBPs

We speculated whether enzyme cleavage of N- and CPBPs may instruct self-assembly, due to the charges borne by the polymers post enzyme-processing. Specifically, proteolysis of the N- and CPBPs exposes carboxylate and protonated amine groups under physiological conditions, respectively (Figure 2.11). To assess this, NPBP1 and CPBP1 (1 mM) were treated with thermolysin (0.1 mM) in Tris buffer for 24 h, then 10% v/v 0.5 mM EDTA was added to quench the reaction as done previously. Controls were prepared in the same fashion with the exception that EDTA was added to the reaction prior to thermolysin treatment. Dry-state transmission electron microscopy (TEM) as well as cryo-EM were used to image the solutions after enzyme treatment. Remarkably, discrete cylinder-like structures were observed for NPBP1 post treatment, while there was no evidence for assembly formation of any kind for CPBP1 (Figure 2.16, 2.17). Although a small amount of NPBP1 substrate was converted in the control solutions as determined by RP-HPLC (~3%), there was

no observable assembly formation by TEM, indicating that the active enzyme is necessary for self-assembly to occur (Figure 2.17). A survey of several other PBPs at various DPs (including N- and CPBP2) also indicates that enzyme-directed self-assembly is a general feature for N-terminus conjugated PBPs but not for C-terminus ones (Figure 2.18).

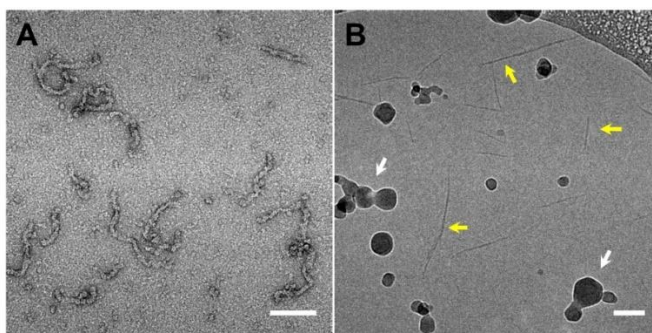


Figure 2.20 (A) Dry-state TEM micrograph and (B) cryo-EM of the enzymatic reaction of 1 mM NPBP1 (m~18) after 24 h treatment with 1 μ M thermolysin at 37 $^{\circ}$ C. Dry-state TEM and RP-HPLC of controls and CPBP1 subjected to thermolysin show no assembly formation (see Figure 2.17). Yellow arrows indicate the presence of cylindrical wormlike micelles and white arrows indicate ice particulates. Scale bar is 100 nm.

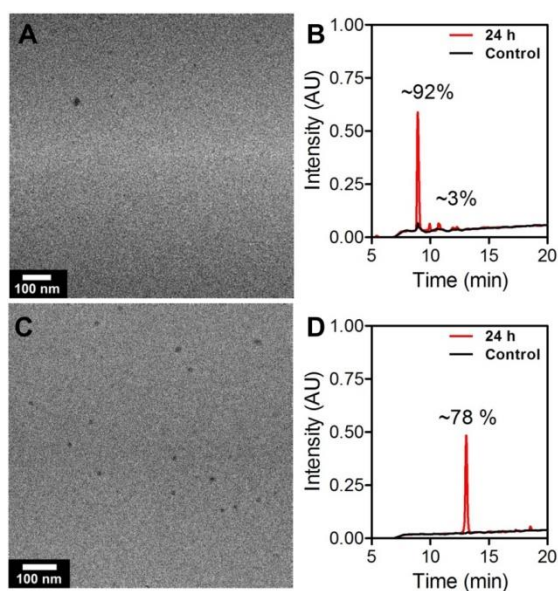


Figure 2.21 Dry-state TEM images and RP-HPLC chromatograms of NPBP1 controls and CPBP1. (A) NPBP1 (m ~18) treated with denatured thermolysin for 24 h. (B) RP-HPLC chromatograms of NPBP1 treated with thermolysin and with denatured thermolysin (control) for 24 h, confirming cleavage. (C) Dry-state TEM image of CPBP1 (m ~ 25) treated with thermolysin for 24 h. Grids appeared similar to untreated CPBP1 (not shown). (D) RP-HPLC chromatograms of CPBP1 treated with thermolysin and with denatured thermolysin (control) for 24 h, confirming cleavage.

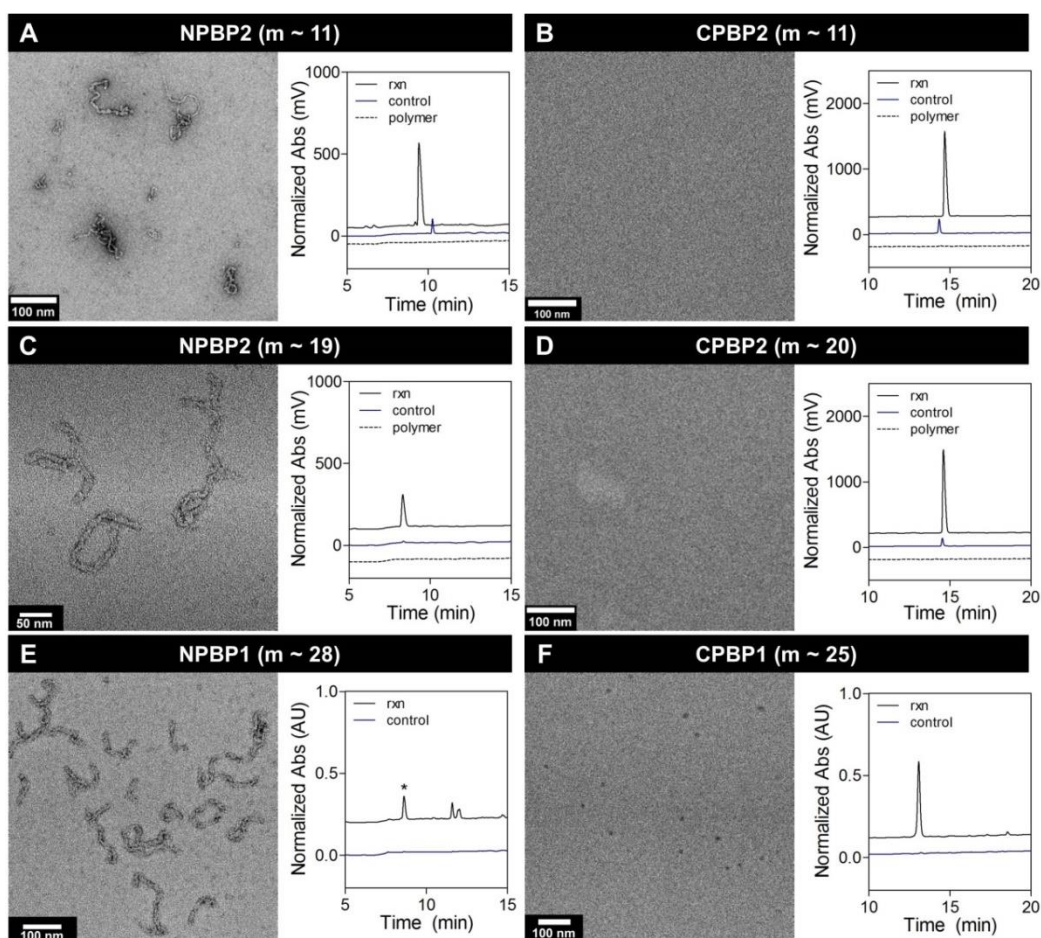


Figure 2.22 Enzyme-triggered assemblies of N-terminus conjugated PBPs (1 mM) formed 19 h or 24 h after treatment by thermolysin (1 μ M) as observed by TEM (left panel). Enzyme cleavage was verified by RP-HPLC (right panel). Cylindrical micelles are observed for (A) NPBP2 (m ~11), 19 h; (C) NPBP2 (m ~19), 24 h; and (E) NPBP1 (m ~28), 24 h. By contrast, no assemblies were observed for (B) CPBP2 (m ~11), 19 h; (D) CPBP2 (m ~20), 19 h; (F) CPBP1 (m ~25), 24 h. NPBPs incubated with denatured thermolysin did not self-assemble as determined by TEM (data not shown).

2.5.5 *In vivo* biodistribution of enzyme-responsive PBPs

Recent work in our laboratory has established that enzyme-responsive nanoparticles (NPs), which display peptides on the NP surface, allow for MMP-9 triggered accumulation in tumors or areas of infarcts.^{9,68} Though this strategy has improved NP accumulation and retention in diseased tissue, there still remains a continuous problem with regards to rapid NP sequestration by macrophages of the Mononuclear Phagocyte System (MPS).⁶⁹ Motivated by

our efforts to improve the design of protease targeted diagnostic and drug delivery vehicles, we reasoned that water-soluble brush polymers, which are on the order of <10 nm in size, may circumvent this problem. Further, enzyme-directed self-assembly of NPBPs could, in principle, enable tumor targeting and retention compared to CPBPs, which do not self-assemble in response to enzyme hydrolysis. To investigate this concept, we first prepared hydrophilic block copolymers, NPBP3 and CPBP3, comprised of peptide substrates for MMP-9 recognition and a Gd-based MRI contrast agent to permit the detection of the material *in vivo* (Scheme 2.3, see methods for details). We note that zwitterionic monomers, N1 and C1, were utilized in order to maximize proteolytic access (Figure 2.15). We verified the response of these polymeric substrates to MMP-9 as well as enzyme-promoted self-assembly of NPBP3, in this case, giving rise to the formation of micrometer-sized aggregates by dry-state TEM. We note that the change in polarity of the peptide block confers the block copolymer with amphiphilic character, likely resulting in the difference in morphology compared to that observed for PBPs.

We then examined the relative *ex vivo* biodistribution analyses of NPBP3 and CPBP3 using a syngeneic 4T1 (murine breast cancer) tumor model. To establish the tumor model, we inoculated balb/c mice (11 weeks) with 5 E5 4T1 cells subcutaneously on both the left and the right inguinal regions to permit the growth of primary tumors. After 1 week and a minimum tumor volume of 50 mm², NPBP3 and CPBP3 were administered (300 nmol with respect to Gd) via a 0.1 mL intravenous (IV) injection to the tail-vein or a 0.05 mL intratumoral (IT) bolus injection in the right solid tumor. After a period of 24 h or 1 week post-injection, mice were sacrificed and organs harvested for HNO₃ digestion, followed by analysis of Gd content using inductively coupled plasma optical emission spectrometry (ICP-OES) (Figure 2.23).

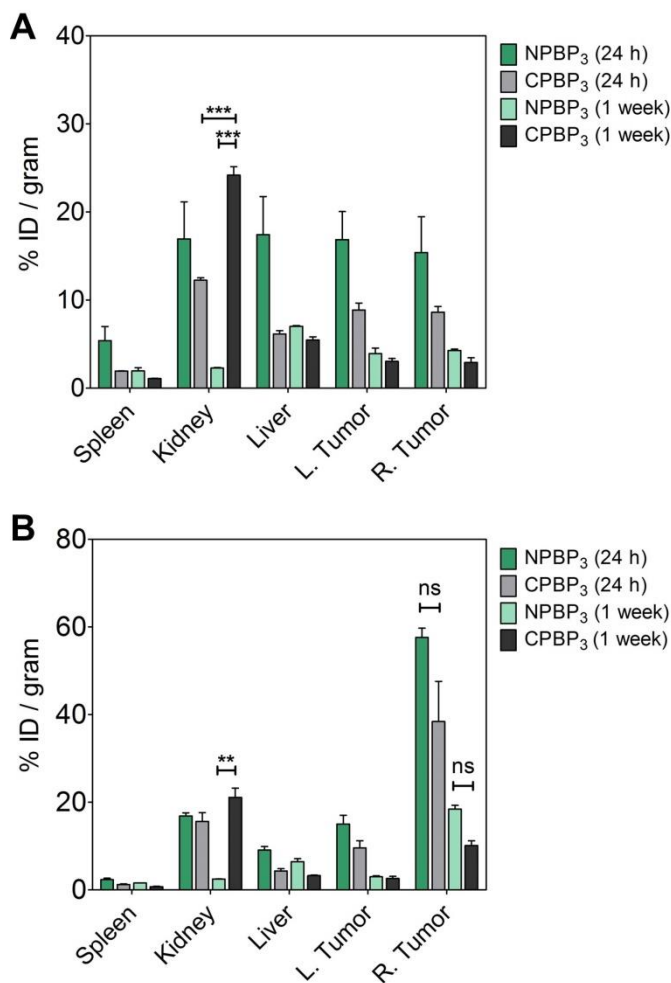


Figure 2.23 *Ex vivo* biodistribution (measured by ICP-OES of Gd) analysis in a syngeneic 4T1 tumor model 24 h and 1 week following (A) intravenous (IV) injection and (B) intratumoral (IT) injection in the right tumor of NPBP3 and CPBP3. For all groups, $n = 3 \pm$ standard error with the exception of NPBP3 at 1 week post IV and IT injections, for which $n = 2$. (** indicates $p < 0.01$ and *** indicates $p < 0.001$, given by unpaired, two-tailed t-tests; ns indicates not significant).

Interestingly, both NPBP3 and CPBP3 exhibited similar tumor biodistributions for either IV or IT administration routes. We note that the small size of the peptide brush polymers, ca. 25 kDa, which was optimally designed to enable renal clearance, may have actually prevented sufficient amounts of material from accumulating in the tumor after administration. Indeed, rapid renal filtration of the NPBP3 was observed within the first 24 h

post-injection, as determined from metabolic experiments (Figure 2.24). In this study, mice injected with NPBP3 were housed in metabolic cages for 1 week following administration and urine and fecal matter were collected at various time points, digested, and analyzed for Gd content by ICP-OES. Approximately 20-25 % of the total injected dose (ID) was accounted for in the excretion of each animal. Due to the high probability of sample loss through absorption into dried food, this figure represents the minimum amount of NPBP3 possibly excreted. Note that the small sample size is not enough to completely rule out the possibility of some clearance through MPS (*via* fecal route).

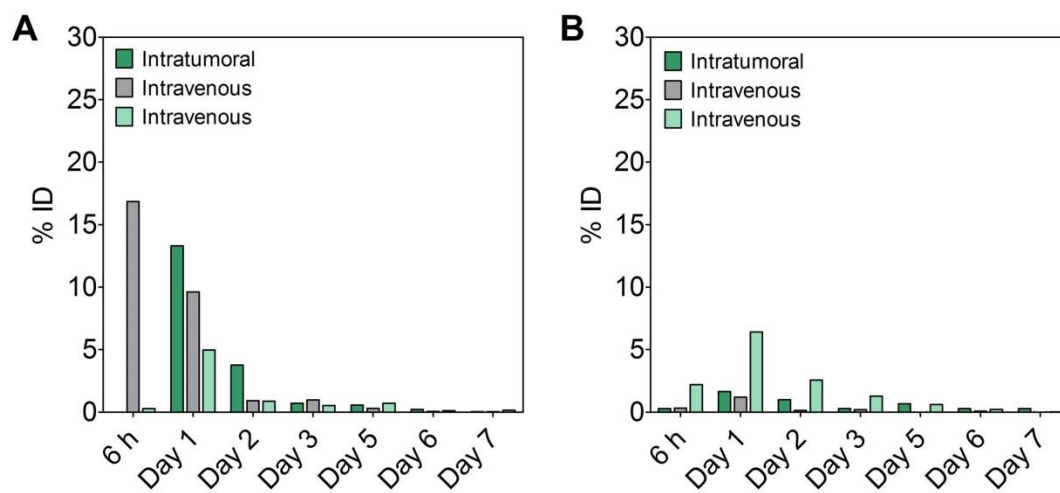


Figure 2.24 Metabolic experiments to determine the manner and duration of clearance of NPBP3. Biodistribution ($n = 3$, IV and IT administration routes, where each individual mouse is shown) in the (A) urine and (B) fecal matter over the course of 7 days.

Nevertheless, minimal liver and spleen biodistribution intensities relative to tumor biodistribution for both materials were encouraging. Specifically, total tumor biodistribution exceeded that of the liver by at least 2-fold. The minimal variation in Gd signal between the two materials 24 h or 1 week post injection may indicate similar circulation times. Despite this, a significant difference between NPBP3 and CPBP3 was measured in the kidney 1 week

post-IV and IT injections. For the IV-route, an approximate 2-fold signal enhancement between the 24 h and 1 week period was observed for CPBP3 whereas at least a 7-fold signal reduction was observed for NPBP3 (Figure 2.23A). Overall, CPBP3 showed 11 times greater Gd signal intensity in the kidney at 1 week post-IV injection than NPBP3. A similar observation was noted for the IT-route 1 week post injection, with approximately 9-fold greater Gd signal intensity detected in the kidney for CPBP3 (Figure 2.23B). We suspect that the unusual retention of CPBP3 in the kidney is likely due to proteolysis of the polymer upon systemic injection, which exposes positively charged amine groups that are able to form electrostatic interactions with the negatively charged glomeruli of the kidney.⁷⁰ NPBP3, once cleaved, forms a negatively charged polymer, which conceivably precludes this interaction.

Indeed, despite the design of PBPs to ensure specificity towards MMP-9, we speculate that the presence of aliphatic amino acids in the peptide sequence may provoke proteolytic activity from other endogenous enzymes such as chymotrypsin, which is produced in gram quantities in the lumen of the small intestine, secreted by the pancreas.⁷¹ Numerous peptidases also present in plasma are involved in the degradation of peptides.⁷² Chymotrypsin is known to cleave the C-terminal end of aromatic and, in some cases, aliphatic residues, of which there are several in the peptide sequence (Figure 2.25). As an *in vitro* test, NPBP3 was incubated with chymotrypsin for 12 h and the reaction analyzed by RP-HPLC. The appearance of cleaved peptide fragments were evident, showing that chymotrypsin is able to cleave this sequence in a non-specific manner (Figure 2.26A). NPBP3 was also subjected to pronase, a cocktail of proteases with broad specificity, and again cleavage fragments appeared by RP-HPLC after 12 h incubation (Figure 2.26B). Despite these results, the experiment fails to reflect the natural environment (i.e. the presence of serum proteins, clotting factors, etc.) where nonspecific cleavage might occur. As such, NPBP3 was also incubated in mouse serum to probe whether proteolysis may occur when systemically

injected. Generally, these data suggest that PBPs may be nonspecifically cleaved by proteases *in vivo* and further optimization may be necessary for their implementation as vehicle carriers, such as for the delivery of peptide therapeutics, or as enzyme-responsive materials for accumulation and retention in diseased tissue.⁹ Nevertheless, the limited MPS organ signal intensities observed for these materials, as described earlier, indicates that soluble polymers provide an improvement over NPs used as biologics.

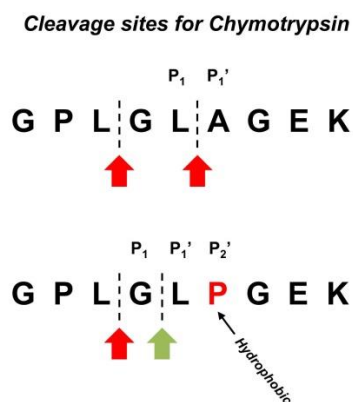


Figure 2.25 Recognition sites for chymotrypsin. Red arrows indicated potential cut sites, while the green arrow indicates the cut site for MMP-9, the enzyme for which this is an optimized sequence. A hydrophobic residue must reside in position P₂' in the peptide sequence to maintain function as a substrate for MMP-9, though replacement with proline, a nonpolar residue, may also mitigate aberrant cleavage by nonspecific proteases.⁵⁶

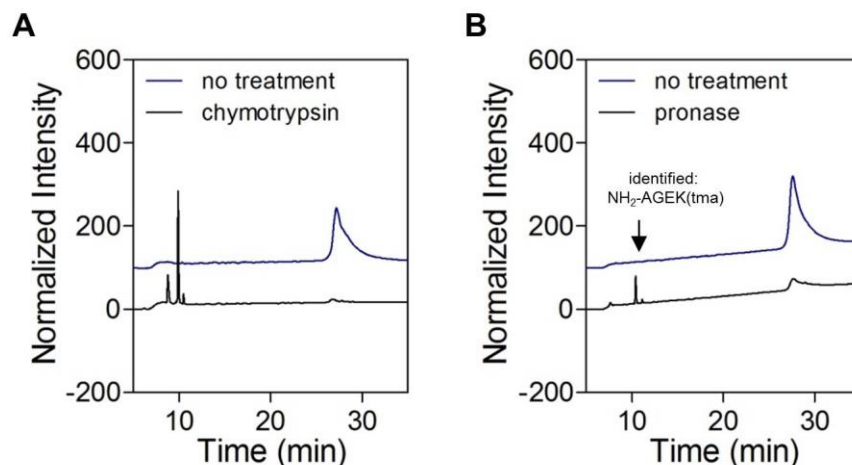


Figure 2.26 RP-HPLC chromatograms of NPBP3 treated with nonspecific proteases for 12 h in Tris pH 7.4 buffer. NPBP3 was incubated with (A) chymotrypsin (1 μ M) with 1 mM substrate; and with (B) pronase (100 nM) with 0.8 mM substrate (with respect to peptide).

2.6 Peptide brush polymers as enzyme-responsive MRI contrast agents

The application of small molecule magnetic resonance imaging (MRI) contrast agents (CA), specifically Gd(III) complexes, have enabled MRI as a powerful diagnostic tool in medicine. Due to its large magnetic moment and long electron-spin relaxation time, Gd is qualified as a constituent in most MRI CA.⁷³ Among other imaging modalities such as fluorescence,⁷⁴ ultrasound,⁷⁵ and computed tomography (CT),⁷⁶ MRI offers several advantages including the lack of ionizing radiation, non-invasive procedures and high anatomical resolution within clinically relevant depths. Despite growing concerns of Gd-associated toxicity,⁷⁷ small molecule contrast agents such as Magnevist® and Dotarem® are FDA approved and used in some 25 % of MR imaging procedures.⁷⁸ In general, these small molecule CAs clear rapidly *via* renal filtration and pose little risk to patients with healthy kidneys, though they suffer from low relaxivity (r_1) and thus, offer minimal contrast

enhancement (described later). Macromolecule-based contrast agents, such as polymers,^{79–81} dendrimers^{82–84} and nanoparticles⁵⁸ are of interest for many reasons related to their intrinsic large molecular size and synthetic versatility. For example, their large size permits greater relaxivity due to slower rotational tumbling, and enhanced circulation times, which may also lead to unique biodistribution profiles not routinely observed for small molecule analogues.⁸⁵ Further, synthetic approaches enable high loading of Gd for polymeric, dendritic, or nanoparticle-based constructs. Among this class, nanoparticle-based MR imaging strategies have been widely explored but their premature removal and retention in MPS organs prevents their use in clinical settings due to the accumulation of Gd in organs and even bone tissue.^{86,87} Though several strategies have been reported in attempt to mitigate this issue, such as pH-degradable polymeric agents,⁸⁸ we proposed a targeted approach using an enzyme-responsive polymeric contrast agent that would lead to enhancement of contrast only within diseased tissues, *via* the accumulation of [Gd] and increase in relaxivity. In the “off” state (stimulus not applied), the polymeric CA would be renally excreted, eliminating off-target accumulation and associated toxicity. In the “on” state, the polymeric CA aggregates in response to the removal of solubilizing groups by way of enzymatic cleavage of peptide side chains. This resultant aggregate thereby has a slower tumbling rate in solution than the uncleaved polymer, enabling an increase in relaxivity (Figure 2.27).

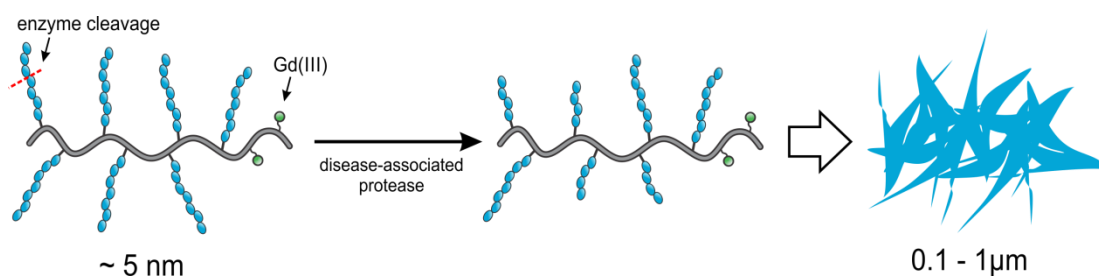


Figure 2.27 Enzyme-triggered assembly of peptide brush polymers bearing a Gadolinium (III) complex leads to an enhancement of relaxivity due to slower rotational tumbling of the aggregate.

2.6.1 Relaxivity properties of enzyme-responsive polymers

MR imaging measures the ^1H NMR signal of water, in which the signal intensity is directly proportional to the relaxation rates of the nuclear spins. In an applied magnetic field, the magnetic moments of protons will align themselves parallel to the magnetic field, until an applied radiofrequency pulse inverts their magnetization and the moments must realign themselves *via* longitudinal (T_1) and transverse (T_2) relaxation pathways.⁸⁹ The inherent heterogeneity of biological tissues enables contrast between them to be visualized *via* local differences in water concentration.⁹⁰ Paramagnetic contrast agents such as Gd(III) complexes can enhance contrast in T_1 -weighted MR images by slowing the T_1 relaxation rate of inner sphere and outer sphere water protons.⁸⁹ A comprehensive overview of relaxation theory in the presence of paramagnetic ions is abstained from this section, though there are published works on the topic.^{91,92} In summary, relaxivity depends on the magnetic field strength and temperature, being directly proportional to Gd(III) concentration and indirectly proportional to the T_1 relaxation rate of water protons:⁸⁹

$$r_1 = \frac{[\text{Gd}]}{T_1}$$

Note that the diamagnetic contribution to proton relaxation (from water in the absence of paramagnetic contrast agent) is also taken account in this equation. Because the inner sphere contribution to relaxivity can be modified *via* the structural properties of the MRI contrast agent, it is considered the major term. Overall there are three parameters that capture the main focus of researchers developing macromolecular MRI contrast agents. These are: q (number of water molecules bound to Gd(III) in the inner sphere or hydration state, which is generally 1), τ_m (the mean residency time of bound water molecules), and τ_r (the rotational correlation time of the contrast agent). The nature of Gd(III) complex generally limits the extent to which q and τ_m can be optimized, although research in the area of CA

development have led to Gd(III) complexes consisting of a q parameter of 2.⁹³ Though the synthetic challenges of making such a contrast agent prevent its widespread application. As such, a simpler approach is to append a Gd(III) contrast agent, such as Gd-DOTA, to a large macromolecule, which increases the value of the τ_r parameter and leads to an increase in relaxivity. Table 2.5 provides some examples of Gd(III) contrast agents and a dendrimer Gd-based CA, which exhibits an increase in relaxivity due to its large molecular size.

Table 2.5 Magnetic relaxivity properties of several commercially available small molecule and macromolecular contrast agents^{94,95}

MRI contrast agent	²⁹⁸ τ_m (ns) ^a	²⁹⁸ $\tau_r \cdot 10^{12}$ (s) ^b	r_1 (mM ⁻¹ s ⁻¹) ^c
[Gd(H ₂ O) ₈] ³⁺	1.2 ± 0.1	29 ± 2	-
[Gd(DTPA)(H ₂ O)]-2 (Magnevist®)	244 ± 18	103 ± 10	4.02 (35 °C)
[Gd(DOTA)(H ₂ O)]- (Dotarem®)	208 ± 17	90 ± 15	3.83 (39 °C)
G₃Gd₂₃ (Dendrimer) ⁹⁶	1.0 E3 ± 100	580 ± 10	14.57 (37 °C)

^a τ_m is the mean residence time of water molecules bound to Gd(III). ^b τ_r is the rotational correlation time. ^c Relaxivity measured at 20 MHz.

We were interested in determining whether enzyme-triggered assembly of peptide brush polymers (PBPs) bearing a Gd-DOTA complex could, in principle, increase relaxivity. To test this concept, we synthesized a block copolymer comprised of the zwitterionic peptide, **N1** and a norbornyl Gd-DOTA, similar to NPBP3 described above. We incubated the polymer with thermolysin for 24 h and verified cleavage-induced aggregation by TEM and RP-HPLC (Figure 2.28). A control solution was prepared, in which thermolysin was chemically denatured prior to incubation using EDTA as described in a previous section. Percent cleavage was quantified using a standard curve of the authentic peptide cleavage fragment and found to be 54 % and 7 % for the reaction and control solutions, respectively. These solutions were then diluted to yield a range of concentrations and the T_1 relaxation times were measured on a 7T MRI instrument at 298 K (Figure 2.29). From a linear least-squared determination of the inverse of T_1 relaxation time as a function of Gd(III)

concentration for each sample, the slope was calculated as the relaxivity, r_1 (Table 2.6). From this data, the relaxivity of the polymer prior to (control solution) and after (reaction solution) enzyme treatment was unchanged. Further, the relaxivity of the polymer was found to be similar to the small molecule contrast agent, Dotarem®. This result is somewhat surprising given that the polymeric contrast agent was expected to yield a relaxivity value somewhere in the range of $6\text{--}8\text{ mM}^{-1}\text{ s}^{-1}$.⁹⁷ Nevertheless, these low relaxivity values are likely due to the inability to observe the slow τ_r -induced changes to the relaxivity at high field strengths.

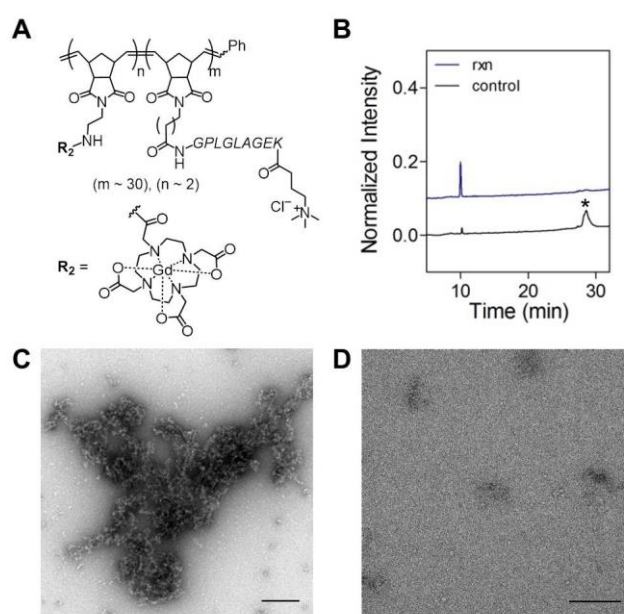


Figure 2.28 Enzyme-triggered aggregation of PBPs bearing a Gd-DOTA complex. (A) Chemical structure of the block copolymer bearing N1 peptide side chains, where $m = 29$ and $n = 1$. (B) RP-HPLC analysis of the polymer (3 mM) incubated with thermolysin (3 μM) for 24 h (rxn). The control solution was prepared in the same fashion but the enzyme was chemically denatured with EDTA as previously described. Dry-state TEM of (C) rxn and (D) control solutions, showing aggregate formation and the absence of assemblies, respectively. The percent cleavage was quantified for the rxn (54 %) and control (7 %) solutions.

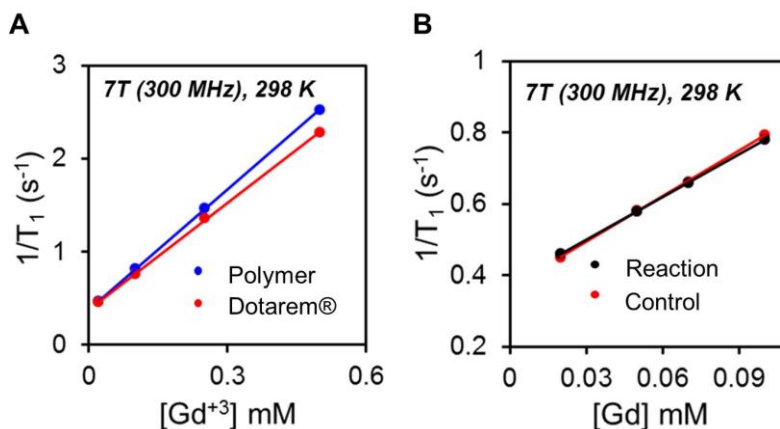


Figure 2.29 T_1 relaxation time using a 7T MRI at 298 K measured as a function of Gd(III) concentration of polymer and a commercially available contrast agent, Dotarem®. The slope of the curve is the relaxivity, r_1 . (A) Comparison of Dotarem®, a small molecule contrast agent, and the Gd(III) polymer. (B) Comparison of the polymer prior to and after enzymatic cleavage (solutions described in Figure 2.28).

Table 2.6 Summary of relaxivity values calculated from plots in Figure 2.29

Sample	r_1 ($mM^{-1} s^{-1}$)
Dotarem	3.820
Polymer	4.288
Reaction	4.005
Control	4.275

To probe the magnetic properties of the polymers and evaluate whether enzyme-triggered assembly is a viable method for enhancing T_1 -weighted contrast, the reaction and control solutions were analyzed by nuclear magnetic resonance dispersion (NMRD). At 310 K and 298 K, and at neutral pH, the NMRD profiles of both enzyme-cleaved and uncleaved solutions show the characteristic line shape of macromolecular structures due to a decrease in the rotational tumbling rate (Figure 2.30).^{90,98} The characteristic features of the NMRD profiles include an area showing constant relaxivity at low field strengths (0.01–1 MHz), and a maximum relaxivity at 20 MHz (0.5 T). Nevertheless, both enzyme-cleaved and uncleaved

polymeric CA display a maximum relaxivity of $\sim 4 \text{ mM}^{-1}\text{s}^{-1}$ at 20 MHz, which is comparable to small molecule contrast agents (Figure 2.30C, Table 2.6). Further, variable temperature NMRD analysis was conducted to identify whether increasing temperature (which increases the water exchange rate, τ_m) may reveal differences between the solutions (Figure 2.30D). Identical behaviors of the two samples were observed, which suggests that the rate of water exchange is a strong limiting factor in the relaxivity.

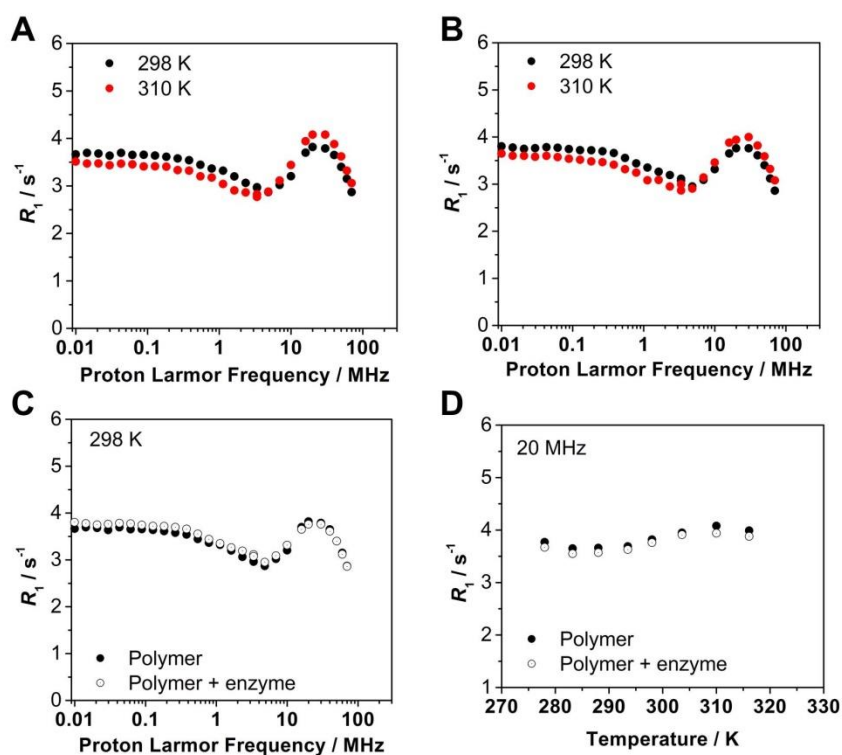


Figure 2.30 Nuclear magnetic resonance dispersion (NMRD) profiles measured at 298 K and 310 K of enzyme-responsive polymers. NMRD profiles of the polymer (A) prior to and (B) after enzyme treatment. (C) NMRD profiles of (A,B) overlaid. (D) Variable temperature NMRD at 20 MHz field comparing the enzyme-treated and un-treated polymer.

Despite these results, the competitive relaxivity value of the polymeric Gd-DOTA CA (compared to small molecule CA) enables its use in MR imaging. In a pilot study, a Gd-DOTA bearing PBP copolymer ($m = 17$, $n \sim 2$) was prepared and investigated for its potential use as a contrast agent for *in vivo* imaging using a metastatic breast cancer mouse model (4T1

murine breast cancer). To generate the model, a bolus intravenous injection of 4T1 cells ($1.00E+5$) was administered *via* the tail vein in the balb/c mouse strain (~14 weeks). After 10 days of tumor growth, a single mouse was anesthetized and imaged by MRI prior to injection. The contrast agent Gd-DOTA PBP (160 nmol with respect to Gd) was injected *via* the tail vein and T_1 -weighted images and anatomical scans (Figure 2.31) were obtained immediately after injection. Bright areas in the axial scans after 40 min were suggestive of areas where the Gd(III) reporter resided in the tissue (Figure 2.31). The animal was then imaged up to 2 days post-injection in order to determine material retention in the lungs.

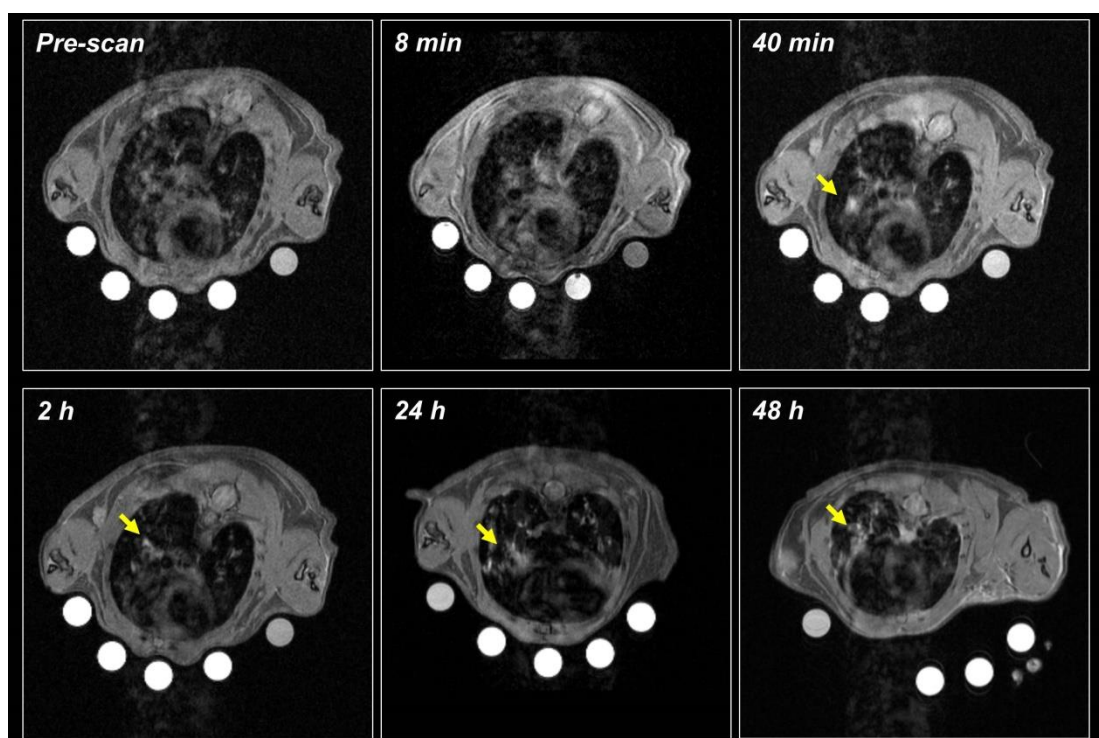


Figure 2.31 Time progression of the contrast enhancement shown in axial T_1 -weighted MR images of the metastatic tumor lung after IV-injection of Gd-DOTA PBP ($m \sim 17$, $n \sim 2$). Yellow arrows indicate potential areas of contrast enhancement. Several areas were sampled at a few time points and T_1 relaxation times calculated, with respect to phantoms (see Figure 2.32). Phantoms, which contained diluted solutions of the same material, were placed underneath the animal during scanning and used for normalizing between scans.

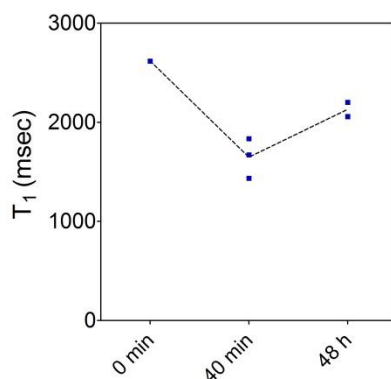


Figure 2.32 Multiple regions of interest were sampled from MR axial scans in Figure 2.31, normalized by comparing the relaxivity of phantoms for each scan to the pre-injection phantom relaxivity, then averaged and converted to T_1 (msec). Blue squares represent the averaged T_1 value from several regions in an individual axial slice and the dotted line connects the mean of each replicate. The scans were performed for a single mouse.

In addition, several areas of interest were measured in each T_1 -weighted image at different time points, normalized to phantoms (dilutions of the same material) and then averaged (Figure 2.32). At 40 min following the injection, a decrease in T_1 relaxation was measured, indicating an increase in relaxivity due to their inverse relationship. At 48 h post injection, partial recovery to baseline T_1 relaxation times was noted, indicating that there may be some material retention in the lungs.

To further elucidate this, *ex vivo* biodistribution analysis was performed on the liver, spleen, lung and kidney tissue using balb/c mice (~13 weeks) inoculated with 4T1 cells to generate the metastatic tumor (n = 2 or 3) or without 4T1 inoculation (n = 2), in order to delineate accumulation of the material following IV injection. Furthermore, a D-amino acid polymer (Figure 2.33A) was synthesized as a negative control in order to compare the effect of enzyme-directed aggregation (due to proteolytic processing of peptide side chains). When incubated with thermolysin for 6 h, the expected cleavage peak (LAGEK(tma)) eluted ~ 9 min for the L polymer and a reduction in polymer peak area (~30 min) was also observed. In

contrast, the D polymer showed no change in the RP-HPLC chromatogram upon thermolysin incubation, specifying that it could not be cleaved by the enzyme.

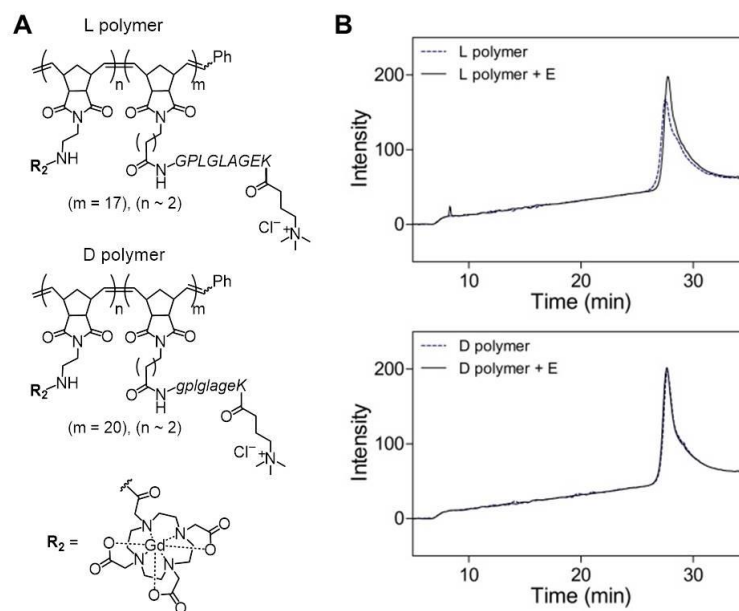


Figure 2.33 Comparison of thermolysin recognition on responsive (L polymer) and non-responsive control (D polymer) Gd-DOTA containing peptide brush polymers (PBPs). (A) Chemical structure of L- and D polymers. Note that lowercase and uppercase amino acid residues indicate D- and L-isomers, respectively. (B) RP-HPLC chromatograms of L polymer (upper panel) and D polymer (lower panel) prior to and after ~ 6 h treatment with thermolysin.

Once the absence of enzyme cleavage was verified for the L- and D- polymers, the *ex vivo* biodistribution was then examined (Figure 2.34). There was relatively little difference observed for the 4T1 and no 4T1 groups following administration of the L polymer (Figure 2.34). However, for the D polymer, the biodistribution profiles particularly in the kidney and the lung appeared somewhat different between groups (Figure 2.34B). Overall, the evidence shows that there was little difference between L- and D polymers in the lung tissue, suggesting that the proposed targeting mechanism of enzyme-triggered assembly is either not functioning as expected or the blood circulation time of the polymers is such that insufficient

amounts of material are able to reach the lung in order to undergo assembly. Aside from these possibilities, evidence in the literature also shows that D amino acid peptides can undergo nonspecific proteolysis *in vivo*, despite being the opposite enantiomer.⁹⁹ To investigate the former reason, blood was collected from the tail ventral artery/vein at various time points (10 min, 40 min, 1.5 h, 3 h, 5, and 24 h) following IV administration of the L- or D polymers for 4T1 or no 4T1 groups (Figure 2.35). The half-life ($t_{1/2}$) for each experiment was then calculated from a least squares fit of a one-phase decay (Table 2.7). Interestingly, the $t_{1/2}$ converged approximately 1.8 – 3.2 h, with the D polymer exhibiting a slightly greater half-life relative to the L polymer. Further, the 4T1 group for both L- and D polymers showed a minor increase in $t_{1/2}$ over the no 4T1 group.

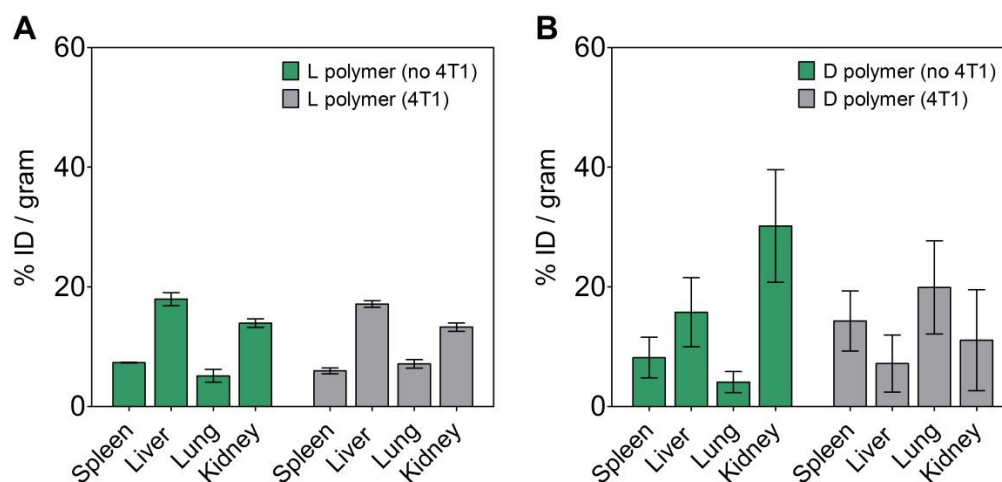


Figure 2.34 *Ex vivo* biodistribution (measured by ICP-OES of Gd) analysis of balb/c mice with and without metastatic 4T1 tumor 48 h following IV injection (160 nmol with respect to Gd(III)) of (A) L- and (B) D polymers (structures shown in Figure 2.33). (A) For these experiments, $n = 2 \pm \text{SD}$. (B) For these experiments, $n = 2 \pm \text{SD}$ for no 4T1 and $n = 3 \pm \text{SD}$ for 4T1 mice.

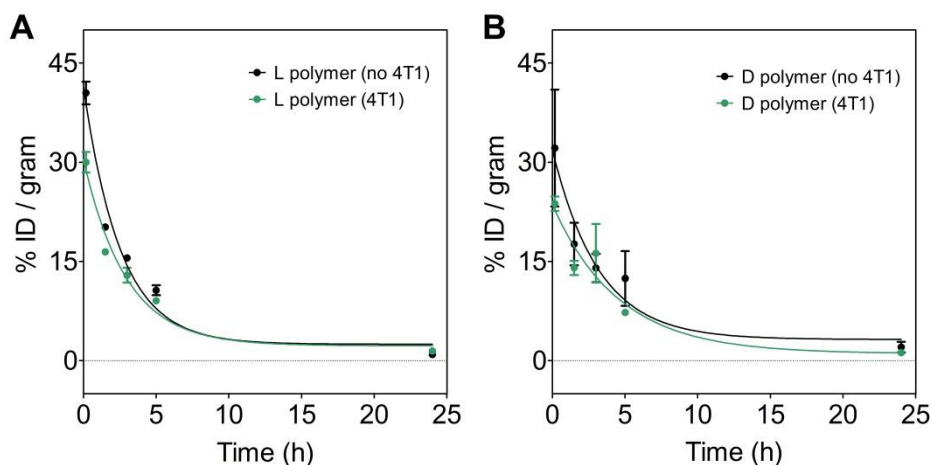


Figure 2.35 Blood circulation time of balb/c mice with and without metastatic 4T1 tumor following IV injection (160 nmol with respect to Gd(III)) of (A) L- and (B) D polymers (structures shown in Figure 2.33). Blood was collected from the tail ventral artery/vein at the indicated time points: 10 min, 40 min, 1.5 h, 3 h, 5, and 24 h. (A) For these experiments, $n = 2$ for both groups of mice. The half-life, $t_{1/2}$, was calculated as 1.76 h and 2.02 h for no 4T1 and 4T1 mice, respectively. (B) For these experiments, $n = 2$ for no 4T1 and $n = 3$ for 4T1 mice. The half-life, $t_{1/2}$, was calculated as 2.20 h and 3.15 h for no 4T1 and 4T1 mice, respectively. Least squares fit of a one-phase decay was used to fit the data. Standard error is plotted.

Table 2.7 Summary of blood circulation times of peptide brush polymers ^a

Polymer	IUPAC	kDa	Strain ^b	Model ^c	Dose (nmol)	$t_{1/2}$ (h) ^d	n ^e
L polymer (NPBP) ($m = 17$)	N1 ₁₇ - <i>b</i> -Gd ₂	21.4	Balb/c	4T1 metastatic	160	2.02	2
			Balb/c	-	160	1.76	2
D polymer (_D NPBP) ($m = 20$)	_D N1 ₂₀ - <i>b</i> -Gd ₂	25.5	Balb/c	4T1 metastatic	160	3.15	3
			Balb/c	-	160	2.20	2
L polymer ($m = 35$)	N1 ₃₅ - <i>b</i> -Gd ₂	47.1	C57/bl/6	-	160	3.12	1 – 4

^a Characterization for peptide brush polymers containing Gd-DOTA described in the main text. ^b mouse strain (balb/c indicates immune compromised while C57/bl/6 is healthy). ^c 4T1 metastatic model prepared by inoculation with 1.00 E5 4T1 (murine breast cancer) cells into the tail vein. ^d Half-life calculated from least squares fit. ^e number of mice used in the experiments.

2.7 Conclusions and future outlook

In summary, preliminary *in vivo* MRI and *ex vivo* elemental analyses indicate that peptide brush polymers may be used for MR imaging following intravenous injection. The half-lives calculated for the different materials are within the realm of what is expected for the molecular weights (Table 2.7). For example, for poly(vinyl alcohol) of 14.8 and 68.0 kDa (PVA15 and PVA70), $t_{1/2}$ was found to be 52.7 min and ~11 h, respectively.¹⁰⁰ One of the most extensively studied polymeric Gd(III) CA, poly(L-lysine) showed a $t_{1/2}$ of 1.90 h for a molecular weight polymer of 48.7 kDa.¹⁰¹ Similar to poly(L-lysine), CPBP3 (described in section 2.5.4) presumably performs as a positively-charged polymer post enzymatic cleavage, which diminishes its value as a contrast agent because of the long retention time in the kidneys. Nevertheless, optimization of the biological responses (i.e. biodistribution profile and circulation time) may warrant further investigation into several parameters of these types of polymeric CA. For one, polymers are deformable and may occupy small hydrodynamic diameters even at large molecular weights (>100 kDa). This feature may enable large molecular weight polymers to still undergo renal clearance through the small pores (~5 nm),¹⁰² while also enhancing circulation time. These properties should not be underestimated when designing biosynthetic polymers for biomedical applications. Indeed, the last three decades encompasses a vast body of literature dedicated to the study of drug-polymer conjugates and the now nearly overlooked *N*-(2-hydroxypropyl)methacrylamide (HPMA)-based systems.^{103–106} Finally, the relentless rat race of developing macromolecular CAs capable of toppling the highest standard of per Gd relaxivity is not necessarily a viable route towards the development of bioactive systems.^{107–109}

At this time, it is unclear whether the active targeting mechanism (enzyme-triggered assembly) of NPBPs (at these molecular weights and compositions) offers enhanced retention

of the material in diseased tissue (either metastatic 4T1 or solid 4T1 tumors generated). Similar systems for which this mechanism is reported as a successfully deployed strategy are based on nanoparticle formulations, which may interact with a biological system in entirely different ways.^{9,21,68} Nevertheless, *in vitro* data based on TEM and RP-HPLC shows that electrostatic-mediated assembly triggered by enzymatic hydrolysis of N- and CPBPs is feasible. Specifically, in section 2.5, the orientation of peptides within PBP structures was shown to have a dramatic effect on assembly post-enzymatic processing as well as kidney biodistribution following 1 week post IT and IV administration of Gd-labeled analogues. Both NPBP3 and CPBP3 showed tumor retention, perhaps due to alternate mechanisms post-enzyme recognition (assembly and positive charge-induced uptake, respectively). Further investigations in our laboratory may verify the reasons for these phenomena; otherwise, the principles learned here could be used to optimize similar polymer scaffolds for therapeutic peptide delivery.

Overall, the design of more effective MRI contrast agents, especially macromolecular CA, requires comprehensive understanding of the underlying mechanisms that influence proton relaxivity. One interesting perspective on this topic (and potentially future direction of this work) may be to investigate structural modifications to norbornyl Gd-DOTA, which may affect the dissociative mechanism (i.e. 8-coordinate transition state) contributing to relaxivity.⁹³ Specifically, increasing the steric crowding of the inner coordination sphere has been shown to increase the water exchange rate ($1/\tau_m$).^{93,110} A proposed modification to the norbornyl Gd-DOTA complex is shown in Figure 2.35, which incorporates a benzoic acid-type ligand. This modification may provide an improvement to the relaxivity in two ways: (i) by increasing the rigidity of the complex and thereby minimizing local rotation and providing better pairing with the global rotation of the macromolecule; and (ii) by increasing the steric crowding of the inner sphere coordination, thus enhancing water exchange.

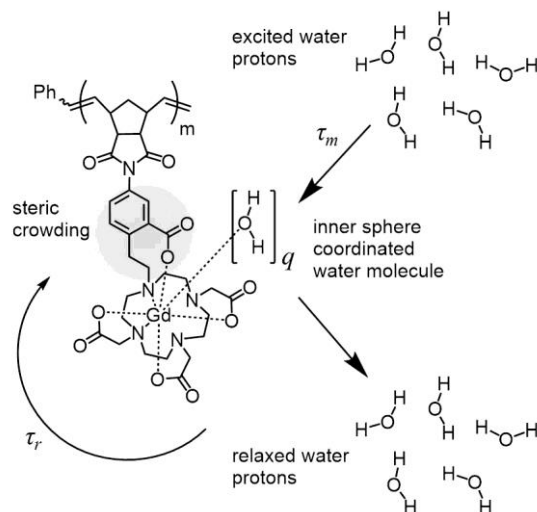


Figure 2.36 Proposed chemical structure of a Gd-DOTA analogue for future study. Minimization of the local rotation of the complex is crucial to couple it with the global rotation, τ_r , of the polymer. The aromatic group provides steric bulk to the inner coordination sphere and may be available for π - π stacking interactions between neighboring phenyl groups on adjacent polymerized Gd(III) chelates. This interaction may help reduce the σ bond rotation of the imide group of the norbornene connecting the complex.

Nevertheless, at field strengths above 1.5 T (~ 60 MHz), the water exchange rate, ($1/\tau_m$), is not as critical to achieving high relaxivity.^{110,111} Since clinically relevant field strengths are moving beyond what is currently in use (1.5 – 3 T), keeping well-informed of not only the biological limitations of these MRI reporters, but also the delicate interplay of physical parameters essential to their relaxivity-enhancing properties, will be key to their medicinal use.⁸¹

2.8 Acknowledgements

Chapter 2 is adapted, in part, from Michael E. Hahn, Lyndsay M. Randolph, Lisa Adamiak, Matthew P. Thompson, and Nathan C. Gianneschi. "Polymerization of a Peptide-based Enzyme Substrate." *Chem. Comm.*, 2013, 49, 2873-2875. Copyright 2013 Royal Society of Chemistry. Permission to use copyrighted images and data in the manuscript was

also obtained from Michael E. Hahn, Lyndsay M. Randolph, Matthew P. Thompson, and Nathan C. Gianneschi. The dissertation author was the third author on this manuscript.

Chapter 2 is adapted, in part, from Jacquelin K. Kammeyer, Angela P. Blum, Lisa Adamiak, Michael E. Hahn, and Nathan C. Gianneschi. "Polymerization of Protecting-Group Free Peptides via ROMP." *Polym. Chem.*, 2013, 4, 3929-3933. Copyright 2013 Royal Society of Chemistry. Permission to use copyrighted images and data in the manuscript was also obtained from Jacquelin K. Kammeyer, Angela P. Blum, Michael E. Hahn, and Nathan C. Gianneschi. The dissertation author was the third author on this manuscript.

Chapter 2 also contains material that is currently being prepared for submission for publication: "Enzyme-triggered Assembly of Peptide Brush Polymers" Lisa Adamiak, Andrea J. Luthi, Clare M. LeGuyader, Michael E. Hahn, Miriam Scadeng, Tomoko Hayashi, Dennis Carson, and Nathan C. Gianneschi. The dissertation author was the first author of this pending manuscript.

2.9 Methods

All materials were purchased from commercial sources, unless otherwise noted. Dotarem was purchased from Macrocyclics. The phenyl norbornyl monomer (*N*-benzyl)-5-norbornene-*exo*-2,3-dicarboximide was prepared as previously published.¹¹² The norbornyl Gd-DOTA mono amide monomer was prepared as previously described.⁵⁸ $(\text{H}_2\text{IMes})(\text{pyr})_2\text{Cl}_2\text{Ru}=\text{CHPh}$ was prepared from $(\text{H}_2\text{IMes})(\text{PCy}_3)\text{Cl}_2\text{Ru}=\text{CHPh}$ according to a literature procedure.¹¹³ Amino acids used in SPPS were purchased from AAPPTec and Novabiochem. RP-HPLC analyses were performed on a Jupiter Proteo90A phenomenex column (150 × 4.60 mm) using a Hitachi-Elite LaChrom L-2130 pump equipped with a UV-Vis detector (Hitachi-Elite LaChrome L-2420) using a binary gradient (Buffer A: 0.1% TFA in water; Buffer B: 0.1% TFA in acetonitrile; Flow rate: 1 mL/min). Peptides were purified

using a Jupiter Proteo90A Phenomenex column (2050 × 25.0 mm) on a Waters DeltaPrep 300 system using a binary gradient (Buffers A and B; Flow rate: 22 mL/min). DLS measurements were obtained using a DynaPro NanoStar (Wyatt Technologies). Mass spectra were obtained from the UCSD Chemical and Biochemistry Molecular Mass Spectrometry Facility.

2.9.1 Peptide synthesis

Peptides were synthesized on solid phase support using Rink Amide MBHA (AAPPTec, cat. #RRZ005), Wang-Gly (AAPPTec, cat. #RWG101), or Wang (AAPPTec, cat. #RWZ001) resins. Briefly, Fmoc deprotection was achieved by shaking peptide-bound resin with 20% methylpiperidine/DMF in a plastic chromatography vessel (Bio-rad, cat. #7321010) for 5 minutes, followed by draining, rinsing 1 × with DMF, and then applying fresh methylpiperidine solution for another 10 min. After thorough rinsing with DMF following deprotection steps, amide coupling reactions proceeded for a minimum of 45 minutes using 3 equiv of Fmoc-protected amino acids (AAs), 2.9 equiv of HBTU, and 6 equiv of DIPEA. Fmoc-Lys(Mtt)-OH residues (AAPPTec, cat. #AFK125) (1.5 equiv) were double-coupled (i.e. subjected to two consecutive applications of fresh AA/HBTU/DIPEA solutions) at the first conjugation step. Peptide Monomers were prepared by double-coupling to 1.5 equiv N-(hexanoic acid)-cis-5-norbornene-exo-dicarboximide (prepared via a published protocol) at the N-terminus of the peptide or at a lysine side chain near the C-terminus. Fluorogenic peptides were prepared by hand and residues Fmoc-Lys(DabcyI)-OH (AAPPTec, cat. #AFK135) and Fmoc-Glu(Edans)-OH (AAPPTec, cat. #AFE150) were double-coupled (1.5 equiv). (3-Carboxypropyl)trimethylammonium chloride was purchased from Sigma (403245) and double-coupled (1.5 equiv) at the N-terminus of the peptide or at a lysine side chain near the C-terminus. Selective deprotection of methyltrityl (Mtt) protecting groups on resin was afforded by shaking the resin 5 x in TFA/TIPS/DCM (3:5:92 v/v/v) (approximately 6 mL per

gram resin) for 7 min each, followed by rinsing with DCM. Full deprotection was confirmed via the Kaiser test. Peptides were cleaved from the resin for 1 h using a solution of TFA/Triisopropylsilane (TIPS) /water (95:2.5:2.5 v/v/v). The TFA solution was drained into a conical tube and evaporated. The concentrated peptide solution was then precipitated in cold ether, centrifuged, and the pellet purified by RP-HPLC. The identity and purity of each peptide were verified via ESI-MS analysis and the presence of a single peak in the analytical RP-HPLC chromatogram.

2.9.2 RP-HPLC analysis of proteolytic studies

The extent of proteolytic cleavage of all materials by Thermolysin (Promega, cat. #V4001) was determined by the comparison of RP-HPLC chromatograms. In a typical procedure, materials (1 mM with respect to peptide substrate) were subjected to Thermolysin (1 μ M) at the indicated time points at 37 °C in Tris cleavage buffer, pH 7.4 (20 mM NaCl, 50 mM Tris, 50 mM CaCl₂, 1 mM ZnCl₂). 10% v/v EDTA pH 8.0 was added to the solution to quench the reaction. Solutions were either immediately analyzed on RP-HPLC or stored in a 4C fridge prior to analysis. RP-HPLC was used to assess the peak areas of cleavage products. The identities of cleavage fragments were confirmed by ESI-MS and peak areas were compared to standard curves of the authentic peptide fragments to assess the percentage of enzymatic degradation.

2.9.3 Standard curves for quantifying enzyme cleavage

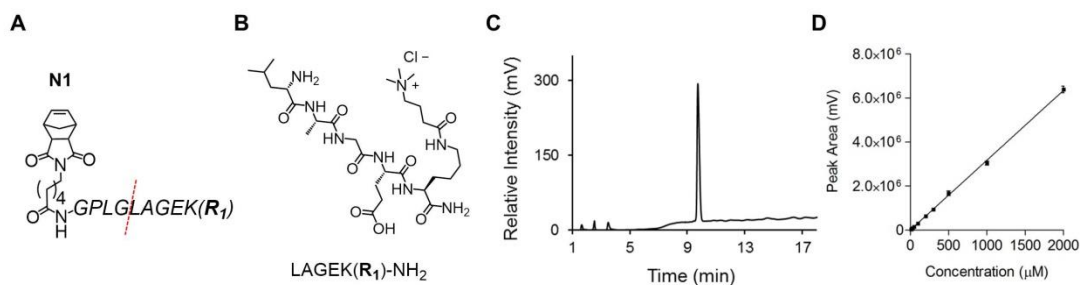


Figure 2.37 Standard curve of the synthesized, authentic **N1** peptide cleavage fragment (LAGEK(R1)). (A) Chemical structure of **N1** depicting the thermolysin cleavage site (dotted red line). (B) Chemical structure of LAGEK(R1). (C) RP-HPLC chromatogram of purified LAGEK(R1). (D) Standard curve generated of LAGEK(R1) using measured peak areas following absorbance at 214 nm.

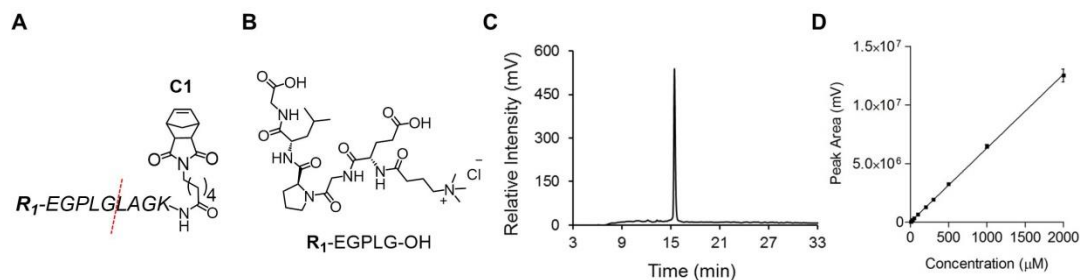


Figure 2.38 Standard curve of the synthesized, authentic **C1** peptide cleavage fragment (R1-EGPLG). (A) Chemical structure of **C1** depicting the thermolysin cleavage site (dotted red line). (B) Chemical structure of R1-EGPLG. (C) RP-HPLC chromatogram of purified R1-EGPLG. (D) Standard curve generated of R1-EGPLG using measured peak areas following absorbance at 214 nm.

Table 2.8 Summary of RP-HPLC, ESI Analyses of Authentic Peptide Cleavage Fragments ^a

Monomer	Cleavage fragment	Gradient (30 min)	RT (min)	Mass (calcd) ^b	Mass (obs) ^b	Slope (μM^{-1}) ^a
N1	LAGEK(R1)-NH ₂	2 – 50 % B	9.7	643.41	643.48	3173
N2	LAGK(R1)-NH ₂	2 – 50 % B	9.4	514.34	514.60	2304
C1	R1 -EGPLG-OH	2 – 50 % B	15.5	599.34	599.50	6310
C2	R1 -GPLG-OH	2 – 50 % B	13.2	470.30	470.60	4829

^a Characterization of cleavage fragments and standard curves as described in Figures 2.25 and 2.26. ^b Measured by ESI-MS

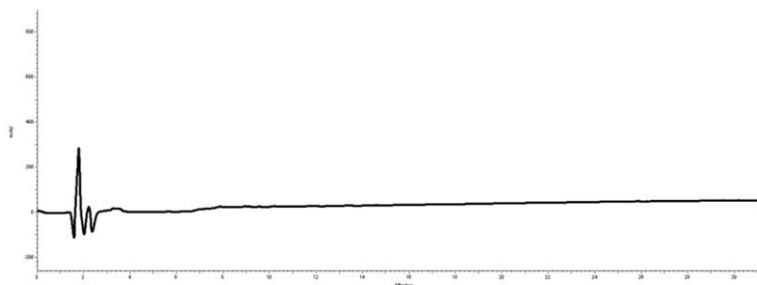


Figure 2.39 Peptides displayed on particle 2 (derived from PPA 2) are not cleaved by the protease MMP-2

2.9.4 Polymerizations

All polymerizations were performed in a glove box under N₂ (g) using dry, deoxygenated DMF obtained by the freeze-pump-thaw method. Polymerizations were conducted in J Young NMR tubes (5 mm diameter) for monitoring *via* 1H-NMR. A typical procedure to synthesize a homopolymer of DP 20 involves adding [Ru] catalyst (0.53 mmol, 1 equiv) to a solution of monomer (21 mmol, 40 equiv, 47 mM) in DMF. Polymerizations that have not been reported previously in the literature were performed in DMF-d₇ and assessed *via* 1H-NMR to confirm the complete consumption of monomer and determine the reaction time required for completion. When the polymerization went to completion, excess ethyl vinyl ether (EVE) was added to terminate the reaction. Block copolymers were prepared by polymerizing *m* equiv of the first block (norbornyl-peptide) to completion, then adding 5 equiv of the second block (Gd-DOTA monomer), then terminating as described above after 4 h. Polymer dispersities and molecular weights were determined by size-exclusion chromatography (Phenomenex Phenogel 5u 10, 1K-75K, 300 x 7.80 mm in series with a Phenomex Phenogel 5u 10, 10K-1000K, 300 x 7.80 mm (0.05 M LiBr in DMF)) using a Shimadzu LC-AT-VP pump equipped with a multi-angle light scattering detector (DAWN-HELIOS: Wyatt Technology), a refractive index detector (Hitachi L-2490) and a UV-Vis

detector (Shimadzu SPD-10AVP) normalized to a 30,000 MW polystyrene standard (Flow rate: 0.75 mL/min).

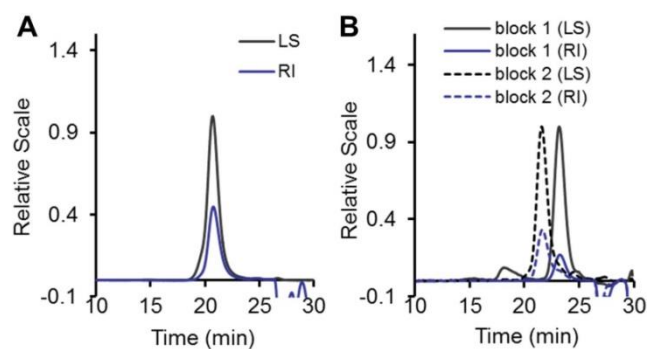


Figure 2.40 SEC-MALS characterization of the fluorogenic (A) homopolymer, where $M_n = 35,090$ g/mol, and dispersity (\mathcal{D}) = 1.048; and (B) block copolymer, where M_n (block 1) = 6,601g/mol, \mathcal{D} (block 1) = 1.119, M_n (copolymer) = 13,640, \mathcal{D} = 1.018.

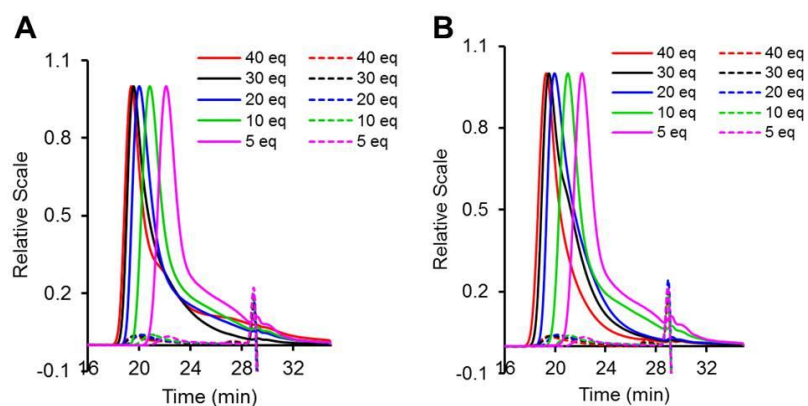


Figure 2.41 SEC-MALS chromatograms of (A) NorAhaFPGPLGLAGK(tma) and (B) tmaGPLGLAGFPK(NorAha)

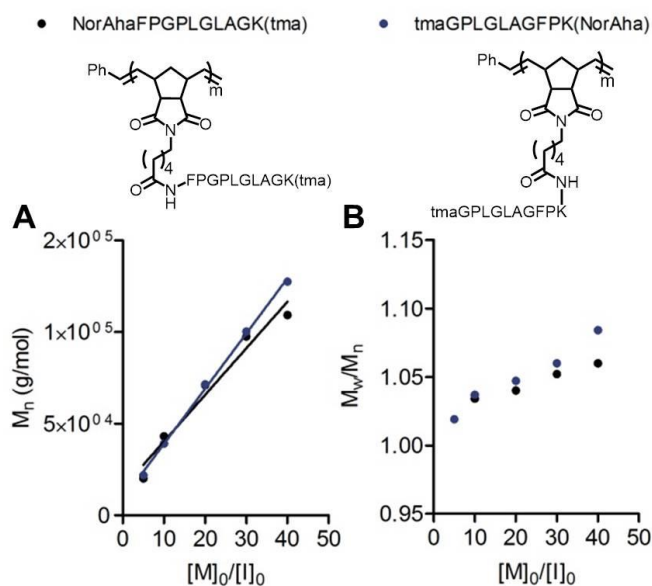


Figure 2.42 Verifying the “livingness” of the polymerization of NorAhaFPGPLGLAGK(tma) and tmaGPLGLAGFPK(NorAha) using [Ru] as the initiator in DMF solvent conditions. (A) M_n plotted as a function of the monomer: initiator feed ratio ($[M]_0/[I]_0$). Linear fits of curves are indicative of a living polymerization. (B) Dispersity, \mathcal{D} or M_w/M_n , plotted as a function of $[M]_0/[I]_0$. Minimal variation in the \mathcal{D} with increasing monomer equivalents is also an indicator of a living polymerization.

Table 2.9 SEC-MALS characterization of NorAhaFPGPLGLAGK(tma) and tmaGPLGLAGFPK(NorAha) peptide homopolymers. Note that Norbornene hexanoic acid (NorAha) is conjugated to the N-terminus of the peptide sequence or to the ϵ -amino group of the C-terminal lysine in the sequence.

	NorAhaFPGPLGLAGK(tma)			tmaGPLGLAGFPK(NorAha)		
$[M]_0/[I]_0$	M_n (g/mol)	\mathcal{D}	DP	M_n (g/mol)	\mathcal{D}	DP
5	20,220	1.019	15	21,950	1.019	16
10	43,230	1.034	32	39,240	1.037	29
20	71,090	1.04	53	71,540	1.047	53
30	97,530	1.052	73	100,300	1.06	75
40	109,300	1.06	81	127,500	1.084	95

2.9.5 Representative polymerization and purification of Gd-DOTA-containing peptide brush polymers

To a solution of norbornyl peptide monomer, N1 (0.22 g, 0.176 mol, 4 mL) was added [Ru] initiator (4.3 mg, 5.9 mmol, 0.3 mL) in anhydrous DMF. After 2 h, an aliquot 40 μ L) was removed for SEC-MALS analysis and the norbornyl Gd-DOTA monomer was added (22 mg, 29.5 mmol, 0.3 mL) in a 20 % MeOH in DMF solvent mixture. The reaction was left in a glove box over 4 h, during which aliquots were removed (30 μ L), mixed with an excess of ethyl vinyl ether (EVE) for 5 min, then dried under high vacuum. The residue was diluted with buffer A and B and the resulting solution injected onto RP-HPLC to analyze monomer consumption. To the remaining mixture, excess EVE was added to quench the reaction following RP-HPLC verification of complete monomer incorporation into the polymer. The polymer was then triturated three times with DMF and ether to remove residual catalyst and then dialyzed in H₂O overnight using 3500 MWCO snakeskin dialysis tubing (Pierce). The solution was then analyzed using the colorimetric Arsenazo III assay to detect the presence of unchelated Gd(III).¹¹⁴ No detectable free Gd(III) was measured after several washes of the polymer solution over Chelex 100 resin (Sigma, used to remove polyvalent metal ions). Note, the limit of detection for the assay is 2 μ g/mL GdCl₃ used for the standard calibration.

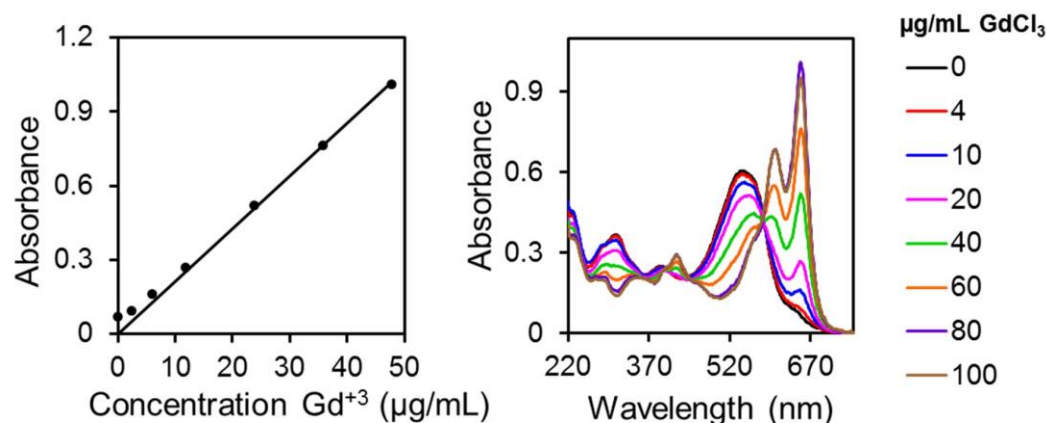


Figure 2.43 Calibration curve generated for the colorimetric Arsenazo III assay to detect the presence of unchelated Gd(III) in solution. GdCl₃ was used to generate the standard curve measured at absorbance of 652 nm.

2.9.6 Formulation and characterization of fluorogenic nanoparticles

The fluorogenic amphiphilic copolymer (derived from Ph₂₆-*b*-peptide₄) (5.85 mg) was dissolved in DMF (4.39 mL) and the solution was vortexed periodically until fully dissolved. A stir bar was added to the vial and a syringe pump (Harvard apparatus syringe infusion pump 22) was programmed to add water (1.46 mL) to the stirring solution at a rate of 49 µL·h⁻¹ over the course of 30 h to reach a final 25 % v/v H₂O in DMF. The cloudy solution, which indicated a colloidal suspension, was transferred to a 3500 MWCO snakeskin dialysis tube and dialyzed against DPBS (2 L). After 8 h, the DPBS was refreshed and the solution dialyzed overnight. The following morning, the DPBS was refreshed for the second time and the solution allowed to continue to dialyze for 8 h. The milky solution was removed from the dialysis tube and several aliquots were removed for lyophilization. The remaining suspension was concentrated with a 3500 MWCO centrifuge filter and analyzed for the polymer concentration using a standard curve generated from the dried aliquots.

2.9.7 Transmission Electron Microscopy (TEM)

TEM and cryo-TEM was performed on a FEI Sphera microscope operating at 200 keV. TEM grids were prepared by depositing small (3.5 mL) aliquots of sample onto grids (formvar stabilized with carbon (5–10 nm) on 400 copper mesh, Ted Pella Inc.) that had previously been glow discharged using an Emitech K350 glow discharge unit and plasma-cleaned for 90 s in an E.A. Fischione 1020 unit. The sample grid was rinsed with three drops of water, followed by staining with 1% uranyl acetate solution (again rinsing with three drops). The excess solution was removed by blotting the edge of the grid with filter paper. Micrographs were recorded on a 2k by 2k Gatan CCD camera. Samples for cryo-TEM were prepared by depositing 3.5 mL of sample to a freshly glow discharged Quantifoil R2/2 TEM grid. The grids were blotted with filter paper under high humidity to create thin films and rapidly plunged into liquid ethane. The grids were transferred to the microscope under liquid nitrogen and kept at < 175 °C while imaging.

2.9.8 Standard curve for Gd(III) determination

The standard curve previously published was used.⁵⁸ Briefly, a 0.1 M stock solution of GdCl_3 in H_2O was prepared. From this stock, concentrations of 3.0, 1.0, 0.5, and 0.01 mM of Gd^{3+} in 2:3:5 HNO_3 : H_2O : D_2O were made. T1 relaxations were determined for each concentration of Gd^{3+} using inversion recovery experiments on a 300 MHz Varian NMR instrument. $1/T_1$ were averaged for three separate samples at the same concentration, then plotted to give a relaxivity of free Gd^{3+} of $13.8 \text{ mM}^{-1} \text{ sec}^{-1} \pm 0.830$ with an R^2 value of 0.9992.

2.9.9 Procedure for Gd(III) concentration determination of polymers

Concentrated nitric acid was used to strip the metal from the chelate in order to determine Gd(III) concentration. First, 40 % v/v HNO_3 (250 μL) was added to an aliquot of

the sample (~10 μL). The mixture was then heated at 65 $^{\circ}\text{C}$ overnight. The sample was diluted with 250 μL of D_2O (to a final concentration ~0.5 mg/mL polymer) and T_1 was determined using an inversion recovery experiment on a 300 MHz Varian NMR. Based the standard curve created above, the concentration of Gd(III) was determined in stock solutions of NPBP3, CPBP3, and L and D polymers. It was later found that the most reliable way to analyze Gd(III) concentration in the samples was to digest with concentrated nitric acid as done previously and prepare several samples for ICP-OES analysis. These samples were compared to a standard curve generated from ICP samples containing digested commercial Gd-DOTA (Dotarem).

2.9.10 MRI procedures

MR images were acquired on a Bruker 7.0 T magnet with Avance II hardware equipped with a 72 mm quadrature transmit/receive coil. Axial MR images were acquired using a standard T_1 -weighted sequence with a repetition time of 3249.2 ms, time to echo of 7.6 ms, with fat suppression, a matrix of 256 x 256, field of view (FOV) of 4.00 x 3.00 cm, resolution of 156 x 117 microns, slice thickness of 1.00 mm, inter-slice distance of 1.00 mm, 80 slices. The decrease in the T_1 time was determined by selecting regions of interest (ROI) using Software ParaVision Version 5.1 from T_1 - T_2 map with the following parameters: Times to echo of 11, 33, 55, 77, and 99 ms and 6 repetition times of 5000, 3000, 2500, 2000, 1500, and 1200 ms, and a flip angle of 180° .

2.9.11 Analysis of T_1 data

To correct for scan-to-scan variations due to noise, the T_1 values were normalized to prescan phantom relaxivities (animal prior to injection with material). Phantoms of Gd-DOTA (Macrocycles) were included in each scan and the concentrations were 0.41, 0.12, 0.033, 0.0095, and 0.0027 mM with respect to Gd(III) in H_2O . It is noted that these

concentrations were too high and registered as similar signal intensities. Prescan relaxivities were generated by averaging $1/T1$ (r_1) values (msec^{-1}) for each phantom concentration over 1 selected slice of the mouse, which contained the largest area of the lung. For the scans at the indicated time points after injection, an average $1/T1$ for 2-3 phantoms were calculated and compared to the pre-scan relaxivity value to generate an adjustment factor for the scan of interest. After organ ROI $T1$ was converted to $1/T1$, each were multiplied by the adjustment factor. $1/T1$ was averaged over each organ and then converted back to $T1$ (msec).

Table 2.10 Relaxivity (r_1) of polymers prior to and after enzymatic cleavage

	r_1	y_{int}
Polymer + denatured enzyme	4.275	0.365
Polymer + enzyme	4.005	0.379
Polymer	4.288	0.385
Dotarem	3.820	0.381

2.9.12 *In vivo* protocols

All animal procedures were approved by University of California, San Diego's institutional animal care and use committee, protocol S10145. Female mice (C57Bl/6, balb/c) of 11-14 weeks old were purchased from Harlan Sprague Dawley or Charles River. Mice with 4T1 tumor burden were received from the Dennis Carson group at Sanford Consortium. Mice were anesthetized with 3% isoflurane in O_2 when subjected to baseline MRI imaging prior to and after injection. Mice were injected with 0.1 mL aqueous solution of polymers *via* the tail vein or 0.05 mL into the right solid tumor. After injection, a single mouse was imaged continuously under anesthesia for two hours and then again at 24 h and 48 h. To correct for minor scan-to-scan variations, the $T1$ values were normalized to prescan phantoms.

2.9.13 *Ex vivo* biodistribution

Mice were sacrificed using a lethal overdose of > 5 % isoflurane in O₂ and a second method (lethal blood withdrawal using cardiac puncture) was used to ensure death. Selected organs were harvested (blood, kidney, liver, spleen, and tumor) and placed on ice. The tissues were weighed in plastic Eppendorf tubes or 15 mL plastic conical tubes and their masses were recorded. 0.5 mL of concentrated nitric acid was added to all tissues except the liver (2 mL). Periodically, the mixtures were vented to prevent overpressure from popping the tube caps. The following day, 30 % v/v H₂O₂ (50 µL) was added to each of the organ solutions (0.1 mL to the liver sample). (Note: mixing H₂O₂ and concentrated HNO₃ generates heat and hazardous nitric oxide NO_x gas pollutants. Extreme caution must be taken to prevent exposure to these chemicals. All procedures were accomplished in a chemical fume hood. A hole was made in plastic caps with a needle and the mixtures were capped with these to prevent overpressure. An aliquot (80 µL) of the solution from digested organ samples was added to nanopure water (3.92 mL, for total 2 % v/v HNO₃) and analyzed by ICP-OES to determine Gd(III) concentration. The final mass of Gd(III) in each organ was normalized to the mass of polymer injected (with respect to Gd(III)) and the organ mass to yield percent injected dose per gram of tissue (% ID / g). For circulation time experiments, blood was collected from the tail ventral artery/vein at the indicated time points (10 min, 40 min, 1.5 h, 3 h, 5 h, and 24 h) by the tail nick method. In brief, the animal was anesthetized under a constant stream of 3 % isoflurane in O₂ gas. Caution was taken to make an incision to remove the tip of the tail, no greater than 3 mm from the base. After blood was collected from the incised region, the area was wiped with a sterile alcohol pad, and styptic powder was applied to encourage clotting. Upon additional samplings, the scab was rubbed away and a sterile needle was used to disturb the wound. Each collection was sufficiently small ~3 – 10 µL to

enable multiple collections from each animal. No no more than 4 collections were made per animal. For digestion of blood samples, 20 μL HNO_3 was added prior to H_2O_2 addition.

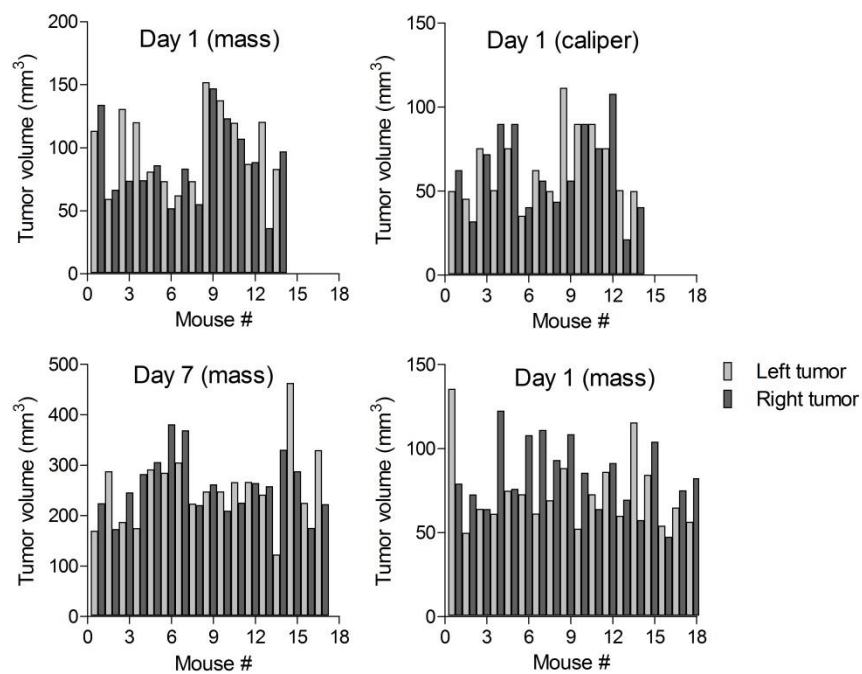


Figure 2.44 Tumor volume measured by calipers or mass at different days to verify similar sizes between experimental groups. A minimum volume of 50 mm³ was typically used for the *in vivo* experiments. The density of the tumor was assumed to be 1.05 g/mL for calculations using mass.

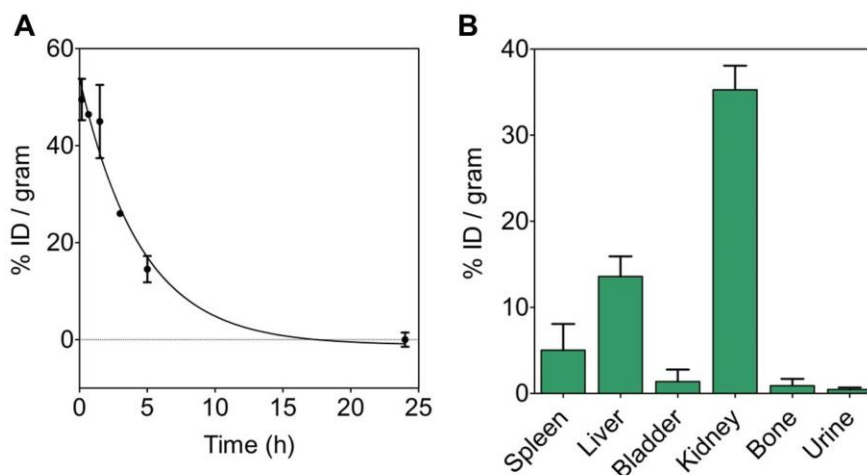


Figure 2.45 Blood circulation time and *ex vivo* biodistribution experiments of healthy (non-immune compromised) C57/bl/6 mice IV injected with Gd-DOTA bearing PBP copolymer ($m = 35$, $n \sim 2$, 160 nmol with respect to Gd(III)). (A) Blood was collected from the tail ventral artery/vein at the indicated time points: 10 min, 40 min, 1.5 h, 3 h, 5, and 24 h. For these experiments, $n = 2-4$, except for 40 min, where $n = 1$ (standard error is plotted). The half-life, $t_{1/2}$, was calculated as 3.12 h by means of least squares fit of a one-phase decay. (B) *Ex vivo* biodistribution 24 h post injection of $n = 3 \pm$ standard error.

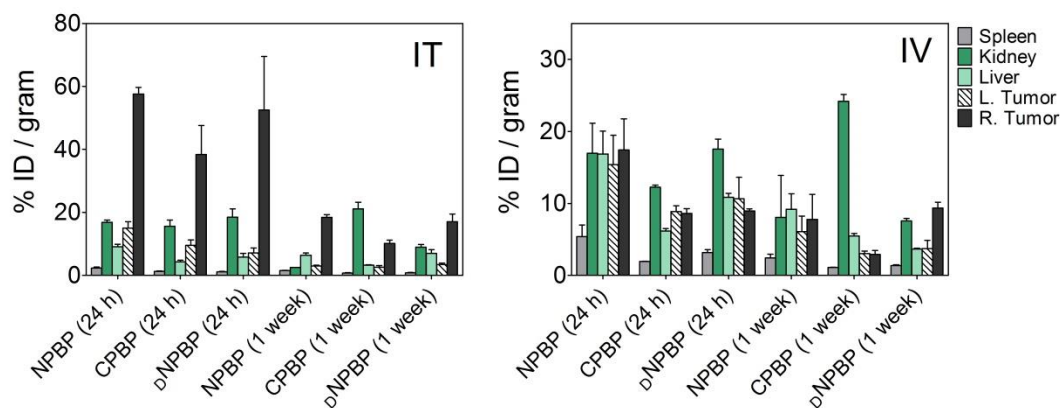


Figure 2.46 Complete data for *ex vivo* biodistribution (complement to Figure 2.23). D polymer was included as a control ($n = 2$ or 3 mice).

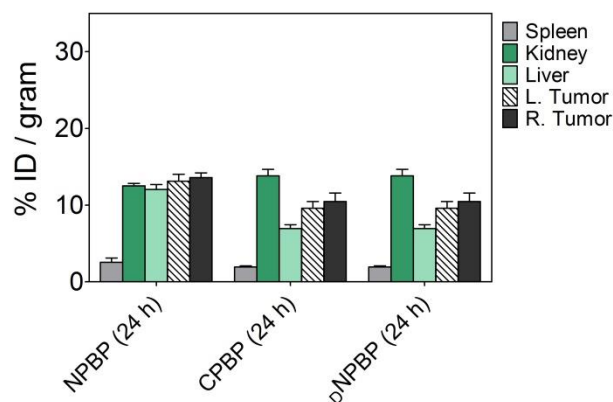


Figure 2.47 *Ex vivo* biodistribution (measured by ICP-OES of Gd) analysis in a syngeneic 4T1 tumor model 24 h following intravenous (IV) injection of N-, CPBP3 or D polymer (_DNPBP). 150 nmol was injected (wrt/ Gd) and these results were used to optimize the dose (complement to Figure 2.23). For all groups, n = 3 ± standard error.

2.9.14 ¹H NMRD Profiles

The nuclear magnetic relaxation dispersion (NMRD) profiles allow a detailed characterization of the paramagnetic solutes in terms of a large set of structural and dynamic parameters. The experimental profiles were measured in aqueous solution at 298 K and 310 K at neutral pH. Proton 1/T₁ NMRD profiles were measured on a Fast Field-Cycling Stellar SMARTracer NMR Relaxometer (Stelar, Mede (PV), Italy) over a continuum of magnetic field strengths from 0.00024 to 0.25 T (corresponding to 0.01-10 MHz proton Larmor frequencies). The analysis of NMRD profiles of paramagnetic macromolecules takes into account the rapid local rotation of the metal complex superimposed to the global rotation of the macromolecules (Lipari–Szabo approach).¹¹⁵ The relaxometer operates under computer control with an absolute uncertainty in 1/T₁ of ± 1%. Additional data points in the range 20-70 and 400 MHz were obtained on a Bruker WP80 NMR electromagnet adapted to variable-field measurements (15-80 MHz proton Larmor frequency) Stellar Relaxometer and Jeol ECP spectrometer (9.39 T), respectively. The ¹H T₁ relaxation times were acquired by the

standard inversion recovery method with typical 90° pulse width of 3.5 μ s, 16 experiments of 4 scans. The temperature was controlled with a Stellar VTC-91 airflow heater equipped with a calibrated copper–constantan thermocouple (uncertainty of ± 0.1 °C). The temperature was determined by previous calibration with a Pt resistance temperature probe. Proton relaxivity was also measured as a function of temperature at 0.5 T in order to evaluate the residence lifetime of the coordinated water molecule.

2.10 References

- (1) Hamley, I. W. *Angew. Chemie Int. Ed.* **2003**, *42* (15), 1692.
- (2) Nayak, S.; Lyon, L. A. *Angew. Chemie Int. Ed.* **2005**, *44* (47), 7686.
- (3) Elsabahy, M.; Wooley, K. L. *Chem. Soc. Rev.* **2012**, *41* (7), 2545.
- (4) Carlini, A. S.; Adamiak, L.; Gianneschi, N. C. *Macromolecules* **2016**, *49* (12), 4379.
- (5) Lutz, J.-F.; Börner, H. G. *Prog. Polym. Sci.* **2008**, *33* (1), 1.
- (6) Gauthier, M. A.; Gibson, M. I.; Klok, H.-A. *Angew. Chemie Int. Ed.* **2009**, *48* (1), 48.
- (7) Espeel, P.; Du Prez, F. E. *Macromolecules* **2015**, *48* (1), 2.
- (8) Tucker, B. S.; Stewart, J. D.; Aguirre, J. I.; Holliday, L. S.; Figg, C. A.; Messer, J. G.; Sumerlin, B. S. *Biomacromolecules* **2015**, *16* (8), 2374.
- (9) Nguyen, M. M.; Carlini, A. S.; Chien, M.-P.; Sonnenberg, S.; Luo, C.; Braden, R. L.; Osborn, K. G.; Li, Y.; Gianneschi, N. C.; Christman, K. L. *Adv. Mater.* **2015**, *27* (37), 5547.
- (10) Bontempo, D.; Maynard, H. D. *J. Am. Chem. Soc.* **2005**, *127* (18), 6508.
- (11) Lin, E.-W.; Maynard, H. D. *Macromolecules* **2015**, *48* (16), 5640.
- (12) García-Valdez, O.; Champagne-Hartley, R.; Saldívar-Guerra, E.; Champagne, P.; Cunningham, M. F. *Polym. Chem.* **2015**, *6* (15), 2827.
- (13) De, P.; Li, M.; Gondi, S. R.; Sumerlin, B. S. *J. Am. Chem. Soc.* **2008**, *130* (34), 11288.
- (14) Blum, A. P.; Kammeyer, J. K.; Gianneschi, N. C. *Chem. Sci.* **2016**, *7* (2), 989.
- (15) Becker, M. L.; Liu, J.; Wooley, K. L. *Chem. Commun.* **2003**, 285 (2), 180.

- (16) Johnson, J. A.; Lu, Y. Y.; Burts, A. O.; Xia, Y.; Durrell, A. C.; Tirrell, D. A.; Grubbs, R. H. *Macromolecules* **2010**, *43* (24), 10326.
- (17) Xia, Y.; Olsen, B. D.; Kornfield, J. A.; Grubbs, R. H. *J. Am. Chem. Soc.* **2009**, *131* (51), 18525.
- (18) Maynard, H. D.; Okada, S. Y.; Grubbs, R. H. *Macromolecules* **2000**, *33* (17), 6239.
- (19) Parry, A. L.; Bomans, P. H. H.; Holder, S. J.; Sommerdijk, N. A. J. M.; Biagini, S. C. G. *Angew. Chemie Int. Ed.* **2008**, *47* (46), 8859.
- (20) Ku, T.-H.; Chien, M.-P.; Thompson, M. P.; Sinkovits, R. S.; Olson, N. H.; Baker, T. S.; Gianneschi, N. C. *J. Am. Chem. Soc.* **2011**, *133* (22), 8392.
- (21) Chien, M.-P.; Thompson, M. P.; Barback, C. V.; Ku, T.-H.; Hall, D. J.; Gianneschi, N. C. *Adv. Mater.* **2013**, *25* (26), 3599.
- (22) Kessenbrock, K.; Plaks, V.; Werb, Z. *Cell* **2010**, *141* (1), 52.
- (23) Mutch, A.; Leconte, M.; Lefebvre, F.; Basset, J.-M. *J. Mol. Catal. A Chem.* **1998**, *133* (1), 191.
- (24) Sutthasupa, S.; Shiotsuki, M.; Masuda, T.; Sanda, F. *J. Am. Chem. Soc.* **2009**, *131* (30), 10546.
- (25) Al Samak, B.; Amir-Ebrahimi, V.; Corry, D. G.; Hamilton, J. G.; Rigby, S.; Rooney, J. J.; Thompson, J. M. *J. Mol. Catal. A Chem.* **2000**, *160* (1), 13.
- (26) Biagini, S. C. G.; Parry, A. L. *J. Polym. Sci. Part A Polym. Chem.* **2007**, *45* (15), 3178.
- (27) Bertin, P. A.; Gibbs, J. M.; Shen, C. K.-F.; Thaxton, C. S.; Russin, W. A.; Mirkin, C. A.; Nguyen, S. T. *J. Am. Chem. Soc.* **2006**, *128* (13), 4168.
- (28) Riess, G. *Prog. Polym. Sci.* **2003**, *28* (7), 1107.
- (29) Rush, A. M.; Thompson, M. P.; Tatro, E. T.; Gianneschi, N. C. *ACS Nano* **2013**, *7* (2), 1379.
- (30) Blum, A. P.; Kammeyer, J. K.; Yin, J.; Crystal, D. T.; Rush, A. M.; Gilson, M. K.; Gianneschi, N. C. *J. Am. Chem. Soc.* **2014**, *136* (43), 15422.
- (31) Kammeyer, J. K.; Blum, A. P.; Adamiak, L.; Hahn, M. E.; Gianneschi, N. C. *Polym. Chem.* **2013**, *4* (14), 3929.
- (32) Patel, P. R.; Kiser, R. C.; Lu, Y. Y.; Fong, E.; Ho, W. C.; Tirrell, D. A.; Grubbs, R. H. *Biomacromolecules* **2012**, *13* (8), 2546.
- (33) Sutthasupa, S.; Shiotsuki, M.; Sanda, F. *Polym. J.* **2010**, *42* (12), 905.

- (34) Ruoslahti, E.; Bhatia, S. N.; Sailor, M. J. *J. Cell Biol.* **2010**, *188* (6), 759.
- (35) Hahn, M. E.; Randolph, L. M.; Adamiak, L.; Thompson, M. P.; Gianneschi, N. C. *Chem. Commun.* **2013**, *49* (28), 2873.
- (36) Leo Benoiton, N. *Chemistry of Peptide Synthesis*; CRC Press, 2005.
- (37) Rankin, D. A.; P'Pool, S. J.; Schanz, H.-J.; Lowe, A. B. *J. Polym. Sci. Part A Polym. Chem.* **2007**, *45* (11), 2113.
- (38) Rule, J.D.; Moore, J. D. R. *Macromolecules* **2002**, *35* (21), 7878.
- (39) Lapinte, V.; Brosse, J.-C.; Fontaine, L. *Macromol. Chem. Phys.* **2004**, *205* (6), 824.
- (40) Alfred, S. F.; Lienkamp, K.; Madkour, A. E.; Tew, G. N. *J. Polym. Sci. Part A Polym. Chem.* **2008**, *46* (19), 6672.
- (41) James, C. R.; Rush, A. M.; Insley, T.; Vuković, L.; Adamiak, L.; Král, P.; Gianneschi, N. C. *J. Am. Chem. Soc.* **2014**, *136* (32), 11216.
- (42) Cobo, I.; Li, M.; Sumerlin, B. S.; Perrier, S. *Nat. Mater.* **2014**, *14* (2), 143.
- (43) Roy, D.; Cambre, J. N.; Sumerlin, B. S. *Prog. Polym. Sci.* **2010**, *35* (1), 278.
- (44) Blum, A. P.; Kammeyer, J. K.; Rush, A. M.; Callmann, C. E.; Hahn, M. E.; Gianneschi, N. C. *J. Am. Chem. Soc.* **2015**, *137* (6), 2140.
- (45) Christie M. Hassan; Francis J. Doyle III, and; Peppas*, N. A. **1997**.
- (46) Satav, S. S.; Bhat, S.; Thayumanavan, S. *Biomacromolecules* **2010**, *11* (7), 1735.
- (47) Savariar, E. N.; Ghosh, S.; Thayumanavan, S.; Thayumanavan, S. *J. Am. Chem. Soc.* **2008**, *130* (16), 5416.
- (48) Chien, M.-P.; Rush, A. M.; Thompson, M. P.; Gianneschi, N. C. *Angew. Chemie Int. Ed.* **2010**, *49* (30), 5076.
- (49) Ding, K.; Alemdaroglu, F. E.; Börsch, M.; Berger, R.; Herrmann, A. *Angew. Chemie Int. Ed.* **2007**, *46* (7), 1172.
- (50) Azagarsamy, M. A.; Sokkalingam, P.; Thayumanavan, S. *J. Am. Chem. Soc.* **2009**, *131* (40), 14184.
- (51) Wang, C.; Chen, Q.; Wang, Z.; Zhang, X. *Angew. Chemie Int. Ed.* **2010**, *49* (46), 8612.
- (52) Rao, J.; Khan, A. *J. Am. Chem. Soc.* **2013**, *135* (38), 14056.
- (53) Rao, J.; Hottinger, C.; Khan, A. *J. Am. Chem. Soc.* **2014**, *136* (16), 5872.

- (54) Amir, R. J.; Zhong, S.; Pochan, D. J.; Hawker, C. J. *J. Am. Chem. Soc.* **2009**, *131* (39), 13949.
- (55) Kühnle, H.; Börner, H. G. *Angew. Chemie Int. Ed.* **2009**, *48* (35), 6431.
- (56) Nagase, H.; Fields, G. B. *Pept. Sci.* **1996**, *40* (4), 399.
- (57) van den Burg, B.; Eijssink, V. In *Handbook of Proteolytic Enzymes*; 2013; pp 540–553.
- (58) Randolph, L. M.; LeGuyader, C. L. M.; Hahn, M. E.; Andolina, C. M.; Patterson, J. P.; Mattrey, R. F.; Millstone, J. E.; Botta, M.; Scadeng, M.; Gianneschi, N. C. *Chem. Sci.* **2016**, *7* (7), 4230.
- (59) Trnka, T. M.; Grubbs, R. H. *Acc. Chem. Res.* **2001**, *34* (1), 18.
- (60) *Handbook of metathesis.*, 2nd ed.; Grubbs, R. H., Wenzel, A. G., O'Leary, D. J., Khosravi, E. (Ezat), Eds.; Wiley.vch.
- (61) Colak, S.; Tew, G. N. *Langmuir* **2012**, *28* (1), 666.
- (62) Colak, S.; Tew, G. N. *Biomacromolecules* **2012**, *13* (5), 1233.
- (63) Keefe, A. J.; Jiang, S. *Nat Chem* **2012**, *4* (1), 59.
- (64) Ma, C. D.; Adamiak, L.; Miller, D. S.; Wang, X.; Gianneschi, N. C.; Abbott, N. L. *Small* **2015**, *11* (43), 5747.
- (65) Lowe, A. B.; McCormick, C. L. *Chem. Rev.* **2002**, *102* (11), 4177.
- (66) Xu, Y.; Bolisetty, S.; Drechsler, M.; Fang, B.; Yuan, J.; Ballauff, M.; Müller, A. H. E. *Polymer (Guildf)*. **2008**, *49* (18), 3957.
- (67) Samarajeewa, S.; Zentay, R. P.; Jhurry, N. D.; Li, A.; Seetho, K.; Zou, J.; Wooley, K. L. *Chem. Commun.* **2014**, *50* (8), 968.
- (68) Callmann, C. E.; Barback, C. V.; Thompson, M. P.; Hall, D. J.; Mattrey, R. F.; Gianneschi, N. C. *Adv. Mater.* **2015**, *27* (31), 4611.
- (69) Gustafson, H. H.; Holt-Casper, D.; Grainger, D. W.; Ghandehari, H. *Nano Today* **2015**, *10* (4), 487.
- (70) Maddox, D. A.; Deen, W. M.; Brenner, B. M. In *Comprehensive Physiology*; John Wiley & Sons, Inc.: Hoboken, NJ, USA, 2011.
- (71) Vlieghe, P.; Lisowski, V.; Martinez, J.; Khrestchatisky, M. *Drug Discov. Today* **2010**, *15* (1), 40.
- (72) Witt, K. A.; Gillespie, T. J.; Huber, J. D.; Egleton, R. D.; Davis, T. P. *Peptides* **2001**, *22* (12), 2329.

- (73) Yang, C.-T.; Chuang, K.-H. *Medchemcomm* **2012**, *3* (5), 552.
- (74) Srinivas, M.; Cruz, L. J.; Bonetto, F.; Heerschap, A.; Figdor, C. G.; de Vries, I. J. M. *Biomaterials* **2010**, *31* (27), 7070.
- (75) Wang, C.-H.; Kang, S.-T.; Lee, Y.-H.; Luo, Y.-L.; Huang, Y.-F.; Yeh, C.-K. *Biomaterials* **2012**, *33* (6), 1939.
- (76) Kinsella, J. M.; Jimenez, R. E.; Karmali, P. P.; Rush, A. M.; Kotamraju, V. R.; Gianneschi, N. C.; Ruoslahti, E.; Stupack, D.; Sailor, M. J. *Angew. Chem. Int. Ed. Engl.* **2011**, *50* (51), 12308.
- (77) Thomsen, H. S. *Radiol. Clin. North Am.* **2009**, *47* (5), 827.
- (78) Aime, S.; Caravan, P. J. *Magn. Reson. Imaging* **2009**, *30* (6), 1259.
- (79) Ladd, D. L.; Hollister, R.; Peng, X.; Donna Wei; Wu, G.; Delecki, D.; Snow, R. A.; Toner, J. L.; Kellar, K.; Eck, J.; Desai, V. C.; Raymond, G.; Kinter, L. B.; Desser, T. S. M. D.; Rubin, D. M. *Bioconjug. Chem.* **1999**, *10* (3), 361.
- (80) Bryson, J. M.; Fichter, K. M.; Chu, W.-J.; Lee, J.-H.; Li, J.; Madsen, L. A.; McLendon, P. M.; Reineke, T. M. *Proc. Natl. Acad. Sci. U. S. A.* **2009**, *106* (40), 16913.
- (81) Huang, C.-H.; Tsourkas, A. *Curr. Top. Med. Chem.* **2013**, *13* (4), 411.
- (82) Rudovský, J.; Hermann, P.; Botta, M.; Aime, S.; Lukeš, I. *Chem. Commun.* **2005**, 99 (18), 2390.
- (83) Langereis, S.; Lussanet, Q. G. de; van Genderen, M. H. P.; Backes, W. H.; Meijer, E. W. *Macromolecules* **2004**, *37* (9), 3084.
- (84) Bryant, L. H.; Brechbiel, M. W.; Wu, C.; Bulte, J. W. M.; Herynek, V.; Frank, J. A. *J. Magn. Reson. Imaging* **1999**, *9* (2), 348.
- (85) Choi, H. S.; Frangioni, J. V. *Mol. Imaging* **2010**, *9* (6), 291.
- (86) Kobayashi, H.; Kawamoto, S.; Jo, S.-K.; Bryant Jr., H. L.; Brechbiel, M. W.; Star, R. A. *Bioconjug. Chem.* **2003**, *14* (2), 368.
- (87) Gibby, W. A.; Gibby, K. A.; Gibby, W. A. *Invest. Radiol.* **2004**, *39* (3), 138.
- (88) Schopf, E.; Sankaranarayanan, J.; Chan, M.; Mattrey, R.; Almutairi, A. *Mol. Pharm.* **2012**, *9* (7), 1911.
- (89) Major, J. L.; Meade, T. J. *Acc. Chem. Res.* **2009**, *42* (7), 893.
- (90) Caravan, P.; Ellison, J. J.; McMurry, T. J.; Lauffer, R. B. *Chem. Rev.* **1999**, *99* (9), 2293.

- (91) Solomon, I. *Phys. Rev.* **1955**, *99* (2), 559.
- (92) Bloembergen, N.; Morgan, L. O. *J. Chem. Phys.* **1961**, *34* (3), 842.
- (93) Raymond, K. N.; Pierre, V. C. *Bioconjug. Chem.* **2004**, *16* (1), 3.
- (94) Caravan, P.; Farrar, C. T.; Frullano, L.; Uppal, R. *Contrast Media Mol. Imaging* **2009**, *4* (2), 89.
- (95) Brasch, R. C. *Magn. Reson. Med.* **1991**, *22* (2), 282.
- (96) Tóth, É.; Pubanz, D.; Vauthey, S.; Helm, L.; Merbach, A. E. *Chem. – A Eur. J.* **1996**, *2* (12), 1607.
- (97) Armitage, F.E.; Richardson, D. E.; , Li, K. C. P. *Bioconjug. Chem.* **1990**, *1* (6), 365.
- (98) Villaraza, A.J.L.; Bumb, A.; Brechbiel, M. W. *Chem. Rev.* **2010**, *110* (5), 2921.
- (99) Olson, E. S.; Jiang, T.; Aguilera, T. A.; Nguyen, Q. T.; Ellies, L. G.; Scadeng, M.; Tsien, R. Y. *Proc. Natl. Acad. Sci.* **2010**, *107* (9), 4311.
- (100) Yamaoka, T.; Tabata, Y.; Ikada, Y. *J. Pharm. Pharmacol.* **1995**, *47* (6), 479.
- (101) Schuhmann-Giampieri, G.; Schmitt-Willich, H.; Frenzel, T.; Press, W. R.; Weinmann, H. J. *Invest. Radiol.* **1991**, *26* (11), 969.
- (102) Ernsting, M. J.; Murakami, M.; Roy, A.; Li, S.-D. *J. Control. Release* **2013**, *172* (3), 782.
- (103) Etrych, T.; Chytil, P.; Mrkvan, T.; Sírová, M.; Říhová, B.; Ulbrich, K. *J. Control. Release* **2008**, *132* (3), 184.
- (104) Ulbrich, K.; Šubr, V.; Strohalm, J.; Plocová, D.; Jelínková, M.; Říhová, B. *J. Control. Release* **2000**, *64* (1), 63.
- (105) Pelegri-O'Day, E. M.; Lin, E.-W.; Maynard, H. D. *J. Am. Chem. Soc.* **2014**, *136* (41), 14323.
- (106) Duncan, R.; Gac-Breton, S.; Keane, R.; Musila, R.; Sat, Y. N.; Satchi, R.; Searle, F. J. *J. Control. Release* **2001**, *74* (1), 135.
- (107) Grogna, M.; Cloots, R.; Luxen, A.; Jérôme, C.; Desreux, J.-F.; Detrembleur, C. *J. Mater. Chem.* **2011**, *21* (34), 12917.
- (108) Li, Y.; Beija, M.; Laurent, S.; Elst, L. vander; Muller, R. N.; Duong, H. T. T.; Lowe, A. B.; Davis, T. P.; Boyer, C. *Macromolecules* **2012**, *45* (10), 4196.
- (109) Manus, L. M.; Mastarone, D. J.; Waters, E. A.; Zhang, X.-Q.; Schultz-Sikma, E. A.; MacRenaris, K. W.; Ho, D.; Meade, T. J. *Nano Lett.* **2010**, *10* (2), 484.

- (110) Cheng, Z.; Thorek, D. L. J.; Tsourkas, A. *Adv. Funct. Mater.* **2009**, *19* (23), 3753.
- (111) Raymond, K. N.; Pierre, V. C. *Bioconjug. Chem.* **2005**, *16* (1), 3.
- (112) Davies, G.-L.; Kramberger, I.; Davis, J. J. *Chem. Commun.* **2013**, *49* (84), 9704.
- (113) Sanford, M. S.; Love, J. A.; Grubbs, R. H. *Organometallics* **2001**, *20* (25), 5314.
- (114) Clogston, J. D.; Patri, A. K. 2011; pp 101–108.
- (115) Lipari, G.; Szabo, A. *J. Am. Chem. Soc.* **1982**, *104* (17), 4546.

Chapter 3

Peptide Brush Polymers and Nanoparticles for Activating and Evading Macrophage Uptake

3.1 Introduction

It is well known that injectable nanoparticles (NPs) suffer from premature removal from systemic circulation by the mononuclear phagocytic system (MPS). The process by which macrophages of the MPS, typically Kupffer cells of the liver, bone marrow and lung, recognize and sequester NPs occurs through the adsorption of proteins to the nanomaterial surface. This process, known as opsonization, involves any adsorbed blood serum protein that can advance phagocytosis, but albumin, immunoglobulins and complement proteins such as C3, C4, and C5 are the predominant type.^{1,2} When combined, these mechanisms form the basis of immediate clearance (on the order of seconds) for injected NPs that are larger than the 10 nm renal filtration limit. For non-biodegradable NPs that cannot be destroyed by phagocytes, accumulation in MPS organs such as the liver and spleen is routinely observed.^{3,4} Long-term retention in MPS organs has raised concerns of heightened immune response or deferred toxicity, ultimately preventing clinical translation of many nano-material-based therapeutics and diagnostics.^{5,6}

To reduce NP susceptibility for opsonization and MPS clearance, many groups have developed strategies which consist of modifying NP surface chemistry,^{4,7-11} shape,¹²⁻¹⁴ size,^{15,16} or even surface topology.¹⁷⁻¹⁹ The most commonly explored surface modification for

rendering NP with enhanced blood retention is conjugation to poly(ethylene glycol) (PEG), also known as PEGylation.^{20,21} PEGylation has been shown to increase NP circulation time by acting as a non-fouling or opsonin-resistant coating. Nonetheless, PEGylation is arguably unsuitable for bioactive NPs for which preservation of protein binding is required.²² Indeed, protein conjugates prepared using other types of hydrophilic moieties, such as poly(carboxybetaine), exhibit similar biostabilizing properties but are markedly better at preserving protein bioactivity.^{23,24} Increasing attention is now being directed towards incorporating charge-neutral, non-fouling coatings such as poly(zwitterion)s as non-toxic and non-immune stimulatory alternatives to PEG.²⁵ These strategies have been mostly disseminated for surface-functionalized gold NP (AuNP), in large part due to the ease of functionalization using alkanethiol ligand exchange reactions and well established approaches for size and shape modifications.^{7,20,25–30} However, general conclusions derived from studies of AuNPs need to be validated for soft materials within the size range suitable for *in vivo* applications.^{4,12} One key factor contributing to this discrepancy is the difficulty in precisely controlling bottom-up fabrication of organic-based NPs that vary systematically in their size, surface chemistries, and other structural components.¹¹ As such, efforts to synthesize well-defined soft materials are necessary for evaluating MPS evasion approaches.

Recent work has established that enzyme-responsive NPs, which display peptides on the NP surface, allow for protease-triggered accumulation in tumor tissue. The peptide moiety encompasses an optimized recognition sequence for matrix metalloproteinase-2 and -9 (MMP-2,-9), which are type 4 collagenases essential to basement membrane degradation processes necessary for angiogenesis, or the formation of new blood vessels.³¹ As a result, MMPs are extensively involved in perpetual ECM remodeling within diseased tissues, which identifies them as key molecular targets for noninvasive NP treatments of conditions like myocardial infarction (MI), hindlimb ischemia, and cancer of all types.^{32,33} Though active-

targeting strategies, such as protease-triggered self-assembly, have improved NP accumulation and retention in tumors or areas of infarcts, there still remains a continuous problem with regards to rapid NP sequestration into MPS organs. Motivated by our efforts to develop protease-targeted diagnostic and drug delivery vehicles with favorable pharmacokinetic and biocompatible properties, we sought to systematically investigate the effects of surface charge, composition, and size of MMP-responsive polymers and polymeric NPs on facilitating macrophage cell recognition and uptake (Figure 3.1).

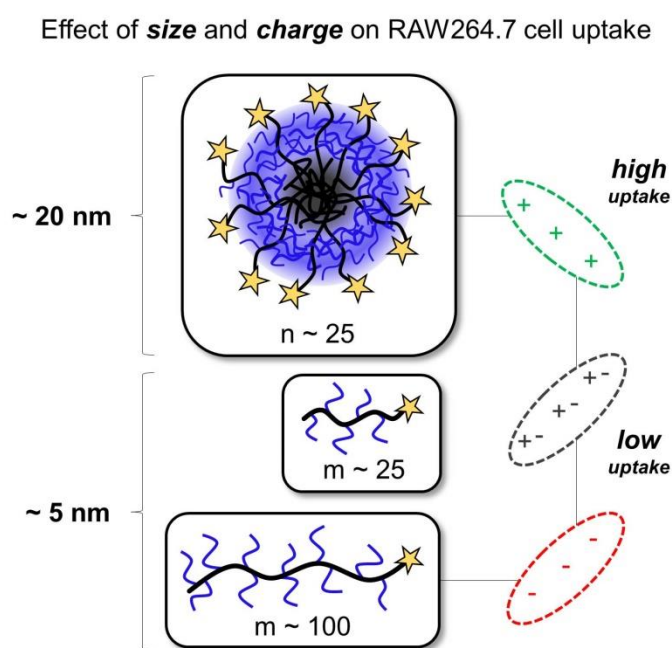


Figure 3.1 Examining size and charge effects of water-soluble peptide brush polymers and polymeric nanoparticles.

3.2 Synthesis of peptide brush polymers and formulation of polymeric NPs

In general, stimuli-responsive systems have not been examined for their influence on macrophage cell recognition despite growing interest in their potential as drug carriers and

diagnostics. Furthermore, previous studies have focused on a limited scope of functional groups presented at the NP surface;¹ in particular, little is known about the effects of biosynthetic polymers on macrophage uptake. Given the recent breakthrough of MMP-triggered therapeutic NP delivery to tumors, we were interested in examining the effects of physiochemical differences before and after proteolysis on this process (Figure 3.2).

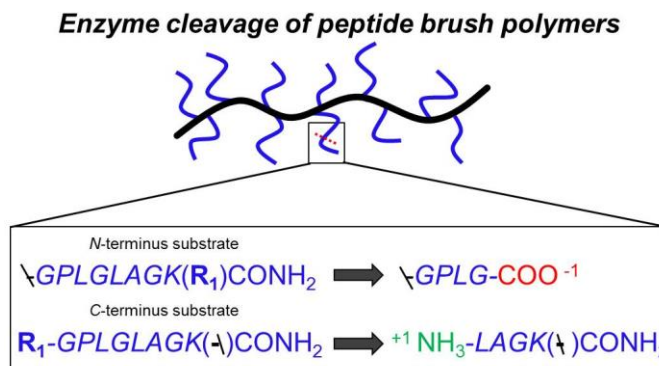


Figure 3.2 Proteolysis of *N*- and *C*-terminus peptide substrates displayed as brush polymers yields carboxylates or protonated amines as physiological pH, respectively.

Incorporating an MMP-9 peptide motif (GPLGLAG) renders the polymeric materials susceptible to cleavage by a model enzyme, thermolysin, a highly active bacterial zinc protease (Figure 3.2).³⁴ Thermolysin was used as an *in vitro* proxy for MMP-9 because it is easily available and can potentially cleave at two sites adjacent to the leucine residues in position P1', which results in discriminate consumption of the peptide. We selected the murine macrophage cell line RAW 264.7 as a model system because it is well documented that macrophages remove most of the administered dose *in vivo*.³ Furthermore, macrophage activity is closely associated with immunotoxicity.⁹ Resolving NP design parameters and their effects on macrophage recognition and uptake may provide insights towards enhancing their targeting capabilities and reducing associated toxicity.

Previous work has detailed optimal conditions for the *graft-through* polymerization of *exo*-norbornyl peptides (see chapter 2), namely the incorporation of a linear alkyl spacer to enhance polymerization rates. Hence, these strategies were employed to construct a library comprised of six *exo*-norbornyl peptide monomers. Peptide monomers were prepared first by solid-phase peptide synthesis (SPPS) using standard fluorenylmethyloxycarbonyl (Fmoc) chemistry to produce the desired peptide sequence; followed by on-resin coupling of norbornene(*N*-hexanoic acid) to either the *N*-terminus or to the ϵ -amino group of a C-terminal lysine residue via an orthogonal deprotection strategy. Minimal variations in the peptide sequences were critical for assessing charge differences while also retaining structural similarity within the library. Additional peptide modifications to the *N*-terminus or the ϵ -amino group of a C-terminal lysine consisted of acylation to afford anionic (an) derivatives or amide coupling with (3-carboxypropyl)trimethylammonium chloride to afford zwitterionic (zw) and cationic (cat) peptides (Table 3.1). Conjugation of the norbornene to the peptide in these two manners afforded structural isomers, which upon enzyme cleavage, rendered two possible norbornyl peptide products containing either a: 1) carboxylic acid (*N*-terminus conjugate); or 2) primary amine (*C*-terminus conjugate) (Figure 3.2). This in turn allowed for the evaluation of cell uptake as a function of size and charge borne by the polymer prior to and post enzyme processing.

Peptide brush polymers were synthesized *via* Ring Opening Metathesis Polymerization (ROMP) using Grubbs' third generation catalyst for several key reasons. Given the recognized high-functional group tolerance of this catalyst, peptide brush polymers can be readily prepared using a *graft-through* approach (as described in chapter 2), obviating the need for post-polymerization modification steps and enabling high incorporations of functional peptide into the polymer. Moreover, the fast initiation kinetics afforded by the catalyst enables low dispersity and allows precise control over polymer composition and

degree of polymerization (DP). Lastly, functional chain transfer agents such as fluorophores can be used to end-label the polymer, enabling visualization and tracking of the material in cells, as our lab has shown previously.³⁵ As such, all norbornyl peptide derivatives were polymerized to specific DP by varying the monomer to initiator ratio ($[M]_0/[I]_0$) accordingly and end-labeling the polymers with fluorescein (Figure 3.3).

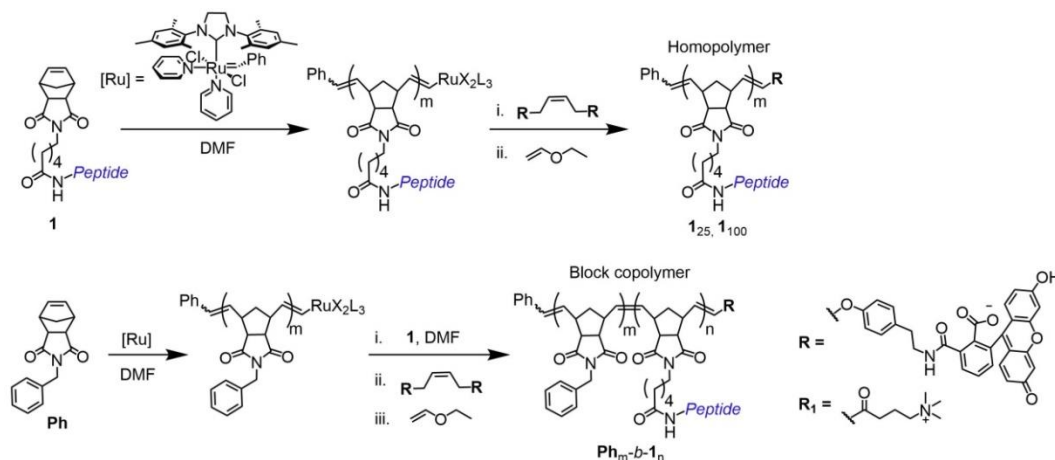


Figure 3.3 Polymerization schemes for the preparation of peptide-containing homopolymers and block copolymers.

Table 3.1 Peptide sequences used to synthesize homopolymers and NPs of various charge

Charge	<i>N</i> -terminus	<i>C</i> -terminus
Zwitterionic (Nzw)	$\text{H-GPLGLAGEK(R}_1\text{)CONH}_2$	(Czw) $\text{R}_1\text{-EGPLGLAGK(}\nabla\text{)CONH}_2$
Cationic (Ncat)	$\text{H-GPLGLAGK(R}_1\text{)CONH}_2$	(Ccat) $\text{R}_1\text{-GPLGLAGK(}\nabla\text{)CONH}_2$
Anionic (Nan)	$\text{H-GPLGLAGEK(Ac)CONH}_2$	(Can) $\text{Ac-EGPLGLAGK(}\nabla\text{)CONH}_2$

Note that $\text{K(R}_1\text{)}$ designates R_1 conjugated to the ϵ -amino group of the lysin residue. All peptides contain a *C*-terminal amide to ensure that charge contributions are only from glutamate (E) residues and trimethylammonium cation (tma, R_1).

Lowe, Tew and coworkers have previously demonstrated that simple betaine-type monomers can be polymerized by ROMP in a living fashion.^{36,37} In section 2.5, pseudo first-

order kinetic plots were generated for *N*- and *C*-terminus conjugated peptide betaines, which demonstrates their ability to polymerize in a living manner in DMF solvent conditions.

To generate the library of materials used in this study, norbornyl peptides were polymerized either as homopolymers or as a discrete block in amphiphilic block copolymers. We note that in order to minimize size variations in NPs formulated from the self-assembly of amphiphilic block copolymers, the DPs of both discrete blocks were conserved across the peptide library. Block copolymers were prepared by polymerizing a norbornyl phenyl monomer (Ph), allocating the solution to separate reaction vials, and finally dispensing the appropriate norbornyl peptide monomer to the living polymer chain (Figure 3.3). In our interest of developing systems comprised of other architectures that we envisioned could retain active targeting; we also polymerized the *N*-zwitterionic peptide monomer in a random distribution with either a norbornyl phenyl or aliphatic C7 monomer (Ph and C7, respectively) to generate amphiphilic random copolymers (Figure 3.4).

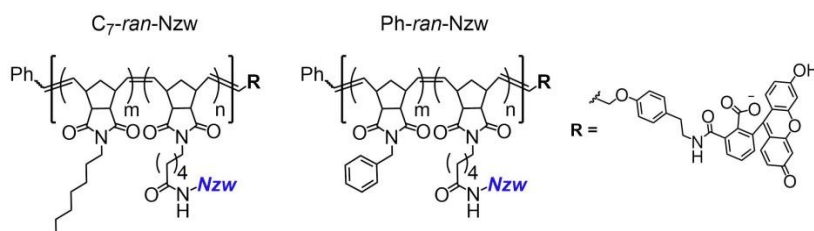


Figure 3.4 Chemical structures of random copolymers comprised of two different hydrophobic groups (phenyl and C7 linear aliphatic) and the Nzw peptide.

In order to accurately produce random copolymers, it was important to first establish the polymerization rates of Ph and C7 monomers using $^1\text{H-NMR}$ (see methods). Once these rates were known, separate reactions were carried out, whereby an aliquot of either monomer was dispensed every 5 minutes over the course of the polymerization of Nzw until monomer consumption was reached after 1.5 h. The monomer feed ratios of each type were kept

constant but the block sizes were varied in order to yield copolymers of different molecular weights (45 and 80 kDa).

Self-assembly of amphiphilic block or random copolymers into spherical NPs was achieved by dissolving the amphiphile in an organic solvent (DMF, acetonitrile, or DMSO) and slowly dialyzing it into aqueous solution (Dulbecco's phosphate-buffered saline, DPBS), a solvent for which only the hydrophilic peptide block portion of the amphiphile is soluble. Uniform spherical NPs approximately 10–20 nm in diameter were formed from block copolymers in DPBS, as measured by dry-state TEM and DLS (Figure 3.5 and Table 3.2, respectively). Interestingly, random copolymers self-assembled in DPBS to form spherical NPs within a similar range in diameter, despite effectively doubling the polymer M_n (Figure 3.6 and Table 3.3). Insufficient signal intensities were measured by DLS and no discernable nanoscale assemblies were observed by TEM (not shown) for water-soluble peptide homopolymers in DPBS (Figures 3.26 and 3.27 in methods), permitting the assessment of cellular uptake as a function of peptide polymer organization either into spherical NP assemblies or as soluble unimers in solution. Zeta potentials were measured for spherical NPs after dialysis from DPBS into a low ionic strength buffer (10 mM Phosphate buffer, at pH 7.5). Obtained values were in good agreement with theoretical values expected from the peptide charge contribution (Table 3.2), with the exception of Nzw NPs, which trended toward negative values. Spherical NPs formulated from random copolymers exhibited similar zeta potential values as the Nzw NP (Table 3.3). All values displayed a small range in magnitude, which was likely due to the low scattering intensities known for small organic-based nanoparticles. It was not practically accessible to measure water-soluble polymers, since they exhibit even smaller scattering and require high concentrations for measuring their electrophoretic mobilities.

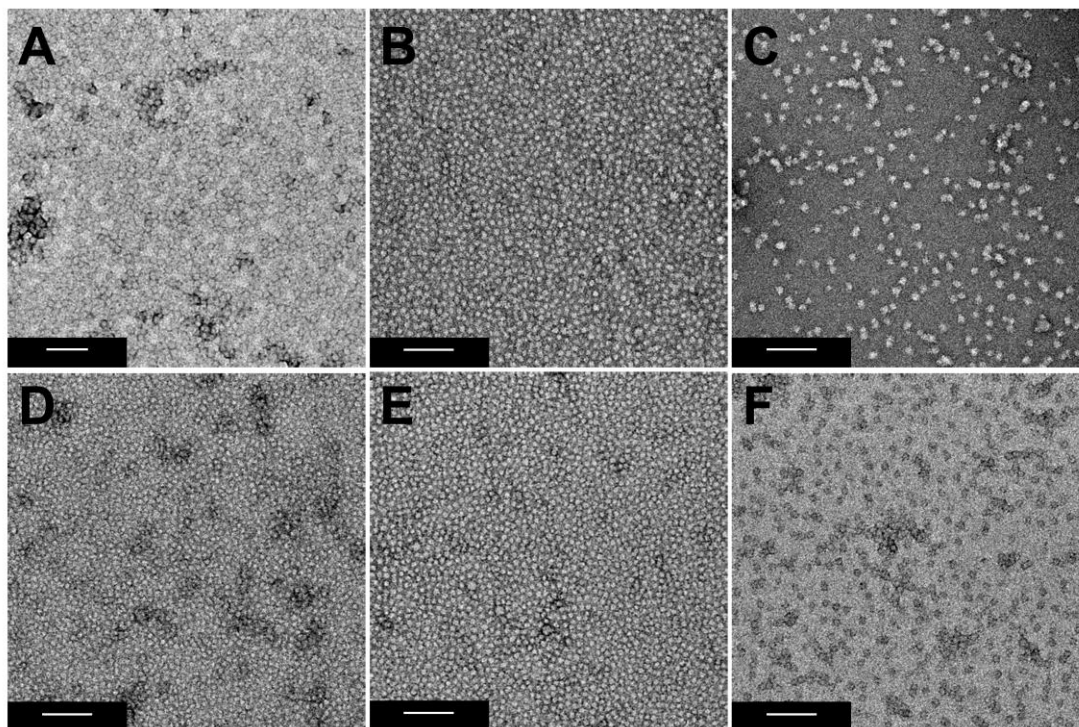


Figure 3.5 Transmission electron microscopy (TEM) images of spherical NPs formulated from A) Nzw; B) Ncat; C) Nan; D) Czw; E) Ccat; and F) C-an prepared by dialysis from organic cosolvents into DPBS (see Methods for details). Scale bar is 100 nm.

Table 3.2 Dynamic Light Scattering and zeta potential measurements of spherical NPs formulated from amphiphilic block copolymers

NP	Copolymer ^a	R_h (Q) ^b	D_h ^c	ζ (mV) ^d	N_w^{agg} ^e
Nzw	Ph ₄₁ - <i>b</i> -Nzw ₂₆	6.0	22.4	-20.5 ± 1.95	61
Ncat	Ph ₄₁ - <i>b</i> -Ncat ₃₂	3.6	15.6	+13.4 ± 0.90	10
Nan	Ph ₄₁ - <i>b</i> -Nan ₂₅	15	18.9	-19.7 ± 1.29	28
Czw	Ph ₄₁ - <i>b</i> -Czw ₁₅	15	9.9	+2.90 ± 0.54	320
Ccat	Ph ₄₁ - <i>b</i> -Ccat ₂₇	19	15.3	+16.7 ± 1.21	17
Can	Ph ₄₁ - <i>b</i> -Can ₂₃	35	17.1	-17.8 ± 1.33	83

^a Amphiphilic copolymer used to formulate NP. ^b Measured by Static Light Scattering (SLS) batch mode. ^c Hydrodynamic diameter measured by Dynamic Light Scattering (DLS). ^d NPs measured in 10 mM Phosphate Buffer (pH 7.5). Average of three measurements. ^e Aggregation number measured by batch-mode static light scattering.

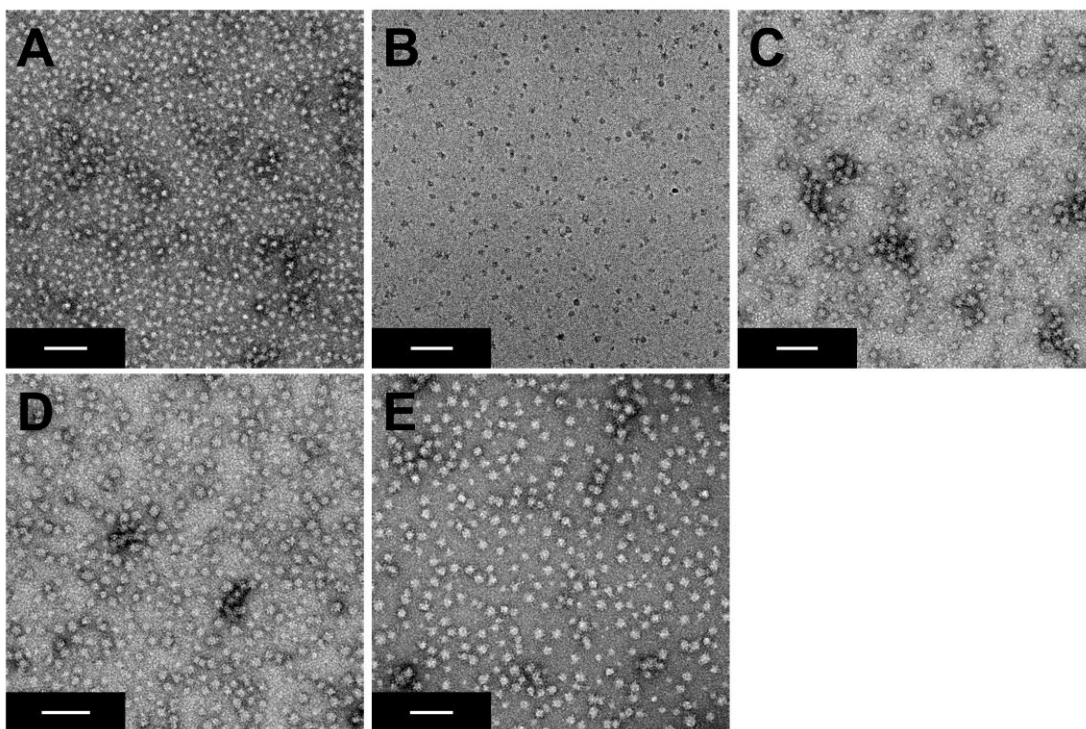


Figure 3.6 TEM images of the random copolymers. Dry-state (A) and cryo-EM (B) of Ph (~ 45 kDa). Dry-state of (C) Ph (~ 80 kDa); (D) C7 (~ 45 kDa); and (E) C7 (~ 80 kDa). Scale bar is 100 nm.

Table 3.3 Characterization of spherical NPs formulated from amphiphilic random copolymers

NP	Copolymer ^a	ζ (mV) ^b	R_h (Q) ^c	D_h ^d	Molar Mass Moment	N_w^{agg} ^e
C7 (~ 45 kDa)	Ph ₃₀ -ran-Nzw ₄₀	-20.0 ± 1.10	1.5	-	8.907 E5	61
C7 (~ 80 kDa)	Ph ₆₀ -ran-Nzw ₈₀	-7.96 ± 0.53	8.0	-	1.821 E6	10
Ph (~ 45 kDa)	Ph ₃₀ -ran-Nzw ₄₀	-15.3 ± 1.44	3.4	-	6.965 E5	17
Ph (~ 80 kDa)	Ph ₆₀ -ran-Nzw ₈₀	-11.9 ± 1.18	28	-	1.858 E6	83

^a Copolymer used to formulate NP. ^b NPs measured in 10 mM Phosphate Buffer (pH 7.5). Average of three measurements. ^c Measured by Static Light Scattering (SLS) batch mode. ^d Hydrodynamic diameter measured by Dynamic Light Scattering (DLS). ^e Aggregation number measured by batch-mode static light scattering.

3.3 Cellular internalization of peptide brush polymers and polymeric NPs by RAW 264.7 cells

Fluorescence-based assays using RAW264.7 murine-derived macrophage cells were used to evaluate the cell uptake of hydrophilic peptide polymers, spherical NPs, and their enzymatically degraded analogues. The objectives of these studies were two-fold: 1) to examine whether prepackaging peptides of different charges as nanoscale assemblies provokes cell entry to a greater extent than as soluble polymers; and 2) to determine whether sequence specific proteolysis of peptide bonds, which exposes positively charged amines or negatively charged carboxylates prompts changes in cell entry and corresponding cell uptake mechanisms. Having established that spherical NPs of different charge showed uniformity in size, all materials were examined for their cytotoxicity by treatment with RAW 264.7 cells at 1 μ M (with respect to polymer) for 24 h. The CellTiter Blue assay was used with RAW264.7 cells to establish > 80 % cell viability for all treatments applied, except for Ccat NP and homopolymer (DP 100), which exhibited 65 % and 63 % viability, respectively, over the 24 h treatment relative to vehicle-treated controls (Figure 3.7). However, the minimal cytotoxicity measured in cell viability experiments ensured that cell uptake of materials by RAW264.7 cells could be evaluated by flow cytometry. All treatments were applied at 1 μ M (with respect to polymer) in aqueous solution and fluorophore labeling for all materials was assumed to be equivalent (one fluorescein dye molecule, **R**, per polymer chain). This ensured that materials were compared fairly on a per polymer basis since measurements made with respect to fluorescein dye would bias concentration measurements (fluorescein is highly sensitive to polarity changes in the local environment). For example, the high dense packaging of amphiphiles or differently sized polymers, along with light scattering contributions, lead to large variations of fluorescein absorbance on the UV spectrometer.

Next, the cellular uptake by RAW 264.7 cells was assessed by flow cytometry and was quantified as the normalized mean fluorescence, which was calculated as the ratio of mean fluorescence count of cells treated with material to the mean fluorescence count of cells treated with vehicle (DPBS). From these experiments, *N*- and *C*-cationic NPs, as well as *N*-anionic NP treatments displayed the greatest fluorescence signal intensities compared to all other materials, with at least a 3-fold enhancement relative to their *N*- or *C*-terminal counterparts (Figure 3.8).

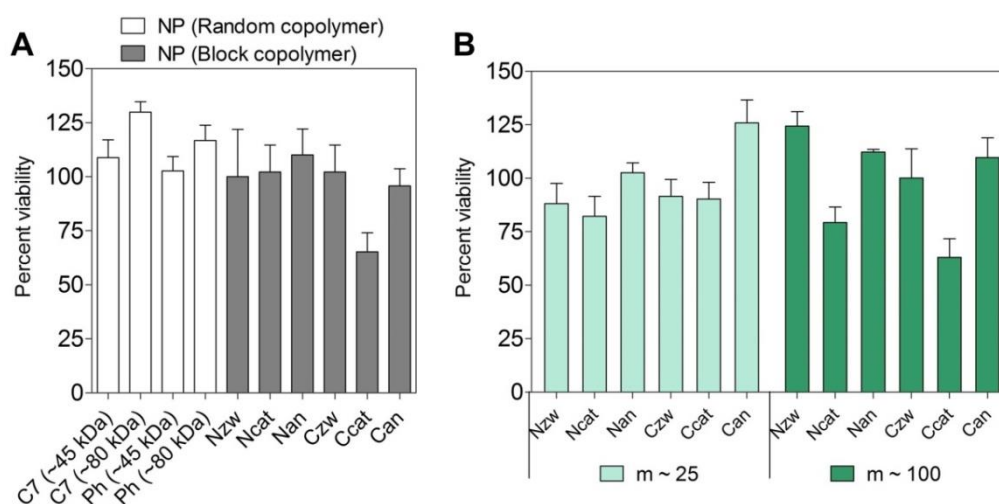


Figure 3.7 Percent viability of materials used for RAW 264.7 uptake experiments. Percent viability of (A) NPs prepared from amphiphilic block and random copolymers and (B) hydrophilic peptide brush homopolymers.

Positively charged NPs are generally known to elicit greater cell internalization relative to other NPs with negative surface charge.³⁸ Interestingly, the fluorescence counts produced from Nan NP treatments showed a 4-fold increase compared to that of the Can NP, which sustained similar levels to vehicle treatment (Figure 3.8). Although these systems are similar in size and zeta potential values, this discrepancy in cellular response may arise from differences in the arrangement of anionic peptides on the NP surface invoked by the *N*- or *C*-terminus connectivity. Additionally, the aggregation numbers (N_w^{agg}), independently

calculated from batch-mode static light scattering (SLS) measurements, indicate that Can NPs consist of nearly three times the number of assembled polymer chains as Nan NPs (Table 3.2). Perhaps the presence of more densely arranged copolymers of Can NPs imparts resistance to cell internalization under these conditions.

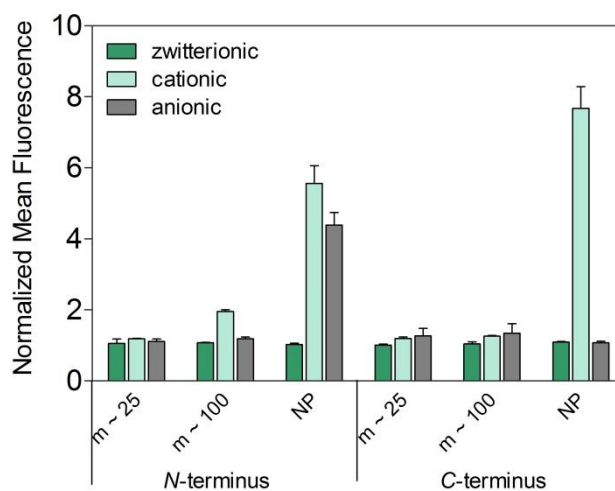


Figure 3.8 Cellular uptake by RAW264.7 cells quantified as normalized mean fluorescence of hydrophilic homopolymers and spherical NPs at 1 μ M after 3 h treatment. Representative histograms depicting fluorescence signal intensities of materials are shown in the methods section.

A large value for N_w^{agg} was also observed for Czw NPs, approximately an order of magnitude higher than other materials, signifying that a small population (< 15 % by mass) of larger species observed by DLS was present. The scattering intensity of polydisperse samples is known to skew in favor of contributions from larger species in solution and so comparison by TEM is necessary in these cases. By TEM, a small population of 100 nm sized vesicles were observed (Figure 3.20), though the sample was mostly comprised of small ~20 nm particles. Nevertheless, in contrast to the other charged NPs, *N*- and *C*-zwitterionic NPs provoked no cellular response. Further, spherical NPs generated from random copolymers bearing Nzw peptides showed minimal cellular uptake (Figure 3.9). These findings are in

agreement with previous reports describing the stealth-like properties imparted by zwitterionic NP surface coatings.^{39,40} Furthermore, all peptides, with the exception of Ncat, incorporated as soluble homopolymers either for DP 25 or DP 100, exhibited negligible cell internalization (approximately the same fluorescence intensity as the vehicle) (Figure 3.8). These data indicate that despite the charge displayed by the peptide, the organization of peptide polymers into spherical NPs generally enhances unwanted macrophage association. Therefore, incorporating functional peptides into soluble polymers may be a general strategy for reducing MPS accumulation of injectable macromolecular peptide therapeutics.

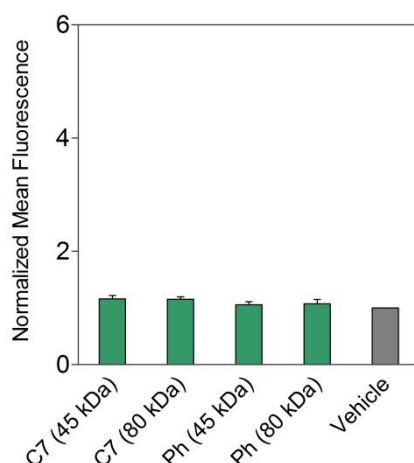


Figure 3.9 Cellular uptake of spherical NPs formulated from Nzw peptide-containing random copolymers. RAW 264.7 cells were incubated for 3 h with each material at 1 μ M.

Next, cells were analyzed using live cell confocal microscopy to confirm that the mean fluorescence counts measured by flow cytometry resulted from internalized materials and not materials associated with the cellular membrane. Live cell confocal analysis was performed due to the artificial uptake observed for cell-penetrating peptides after cell fixation.^{41,42} A Z-stack analysis was performed to investigate the subcellular location of internalized material and merged with the bright field channel to confirm cell internalization. Overall, it was difficult to observe cell internalization of materials, likely due to bleaching of

fluorescein during the duration of the image scan (Figure 3.10).^{43,44} However, cells treated with Czw NPs exhibited minimal fluorescence, indicating that the zwitterionic character of spherical NPs is sufficient to prevent cell uptake. In contrast, cells treated with Ccat and Ncat NPs showed punctate fluorescence, with some background signal (Figure 3.10). This suggests that these spherical NPs are localized *via* endocytosis compartments. The Ccat homopolymer ($m \sim 100$) showed minimal fluorescence, confirming that the spherical arrangement of amphiphilic polymers bearing a permanent cation per peptide side chain is necessary for internalization.

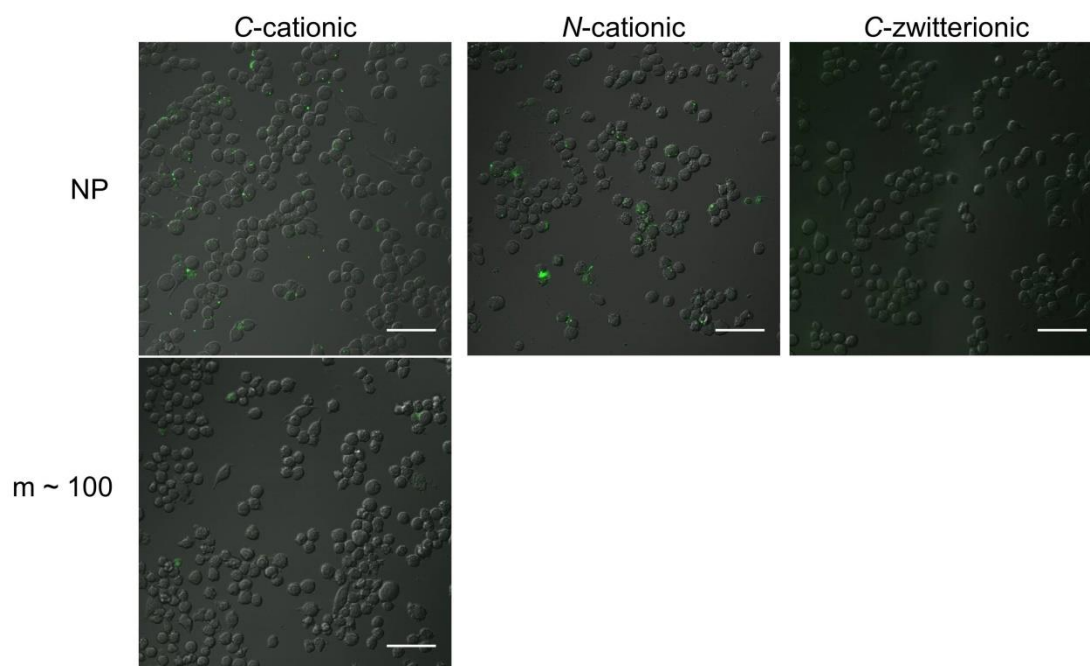


Figure 3.10 Merged bright field and epifluorescence channels from Z-stack live-cell confocal analysis of RAW 264.7 cells treated with fluorescently labeled spherical NPs and homopolymer (DP 100). Punctate fluorescence was observed for Ccat and Ncat spherical NPs but not for Czw NP or Ccat homopolymer ($m \sim 100$). Scale bars are 50 μm . Objective is 40X.

We were also interested in examining the batch-to-batch variability in the bottom-up strategy utilized to formulate spherical NPs. The cellular uptake by RAW 264.7 cells was assessed by flow cytometry of spherical NPs formulated from newly synthesized block

copolymers (DLS/TEM not shown, Table 3.5 for copolymer characterization) and compared with the first set (Figure 3.11). There was minimal variation between batches, except for anionic derivatives (Nan and Can). This may be due to the larger number of polymerized Nan peptides ($n = 35$ for batch 2 and $n = 25$ for batch 1); however, Nzw spherical NPs also displayed a similar peptide block variation ($n = 34$ for batch 2 and $n = 26$ for batch 1) and maintained similar bioactivities. This also does not explain the slight increase in uptake for Can NP observed for batch 2, despite maintaining similar block sizes. A second reason may be the propensity of anionic copolymers to aggregate in aqueous solution (see chapter 2 on *N*- and *C*-terminus peptide polymers). Nevertheless, this data further demonstrates that zwitterionic coatings promote stealth or evasion of macrophage recognition and uptake.

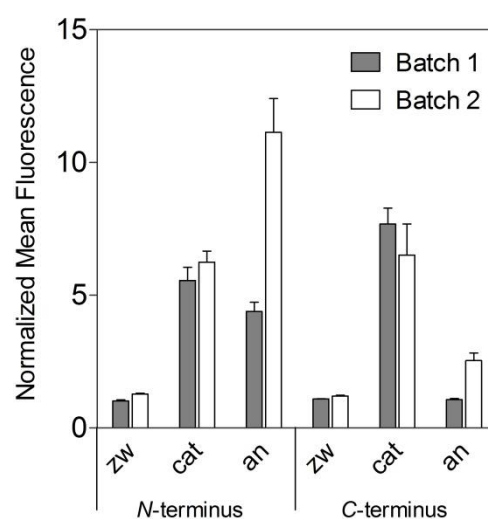


Figure 3.11 Batch variation of spherical NPs on RAW 264.7 cell uptake at 1 μM after 3 h treatment.

3.3.1 Mechanism of cellular uptake

To probe whether the mechanism of cellular uptake of spherical NPs involves passive diffusion across the cellular membrane or receptor-mediated internalization (an active,

energy-dependent process), flow cytometry uptake experiments were repeated at low temperature (4 °C). At low temperatures, surface receptor-mediated cell uptake has been shown to be dramatically reduced.^{45,46} All spherical NPs (predominantly cationic and anionic analogues) showed suppressed cell uptake at 4 °C, which suggests that the internalization mechanism may be through a receptor-mediated process (Figure 3.12). However, this primary observation requires further investigation, such as the employment of pharmacological inhibitors in order to assign a specific mechanism.⁴⁷

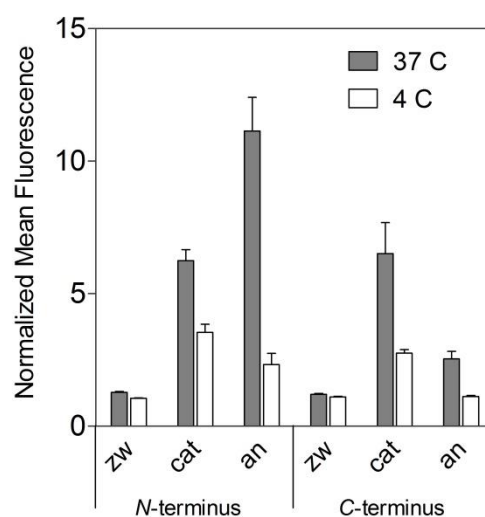


Figure 3.12 Mechanism of cellular uptake of *N*- and *C*-terminus NPs of various charge using low temperature incubation with RAW264.7 cells for 3 h.

3.3.2 Serum-dependent cellular uptake

Next, the cellular uptake of spherical NPs was assessed by flow cytometry using serum-free and competent serum conditions. Studies on the cellular uptake of a variety of spherical NPs in biological environments show that the protein corona plays a central role in the resulting cellular-NP interactions.^{7,26,29,48–50} Competent fetal bovine serum (FBS) was used since it contains complement proteins (not heat inactivated) that play a prominent role in opsonin-macrophage recognition processes.^{16,51–53} RAW 264.7 cells were treated with each

material for 3 h in the presence of competent serum or no serum. The flow cytometry results of cationic (Ncat and Ccat) NPs showed a significant increase in cell uptake in the absence of serum (Figure 3.13). No difference in the uptake between competent serum and heat-inactivated serum conditions were found.

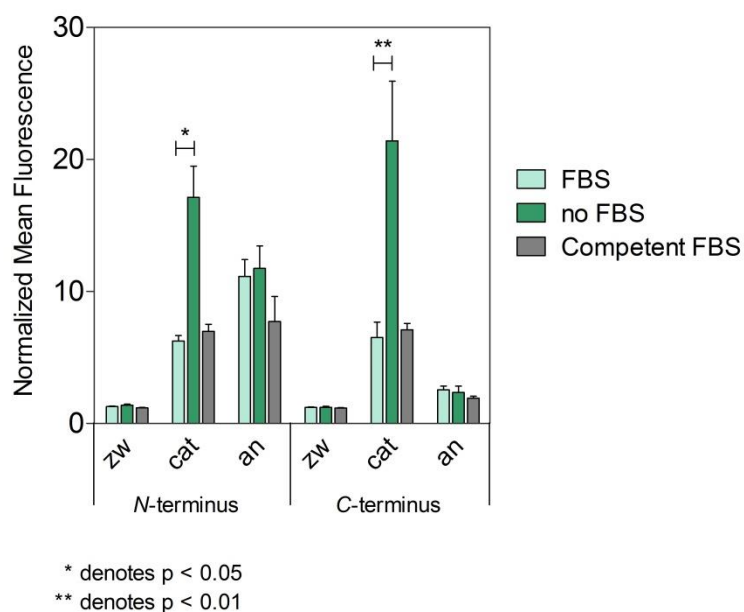


Figure 3.13 Comparing the effect of serum on the cellular uptake of *N*- and *C*-terminus NPs of various charge with RAW 264.7 cells.

Notably, zwitterionic coatings maintained similar fluorescence counts to the vehicle, which may suggest the absence of a hard corona for these charged NPs; for example, Rotello and coworkers observed that internalization of zwitterionic AuNPs was the same in serum or serum-free conditions.⁵⁴ The serum-dependent uptake of anionic NPs by phagocytic cells has been observed by other groups,^{55,56} though in these cases (50 nm and 100 nm iron oxide NPs or carboxylate-modified microspheres of 20 and 200 nm), the presence of serum increased the cytotoxicity and cell uptake of the material, relative to serum-free conditions. Further, Simmet and coworkers showed intravenously injected carboxy-functionalized polystyrene

NPs of 100 nm in diameter preferentially accumulated in the liver, where Kupfer cells reside, compared to amine-functionalized analogues.⁵⁷ For the cell uptake of carboxylate-coated NPs by non-phagocytic cells (HeLa and MDCK), it has been shown that pre-incubation of NPs with serum reduces NP uptake; the authors speculated that serum directly impacts the ability of NPs to interact with the cell surface, possibly due to reversible adsorption and a decrease in the NP zeta potential, despite no change in NP size by DLS.⁵⁸ In general, non-phagocytic cells preferentially internalize cationic NPs whereas phagocytic cells take up anionic NPs.⁵⁹ Intriguingly, the flow cytometry data show the reverse trend. Further investigation into the identity of opsonins coating the surface of the differentially charged spherical NPs may shed light on the serum-dependent cellular uptake. To determine whether the spherical arrangement of charged peptides causes high uptake under serum-free conditions, the serum-free cell uptake of hydrophilic polymers (DP 25) was also examined. No difference in the flow cytometry data between serum and serum-free conditions was observed (Figure 3.14).

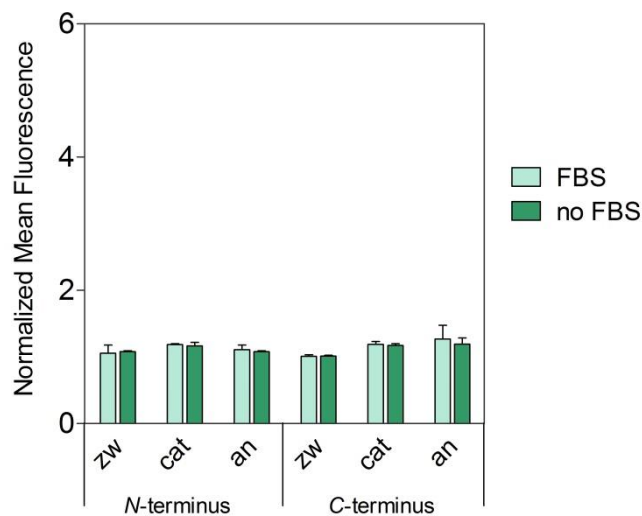


Figure 3.14 Comparing the effect of serum on the cellular uptake of *N*- and *C*-terminus homopolymers (DP 25) of various charge with RAW 264.7 cells.

3.4 Enzyme-activated uptake of polymeric NPs

Next, the effect of enzyme-cleavage of several model NPs on cellular uptake was examined. We reasoned that the exposure of carboxylates and protonated amines for N- and C-conjugated materials (Figure 3.2) under physiological conditions revealed by enzymatic hydrolysis could affect the cellular uptake of these materials. Further, enzymatic stimuli have been used by others as an activatable uptake mechanism, though the macrophage cell uptake of these types of materials have not been examined.⁶⁰⁻⁶² In these experiments, Czw NP was used as a model activatable system and Ccat and Ncat NPs were used as model controls. Nan and Can NPs were not chosen in this study due to the variability in their cell uptake shown earlier (Figure 3.12). We hypothesized that the Czw NP, which shows no cell uptake initially, would expose amine residues after enzyme cleavage that may activate internalization. In the same vein, Ccat NP is expected to maintain internalization (due to a positive-to-positive charge switch). In contrast, Ncat NP exposes anionic residues after enzyme cleavage, which may restrict cell uptake (positive-to-negative charge switch). For these experiments, materials were subjected to thermolysin for 15 h and the enzyme chemically denatured with 10 % EDTA prior to incubation with RAW 264.7 cells. Enzyme cleavage was verified by RP-HPLC and TEM was used to observe disruption in morphology, due to truncation of the hydrophilic block.⁶³ Controls were also prepared in the same fashion except that thermolysin was denatured prior to incubation with NPs.

Thermolysin-processing of the NPs generally resulted in aggregation of the materials as expected (Figure 3.15). The formation of micrometer-sized aggregates was apparent, though much of the product remained as discrete spherical NPs, and in some case (Ncat NP), the formation of NP clusters was observed (Figure 3.15C). Flow cytometry was used to quantify the extent of cell uptake in these experiments, as done previously.

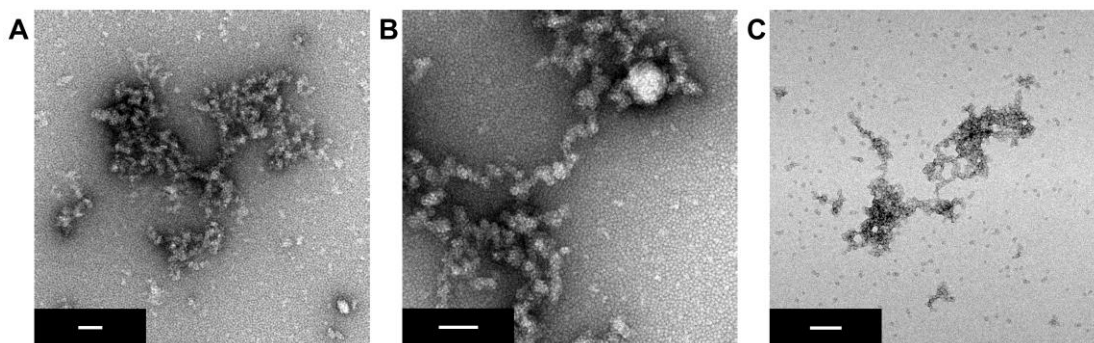


Figure 3.15 Transmission electron microscopy (TEM) images of (A) Ccat NP; (B) Czw NP and (C) Ncat NP after enzyme treatment with thermolysin for 15 h. Scale bar is 100 nm.

From these experiments, the cell uptake of both Ncat and Ccat NPs was unchanged after enzyme treatment (Figure 3.16). However, Czw NP showed significant uptake after enzyme treatment, presumably due to the zwitterionic-to-cationic charge switch. RP-HPLC confirmed the presence of the peptide fragment after enzyme treatment (Figure 3.16B).

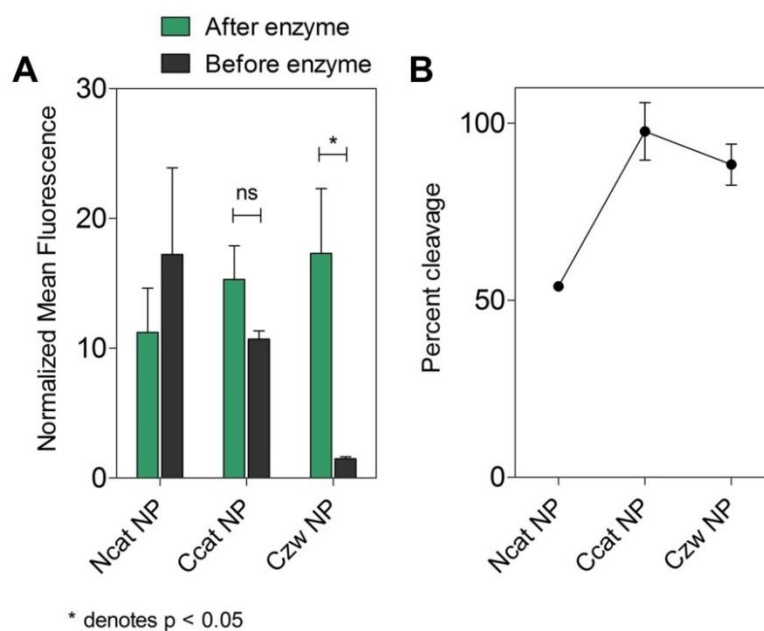


Figure 3.16 Cellular uptake of spherical NPs of various charges before and after treatment with 0.3 μ M thermolysin for 15 h. (A) Cellular uptake plotted as normalized mean fluorescence. RAW 264.7 cells were incubated for 3 h with each material at 1 μ M. SEM is shown. (B) Percent cleavage of the materials after enzyme treatment.

To verify that the enzyme-activated Czw NP product was internalized by RAW 264.7 cells and not simply bound to the cell membrane, Z stack analysis by live-cell confocal microscopy was performed. The appearance of punctate fluorescence after enzyme treatment indicated that the enzyme-cleaved material was internalized. Further, the Ccat NP indicated similar internalized fluorescence before and after enzyme treatment, corroborating the flow cytometry data. We hypothesized that Ncat NP (which exhibited ~50 % cleavage) should be zwitterionic (bearing side chains with approximately 1:1 ratio of permanent cation and carboxylate), which would then suppress cell uptake. However, the micrometer-sized particle clusters formed after enzyme treatment could lead to enhanced uptake by phagocytic cells, which preferentially internalize particles between 2–3 μm .⁶⁴

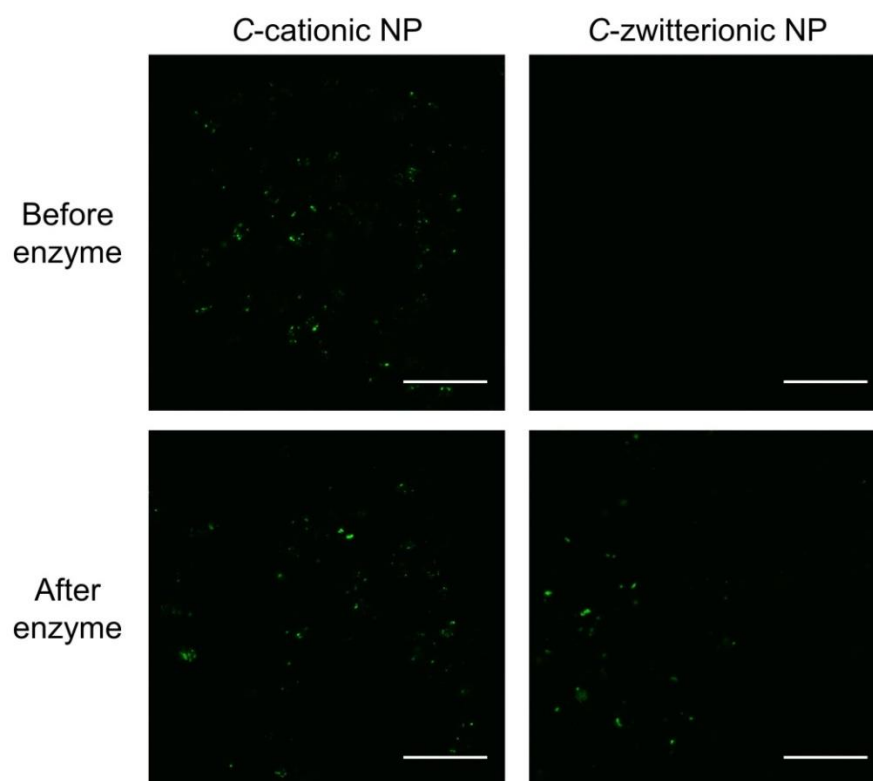


Figure 3.17 Live cell confocal microscopy of RAW 264.7 cells incubated with Ccat and Czw NPs before and after thermolysin treatment. Ccat and Czw NPs were incubated with thermolysin for 15 h prior to incubation with cells. Scale bars are 50 μm .

To determine whether the enzyme-activated strategy could be applied to hydrophilic polymers, Ncat, Ccat, and Czw polymers (DP 25 and 100) were pre-incubated with thermolysin under the same conditions and treated with RAW 264.7 cells. Interestingly, polymers of DP 25 sustained minimal fluorescence counts (Figure 3.18). In contrast, polymers of DP 100 showed an increase in cell internalization after enzyme treatment. Analysis of the reaction solutions by RP-HPLC confirms the presence of cleavage fragments (Figure 3.18B), indicating that proteolysis did, in fact, occur. These results suggest that a minimal size for hydrophilic polymers is required to ensure enzyme-activated uptake, perhaps due to the aggregation observed post-treatment for DP 100 polymers but not for DP 25 polymers (Figure 3.19).

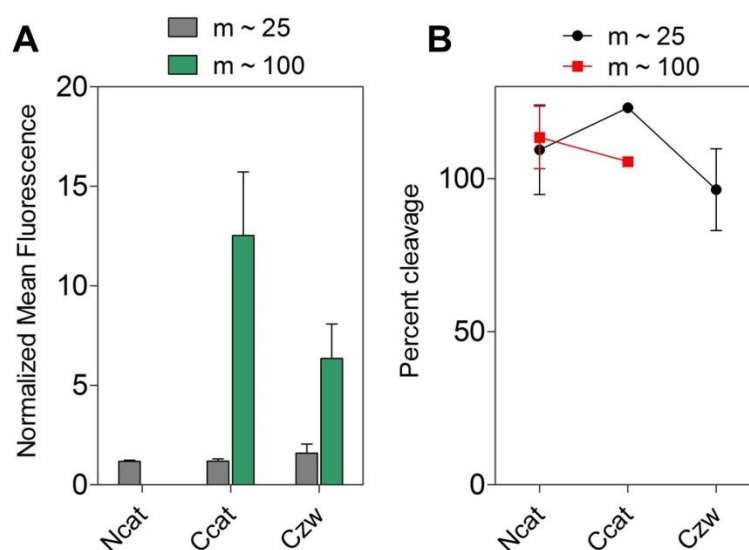


Figure 3.18 Cellular uptake of hydrophilic polymers of various charges after treatment with 0.3 μM thermolysin for 15 h. (A) Cellular uptake plotted as normalized mean fluorescence. RAW 264.7 cells were incubated for 3 h with each material at 1 μM . (B) Percent cleavage of the materials after enzyme treatment.

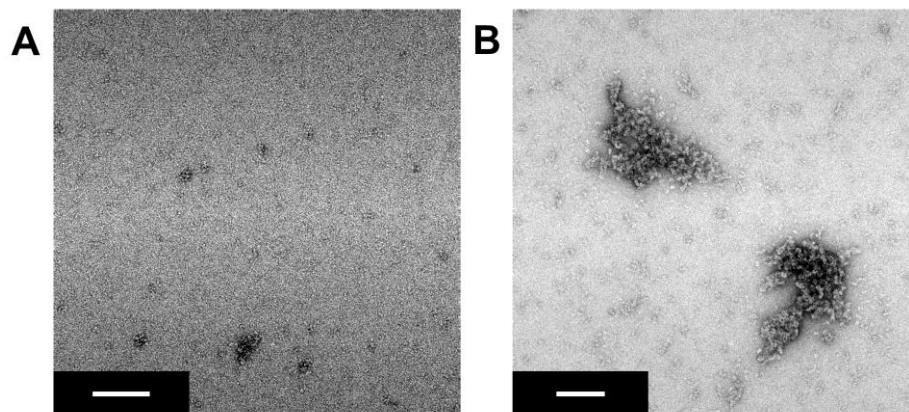


Figure 3.19 Dry-state TEM images of hydrophilic peptide brush polymers treated with thermolysin. (A) Ncat (m ~25) and (B) Ncat (m ~100) were treated with 0.3 μM thermolysin for 15 h prior to incubation with RAW 264.7 cells.

We also examined whether the enzymatically-degraded analogues of Ncat, Ccat, and Czw polymers and spherical NPs were cytotoxic. The CellTiter Blue assay was used to assess the cell viability of RAW 264.7 cells after 24 h treatment with each material. Greater than 75 % cell viability was measured for the materials relative to vehicle (Figure 3.20). It was noted that a reduction in the cell viability for the Czw NP prior to and post enzyme treatment was observed (~100 % and 75 %, respectively). It is noted in the literature that (for non-phagocytic cells) cytotoxicity generally increases along with cell internalization ability for cationic nanoparticles.⁵⁹

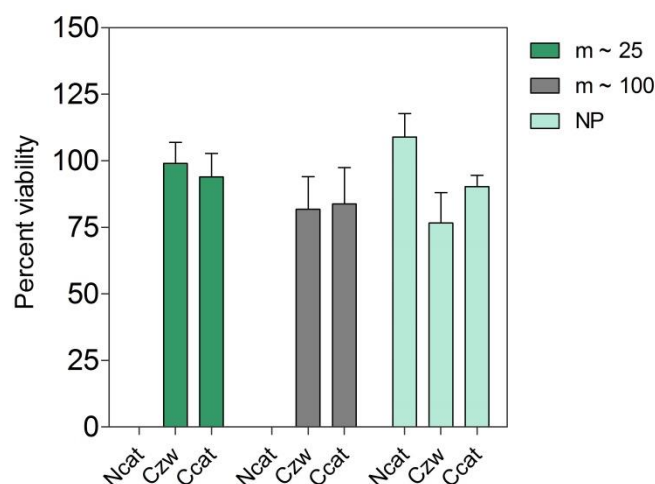


Figure 3.20 Percent viability of enzyme-treated materials used for RAW 264.7 uptake experiments.

3.5 Conclusions and future outlook

In summary, we have described a systematic study exploring the effect of size and surface charge on macrophage cell uptake. ROMP was used to synthesize a library of materials, encompassing hydrophilic peptide brush polymers of varying degrees of polymerization (DP of 25, 100) and spherical NPs (of approximately 20 nm diameter), formulated from amphiphilic *N*- or *C*-terminus conjugated peptide block copolymers. The precise synthesis of block copolymers permitted the production of remarkably discrete nanostructures after dialysis, which has been noted previously for analogues systems.⁶⁵ Given the exceptionally narrow range in NP diameter, these materials were good candidates to assess the effect of charge on cellular uptake by RAW 264.7 cells. Cationic and anionic analogues showed the greatest internalization, as quantified by flow cytometry and verified by live cell confocal microscopy. Interestingly, batch-dependent cellular uptake of anionic analogues varied significantly, while spherical NPs bearing a permanent cation (either zwitterionic or cationic) maintained consistent degrees of internalization. This suggests that

the trimethyl ammonium cation can facilitate micellization in a reproducible manner. Moreover, zwitterionic NP analogues showed minimal cell uptake, even when formulated from random copolymers, suggesting that overall charge is important in these processes. Hydrophilic polymers of either DP 25 or 100 showed no cell internalization, suggesting that their small size (~ 5 nm) is sufficient to thwart macrophage recognition and uptake. This is particularly notable, given that packaging peptide therapeutics in this manner may provide an easily accessible route for producing macromolecular drugs which avoid MPS accumulation; however, it is noted that hydrophilic polymers bearing peptide side chains, which incorporate lysine (K) and arginine (R) residues, have been shown to facilitate cell uptake in HeLa cells in a charge-dependent manner.⁶⁶

Future work is necessary to identify the mechanism of internalization of these materials.^{45,47} Particularly interesting is the serum-dependence on cellular uptake; specifically, evaluating the identity of opsonins comprising the protein corona is not only an intellectual curiosity, but is necessary for optimizing related biomaterials for *in vivo* use.^{67,68} Most work in this area has been completed for gold nanoparticles, of which there are many reported methods, to readily identify binding of opsonins that form both hard and soft corona⁶⁹⁻⁷¹ Soft materials are more challenging to study, because of the inherent absence of plasmon resonance phenomena, along with the difficulty of separating bound from unbound proteins.⁷² A useful strategy may be a “click” chemistry-inspired approach, whereby a reactive handle (in the form of a chain transfer agent) is appended to the end of the polymer.⁷³ The chemical handle can be used to later conjugate to a chemically functionalized surface following incubation in serum. Unbound serum can then be cautiously rinsed away, while bound serum can be analyzed by known methods, i.e. typical procedures that entail digestion of bound proteins and separation by gel electrophoresis or size exclusion chromatography.

Given that the materials in this study were composed of peptide side chains, which contained an optimized sequence for proteolytic enzymes, we examined whether enzyme hydrolysis of peptide side chains on several model systems could affect cellular uptake, by virtue of a charge switch. Notably, Czw NPs were able to undergo cellular internalization by RAW 264.7 cells after proteolytic cleavage (zwitterionic-to-cationic charge switch). It was also shown that hydrophilic polymers generally avoided uptake even after proteolysis; however, by increasing the degree of polymerization, Ccat and Czw hydrophilic polymers did undergo internalization after enzyme cleavage. In summary, the results reported show that enzyme-activatable cell uptake offers a means by which to target areas where a specific cell surface enzyme is present.

We speculate that this enzyme-targeting strategy may be useful for promoting macrophage differentiation, for applications in activating tumor-associated macrophages (TAMs) to “eat” cancer.⁷⁴⁻⁷⁷ For example, macrophages can exhibit pro-inflammatory (M1) and anti-inflammatory (M2) phenotypes in response to external cues, which is especially critical in the success of implantable biomaterials.⁷⁸ Both M1 and M2 macrophages are thought to be essential and opposing forces in inflammatory environments and diseased tissue (such as tumors). In the tumor microenvironment, the expression of M2 macrophages (or often referred to as TAMs) is elevated, causing subdual of tumor immunity and enhancement of vascularization.^{79,80} Efforts to develop TAM-targeted strategies have resulted in studies generating these phenotypes from monocytes, by application of lipopolysaccharide (LPS) or the cytokine interferon gamma (IFN- γ) to generate M1 and M2 phenotypes, respectively, then exploring the cellular uptake of synthetic nanomaterials.⁸¹⁻⁸³ Future work for the systems described herein may benefit this area of research.

3.6 Acknowledgements

Chapter 3 contains material that is currently being prepared for submission for publication: "Peptide Brush Polymers and Nanoparticles for Evading and Activating Macrophage Uptake" Lisa Adamiak and Nathan C. Gianneschi. The dissertation author was the primary author of this pending manuscript.

3.7 Methods

For general methods, see chapter 2. For standard SEC-MALS conditions, see chapter 2. DLS measurements were obtained using a DynaPro NanoStar (Wyatt Technologies). ¹H NMR spectra were recorded on a 400 MHz Varian Mercury Plus spectrometer. Chemical shifts are reported in ppm relative to DMF-d7 residual peaks.

3.7.1 Transmission electron microscopy

TEM preparation was done by depositing 5 μ L of sample (~ 0.5 mg/mL polymer) onto carbonformavar-coated copper grids (Ted Paella, Inc.) and letting sit for 5 min; followed by washing with several drops of glass distilled water, staining with 1 % w/w uranyl acetate, and blotting the grid to dryness. Prepared sample grids were then imaged on a Technai G2 Sphera operating at an accelerating voltage of 200 kV. For cryo-EM, see chapter 2 methods.

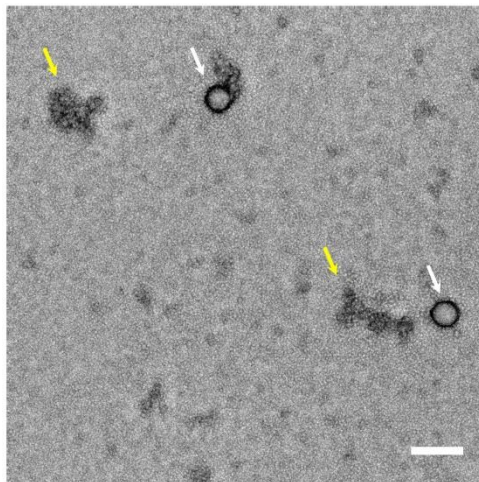


Figure 3.21 Dry-state TEM image of Czw NPs. White arrows indicate larger vesicle structures and yellow arrows indicate particle clusters at high concentrations (1 mg/mL). Scale bar is 200 nm.

3.7.2 Peptide synthesis

Peptides were synthesized using standard Fmoc Solid Phase Peptide Synthesis (SPPS) procedures on an AAPPTec Focus XC automated synthesizer. Peptides were prepared on Rink Amide MBHA (AAPPTec, cat. #RRZ005), Wang-Gly (AAPPTec, cat. #RWG101), or Wang (AAPPTec, cat. #RWZ001) resins. Briefly, Fmoc deprotection was achieved by shaking peptide-bound resin with 20% methylpiperidine/DMF in a plastic chromatography vessel (Bio-rad, cat. #7321010) for 5 minutes, followed by draining, rinsing 1 x with DMF, and then applying fresh methylpiperidine solution for another 10 min. After thorough rinsing with DMF following deprotection steps, amide coupling reactions proceeded for a minimum of 45 minutes using 3 equiv of Fmoc-protected amino acids (AAs), 2.9 equiv of HBTU, and 6 equiv of DIPEA. Fmoc-Lys(Mtt)-OH residues (AAPPTec, cat. #AFK125) (1.5 equiv) were double-coupled (i.e. subjected to two consecutive applications of fresh AA/HBTU/DIPEA solutions) at the first conjugation step. Peptide Monomers were prepared by double-coupling to 1.5 equiv *N*-(hexanoic acid)-cis-5-norbornene-exo-dicarboximide

(prepared via a published protocol) at the N-terminus of the peptide or at a lysine side chain near the C-terminus. (3-Carboxypropyl)trimethylammonium chloride was purchased from Sigma (403245) and double-coupled (1.5 equiv) at the N-terminus of the peptide or at a lysine side chain near the C-terminus. Selective deprotection of methyltrityl (Mtt) protecting groups on resin was afforded by shaking the resin 5 x in TFA/TIPS/DCM (3:5:92 v/v/v) (approximately 6 mL per gram resin) for 7 min each, followed by rinsing with DCM. Full deprotection was confirmed *via* the Kaiser test. Peptides were cleaved from the resin for 1 h using a solution of TFA/Triisopropylsilane (TIPS) /water (95:2.5:2.5 v/v/v). The TFA solution was drained into a conical tube and evaporated. The concentrated peptide solution was then precipitated in cold ether, centrifuged, and the pellet purified by RP-HPLC. The identity and purity of each peptide were verified *via* ESI-MS analysis and the presence of a single peak in the analytical RP-HPLC chromatogram.

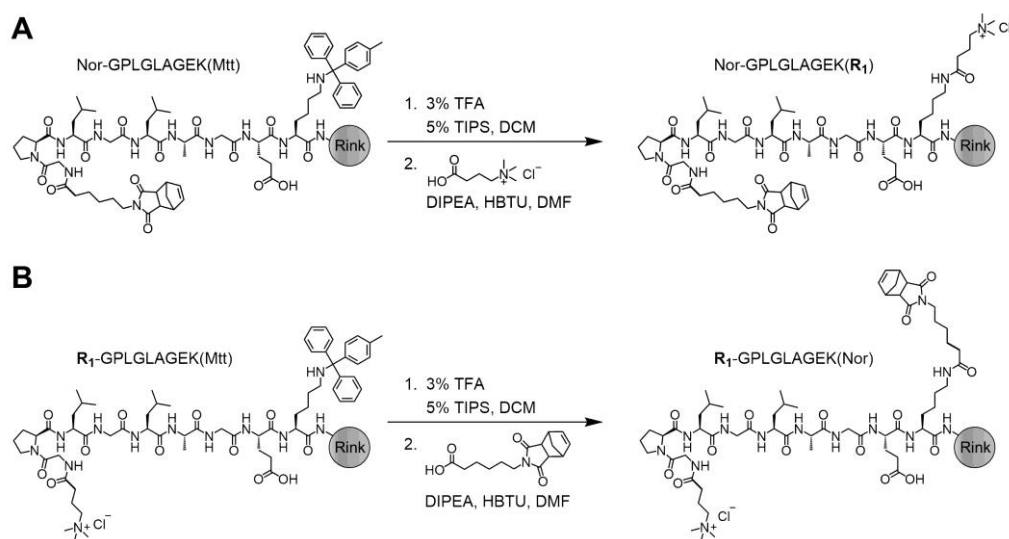


Figure 3.22 Solid phase synthesis of (A) Nzw and (B) Czw monomers using an orthogonal methyltrityl (Mtt) deprotection strategy.

3.7.3 Polymerizations

All polymerizations were performed in a glove box under N₂ (g) using dry, deoxygenated DMF obtained by the freeze-pump-thaw method. An example of a typical procedure is given in chapter 2 methods section. Polymerizations that have not been reported previously in the literature were performed in DMF-d₇ and assessed *via* ¹H-NMR to confirm the complete consumption of monomer and determine the reaction time required for completion. End-functionalization was achieved by adding a fluorescein chain transfer agent (1.5 equiv) for 3 h as described previously⁸⁴ followed by the addition of excess ethyl vinyl ether (EVE) to ensure complete termination. Block copolymers were prepared by polymerizing 40 equiv of the first block (norbornyl-phenyl) to completion, splitting the reaction into six vials, then adding 20 equiv of the second block (appropriate peptide monomer), and finally end-labeling with fluorescein and terminating as described above. Fluorescein-containing polymers were treated with NH₄OH (aq) for 30 min to remove the pivalate protecting groups and subsequently characterized by SEC-MALS in DMF.

Table 3.4 Summary of SEC-MALS characterization of water-soluble homopolymers and amphiphilic block copolymers

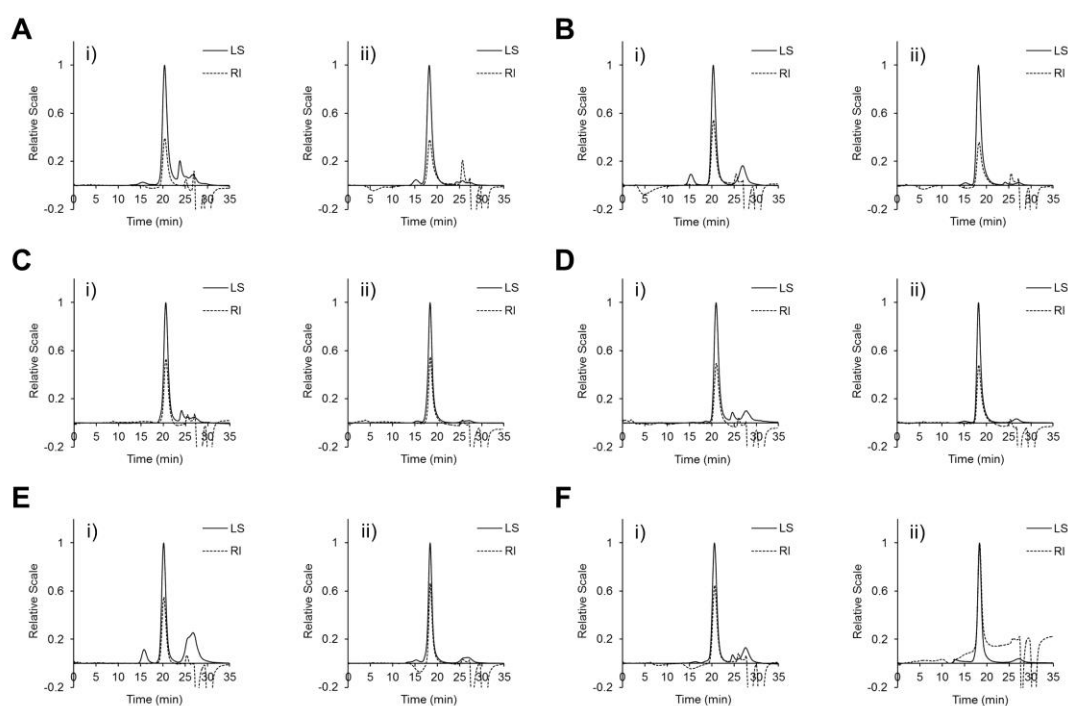
Material Name	IUPAC	DP (m) ^a	DP (n) ^a	M _n ^b	Đ ^c
Nzw, m ~ 25	Nzw ₂₈	28	-	34,220	1.024
Ncat, m ~ 25	Ncat ₂₇	27	-	31,230	1.016
Nan, m ~ 25	Nan ₂₃	23	-	26,430	1.014
Czw, m ~ 25	Czw ₂₃	23	-	27,870	1.013
Ccat, m ~ 25	Ccat ₂₄	24	-	25,890	1.019
Can, m ~ 25	Can ₂₅	25	-	28,270	1.016
Nzw, m ~ 100	Nzw ₁₀₅	105	-	128,300	1.114
Ncat, m ~ 100	Ncat ₁₄₈	148	-	162,900	1.057
Nan, m ~ 100	Nan ₉₅	95	-	108,100	1.052
Czw, m ~ 100	Czw ₁₀₈	108	-	132,500	1.109
Ccat, m ~ 100	Ccat ₁₁₀	110	-	121,100	1.046
Can, m ~ 100	Can ₈₉	89	-	101,100	1.036
Nzw NP	Ph ₄₁ -b-Nzw ₂₆	41 (40)	26 (20)	42,000	1.018
Ncat NP	Ph ₄₁ -b-Ncat ₃₂	41 (40)	32 (20)	45,560	1.046
Nan NP	Ph ₄₁ -b-Nan ₂₅	41 (40)	25 (20)	38,590	1.005
Czw NP	Ph ₄₁ -b-Czw ₁₅	41 (40)	15 (20)	29,280	1.049
Ccat NP	Ph ₄₁ -b-Ccat ₂₇	41 (40)	27 (20)	40,260	1.017
Can NP	Ph ₄₁ -b-Can ₂₃	41 (40)	23 (20)	36,770	1.036

^a Degree of polymerization, m and n refer to the theoretical values for the first block and second block, respectively. ^b Number-average molecular weight. ^c Dispersity (M_w/M_n) of homopolymer or copolymer.

Table 3.5 SEC-MALS characterization of amphiphilic block copolymers (batch 2)

Material Name	IUPAC	DP (m) ^a	DP (n) ^a	M _n ^b	Đ ^c
Nzw NP (batch2)	Ph ₄₇ - <i>b</i> -Nzw ₃₄	47 (40)	34 (20)	53,290	1.013
Ncat NP (batch2)	Ph ₃₉ - <i>b</i> -Ncat ₂₅	39 (40)	25 (20)	37,620	1.023
Nan NP (batch2)	Ph ₄₇ - <i>b</i> -Nan ₃₅	47 (40)	35 (20)	52,070	1.034
Czw NP (batch2)	Ph ₃₉ - <i>b</i> -Czw ₂₇	39 (40)	27 (20)	43,080	1.043
Ccat NP (batch2)	Ph ₃₉ - <i>b</i> -Ccat ₂₇	39 (40)	27 (20)	39,930	1.033
Can NP (batch2)	Ph ₄₇ - <i>b</i> -Can ₂₂	47 (40)	22 (20)	36,470	1.164

^a Degree of polymerization, m and n refer to the theoretical values for the first block and second block, respectively. ^b Number-average molecular weight. ^c Dispersity (M_w/M_n) of homopolymer or copolymer.

**Figure 3.23** Peptide homopolymers of theoretical (i) DP 25 and (ii) DP 100 characterized by SEC-MALS. Light scattering (LS) is indicated by the solid black line and refractive index (RI) is indicated by dotted black line. Chromatograms are presented for (A) Nzw; (B) Czw; (C) Ncat; (D) Ccat; (E) Nan; and (F) Can.

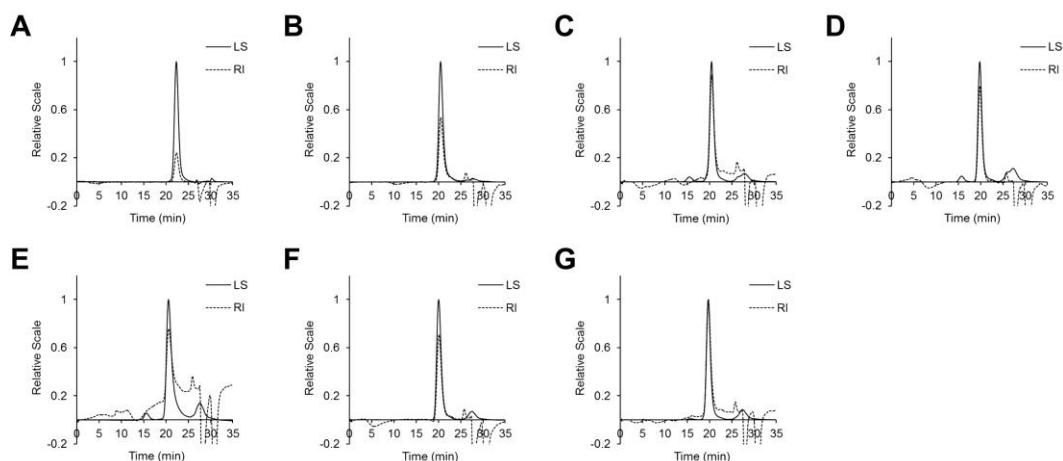


Figure 3.24 Peptide block copolymers characterized by SEC-MALS. Light scattering (LS) is indicated by the solid black line and refractive index (RI) is indicated by dotted black line. Chromatograms are presented for (A) First block, m (Ph), used for all block copolymers; and for copolymers: (B) Ph-*b*-Nzw; (C) Ph-*b*-Ncat; (D) Ph-*b*-Nan; (E) Ph-*b*-Czw; (F) Ph-*b*-Ccat; (G) Ph-*b*-Can.

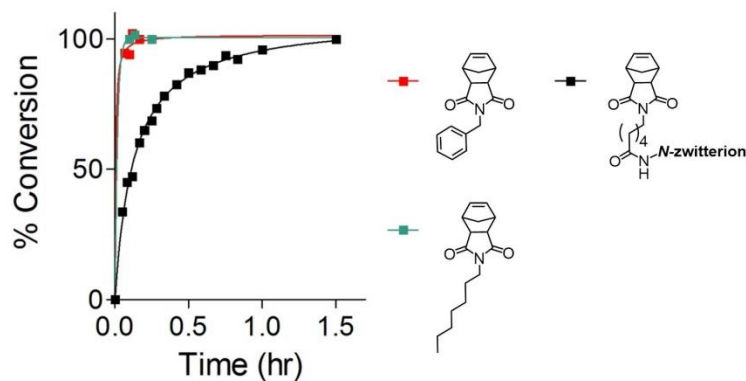


Figure 3.25 Polymerization kinetics of norbornene peptide (Nzw) and hydrophobic monomers measured by $^1\text{H-NMR}$. Data of Nzw was previously shown in chapter 2. Percent conversions are determined from the relative integration of monomer vinyl protons to olefin resonances of the polymer backbone. Note that first-order kinetic profiles could not be generated for C7 or Ph due to the rapid consumption of each monomer within minutes.

Table 3.6 Summary of SEC-MALS characterization and kinetic values for homopolymers

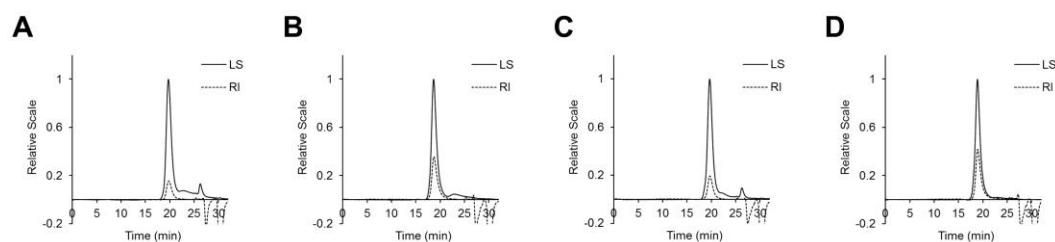
Monomer	$[M]_0/[I]_0$ ^b	M_n ^c	\mathcal{D} ^d	DP ^e	k_p L(mol s) ^f	Completion Time ^g
Nzw ^a	25	42,910	1.016	35	0.9947	90
Ph	20	6,164	1.018	24	-	7
C7	20	3,919	1.028	15	-	6

^a Data reproduced from chapter 2. ^b Monomer to initiator ratio. ^c Number-average molecular weight. ^d Dispersity (M_w/M_n). ^e Degree of polymerization. ^f Rate constant of propagation measured from pseudo-first order plots of the kinetic data. Note that plots could not be generated for C7 or Ph monomers. ^g Length of time required for complete consumption of monomer.

Table 3.7 SEC-MALS characterization of random copolymers

Copolymer	m ^a	n ^a	M_n ^a	M_n ^b	\mathcal{D} ^c
C7 ₃₀ -ran-Nzw ₄₀	30	40	56,904	45,470	1.022
C7 ₆₀ -ran-Nzw ₈₀	60	80	113,807	77,780	1.040
Ph ₃₀ -ran-Nzw ₄₀	30	40	56,661	46,400	1.018
Ph ₆₀ -ran-Nzw ₈₀	60	80	113,323	86,270	1.057

^a Theoretical values of block 1 (m), block 2 (n), and number-average molecular weight. ^b Number-average molecular weight. ^c Dispersity (M_w/M_n).

**Figure 3.26** Random copolymers, synthesized with the N-zwitterionic peptide monomer, characterized by SEC-MALS. Light scattering (LS) is indicated by the solid black line and refractive index (RI) is indicated by dotted black line. Chromatograms are presented for (A) C7-ran-Nzw (~ 45 kDa); (B) C7-ran-Nzw (~ 80 kDa); (C) Ph-ran-Nzw (~ 45 kDa); and (D) Ph-ran-Nzw (~ 80 kDa).

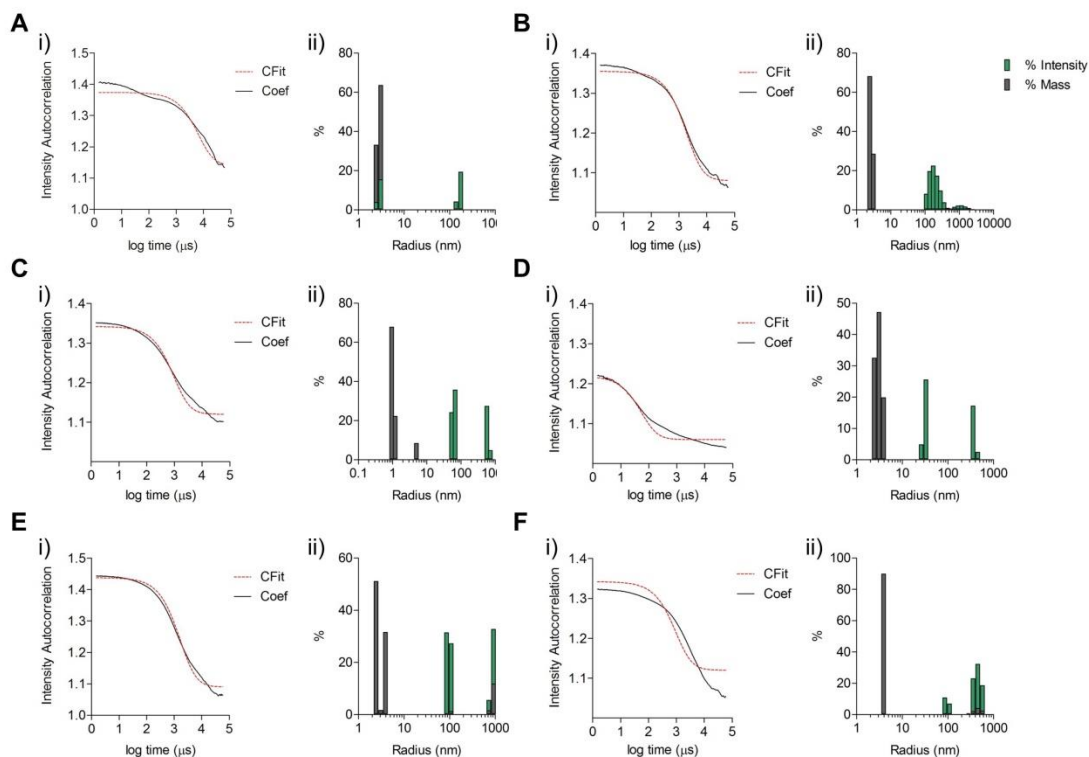


Figure 3.27 Intensity correlation curves (i) from which DLS data (ii) are derived of the DP 25 homopolymers in DPBS. (A) Nzw ($m \sim 25$); (B) Czw ($m \sim 25$); (C) Ncat ($m \sim 25$); (D) Ccat ($m \sim 25$); (E) Nan ($m \sim 25$); and (F) Can ($m \sim 25$). For (i), the exponential decay is related to the diffusion coefficient of the polymer (solid black line) and the fit of the decay is shown by the dotted red line. For (ii), the percent intensity and percent mass are given. Small populations of large species, which scatter more light (likely dust), may contribute to the slow decay functions; further, the lack of smoothness for all curves is indicative of a poor data quality despite increasing acquisition times.

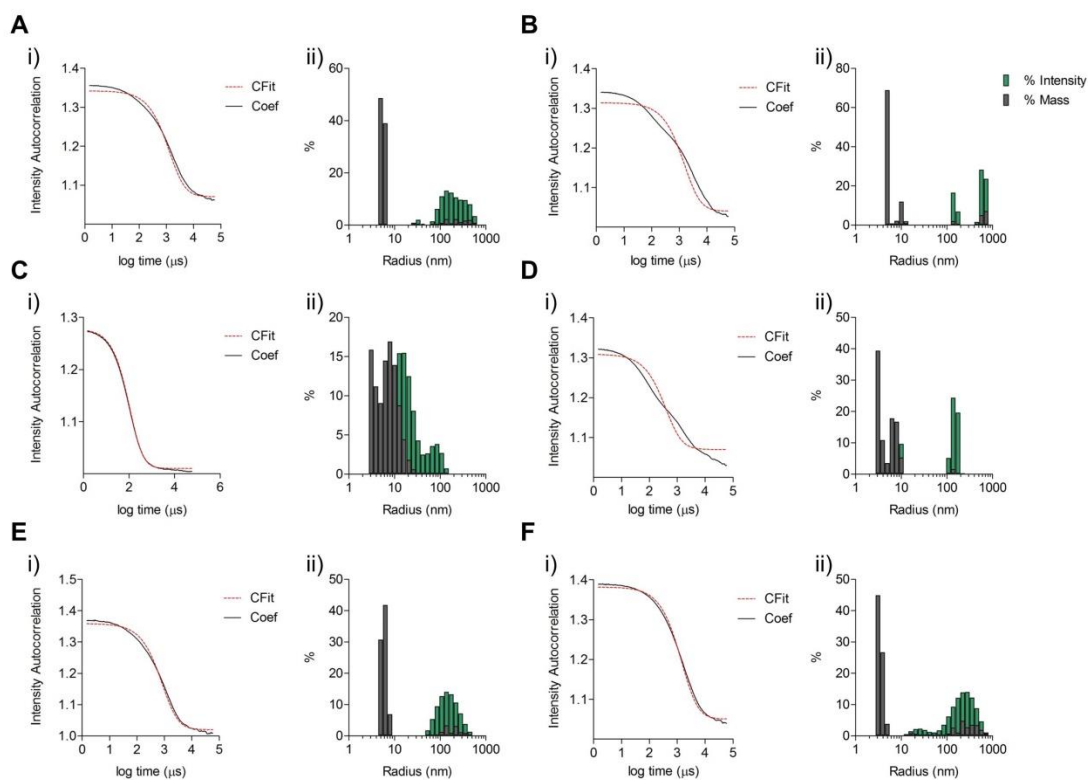


Figure 3.28 Intensity correlation curves (i) from which DLS data (ii) are derived of DP 100 homopolymers in DPBS. (A) Nzw ($m \sim 100$); (B) Czw ($m \sim 100$); (C) Ncat ($m \sim 100$); (D) Ccat ($m \sim 100$); (E) Nan ($m \sim 100$); and (F) Can ($m \sim 100$). For (i), the exponential decay is related to the diffusion coefficient of the polymer (solid black line) and the fit of the decay is shown by the dotted red line. For (ii), the percent intensity and percent mass are given. Small populations of large species (likely dust), which scatter more light, may contribute to the slow decay functions; further, the lack of smoothness for all curves (except for (C)) is indicative of a poor data quality despite increasing acquisition times.

3.7.4 Formulation of polymeric nanoparticles

Block copolymers were dissolved in either DMF, DMSO or acetonitrile. MilliQ water was added dropwise and the solution mixed by hand until 10 % v/v H₂O was reached (1 mg/mL polymer concentration). The solutions were equilibrated for approximately 3 h prior to dialysis. The solutions were transferred to a 3500 MWCO snakeskin dialysis tube and dialyzed against 1 L of MilliQ H₂O. The water was refreshed after 8 h. This process was repeated once more and the milky suspensions were removed and concentrated using a 10,000 MWCO centrifugal filter (Millipore). A few aliquots were removed and lyophilized in

tared vials. These lyophilized aliquots were used to generate standard curves of the material, from which the solution stocks were measured to determine concentration of polymer.

3.7.5 Concentration determination of polymeric nanoparticles

Standard curves of polymers were generated using 10 % H₂O in DMF solvent conditions. First, DMF was added to lyophilized polymers and then H₂O was added slowly to ensure the polymers would remain in solution. Absorbance was measured at 260 nm and subtracted from background absorbance at ~570 nm. A set of three solutions were prepared and measured, then averaged to yield the standard curves. Standard deviation is plotted. The concentration of stock solutions was determined by dissolving an aliquot into DMF to yield a sample solution (10 % v/v H₂O), then measuring the absorbance at 260 nm.

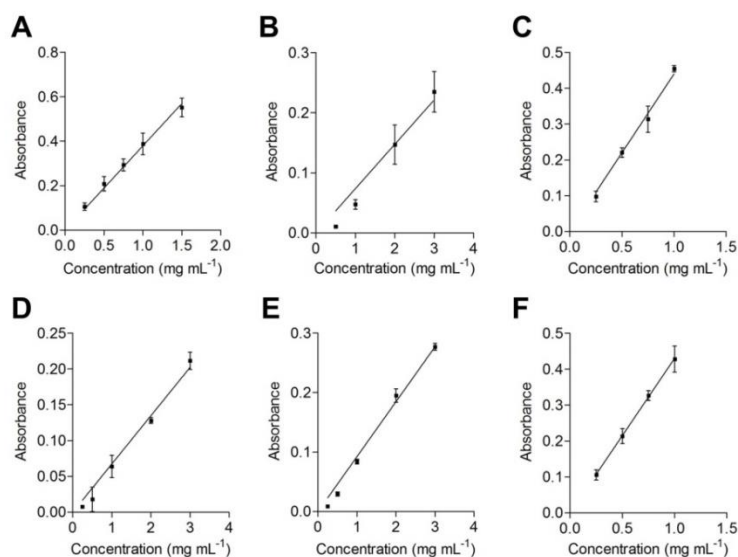


Figure 3.29 Standard curves generated by measuring absorbance at 260 nm for spherical NPs formulated from block copolymers dissolved in 10% H₂O in DMF. Curves are shown for: (A) Nzw NP, slope = 0.3798 (mg/mL)⁻¹; (B) Ncat NP, slope = 0.07381 (mg/mL)⁻¹; (C) Nan NP, slope = 0.4403 (mg/mL)⁻¹; (D) Czw NP, slope = 0.06745 (mg/mL)⁻¹; (E) Ccat NP, slope = 0.09236 (mg/mL)⁻¹; and (F) Can NP, slope = 0.4302 (mg/mL)⁻¹. Note that curves were generated using either a NanoDrop or UV Spectrometer.

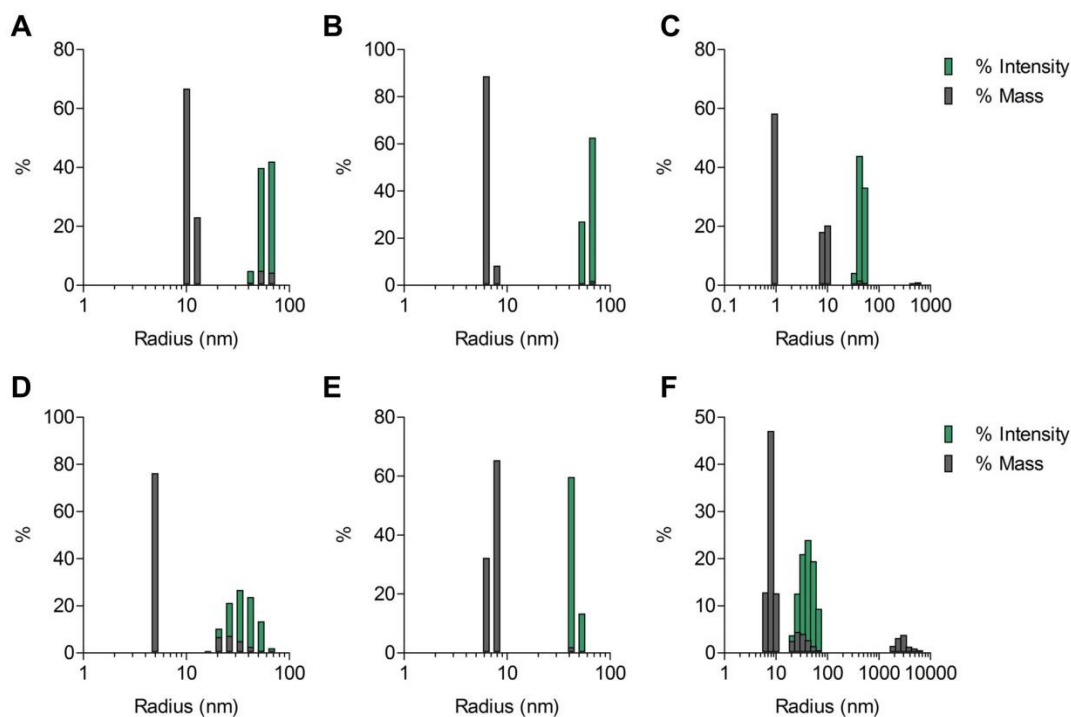


Figure 3.30 Dynamic light scattering (DLS) plots of block copolymers formulated into nanoparticles (NPs) in DPBS. Percent intensity and percent mass are plotted for: (A) Nzw NP, (B) Ncat NP, (C) Nan NP, (D) Czw NP, (E) Ccat NP, and (F) Can NP. Hydrodynamic diameters for the largest population contributing to mass are reported in Table 3.2. Note that small contributions from larger species for are likely due to dust.

3.7.6 Cell culture

RAW 264.7 cells were purchased from ATCC (TIB-71) or received as a gift from the Yeo lab at the Sanford Consortium. Cells were cultured at 37 °C under 5 % CO₂ in phenol red-containing Dulbecco's Modified Eagle Medium (DMEM; Gibco Life Tech., cat. #11960-044) supplemented with 10 % heat-inactivated fetal bovine serum (Omega scientific, cat. #FB02) and with 1x concentrations of nonessential amino acids (Gibco Life Tech., cat. #11140-050), sodium pyruvate (Gibco Life Tech., cat. #11360-070), L-glutamine (Gibco Life Tech., cat. #35050-061), and the antibiotics penicillin/streptomycin (Corning Cellgro, cat. #30-002-C1). Cells were subcultured in T-75 flasks at 70-80% confluency every 3–4 days.

Experiments were performed using low cell passage numbers (less than 20) and strongly adherent cells were lifted using a cell scraper in order to discourage genetic drift.

3.7.7 Analysis of cellular uptake in RAW264.7 cells by flow cytometry

RAW 264.7 cells were seeded on 24-well plates at a density of 200,000 cells per well and allowed to adhere for 24 h. Materials were dissolved in Dulbecco's Phosphate Buffered Saline (DPBS; Corning Cellgro, cat. #21-031-CM) at 10 x the desired concentration and diluted in DMEM and added to the wells. Two technical replicates (three total wells) were performed for each treatment. The cells were then incubated for 3 h at 37 °C. The medium was removed and the cells were washed 3 x with DPBS (0.5 mL). For cells treated with thermolysin-incubated materials, the medium was removed and the cells were washed 2 x with DPBS (0.5 mL), incubated 3 x for 5 min with 0.35 mL heparin (0.5 mg/mL in DPBS; Affymetrix, cat. #16920) and finally rinsed with DPBS (0.5 mL). The cells were trypsinized (0.25 mL of 0.25% trypsin with EDTA; GIBCO Life Tech., cat. #15090-046) for 15 min. The trypsin solution was pipetted up and down several times to dislodge the cells and transferred to Eppendorf tubes. Fresh DMEM (0.45 mL) was added to the wells to collect any remaining cells and transferred to the Eppendorf tubes. Finally, DPBS (0.7 mL) was added to the tubes, and the suspensions were centrifuged. After aspirating the supernatant, cell pellets were suspended in 60 µL DPBS and stored on ice prior to flow cytometry measurements. Fluorescence activated cell sorting (FACS) data (10,000 events on three separate cell cultures) were acquired on an Accuri C6 flow cytometer set to default "3 blue 1 red" configuration with standard optics and slow fluidics (14 µL/min). For proteolysis studies, materials (10 µM with respect to polymer concentration) were pre-treated with 0.3 µM Thermolysin for approximately 15 h at 37 °C in Tris cleavage buffer, after which 25 µL of the sample was injected onto RP-HPLC for analysis. Cells were incubated and prepared for

flow cytometry analysis as described above. Data are reported as the normalized mean fluorescence, which is the ratio of mean fluorescence intensity of cells treated with material to cells treated with vehicle (DPBS). Data were analyzed using FlowJo software. Experiments were performed three times on at least three separate subcultures. Standard error is plotted for all experiments.

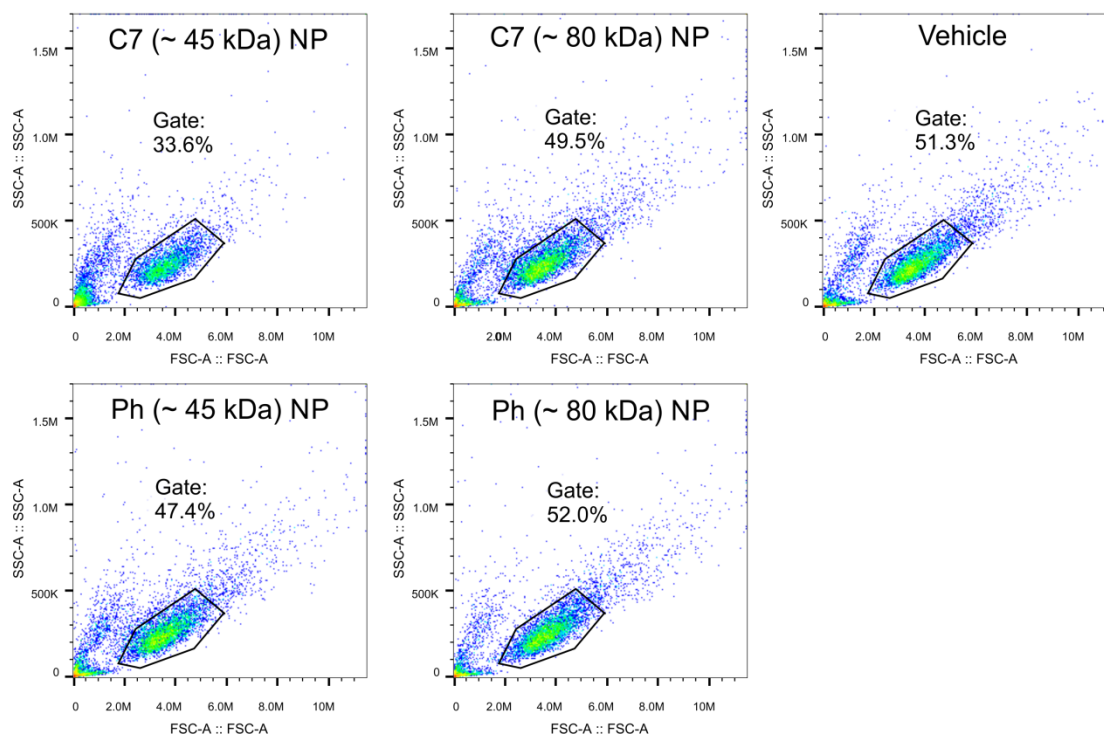


Figure 3.31 Representative gating for spherical NPs formulated from random copolymers. Samples were measured by flow cytometry (10,000 events were measured) and each sample was gated using the vehicle control (DPBS).

3.7.8 Mechanistic studies by flow cytometry

For mechanistic studies, cells were plated and treated as described in the flow cytometry experiments. For studies at reduced temperature, cells were incubated at 4 °C immediately following the addition of the treatment and during incubation. For studies without FBS, cells were treated with material dissolved in DMEM supplemented with all the components as described except for heat inactivated FBS. For studies in competent FBS, cells

were treated with material dissolved in DMEM supplemented with all the components as described except heat inactivated FBS was replaced with non-heat inactivated FBS (Omega, FB-01). Data is reported as the normalized mean fluorescence, as described in the previous section. Experiments were performed three times on at least three separate subcultures. Standard error is plotted for all experiments.

3.7.9 Live cell confocal microscopy

RAW 264.7 cells were plated on glass-bottom 24-well plates at a density of 200,000 cells per well and allowed to adhere for 24 h. The medium was removed and cells were washed 1x with DPBS (1 mL). Materials dissolved in DPBS (at 10x the desired concentration) were diluted with DMEM lacking phenol red (0.5 mL) and added to the wells. Cells were incubated for 3 h at 37 °C. The washing procedure used in the flow cytometry experiments (3 x DPBS) for materials or (2 x DPBS, 3 x heparin for 5 min ea, 1 x DPBS) was used for thermolysin-treated materials. Fresh media lacking phenol red (0.5 mL) was then added to each well. Live cells were imaged on an Olympus FV1000 confocal microscope using 40x, 60x or 100x objective. For proteolysis studies, materials were prepared according to the enzyme treatment protocol.

3.7.10 Enzyme-treatment of materials prior to cell incubation

For proteolysis studies, materials at 1 μM (with respect to polymer) were pretreated with 0.3 μM of Thermolysin at 37 °C for 15 - 18 h in Tris cleavage buffer, after which the protease was chemically denatured with 10 % v/v 0.5 mM EDTA and immediately used for cell experiments. Controls were prepared by incubating the materials in Tris buffer containing 10 % v/v mM EDTA and denatured Thermolysin. Aliquots of the reaction were removed and analyzed on RP-HPLC for the identification of peptide cleavage fragments. Comparison of

the cleavage fragment peak areas to standard curves of the authentic peptide fragment were used to calculate percent cleavage.

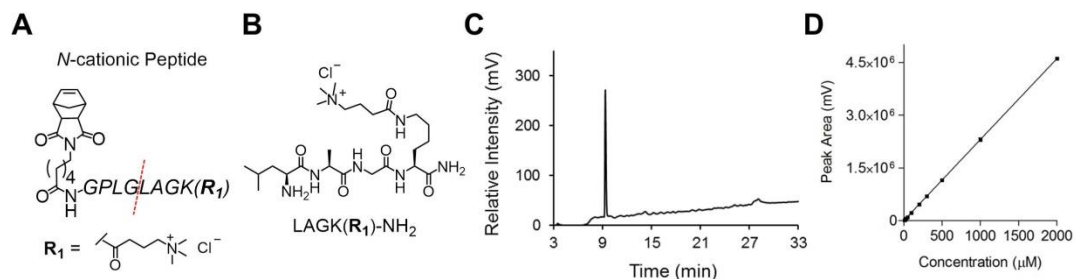


Figure 3.32 Standard curve of the synthesized, authentic *N*-cationic (Ncat) peptide cleavage fragment ($LAGK(R_1)$). (A) Chemical structure of Ncat peptide monomer depicting the thermolysin cleavage site (dotted red line). (B) Chemical structure of $LAGK(R_1)$. (C) RP-HPLC chromatogram of purified $LAGK(R_1)$. (D) Standard curve generated of $LAGK(R_1)$ using measured peak areas following absorbance at 214 nm.

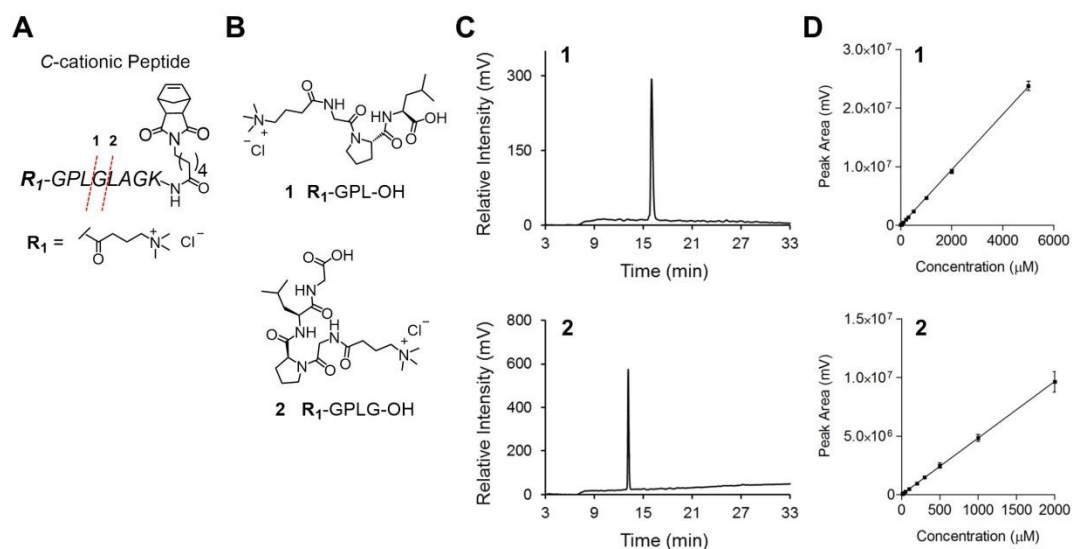


Figure 3.33 Standard curve of the synthesized, authentic *C*-cationic peptide cleavage fragments (R_1-GPL , **1**, and R_1-GPLG , **2**). (A) Chemical structure of *C*-cationic peptide monomer depicting the two Thermolysin cleavage sites (dotted red lines). (B) Chemical structures of **1** and **2**. (C) RP-HPLC chromatograms of purified **1** and **2**. (D) Standard curves generated of **1** and **2** using measured peak areas following absorbance at 214 nm.

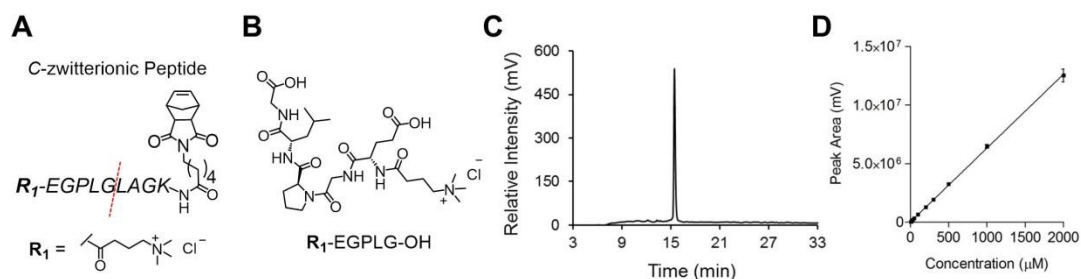


Figure 3.34 Standard curve of the synthesized, authentic C-zwitterionic peptide cleavage fragment (R_1 -EGPLG). (A) Chemical structure of C-zwitterionic peptide monomer depicting the Thermolysin cleavage site (dotted red line). (B) Chemical structure of R_1 -EGPLG. (C) RP-HPLC chromatogram of purified R_1 -EGPLG. (D) Standard curve generated of R_1 -EGPLG using measured peak areas following absorbance at 214 nm.

Table 3.8 Summary of RP-HPLC and ESI characterization for authentic peptide cleavage fragments

Monomer	Cleavage Frag	Gradient (30 min)	RT (min)	Mass calcd	Mass obs ^a	Slope (μ M ⁻¹)
Ncat	LAGK(R_1)-NH ₂	2 – 50 % B	9.4	514.37	514.6	2304
Ccat	R_1 -GPL-OH	2 – 50 % B	16.0	413.28	413.42	4727
	R_1 -GPLG-OH	2 – 50 % B	13.2	470.30	470.6	4829
Czw	R_1 -EGPLG-OH	2 – 50 % B	15.5	599.34	599.50	6310

^a Measured by ESI-MS

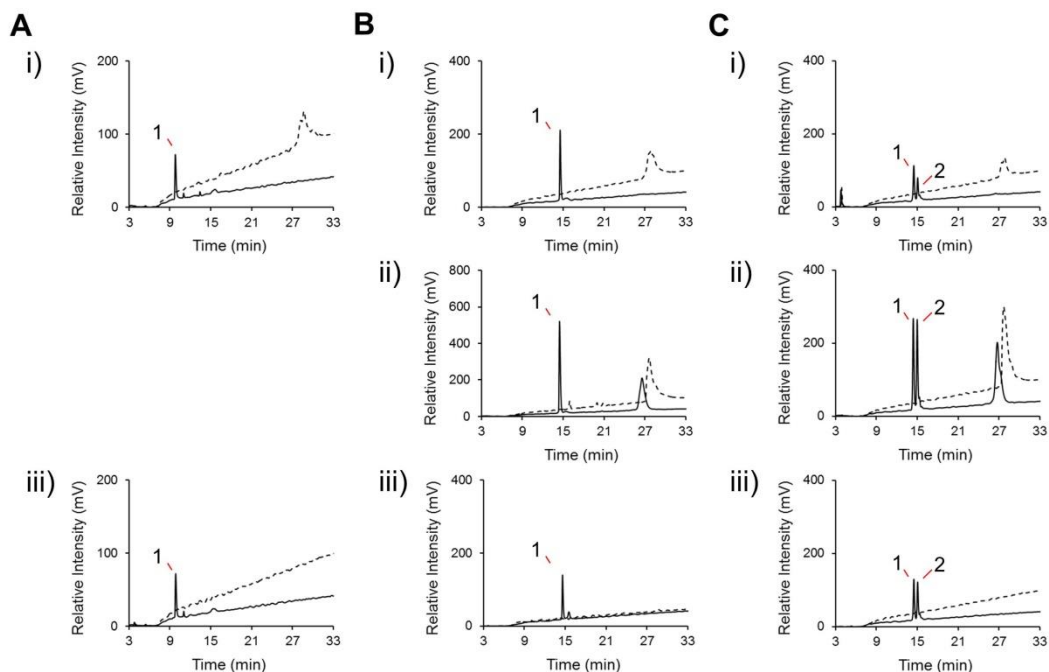


Figure 3.35 Representative RP-HPLC traces of materials prior to thermolysin treatment (dotted line) and after treatment (solid line) with thermolysin for 15 h. The materials tested consisted of polymers of theoretical (i) DP 25 and (ii) DP 100; as well as (iii) spherical NPs. The areas of numbered peaks, which correspond to cleaved peptide fragments, were used to analyze peptide substrate consumption. Gradient used for all samples: 2-50 % B over 30 min. RP-HPLC chromatograms are given for (A) Ncat; (B) Czw; and (C) Ccat materials.

Table 3.9 Characterization of peptide cleavage fragments from materials incubated with thermolysin^a

Substrate	Peak	Gradient (30 min)	Peak RT (min)	Mass calcd	Mass obs ^a	Product identity
Ncat	1	2 – 50 % B	11	514.37	514.37	LAGK(R ₁)-NH ₂
Ccat	1	2 – 50 % B	15.1	413.28	413.46	R ₁ -GPL-OH
	2	2 – 50 % B	16	470.30	470.43	R ₁ -GPLG-OH
Czw	1	2 – 50 % B	14.8	599.34	598.50	R ₁ -EGPLG-OH

^a Identification of RP-HPLC peaks shown in RP-chromatograms of thermolysin reactions.

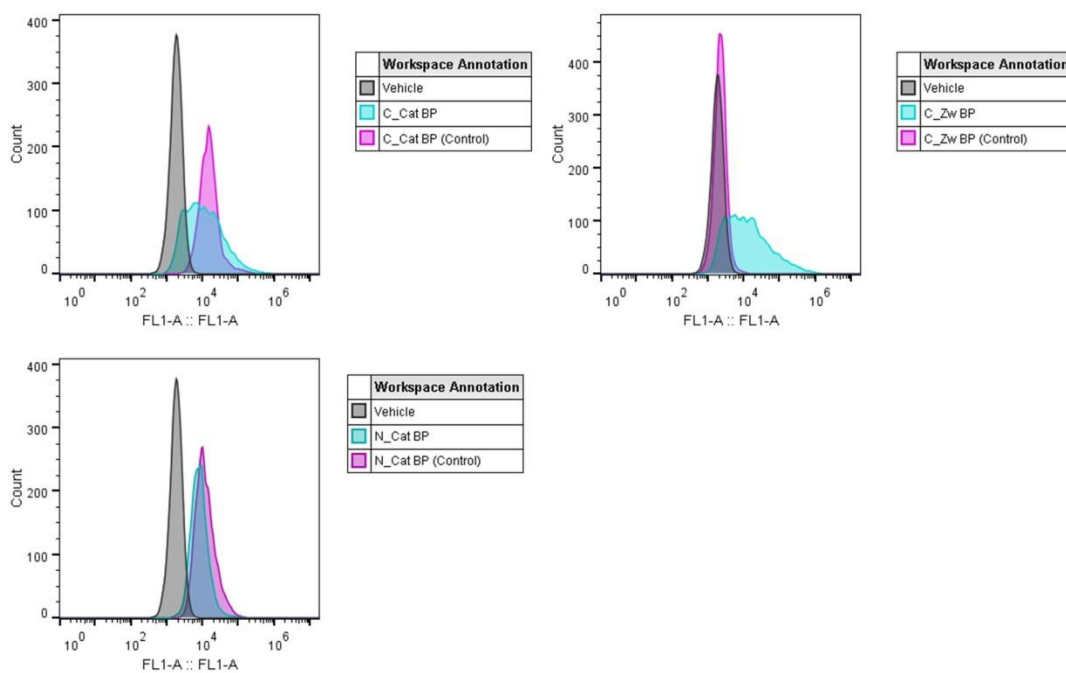


Figure 3.36 Example histograms from flow cytometry analysis of enzyme-treated and control experiments with Ncat, Ccat, and Czw NPs. Healthy populations were gated identically and referenced to the vehicle control. 10,000 counts were acquired.

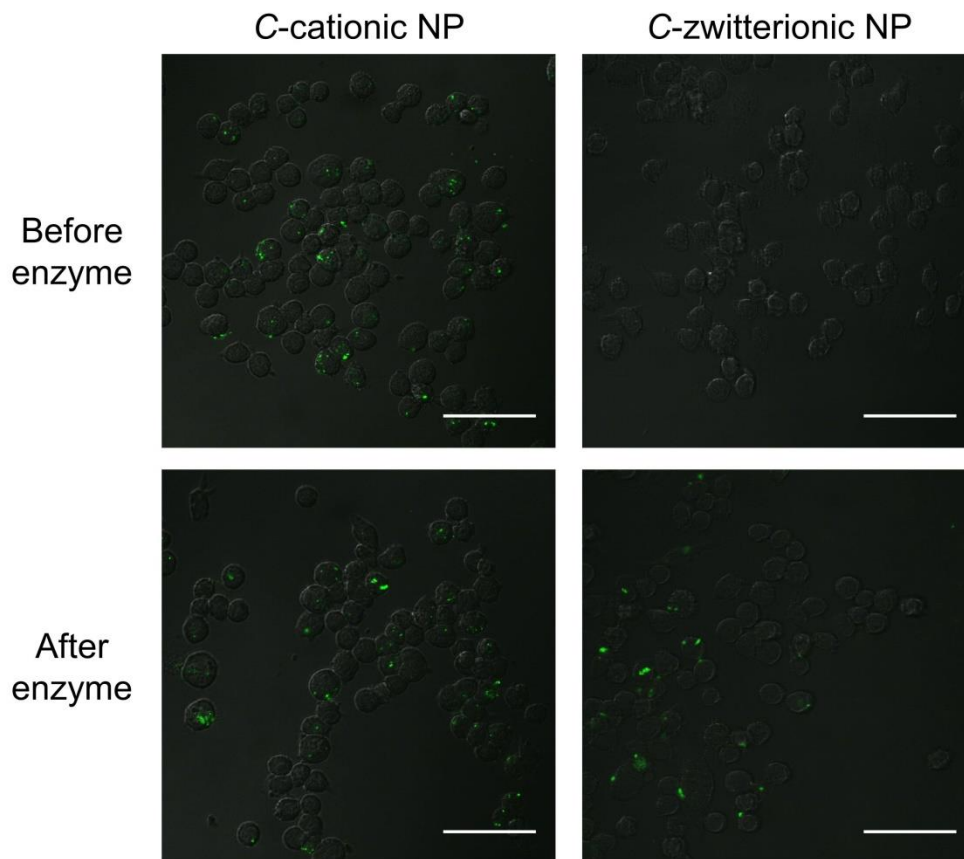


Figure 3.37 Merged bright field and epifluorescence channels. Z-stack Live cell confocal microscopy of RAW 264.7 cells incubated with Ccat and Czw NPs before and after thermolysin treatment. Ccat and Czw NPs were incubated with thermolysin for 15 h prior to incubation with cells. Scale bars are 50 μm .

3.7.11 Cell viability assay

The CellTiter-Blue fluorescent assay (Promega, cat. #G8081) measures the ability of viable cells to reduce resazurin into a fluorescent product, resarufin. RAW 264.7 cells were plated at a density of 35,000 cells per well of a 96-well plate and allowed to adhere for 24 h. Materials dissolved in DPBS were diluted in DMEM (at a final concentration of 1 μM with respect to polymer) and added to the wells along with a positive control (10% DMSO). Cells were incubated for 24 h at 37 $^{\circ}\text{C}$. The medium was removed and cells were washed 1 x with DPBS (150 μL). Fresh media (100 μL) without phenol red was added followed by 20 μL of

the CellTiter-Blue reagent. Cells were incubated for 3 h prior to measuring fluorescence on a plate reader using 560 nm excitation and 590 nm emission wavelengths. Fluorescence measurements were corrected for background fluorescence of the CellTiter-Blue reagent by subtracting the values of wells containing the reagent in media in the absence of cells. Percent viability was then calculated as:

$$\% \text{ viable} = \frac{\text{Mean Fluorescence of cells treated with material}}{\text{Mean Fluorescence of cells treated with DPBS}} \times 100$$

At least two technical replicates were performed for each treatment. For all cell experiments, 10 % DMSO control yielded approximately 0 % cell viability.

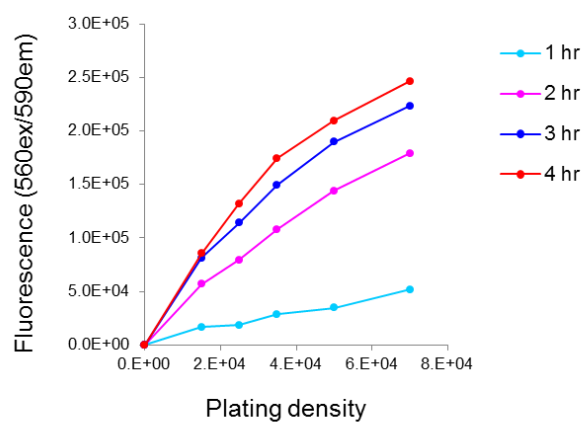


Figure 3.38 Optimization of RAW 264.7 cell plating density and incubation time with CellTiter Blue.

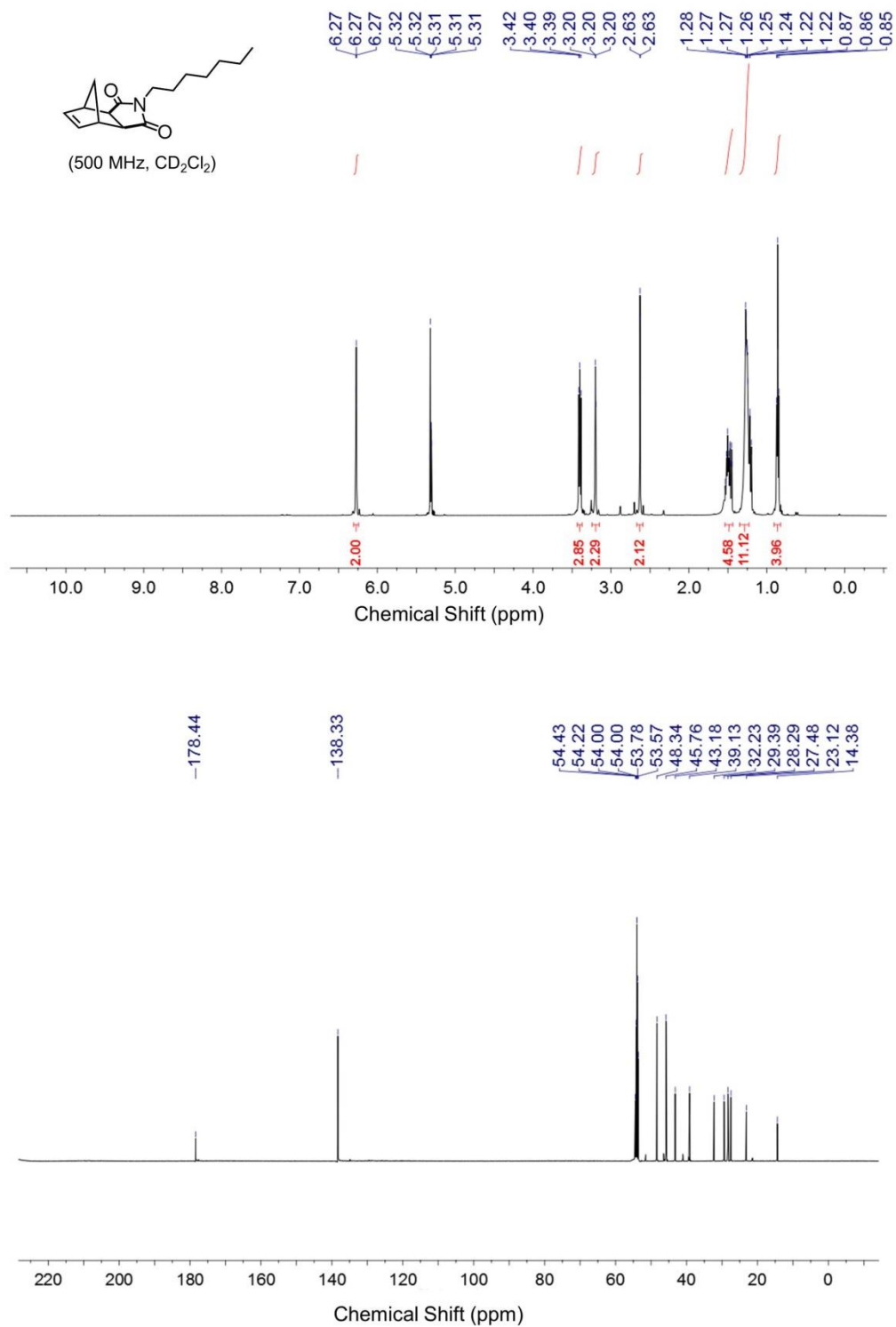


Figure 3.39 ¹H and ¹³C NMR Spectrum of C7 Monomer.

3.8 References

- (1) Owens Iii, D. E.; Peppas, N. A.; Owens, D. E.; Peppas, N. A. *Int. J. Pharm.* **2006**, *307* (1), 93.
- (2) Frank, M. M.; Fries, L. F. *Immunol. Today* **1991**, *12* (9), 322.
- (3) Gustafson, H. H.; Holt-Casper, D.; Grainger, D. W.; Ghandehari, H. *Nano Today* **2015**, *10* (4), 487.
- (4) He, C.; Hu, Y.; Yin, L.; Tang, C.; Yin, C. *Biomaterials* **2010**, *31* (13), 3657.
- (5) Green, A. E.; Rose, P. G. *Int. J. Nanomedicine* **2006**, *1* (3), 229.
- (6) Szebeni, J.; Alving, C. R.; Rosivall, L.; Bünger, R.; Baranyi, L.; Bedöcs, P.; Tóth, M.; Barenholz, Y. *J. Liposome Res.* **2007**, *17* (2), 107.
- (7) Walkey, C. D.; Olsen, J. B.; Guo, H.; Emili, A.; Chan, W. C. W. *J. Am. Chem. Soc.* **2011**, *134* (4), 2139.
- (8) Zahr, A. S.; Davis, C. A.; Pishko, M. V. *Langmuir* **2006**, *22* (19), 8178.
- (9) Ernsting, M. J.; Murakami, M.; Roy, A.; Li, S.-D. *J. Control. Release* **2013**, *172* (3), 782.
- (10) Wang, D.; Phan, N.; Isely, C.; Bruene, L.; Bratlie, K. M. *Biomacromolecules* **2014**, *15* (11), 4102.
- (11) Bai, Y.; Xing, H.; Wu, P.; Feng, X.; Hwang, K.; Lee, J. M.; Phang, X. Y.; Lu, Y.; Zimmerman, S. C. *ACS Nano* **2015**, *9* (10), 10227.
- (12) Sharma, G.; Valenta, D. T.; Altman, Y.; Harvey, S.; Xie, H.; Mitragotri, S.; Smith, J. W. *J. Control. Release* **2010**, *147* (3), 408.
- (13) Geng, Y.; Dalhaimer, P.; Cai, S.; Tsai, R.; Tewari, M.; Minko, T.; Discher, D. E. *Nat. Nanotechnol.* **2007**, *2* (4), 249.
- (14) Herd, H.; Daum, N.; Jones, A. T.; Huwer, H.; Ghandehari, H.; Lehr, C.-M. *ACS Nano* **2013**, *7* (3), 1961.
- (15) Townson, J. L.; Lin, Y.-S.; Agola, J. O.; Carnes, E. C.; Leong, H. S.; Lewis, J. D.; Haynes, C. L.; Brinker, C. J. *J. Am. Chem. Soc.* **2013**, *135* (43), 16030.
- (16) Pedersen, M. B.; Zhou, X.; Larsen, E. K. U.; Sorensen, U. S.; Kjems, J.; Nygaard, J. V.; Nyengaard, J. R.; Meyer, R. L.; Boesen, T.; Vorup-Jensen, T. *J. Immunol.* **2010**, *184* (4), 1931.

- (17) Massignani, M.; LoPresti, C.; Blanazs, A.; Madsen, J.; Armes, S. P.; Lewis, A. L.; Battaglia, G. *Small* **2009**, *5* (21), 2424.
- (18) LoPresti, C.; Massignani, M.; Fernyhough, C.; Blanazs, A.; Ryan, A. J.; Madsen, J.; Warren, N. J.; Armes, S. P.; Lewis, A. L.; Chirasatitsin, S.; Engler, A. J.; Battaglia, G. *ACS Nano* **2011**, *5* (3), 1775.
- (19) Gao, Y.; Yu, Y. *Langmuir* **2015**, *31* (9), 2833.
- (20) Yang, Q.; Jones, S. W.; Parker, C. L.; Zamboni, W. C.; Bear, J. E.; Lai, S. K. *Mol. Pharm.* **2014**, *11* (4), 1250.
- (21) Kah, J. C. Y.; Wong, K. Y.; Neoh, K. G.; Song, J. H.; Fu, J. W. P.; Mhaisalkar, S.; Olivo, M.; Sheppard, C. J. R. *J. Drug Target.* **2009**, *17* (3), 181.
- (22) Parrott, M. C.; DeSimone, J. M. *Nat. Chem.* **2012**, *4* (1), 13.
- (23) Keefe, A. J.; Jiang, S. *Nat Chem* **2012**, *4* (1), 59.
- (24) Pelegri-O'Day, E. M.; Lin, E.-W.; Maynard, H. D. *J. Am. Chem. Soc.* **2014**, *136* (41), 14323.
- (25) Liu, J.; Yu, M.; Ning, X.; Zhou, C.; Yang, S.; Zheng, J. *Angew. Chemie* **2013**, *125* (48), 12804.
- (26) Larson, T. A.; Joshi, P. P.; Sokolov, K. *ACS Nano* **2012**, *6* (10), 9182.
- (27) Jiang, Y.; Huo, S.; Mizuhara, T.; Das, R.; Lee, Y.-W.; Hou, S.; Moyano, D. F.; Duncan, B.; Liang, X.-J.; Rotello, V. M. *ACS Nano* **2015**, *9* (10), 9986.
- (28) Elci, S. G.; Jiang, Y.; Yan, B.; Kim, S. T.; Saha, K.; Moyano, D. F.; Yesilbag Tonga, G.; Jackson, L. C.; Rotello, V. M.; Vachet, R. W. *ACS Nano* **2016**, *10* (5), 5536.
- (29) Cheng, X.; Tian, X.; Wu, A.; Li, J.; Tian, J.; Chong, Y.; Chai, Z.; Zhao, Y.; Chen, C.; Ge, C. *ACS Appl. Mater. Interfaces* **2015**, *7* (37), 20568.
- (30) Yang, W.; Zhang, L.; Wang, S.; White, A. D.; Jiang, S. *Biomaterials* **2009**, *30* (29), 5617.
- (31) Jabłońska-Trypuć, A.; Matejczyk, M.; Rosochacki, S. *J. Enzyme Inhib. Med. Chem.* **2016**, *1*.
- (32) Kessenbrock, K.; Plaks, V.; Werb, Z. *Cell* **2010**, *141* (1), 52.
- (33) Johnsen, M.; Lund, L. R.; Rømer, J.; Almholt, K.; Danø, K. *Curr. Opin. Cell Biol.* **1998**, *10* (5), 667.
- (34) van den Burg, B.; Eijssink, V. In *Handbook of Proteolytic Enzymes*; 2013; pp 540–553.

- (35) Blum, A. P.; Kammeyer, J. K.; Yin, J.; Crystal, D. T.; Rush, A. M.; Gilson, M. K.; Gianneschi, N. C. *J. Am. Chem. Soc.* **2014**, *136* (43), 15422.
- (36) Colak, S.; Tew, G. N. *Langmuir* **2012**, *28* (1), 666.
- (37) Lowe, A. B.; McCormick, C. L. *Chem. Rev.* **2002**, *102* (11), 4177.
- (38) Miller, C. R.; Bondurant, B.; McLean, S. D.; McGovern, K. A.; O'Brien, D. F. *Biochemistry* **1998**, *37* (37), 12875.
- (39) Yuan, Y.-Y.; Mao, C.-Q.; Du, X.-J.; Du, J.-Z.; Wang, F.; Wang, J. *Adv. Mater.* **2012**, *24* (40), 5476.
- (40) Verma, A.; Stellacci, F. *Small* **2010**, *6* (1), 12.
- (41) Richard, J. P.; Melikov, K.; Vives, E.; Ramos, C.; Verbeure, B.; Gait, M. J.; Chernomordik, L. V.; Lebleu, B. *J. Biol. Chem.* **2003**, *278* (1), 585.
- (42) Lundberg, M.; Wikström, S.; Johansson, M. *Mol. Ther.* **2003**, *8* (1), 143.
- (43) Song, L.; Hennink, E. J.; Young, I. T.; Tanke, H. J. *Biophys. J.* **1995**, *68* (6), 2588.
- (44) *Handbook Of Biological Confocal Microscopy*; Pawley, J. B., Ed.; Springer US: Boston, MA, 2006.
- (45) Silverstein, S. C.; Steinman, R. M.; Cohn, Z. A. *Annu. Rev. Biochem.* **1977**, *46* (1), 669.
- (46) Schmid, S. L.; Carter, L. L. *J. Cell Biol.* **1990**, *111* (6 Pt 1), 2307.
- (47) Ivanov, A. I. *Methods Mol. Biol.* **2008**, *440*, 15.
- (48) Schöttler, S.; Landfester, K.; Mailänder, V. *Angew. Chemie Int. Ed.* **2016**, *55* (31), 8806.
- (49) Yan, Y.; Gause, K. T.; Kamphuis, M. M. J.; Ang, C.-S.; O'Brien-Simpson, N. M.; Lenzo, J. C.; Reynolds, E. C.; Nice, E. C.; Caruso, F. *ACS Nano* **2013**, *7* (12), 10960.
- (50) Mirshafiee, V.; Kim, R.; Park, S.; Mahmoudi, M.; Kraft, M. L. *Biomaterials* **2016**, *75*, 295.
- (51) Hamad, I.; Al-Hanbali, O.; Hunter, A. C.; Rutt, K. J.; Andresen, T. L.; Moghimi, S. M. *ACS Nano* **2010**, *4* (11), 6629.
- (52) Mosqueira, V. C. F.; Legrand, P.; Gulik, A.; Bourdon, O.; Gref, R.; Labarre, D.; Barratt, G. *Biomaterials* **2001**, *22* (22), 2967.
- (53) Moghimi, S. M.; Andersen, A. J.; Ahmadvand, D.; Wibroe, P. P.; Andresen, T. L.; Hunter, A. C. *Adv. Drug Deliv. Rev.* **2011**, *63* (12), 1000.

- (54) Moyano, D. F.; Saha, K.; Prakash, G.; Yan, B.; Kong, H.; Yazdani, M.; Rotello, V. M. *ACS Nano* **2014**, *8* (7), 6748.
- (55) Rogers, W. J.; Basu, P. *Atherosclerosis* **2005**, *178* (1), 67.
- (56) Clift, M. J. D.; Bhattacharjee, S.; Brown, D. M.; Stone, V. *Toxicol. Lett.* **2010**, *198* (3), 358.
- (57) Lunov, O.; Syrovets, T.; Loos, C.; Beil, J.; Delacher, M.; Tron, K.; Nienhaus, G. U.; Musyanovych, A.; Mailänder, V.; Landfester, K.; Simmet, T. *ACS Nano* **2011**, *5* (3), 1657.
- (58) Smith, P. J.; Giroud, M.; Wiggins, H. L.; Gower, F.; Thorley, J. A.; Stolpe, B.; Mazzolini, J.; Dyson, R. J.; Rappoport, J. Z. *Int. J. Nanomedicine* **2012**, *7*, 2045.
- (59) Fröhlich, E. *Int. J. Nanomedicine* **2012**, *7*, 5577.
- (60) Bode, S. A.; Hansen, M. B.; Oerlemans, R. A. J. F.; van Hest, J. C. M.; Löwik, D. W. P. M. *Bioconjug. Chem.* **2015**, *26* (5), 850.
- (61) Shin, W. S.; Han, J.; Verwilst, P.; Kumar, R.; Kim, J.-H.; Kim, J. S. *Bioconjug. Chem.* **2016**, *27* (5), 1419.
- (62) Barbieri, S.; Sonvico, F.; Como, C.; Colombo, G.; Zani, F.; Buttini, F.; Bettini, R.; Rossi, A.; Colombo, P. J. *Control. Release* **2013**, *167* (3), 276.
- (63) Ku, T.-H.; Chien, M.-P.; Thompson, M. P.; Sinkovits, R. S.; Olson, N. H.; Baker, T. S.; Gianneschi, N. C. *J. Am. Chem. Soc.* **2011**, *133* (22), 8392.
- (64) Champion, J. A.; Walker, A.; Mitragotri, S. *Pharm. Res.* **2008**, *25* (8), 1815.
- (65) Hahn, M. E.; Randolph, L. M.; Adamiak, L.; Thompson, M. P.; Gianneschi, N. C. *Chem. Commun.* **2013**, *49* (28), 2873.
- (66) Blum, A. P.; Kammeyer, J. K.; Gianneschi, N. C. *Chem. Sci.* **2016**, *7* (2), 989.
- (67) Chien, M.-P.; Carlini, A. S.; Hu, D.; Barback, C. V.; Rush, A. M.; Hall, D. J.; Orr, G.; Gianneschi, N. C. *J. Am. Chem. Soc.* **2013**, *135* (50), 18710.
- (68) Callmann, C. E.; Barback, C. V.; Thompson, M. P.; Hall, D. J.; Mattrey, R. F.; Gianneschi, N. C. *Adv. Mater.* **2015**, *27* (31), 4611.
- (69) Patra, A.; Ding, T.; Engudar, G.; Wang, Y.; Dykas, M. M.; Liedberg, B.; Kah, J. C. Y.; Venkatesan, T.; Drum, C. L. *Small* **2016**, *12* (9), 1174.
- (70) Cedervall, T.; Lynch, I.; Lindman, S.; Berggard, T.; Thulin, E.; Nilsson, H.; Dawson, K. A.; Linse, S. *Proc. Natl. Acad. Sci.* **2007**, *104* (7), 2050.
- (71) Mahmoudi, M.; Lohse, S. E.; Murphy, C. J.; Fathizadeh, A.; Montazeri, A.; Suslick, K. S. *Nano Lett.* **2014**, *14* (1), 6.

- (72) Docter, D.; Distler, U.; Storck, W.; Kuharev, J.; Wunsch, D.; Hahlbrock, A.; Knauer, S. K.; Tenzer, S.; Stauber, R. H. *Nat. Protoc.* **2014**, *9* (9), 2030.
- (73) Espeel, P.; Du Prez, F. E. *Macromolecules* **2015**, *48* (1), 2.
- (74) Kershaw, M. H.; Smyth, M. J. *Science* **2013**, *341* (6141), 41.
- (75) Komohara, Y.; Fujiwara, Y.; Ohnishi, K.; Takeya, M. *Adv. Drug Deliv. Rev.* **2016**, *99*, 180.
- (76) Niu, M.; Valdes, S.; Naguib, Y. W.; Hursting, S. D.; Cui, Z. *Mol. Pharm.* **2016**, *13* (6), 1833.
- (77) Fan, Q.-M.; Jing, Y.-Y.; Yu, G.-F.; Kou, X.-R.; Ye, F.; Gao, L.; Li, R.; Zhao, Q.-D.; Yang, Y.; Lu, Z.-H.; Wei, L.-X. *Cancer Lett.* **2014**, *352* (2), 160.
- (78) Sica, A.; Mantovani, A. *J. Clin. Invest.* **2012**, *122* (3), 787.
- (79) Sica, A.; Larghi, P.; Mancino, A.; Rubino, L.; Porta, C.; Totaro, M. G.; Rimoldi, M.; Biswas, S. K.; Allavena, P.; Mantovani, A. *Semin. Cancer Biol.* **2008**, *18* (5), 349.
- (80) Tabas, I. *Nat. Rev. Immunol.* **2010**, *10* (1), 36.
- (81) Agrawal, A.; Manchester, M. *Biomacromolecules* **2012**, *13* (10), 3320.
- (82) Rostam, H. M.; Singh, S.; Salazar, F.; Magennis, P.; Hook, A.; Singh, T.; Vrana, N. E.; Alexander, M. R.; Ghaemmaghami, A. M. *Immunobiology* **2016**, *221* (11), 1237.
- (83) Farokhzad, O. C.; Langer, R. *Advanced Drug Delivery Reviews*. 2006, pp 1456–1459.
- (84) Thompson, M. P.; Randolph, L. M.; James, C. R.; Davalos, A. N.; Hahn, M. E.; Gianneschi, N. C. *Polym. Chem.* **2014**, *5* (6), 1954.

Chapter 4

Programming Liquid Crystal Interfaces with Enzyme-Responsive Polymers and Surfactants

4.1 Introduction

General strategies that permit amplification and transduction of molecular recognition events over multiple length scales are of tremendous interest for a range of applications, including advanced sensor design and responsive, smart materials.¹⁻³ Liquid crystals (LCs) provide an exciting opportunity in this regard as the supramolecular organization of mesogens within LC phases can be dynamically coupled to nanoscopic and molecular-scale interfacial events such that the response of the LC results in a detectable optical signal on the micrometer length scale. For example, biological recognition events, including enzymatic reactions, occurring at the aqueous interfaces of thermotropic LCs show promise as the basis of biomolecular triggers of LC reorganization that can be conveniently, transduced using optical methods.⁴ While several examples of LCs triggered by biomolecular events do exist,⁵⁻⁹ general design strategies that can be applied broadly to interfacial assemblies and transformations of biomolecules are yet to be established. Such principles, if identified, would significantly advance and expand the potential utility of LCs as the basis of triggerable supramolecular materials.

In this chapter, we report the design and synthesis of biologically active peptide-polymer amphiphiles (PPA) that mediate enzymatically triggered optical responses in

thermotropic liquid crystal (LC) microdroplets. The PPAs were designed with biphenyl side-chains to promote co-assembly at the aqueous interfaces of LC microdroplets and with peptidic moieties for enzymatic processing. We show that enzymatic cleavage of the PPAs triggers changes in PPA-surfactant complexes formed at the interface of the LC, thus giving rise to an easily observable optical response to the enzymatic reaction. The combined use of PPAs and surfactants represents a simple and modular strategy for targeting and triggering biomolecular events at LC microdroplet interfaces.

4.2 Strategy for triggering liquid crystal ordering transitions using peptide polymer amphiphiles and surfactants

The strategy described for the design of biomolecular triggers of LC ordering transitions is based on the synthesis of biologically active peptide-polymer amphiphiles (PPAs)^{10,11} that form interfacial complexes with synthetic surfactants and thus regulate the ordering of LC microdroplets. The design incorporates PPAs with (i) biphenyl side-chains that promote co-assembly of the PPAs at the aqueous interfaces of LCs, and (ii) peptidic side-chains that can be enzymatically processed at the LC interface (Figure 4.1). A surfactant is selected to differentially interact with the PPA before and after enzymatic processing to change the ordering of the LC. The approach builds from past studies demonstrating that interfacial assemblies formed by polymer and surfactants depend sensitively on the chemical functionality and architecture of both species,¹²⁻¹⁸ and that the mesoscale reordering of LCs can be triggered by subtle changes in the organization of interfacial molecular assemblies.^{6,19-23} The LC used in the current study is a nematic phase of 4-cyano-4'-pentylbiphenyl (5CB) formulated as micrometer-sized droplets dispersed in aqueous phosphate buffered saline (PBS) (Figure 4.1).

(GPLGLAGK for PPA1, GPLGLAG for PPA2) to form hydrophobic and hydrophilic blocks, respectively (resulting ring-opened products as polymers are shown in Figure 4.2).^{10,11,30} The biphenyl group was used as the hydrophobic block to promote the co-assembly of the PPA at the interface of the biphenyl-based LC. The amino acid sequence of the peptidic moieties incorporated into the PPAs was selected to be enzymatically processable by Thermolysin.³¹ We prepared PPA3 to serve as an analogue of the enzymatic product of PPA1 and 2 (Figure 4.2).

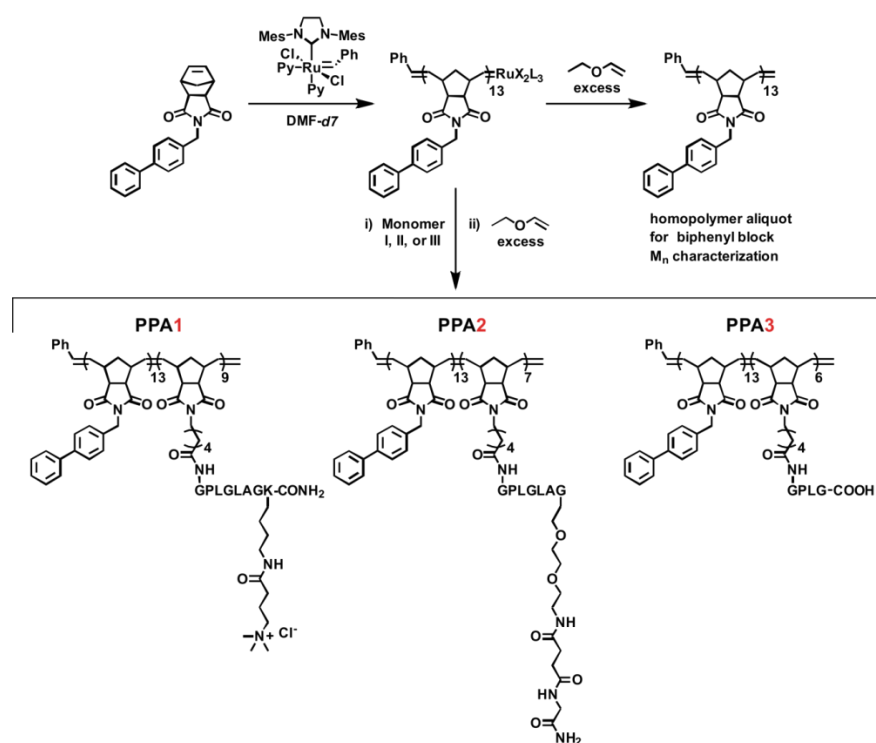


Figure 4.2 Block copolymer synthesis of PPA 1, 2, and 3 *via* ROMP.

4.3 Surface activities of PPA-decorated LC microdroplets

Prior to assembly of PPAs at the interfaces of LC microdroplets and to our exploration of the influence of PPA-surfactant complexes on LC ordering, we characterized

the surface activity of the PPAs by measuring their surface pressure-area (Π -A) isotherms at the aqueous/air interface at physiological pH 7.4 (Figure 4.3).

Inspection of Figure 4.3A reveals that PPAs form stable monolayers at the surface of PBS solutions and that the Π -A isotherms are dependent on the structure of the PPAs. By rescaling the Π -A isotherms to the interfacial concentration of peptidic moieties presented by each PPA, we found that PPA1 and PPA2 were similar to each other but significantly different from PPA3 (Figure 4.3B). This result indicates that the peptidic moieties of PPA1 and PPA2 play a central role in determining the interfacial properties of the PPAs, and that enzymatic cleavage of the peptide side-chain, which generates structures analogous to PPA3, should lead to substantial changes in interfacial properties.

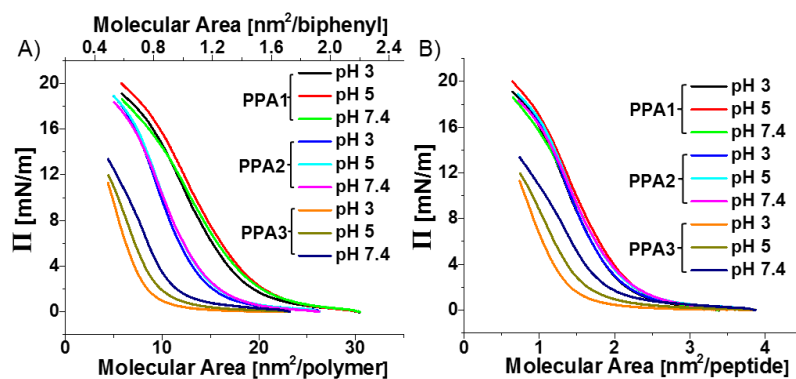


Figure 4.3 Surface pressure (Π) –area isotherms of the PPAs measured on aqueous PBS solutions at 25 °C with varying pH. Molecular area was scaled to the number of (A) polymer molecules along with the number of (A) biphenyl and (B) peptide groups within the PPA.

In addition, we note that PPA3 differs from PPA1 and PPA2 by the presence of a C-terminal carboxylic acid (Figure 4.1). Based on this difference in chemical functionality, we predicted that the Π -A isotherms of PPA3 but not PPA1 nor PPA2 would change with acidification of the PBS. The pH-dependent change in the Π -A isotherm of PPA3 confirms this prediction (Figure 4.3) and is consistent with protonation of carboxylate groups and

reduction in the electrostatic contribution to the surface pressure. In the section that follows, we return to the pH-dependent rearrangement of PPA3 in the context of tuning the interactions of surfactants with PPA-decorated interfaces of LCs.

Next, we formed LC-in-PBS emulsions at pH 7.4 with PPAs dissolved in the 5CB microdroplets at concentrations of 1 to 100 mg PPA/mL 5CB. Electrophoretic mobility measurements revealed microdroplets of pure 5CB in PBS to possess a negative ζ -potential of -28 ± 3 mV, similar to previous studies showing that hydrophobic surfaces acquire excess negative surface charge density in aqueous solutions.³²⁻³⁴ By contrast, 5CB microdroplets doped with 10 mg/ml PPA1, PPA2 or PPA3 exhibited either positive (30 ± 3 mV), neutral (-5 ± 1 mV) or negative (-55 ± 4 mV) values of ζ -potentials, respectively (Table 4.1).

Table 4.1 ζ -potentials (mV) of PPA-laden 5CB droplets at various PPA concentrations, measured in PBS at pH 7.4.

	1 mg PPA/ mL 5CB	10 mg PPA/ mL 5CB	100 mg PPA/ mL 5CB
PPA1	1 ± 3	30 ± 3	28 ± 2
PPA2	-10 ± 2	-5 ± 1	-5 ± 1
PPA3	-48 ± 3	-55 ± 4	-55 ± 3

The PPA-dependent ζ -potentials are consistent with the influence of quaternary ammonium, amide and carboxylic acid groups of PPA1, PPA2 and PPA3, respectively, on the interfacial charging of the LC microdroplets (Figure 4.3), and thus provide evidence that the PPAs added to the 5CB spontaneously assemble at the aqueous interface of the LC droplets. Furthermore, for all PPAs, the ζ -potential changed significantly when PPA concentration increased from 1 to 10 mg PPA/mL 5CB but remained constant when the PPA concentration increased from 10 to 100 mg PPA/mL 5CB. These results indicate that 10 mg PPA/mL in 5CB corresponds to saturation coverage. We also calculated the ζ -potentials for PPA1 and

PPA3-coated 5CB droplets (with 10 mg PPA/mL 5CB, Table 4.1) to correspond to surface charge densities of 0.18 e/nm^2 and -0.38 e/nm^2 , respectively (see methods). The corresponding molecular areas of PPA1 and PPA3 obtained from Figure 4.3B are ~ 2.4 and $\sim 2 \text{ nm}^2/\text{peptide}$, respectively, consistent with each peptide group at the interface bringing approximately one charge to the interface. Finally, we note that acidification had the largest effect on the ζ -potentials of the LC droplets decorated with PPA3 as compared to PPA1 and PPA2 (Table 4.2), consistent with our measurements of Π -A isotherms as a function of pH (Figure 4.3).

Table 4.2 ζ -potentials (mV) of bare and PPA-laden 5CB droplets doped at 10 mg PPA/mL 5CB, measured in PBS at pH 3 or 7.4, with or without 1mM SDS.

	pH 7.4	pH 7.4 w/ SDS	pH 3	pH 3 w/ SDS
5CB	-28 ± 3	-70 ± 5	-7 ± 2	-73 ± 5
PPA1	30 ± 3	-48 ± 2	28 ± 2	-47 ± 2
PPA2	-5 ± 1	-35 ± 2	-5 ± 1	-32 ± 2
PPA3	-55 ± 4	-50 ± 4	-6 ± 2	-38 ± 2

Past studies have shown that the charge status of polymers can regulate the organization of interfacial polymer-surfactant assemblies.^{12,19,21,22} Therefore, we hypothesized that the transformation of PPA1 or PPA2 to generate structures analogous to PPA3 could lead to changes in polymer-surfactant complexation at the interface of the LCs and thus changes in the ordering of the LCs.

4.4 Characterization of liquid crystal microdroplets in the presence of surfactants by polarized light microscopy

To characterize the influence of interfacial PPAs and PPA-surfactant complexes on the internal ordering of the LC microdroplets (containing 10 mg PPA/mL 5CB), we used polarized light microscopy (Figure 4.4). We measured the PPA-decorated LC microdroplets to exhibit optical signatures characteristic of a so-called bipolar configuration of the LC, which results from LC anchored parallel to the PPA-decorated droplet interface (Figure 4.4C).^{35,36}

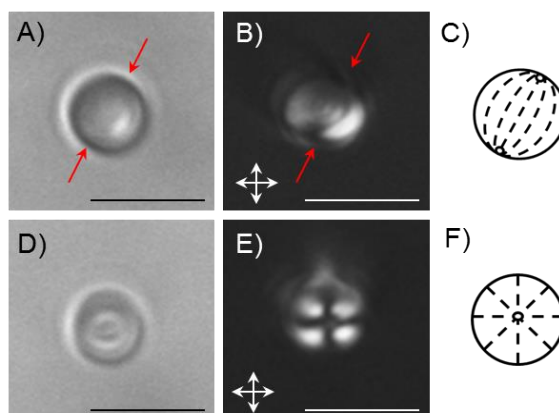


Figure 4.4 Representative optical micrographs of PPA3-decorated LC microdroplets in the presence of SDS at (A-B) pH 3 and (D-E) 7.4. A and D are bright field images whereas B and E were obtained using crossed-polars. C and F are schematic illustrations of the ordering of the LC within the microdroplets. Red arrows indicate boojums at the LC microdroplet/aqueous interface. Scale bars are 5 μm .

However, in contrast to the PPAs, past studies have shown that a range of surfactants with linear aliphatic tails, such as sodium dodecylsulfate (SDS) and dodecyltrimethylammonium bromide (DTAB), cause perpendicular orientations of LCs at aqueous interfaces due to interdigitation of the surfactant tails into the LC.³⁷⁻³⁹ For LC microdroplets, the perpendicular orientation of the LC leads to a so-called radial

configuration (Figure 4.4F).^{35,36} However, surfactants with branched tails, such as Triton X-100, do not perturb LC microdroplets from bipolar configurations (Figure 4.4C).^{37,39} To explore the influence of interfacial PPA-surfactant complexes on LC ordering transitions, we next screened PPA-decorated LC microdroplets against solutions of surfactants (Triton X-100, DTAB and SDS), by adding 1 mM surfactant to the aqueous phase after formation of the PPA-laden 5CB droplets. At pH 7.4, we observed all three types PPA-coated 5CB droplets with or without Triton X-100 to exhibit bipolar configurations. In contrast, exposure to DTAB at pH 7.4 caused radial configurations for bare LC droplets and bipolar configurations when DTAB complexed with PPA interfacial assemblies, indicating that the PPAs changed the interaction between DTAB and the 5CB. SDS at pH 7.4 triggered formation of radial droplets for bare and PPA-laden 5CB droplets (Figure 4.4D-F), indicating that SDS can complex with the interfacial PPA layer such that interdigitation with 5CB is preserved.

Because the Π -A isotherms and ζ -potential measurements reported above revealed that PPA3 but not PPA1 nor PPA2 exhibit pH-dependent interfacial activity (Figure 4.3, Table 4.2), we also explored the effect of changes in pH on the PPA-mediated interactions of SDS with the LC microdroplets. Significantly, at pH 3, radial configurations were observed for 5CB droplets decorated with PPA1 and PPA2 while bipolar droplets were found for PPA3-laden 5CB droplets (Figure 4.4A-C). We note that the carboxylic acid groups of PPA3 are expected to have a pK_a between 2 (pK_a of glycine carboxylic acid) and 5 (pK_a of acetic acid), leading us to conclude that protonation of the carboxylates of PPA3 at pH 3 leads to an interfacial PPA3-SDS complex that prevents the interdigitation of SDS with 5CB.

The results above demonstrate that PPA1 and PPA2 modulate the interaction of SDS with the LC microdroplets at pH 3 in a manner that is distinct from PPA3. To provide insight into this observation, we sought to determine if the differential effect of PPA3 relative to PPA1 and PPA2 occurred via differences in either (i) the extent of adsorption of SDS with

the PPA-decorated microdroplet or (ii) the organization of co-assemblies formed by PPA and SDS at the LC interface. Accordingly, we performed electrophoretic mobility measurements at pH 3 and 7.4 using PPA-decorated LC microdroplets with and without SDS (Table 4.2). Significantly, at pH 3, the ζ -potentials of all PPA-decorated 5CB droplets became more negative upon exposure to SDS (Table 4.2), consistent with SDS adsorption onto the microdroplet interface. This result thus supports our hypothesis that the PPAs mediate the surfactant-triggered response of the LCs not through changes in the extent of adsorption but rather through changes in the organization of PPA interfacial assemblies and SDS at the interface.

4.5 *In situ* detection of proteolytic degradation of peptide polymer amphiphile-coated liquid crystal microdroplets

A key result, described above, is identification of experimental conditions under which SDS can be used to develop a differential LC response to PPA3 (the analogue of an enzymatically cleaved PPA1 or PPA2) relative to PPA1 and PPA2. To further evaluate this finding as the basis of a modular and general strategy for triggering LC ordering transitions using biomolecular events, we next characterized the response of LC microdroplets to *in situ* enzymatic treatment of PPA1 and PPA2 decorated 5CB droplets. We formed PPA-containing 5CB aqueous emulsions at pH 7.4 and then incubated the LC droplets against Thermolysin. After incubation, the response of the emulsion was “developed” using acidified SDS aqueous solutions (Figure 3.1). Initially, LC droplets decorated with PPA1 and PPA2 exhibited radial configurations after acidified SDS development (0 hr, Figure 4.5). However, upon incubation with Thermolysin, the fraction of LC droplets exhibiting radial configurations decreased with increasing time of Thermolysin incubation. Specifically, we observed the optical response of

the LC microdroplets to correlate closely with the extent of conversion of the PPA as determined by HPLC (Figure 4.6).

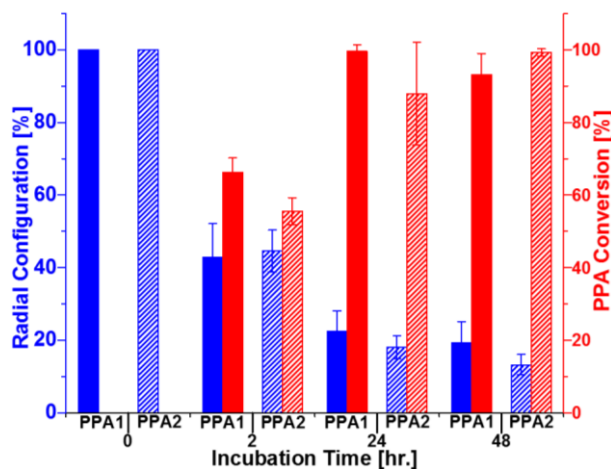


Figure 4.5 Optical response of LC microdroplets triggered by enzymatic processing of either PPA1 or PPA2, as a function of time of incubation against Thermolysin (left axis, blue bars). Extent of PPA conversion, as determined by HPLC (right axis, red bars). Error bars represent triplicates with > 400 droplets analyzed.

We note that the presence of Thermolysin alone does not induce LC ordering transitions in PPA-free LC droplets and Thermolysin alone also does not prevent SDS interdigitation with LC mesogens at the interface of PPA-free LC droplets (see methods section). In summary, these results demonstrate that SDS can “develop” the optical response of the LC microdroplets to enzymatically triggered processing of PPAs.

4.6 Conclusion and future outlook

In conclusion, we have demonstrated the design of biologically active PPAs with oligopeptide and biphenyl side-chains that spontaneously assemble at the aqueous interface of LC microdroplets. PPAs can be enzymatically processed to regulate the formation of PPA-surfactant complexes at the LC microdroplet aqueous interface, thus triggering changes in the optical properties of the microdroplets. A significant merit of the approach is that the design

of the system is modular, involving specification of (i) the LC-directing functional side-chain of the PPA, (ii) the biologically active oligopeptide of the PPA, and (iii) the synthetic surfactant that differentially interacts with the PPA before and after enzymatic processing. This modularity offers the promise of a generalizable approach that makes possible the triggering of changes in LC microdroplet optical properties by a wide range of biomolecular transformations. When combined with recently developed high throughput (10,000 droplets per second) flow-based methods of optically transducing LC microdroplets,²⁵ such a capability would form the basis of a new and broadly useful class of stimuli-responsive supramolecular systems, such as programmable emulsions, droplet-based microreactors or microanalytical systems.

4.7 Acknowledgements

Chapter 4 is adapted from C. Derek Ma, Lisa Adamiak, Daniel S. Miller, Xiaoguang Wang, Nathan C. Gianneschi, and Nicholas L. Abbott. “Liquid Crystal Interfaces Programmed with Enzyme-Responsive Polymers and Surfactants.” *Small*, **2015**, *11*, 5747–5751. Copyright 2015 Wiley. Permission to use copyrighted images and data in the manuscript was also obtained from C. Derek Ma, Daniel S. Miller, Xiaoguang Wang, Nathan C. Gianneschi and Nicholas L. Abbott. The dissertation author was the co-first author on this manuscript.

4.8 Methods

4.8.1 General methods

All reagents were purchased from commercial sources and used without further purification. A Malvern Zetasizer Nano ZSP was used to obtain ζ -potentials of emulsions. Sealed ampules of DMF-*d*₇ (Cambridge Isotopes) were used without further modification.

Amino acids were purchased from AAPPTEC and Novabiochem. Peptides were either synthesized by hand or using an APPTTEC Focus XC automated synthesizer. Monomer *N*-(hexanoic acid)-*cis*-5-norbornene-*exo*-dicarboximide was prepared as previously described.⁴⁰ Grubbs' initiator (IMesH₂)(Cl)₂(C₅H₅N)₂Ru=CHPh [IMesH₂ = 1,3-dimesityl-4,5-dihydroimidazol-2-ylidene] was prepared according to methods described by Sanford *et al.*²⁸ Flash column chromatography of *N*-(4-phenylbenzyl)-*cis*-5-norbornene-*exo*-dicarboximide was performed using silica gel 60 (230 - 400 mesh). All polymerizations were conducted in J Young NMR tubes (5 mm diameter) in a glove box under dinitrogen atmosphere at room temperature using DMF-*d*₇ from sealed ampules. Polymer dispersities and molecular weights were determined by size-exclusion chromatography (Phenomenex Phenogel 5u 10, 1K-75K, 300 x 7.80 mm in series with a Phenomex Phenogel 5u 10, 10K-1000K, 300 x 7.80 mm (0.05 M LiBr in DMF)) using a Shimadzu LC-AT-VP pump equipped with a multi-angle light scattering detector (DAWN-HELIOS: Wyatt Technology), a refractive index detector (Hitachi L-2490) and a UV-Vis detector (Shimadzu SPD-10AVP) normalized to a 30,000 MW polystyrene standard (Flow rate: 0.75 mL/min). The dn/dc value used for each polymer was 0.179. ¹H NMR (400 MHz) and ¹³C NMR (100 MHz) spectra were recorded on Varian Mercury Plus spectrometers. All NMR spectra were recorded in DMF-*d*₇ or CDCl₃ and referenced to the residual protons. RP-HPLC analyses were performed on a Jupiter Proteo90A phenomenex column (150 x 4.60 mm) using a Hitachi-Elite LaChrom L-2130 pump equipped with a UV-Vis detector (Hitachi-Elite LaChrome L-2420) using a binary gradient (Buffer A: 0.1% TFA in water; Buffer B: 0.1% TFA in acetonitrile; Flow rate: 1 mL/min). Peptides were purified using a Jupiter Proteo90A Phenomenex column (2050 x 25.0 mm) on a Waters DeltaPrep 300 system using a binary gradient (Buffers A and B; Flow rate: 22 mL/min). Mass spectra were obtained at the UCSD Chemistry and Biochemistry Molecular Mass Spectrometry Facility.

4.8.2 Estimation of charge densities

The surface charge density (σ) of a colloid can be estimated from its ζ -potential (ζ) using:⁴¹

$$\sigma = \frac{2\varepsilon_r\varepsilon_0k_B T}{ve\lambda_D} \sinh\left(\frac{ve\zeta}{2k_B T}\right) \left[1 + \frac{\lambda_D}{r} \frac{1}{\cosh^2(ve\zeta/4k_B T)}\right] \quad [1]$$

where ε_r and ε_0 are the permittivity of water at room temperature ($\varepsilon_r = 78.54 \text{ C}^2\text{J}^{-1}\text{m}^{-1}$) and vacuum ($\varepsilon_0 = 8.85 \times 10^{-12} \text{ C}^2\text{J}^{-1}\text{m}^{-1}$), respectively, k_B is the Boltzmann constant, T is the temperature, v is the valence number ($v = 1$), e is the electron charge ($e = 1.6 \times 10^{-19} \text{ C}$), r is the radius of the LC microdroplet ($r \sim 2 \text{ }\mu\text{m}$), and λ_D is the Debye screening length:⁴²

$$\lambda_D = \left(\frac{\varepsilon_r\varepsilon_0k_B T}{e^2 \sum_i z_i^2 M_i}\right)^{\frac{1}{2}} \quad [2]$$

where z_i is the ionic charge and M_i is the molar concentration of the salt in bulk solution. From equation 2, we estimate λ_D to be 0.74 nm for 10 mM PBS.

4.8.3 Response of LC microdroplets to Thermolysin

Bare 5CB droplets were incubated in the presence of Thermolysin under the same conditions as described for the PPA-laden 5CB microdroplets in section 3.5. The presence of Thermolysin resulted in bipolar LC microdroplets for all conditions tested. For bare 5CB droplets incubated against Thermolysin, the addition of SDS triggered a LC ordering transition from a bipolar to a radial configuration (for all incubation times reported in Figure 4.5). Furthermore, the addition of SDS at pH 7.4 to Thermolysin-treated, PPA-laden 5CB droplets triggered LC ordering transitions from bipolar to radial configurations (for all incubation times reported in Figure 4.5). We thus conclude that the adsorption of Thermolysin onto the LC/PBS interface does not induce LC ordering transitions and that its presence does not interfere with SDS induced LC ordering transitions.

4.8.4 Peptide synthesis and purification

Peptide monomers were synthesized *via* standard Fmoc-based solid phase synthesis using Rink Amide MBHA resin (AAPPTeC) for the preparation of a C-terminal amide or Fmoc-Gly-Wang resin (Novabiochem) for the preparation a C-terminal carboxylate. In brief, Fmoc deprotection was performed using 20% 4-methylpiperidine in DMF. Amino acid couplings were carried out using HBTU and DIPEA (resin/amino acid/HBTU/DIPEA 1:3:2.9:6). Fmoc-Peg₂-Suc-OH (Anaspec) was coupled in the same way as other amino acids. To ensure complete loading, the initial amino acid was double coupled (i.e. loaded onto the resin for 45 min followed by a rinse cycle with DMF and a second application of fresh amino acid/coupling reagent for another 45 min). *N*-(hexanoic acid)-*cis*-5-norbornene-exo-dicarboximide was double coupled to the N-terminus of the peptide (2.5 equiv). Side chain deprotection of Lys(Mtt) groups was afforded by shaking with DCM/TIPS/TFA 92:5:3 for five cycles (6 min each). Between each deprotection cycle, the resin was rinsed twice with DCM. (3-Carboxypropyl)trimethylammonium chloride (Sigma-Aldrich) was double-coupled to the Lys residue following deprotection (2.5 equiv). The resin was rinsed several times with DCM prior to cleavage of the final peptide. The final peptide monomers were cleaved from the resin using a mixture of trifluoroacetic acid (TFA), water, and triisopropylsilane (TIPS) (TFA/H₂O/TIPS 95:2.5:2.5) for 1 hr. The desired peptide was precipitated with cold ether followed by centrifugation at 3000 rpm for 7 min. The ether was decanted and the remaining pellet was dissolved in buffer A with minimal amounts of buffer B. Peptides were analyzed using RP-HPLC and purified using preparative RP-HPLC. Peptide identity and purities were confirmed using ESI-MS and RP-HPLC monitoring at $I_{\text{Abs}} = 214 \text{ nm}$.

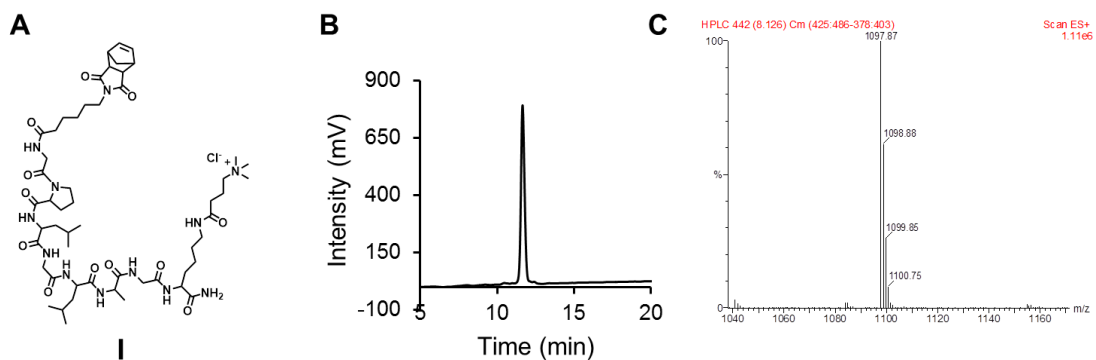


Figure 4.6 Purification of peptide monomer (I), (A) N-(Hexanamide-Gly-Pro-Leu-Gly-Leu-Ala-Gly-Lys(4-trimethylammonium butyramide))-cis-5-norbornene-exo-dicarboximide. (B) RP-HPLC analysis post-purification (20-60 % buffer B, retention time = 12.5 min). (C) ESI-MS: Mass calcd: 1097.67; Mass obs: $[M]^+$ 1097.87.

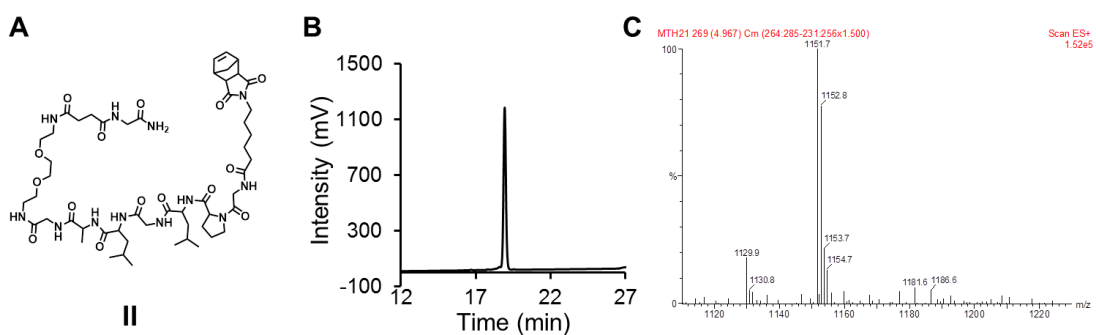


Figure 4.7 Purification of peptide monomer (II), (A) N-(Hexanamide-Gly-Pro-Leu-Gly-Leu-Ala-Gly-Peg-Succ-Gly)-cis-5-norbornene-exo-dicarboximide. (B) RP-HPLC analysis post-purification (20-60 % buffer B, retention time = 18.5 min). (C) ESI-MS: Mass calcd: 1128.62; Mass obs: $[M+H]^+$ 1129.9, $[M+Na]^+$ 1151.7.

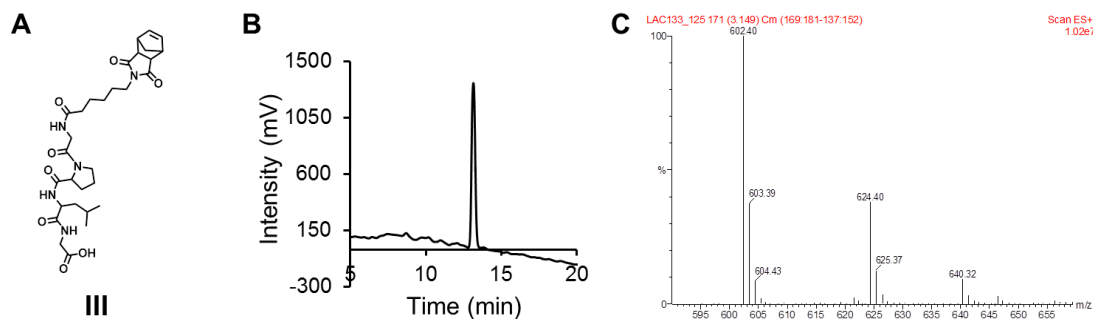
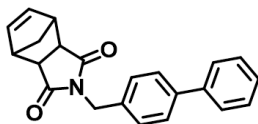


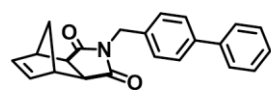
Figure 4.8 Purification of peptide monomer (III), (A) *N*-(Hexanamide-Gly-Pro-Leu-Gly)-*cis*-5-norbornene-*exo*-dicarboximide. (B) RP-HPLC analysis post-purification (20-60 % buffer B, retention time = 13 min). (C) ESI-MS: Mass calcd: 601.31; Mass obs: $[M+H]^+$ 602.40, $[M+Na]^+$ 624.40, $[M+K]^+$ 640.32.

4.8.5 Synthesis of biphenyl monomer



N-(4-phenylbenzyl)-*cis*-5-norbornene-*exo*-dicarboximide (Nor-biphenyl). A round-bottom flask was charged with *cis*-5-norbornene-*exo*-2,3-dicarboxylic anhydride (2.5 g, 15.2 mmol) and 4-phenylbenzylamine (2.9 g, 15.8 mmol). To the solid mixture was added toluene (40 mL), followed by sonication for several minutes. Et₃N (212 μL, 1.52 mmol) was added. The flask was heated to reflux for 12 h. The mixture was then allowed to cool to room temperature and concentrated. The reaction mixture was diluted with CH₂Cl₂ (40 mL) and washed with 1 M aqueous HCl (2 × 20 mL). The organic layer was washed with saturated aqueous NaCl (20 mL), dried Na₂SO₄, filtered, and concentrated under reduced pressure. Purification by flash chromatography (4:1, hexanes:EtOAc) gave the desired product (3.0 g, 60%) as a white solid: ¹H-NMR (400 MHz, CDCl₃) δ 7.32 - 7.58 (m, 9H), 6.28 (t, 2H, *J* = 1.8 Hz), 4.67 (s, H), 3.27 (m, 2H), 2.69 (d, 2H, *J* = 1.3 Hz), 1.42 - 1.44 (m, 1H), 1.10 - 1.13 (m, 1H); ¹³C NMR (100 MHz, CDCl₃) δ 177.7, 140.8, 140.6, 137.9, 134.9, 129.4, 128.8, 127.41,

127.38, 127.1, 47.9, 45.3, 42.7, 42.1; HRMS expected: 329.14 [M + H]⁺, found: 352.13 [M + Na]⁺



(400 MHz, CDCl₃)

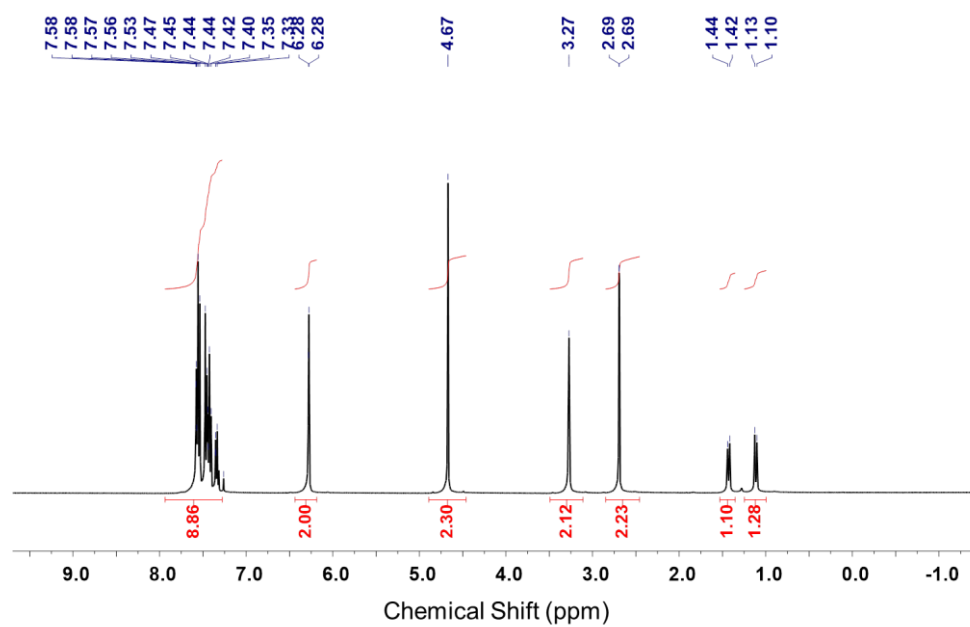


Figure 4.9 ¹H NMR spectrum of Nor-biphenyl.

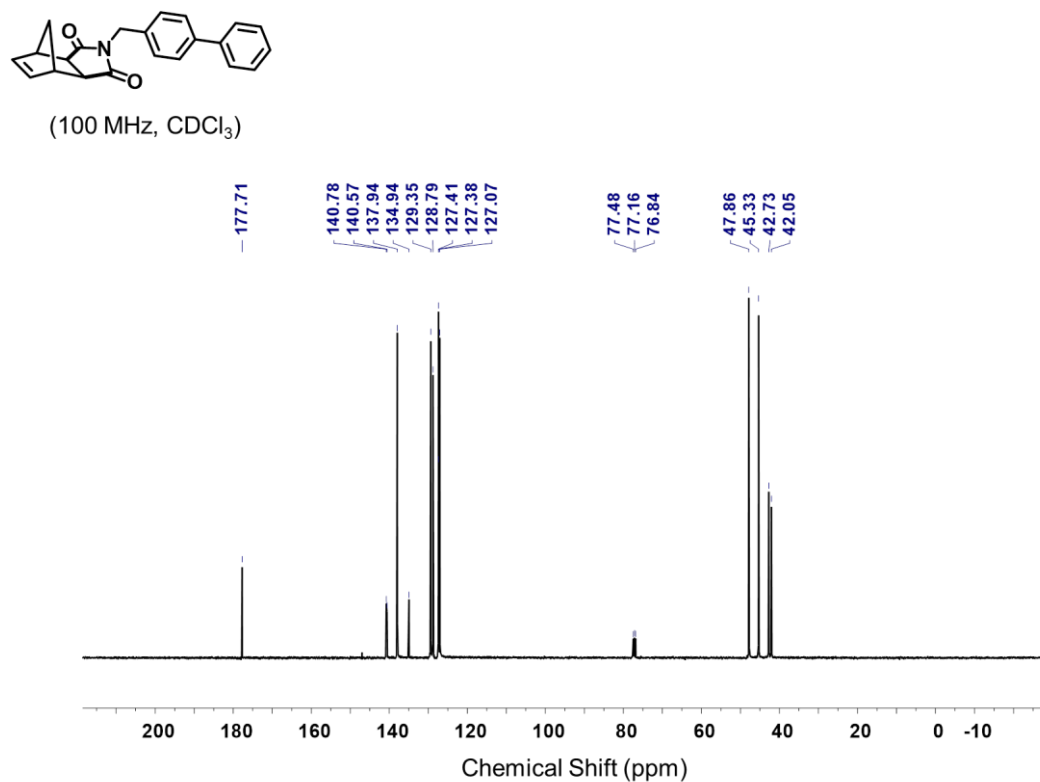


Figure 4.10 ¹³C NMR spectrum of Nor-biphenyl.

4.8.6 Polymer synthesis and purification

All polymerization reactions were accomplished in a glove box under dinitrogen atmosphere with anhydrous solvents. Grubbs' modified second generation catalyst (IMesH₂)(Cl)₂(C₅H₅N)₂Ru=CHPh (1 equiv) was dissolved in DMF-*d*₇ and added to the Nor-biphenyl monomer (15 equiv) in DMF-*d*₇ to a final volume of 450 μL in a J Young NMR tube. The tube was inverted several times to ensure mixing. A ¹H NMR spectrum was recorded to confirm complete monomer consumption at 30 min. An aliquot (20 μL) of the homopolymer was removed from the glove box and terminated with 20 μL ethyl vinyl ether. The homopolymer solution was split into three portions and the respective peptides in DMF-*d*₇ were added (0.1 mL, 15 equiv). The copolymer solutions were then transferred to three J Young NMR tubes. ¹H NMR spectra were recorded to confirm the complete consumption of

the peptide monomers at 1.5 hr. The copolymer solutions were transferred to vials and each polymerization reaction was terminated with excess ethyl vinyl ether (50 μ L). Characterization of polymer molecular weights and dispersities was afforded via SEC-MALS. All polymers were triturated with DMF and cold ether and centrifuged at 3000 rpm for 7 min. The ether was decanted and the process was repeated 3 times. The remaining pellet was dissolved in water with a minimal amount of acetonitrile and lyophilized to afford a white powder.

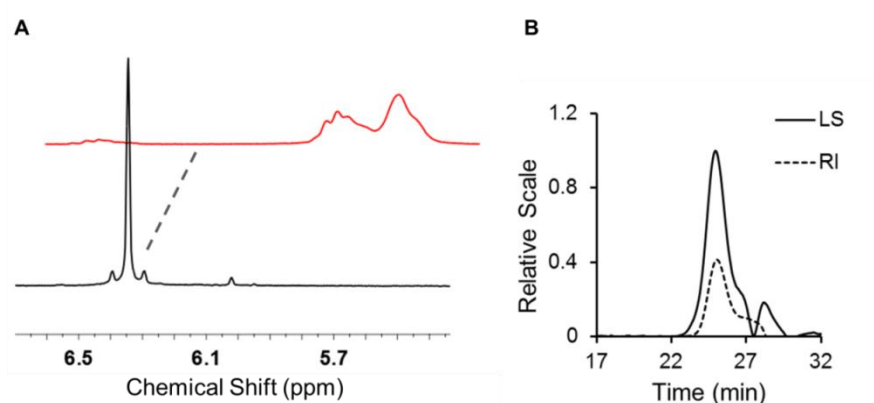


Figure 4.11 Characterization of Nor-biphenyl homopolymer *via* ^1H NMR and SEC-MALS, respectively. (A) Complete consumption of the norbornene olefin was observed after 30 min by monitoring the disappearance of the proton resonance at 6.34 ppm. (B) SEC-MALS characterization ($dn/dc = 0.179$, $M_n = 4,302$, $M_n/M_w = 1.029$); Degree of polymerization (DP) = 13.

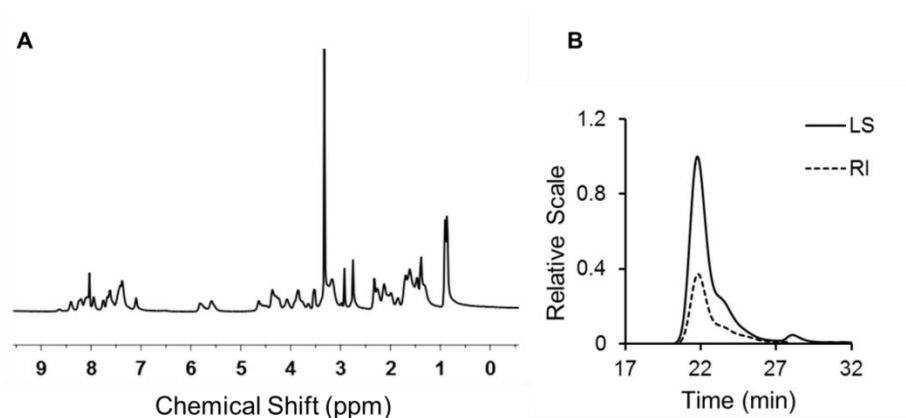


Figure 4.12 Characterization of PPA 1 block copolymer via ¹H NMR and SEC-MALS, respectively. (A) Complete consumption of the norbornene peptide monomer I olefin was observed after 1.5 hr. (B) SEC-MALS characterization ($dn/dc = 0.179$, $M_n = 14,030$, $M_n/M_w = 1.007$), DP = 13-*b*-9.

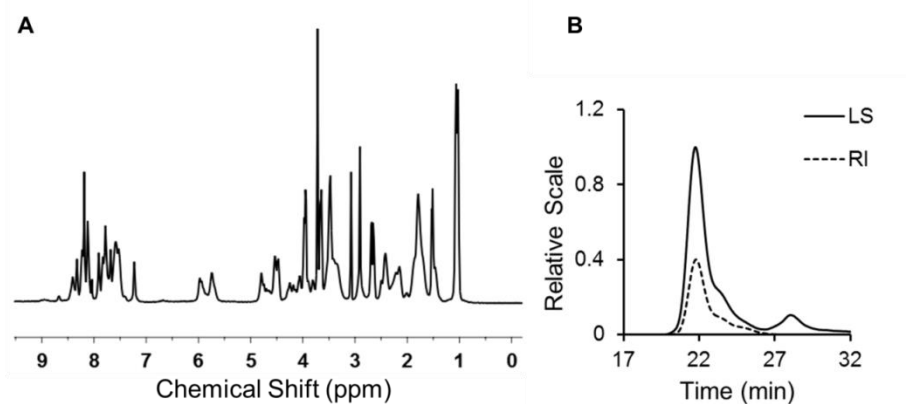


Figure 4.13 Characterization of PPA 2 block copolymer via ¹H NMR and SEC-MALS, respectively. (A) Complete consumption of the norbornene peptide monomer II olefin was observed after 1.5 hr. (B) SEC-MALS characterization ($dn/dc = 0.179$, $M_n = 12,100$, $M_n/M_w = 1.007$), DP = 13-*b*-7.

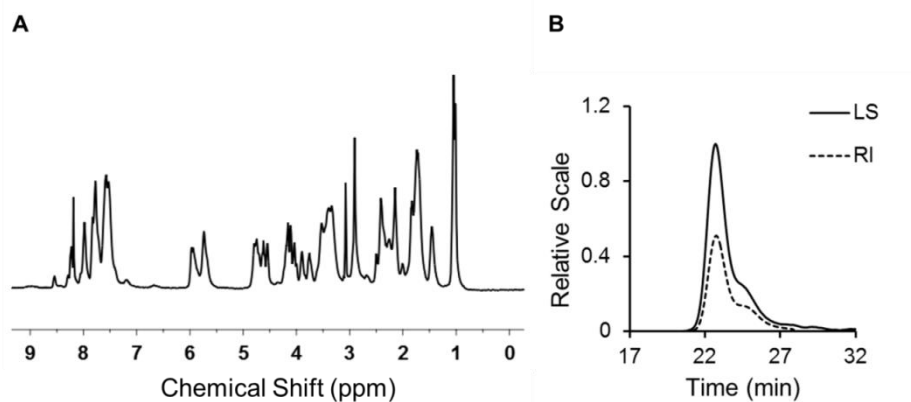


Figure 4.14 Characterization of PPA 3 block copolymer via ¹H NMR and SEC-MALS, respectively. (A) Complete consumption of the norbornene peptide monomer III olefin was observed after 1.5 hr. (B) SEC-MALS characterization ($dn/dc = 0.179$, $M_n = 8,027$, $M_w/M_n = 1.010$), DP = 13-*b*-6.

4.8.7 Preparation of LC emulsions

10 mM PBS (prepared from powder packets obtained from Sigma-Aldrich) used throughout our experiments contained 0.5 mM calcium chloride (CaCl_2 dihydrate from Sigma-Aldrich), which was added to ensure the structural stability of Thermolysin. The pH of the PBS was adjusted with concentrated HCl (25 vol. % from Fisher Scientific) and 2 M NaOH (Fisher Scientific) as needed. To prepare PPA-decorated microdroplets of 5CB (4-cyano-4'-pentylbiphenyl, Merck), 10 μL of the PPA in methanol (HPLC grade from Fisher Scientific) at 1 mg/mL PPA was added to 1 μL 5CB in disposable glass culture tubes (VWR), then the PPA doped 5CB was dried under a gentle stream of nitrogen and placed under vacuum for 1 hr. Following removal of all volatiles, 1 mL PBS at pH 7.4 was added to the PPA doped 5CB for emulsification. The two-phase system was emulsified by repeated cycles of vortexing (2500 rpm for 10 s.) and sonication (1 min.) until the solution became milky white in appearance. Note: the water for the sonication bath (2 L) was replaced with the recommended volume fresh to ensure homogeneity between emulsion batches.

4.8.8 Thermolysin treatment of PPA-laden 5CB droplets

Thermolysin (purchased from Promega) was reconstituted in PBS at pH 7.4 and stored at -20 °C for a maximum duration of two weeks. The reconstituted Thermolysin was equilibrated to room temperature for a minimum of 30 min. prior to use. Thermolysin was then added to emulsions that had equilibrated for at least 15 min to obtain a final Thermolysin concentration of 0.2 μ M in the emulsions. The Thermolysin-containing emulsions were then gently inverted several times to distribute the enzyme throughout the emulsions. Emulsions were incubated in the presence of Thermolysin at room temperature with periodic gentle mixing of the reaction to prevent sedimentation. 20 μ L of 0.5 M ethylenediaminetetraacetic acid (EDTA, Sigma-Aldrich) in aqueous at pH 8 was added to 100 μ L of the enzyme-treated emulsions to quench the reaction at the desired incubation times. After quenching the enzyme reaction, the emulsion was lyophilized for storage. To determine the percent conversion of the peptide substrates displayed on the PPAs, the lyophilized samples were reconstituted in 0.1 mL H₂O and then monitored *via* RP-HPLC. Percent conversion was calculated from the concentration of product determined against standard curves of the authentic cleaved peptide fragments. The peaks corresponding to the enzymatically cleaved products were collected from RP-HPLC and the fragment identities were confirmed by ESI-MS. A binary gradient was used (2 - 50 % buffer B over 30 minutes) for sample analysis.

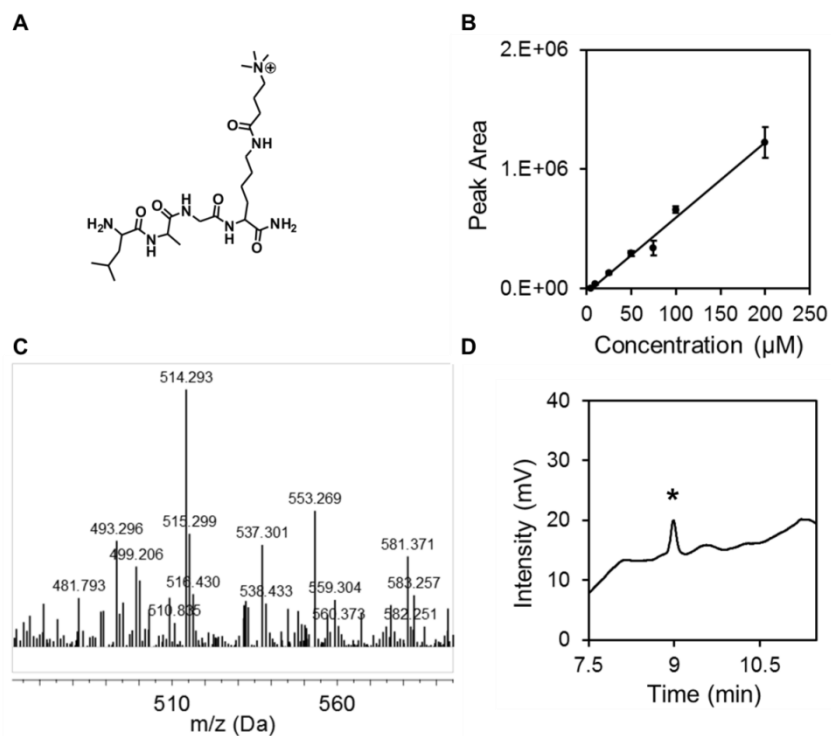


Figure 4.15 Analysis of Thermolysin-treated PPA 1-laden 5CB droplets. (A) Chemical structure of the cleaved peptide fragment from PPA 1. (B) Standard curve of the authentically cleaved peptide fragment performed in triplicate. (C) ESI-MS confirming the enzymatically cleaved peptide identity of the peak collected from RP-HPLC. ESI-MS: Mass calcd: 514.37; Mass obs: $[M]^+$ 514.29. (D) Peak corresponding the enzymatically cleaved product as indicated from RP-HPLC.

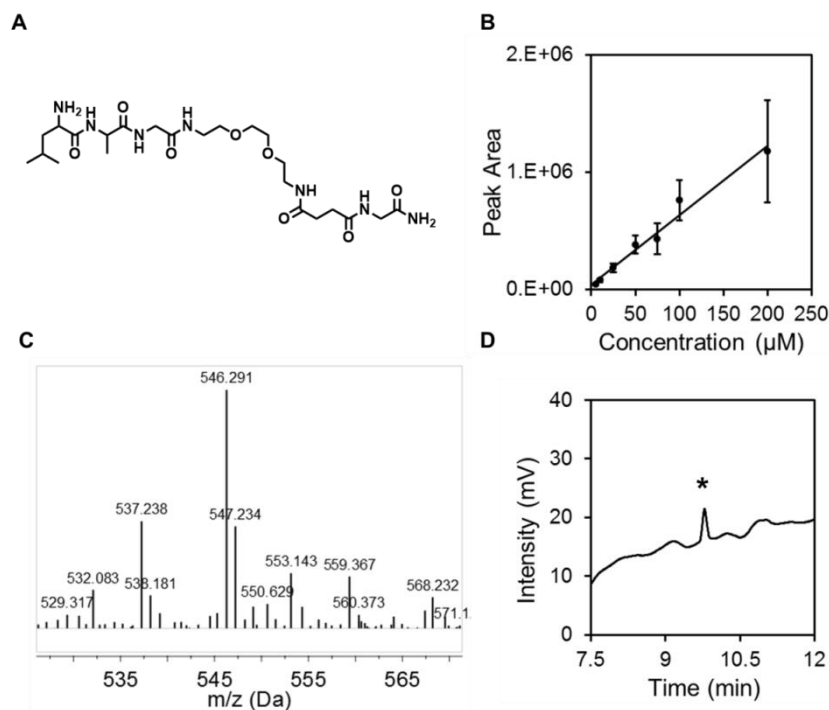


Figure 4.16 Analysis of Thermolysin-incubated PPA 2-laden 5CB droplets. (A) Chemical structure of the cleaved peptide fragment from PPA 2. (B) Standard curve of the authentically cleaved peptide fragment performed in triplicate. (C) ESI-MS confirming the enzymatically cleaved peptide identity of the peak collected from RP-HPLC. ESI-MS: Mass calcd: 545.32; Mass obs: $[M + H]^+$ 546.29. (D) Peak corresponding to the enzymatically cleaved product as indicated from RP-HPLC.

4.8.9 Amphiphilic development with surfactants

The Triton X-100, dodecyltrimethylammonium bromide (DTAB), and sodium dodecylsulfate (SDS) were purchased from Sigma-Aldrich and used without further purification. For amphiphilic development, 2 mM surfactant solutions in PBS at the corresponding emulsion pH were diluted into the appropriate emulsions to obtain a final surfactant concentration of 1 mM.

4.8.10 LC droplet characterization with microscopy

LC droplets were imaged using an Olympus IX71 inverted microscope with either a 60 x objective or 100 x oil immersion objective. Bright-field and polarized light micrographs

of the LC droplets were collected with a Hamamtsu 1394 ORCAER CCD camera connected to a computer and controlled through SimplePCI imaging software. LC droplet characterization was limited to only LC droplets that were diffusing (translating and/or rotating).

4.8.11 Surface pressure-area isotherms

Langmuir films of the PPAs were formed at the PBS/air interface on a Nima 602A film balance equipped with a Wilhelmy plate (filter paper) to monitor the surface pressure. Prior to depositing the PPA onto the PBS/air interface, the Wilhelmy plate (filter paper) was equilibrated in PBS for 30 min. No significant surface pressure was observed from full compression of the bare PBS/air interface. A known volume of PPA solution in methanol was then spread uniformly across the PBS/air interface in a drop wise fashion. A 20 min equilibration period followed before film compression began. Symmetric compression of the PPA films, at a rate of 35 cm²/min with the PBS subphase maintained at 25 °C, was used to collect the surface pressure-area isotherms.

4.9 References

- (1) Boal, A. K.; Ilhan, F.; DeRouchey, J. E.; Thurn-Albrecht, T.; Russell, T. P.; Rotello, V. M. *Nature* **2000**, *404* (6779), 746.
- (2) Randolph, L. M.; Chien, M.-P.; Gianneschi, N. C. *Chem. Sci.* **2012**, *3* (5), 1363.
- (3) Ringsdorf, H.; Schlarb, B.; Venzmer, J. *Angew. Chemie Int. Ed. English* **1988**, *27* (1), 113.
- (4) Carlton, R. J.; Hunter, J. T.; Miller, D. S.; Abbasi, R.; Mushenheim, P. C.; Tan, L. N.; Abbott, N. L. *Liq. Cryst. Rev.* **2013**, *1* (1), 29.
- (5) Aliño, V. J.; Pang, J.; Yang, K.-L. *Langmuir* **2011**, *27* (19), 11784.
- (6) Bai, Y.; Abbott, N. L. *J. Am. Chem. Soc.* **2012**, *134* (1), 548.

- (7) Brake, J. M.; Daschner, M. K.; Luk, Y.-Y.; Abbott, N. L. *Science* **2003**, *302* (5653), 2094.
- (8) Noonan, P. S.; Roberts, R. H.; Schwartz, D. K. *J. Am. Chem. Soc.* **2013**, *135* (13), 5183.
- (9) Price, A. D.; Schwartz, D. K. *J. Am. Chem. Soc.* **2008**, *130* (26), 8188.
- (10) Hahn, M. E.; Randolph, L. M.; Adamiak, L.; Thompson, M. P.; Gianneschi, N. C. *Chem. Commun.* **2013**, *49* (28), 2873.
- (11) Ku, T.-H.; Chien, M.-P.; Thompson, M. P.; Sinkovits, R. S.; Olson, N. H.; Baker, T. S.; Gianneschi, N. C. *J. Am. Chem. Soc.* **2011**, *133* (22), 8392.
- (12) Alexandridis, P.; Alan Hatton, T. *Colloids Surfaces A Physicochem. Eng. Asp.* **1995**, *96* (1–2), 1.
- (13) Biggs, S.; Selb, J.; Candau, F. *Langmuir* **1992**, *8* (3), 838.
- (14) Guillemet, F.; Piculell, L. *J. Phys. Chem.* **1995**, *99* (22), 9201.
- (15) Hansson, P.; Lindman, B. *Curr. Opin. Colloid Interface Sci.* **1996**, *1* (5), 604.
- (16) Piculell, L.; Guillemet, F.; Thuresson, K.; Shubin, V.; Ericsson, O. *Adv. Colloid Interface Sci.* **1996**, *63*, 1.
- (17) Tanaka, R.; Meadows, J.; Williams, P. A.; Phillips, G. O. *Macromolecules* **1992**, *25* (4), 1304.
- (18) Yekta, A.; Duhamel, J.; Brochard, P.; Adiwidjaja, H.; Winnik, M. A. *Macromolecules* **1993**, *26* (8), 1829.
- (19) Khan, W.; Choi, J. H.; Kim, G. M.; Park, S.-Y. *Lab Chip* **2011**, *11* (20), 3493.
- (20) Kinsinger, M. I.; Buck, M. E.; Campos, F.; Lynn, D. M.; Abbott, N. L. *Langmuir* **2008**, *24* (23), 13231.
- (21) Kinsinger, M. I.; Sun, B.; Abbott, N. L.; Lynn, D. M. *Adv. Mater.* **2007**, *19* (23), 4208.
- (22) Lee, D.-Y.; Seo, J.-M.; Khan, W.; Kornfield, J. A.; Kurji, Z.; Park, S.-Y. *Soft Matter* **2010**, *6* (9), 1964.
- (23) Seo, J.-M.; Khan, W.; Park, S.-Y. *Soft Matter* **2012**, *8* (1), 198.
- (24) Kinsinger, M. I.; Buck, M. E.; Abbott, N. L.; Lynn, D. M. *Langmuir* **2010**, *26* (12), 10234.
- (25) Miller, D. S.; Wang, X.; Buchen, J.; Lavrentovich, O. D.; Abbott, N. L. *Anal. Chem.* **2013**, *85* (21), 10296.

- (26) Lin, I.-H.; Miller, D. S.; Bertics, P. J.; Murphy, C. J.; de Pablo, J. J.; Abbott, N. L. *Science* **2011**, *332* (6035), 1297.
- (27) Smith, D.; Pentzer, E. B.; Nguyen, S. T. *J. Macromol. Sci. Part C Polym. Rev.* **2007**, *47* (3), 419.
- (28) Sanford, M. S.; Love, J. A.; Grubbs, R. H. *Organometallics* **2001**, *20* (25), 5314.
- (29) Bielawski, C. W.; Grubbs, R. H. *Prog. Polym. Sci.* **2007**, *32* (1), 1.
- (30) Kammeyer, J. K.; Blum, A. P.; Adamiak, L.; Hahn, M. E.; Gianneschi, N. C. *Polym. Chem.* **2013**, *4* (14), 3929.
- (31) van den Burg, B.; Eijsink, V. In *Handbook of Proteolytic Enzymes*; 2013; pp 540–553.
- (32) Tian, C. S.; Shen, Y. R. *Proc. Natl. Acad. Sci.* **2009**, *106* (36), 15148.
- (33) Vácha, R.; Rick, S. W.; Jungwirth, P.; de Beer, A. G. F.; de Aguiar, H. B.; Samson, J.-S.; Roke, S. *J. Am. Chem. Soc.* **2011**, *133* (26), 10204.
- (34) Zangi, R.; Engberts, J. B. F. N. *J. Am. Chem. Soc.* **2005**, *127* (7), 2272.
- (35) Lavrentovich, O. D. *Liq. Cryst.* **1998**, *24* (1), 117.
- (36) Prishchepa, O. O.; Shabanov, A. V.; Zyryanov, V. Y. *Phys. Rev. E* **2005**, *72* (3), 31712.
- (37) Brake, J.M.; Mezera, A.D.; Abbott, N. L. *Langmuir* **2003**, *19* (16), 6436.
- (38) Gupta, J. K.; Zimmerman, J. S.; de Pablo, J. J.; Caruso, F.; Abbott, N. L. *Langmuir* **2009**, *25* (16), 9016.
- (39) Lockwood, N. A.; de Pablo, J. J.; Abbott, N. L. *Langmuir* **2005**, *21* (15), 6805.
- (40) Patel, P. R.; Kiser, R. C.; Lu, Y. Y.; Fong, E.; Ho, W. C.; Tirrell, D. A.; Grubbs, R. H. *Biomacromolecules* **2012**, *13* (8), 2546.
- (41) Makino, K.; Ohshima, H. *Langmuir* **2010**, *26* (23), 18016.
- (42) Hiemenz, P. C.; Rajagopalan, R. *Principles of colloid and surface chemistry.*; Marcel Dekker, 1997.

Chapter 5

Design of Triggerable Amphiphiles with Mesogenic Side Chains for Multi-Scale Responses with Liquid Crystals

5.1 Introduction

Recent studies have emerged that describe the use of responsive amphiphilic copolymers to generate stimuli-responsive liquid crystal (LC) systems.^{1,2} Among those reported, several incorporate chemical functionality which enable a response to changes in pH,¹⁻⁴ the presence of polyelectrolytes of opposite charge,⁵ or enzymatic cleavage.⁶ A common strategy to this end is the design of block copolymers consisting of a “LC-philic” unit (highlighted in blue) and a responsive hydrophilic block (Figure 5.1). For example, Lee and coworkers synthesized the block copolymer, PAA-*b*-LCP, using reversible addition-fragmentation chain transfer (RAFT) polymerization consisting of polyacrylic acid (PAA) as the pH-responsive component and the hydrophobic unit consisting of the mesogenic side-chain 4-cyanobiphenyl-4'-oxyundecrylacrylate (LCP) (Figure 5.1A).⁴ This side-chain mesogen, which is closely related to the liquid crystal, 4'-undecyloxy-biphenyl-4-carbonitrile (commonly known as 11OCB), was incorporated with a side-chain ratio (PAA : LCP units) of 0.93:0.07. In this study, the interface of a 5CB LC film was decorated with PAA-*b*-LCP by way of a Langmuir-Schaefer transfer with an interfacial density of $\sim 1271 \text{ \AA}^2$ per polymer or

$\sim 84.7 \text{ \AA}^2$ per LCP group. The LC film decorated with PAA-*b*-LCP responded to changes in the bulk aqueous pH. Specifically, the copolymer transitioned from planar anchoring at pH 2 to homeotropic anchoring at pH 10, enabling the LC geometry transition from bipolar to radial, respectively. Kinsinger and coworkers designed amine-based amphiphilic polymers with aliphatic side-chains to design LCs that amplify changes in the aqueous solution pH² or electrolyte composition⁵ into optical outputs (Figure 5.1B). To decorate 5CB films, Kinsinger performed a Langmuir-Schaefer transfer of the random copolymer (Figure 5.1B left structure), supported on a PBS subphase at pH 5, onto the interface of a 5CB film at surface densities of $\sim 38 \text{ \AA}^2$, 40–48 \AA^2 , or 52 \AA^2 per aliphatic group and observed that the LC anchoring at the polymer decorated interface was homeotropic, tilted and planar, respectively. Sodium poly(styrene sulfonate), a strong anionic polyelectrolyte, was applied to the aqueous subphase and a homeotropic to planar anchoring transition was observed over the course of 15 minutes.⁵ Further, LC films decorated with a similar copolymer were sensitive to pH changes in the aqueous phase.² An alternative random copolymer (Figure 5.1B, right structure), was also used to immobilize LC droplets on chemically functionalized surfaces.⁷ A change in the LC droplet anchoring was found to depend on the nature of the surface at which the droplets were immobilized. Ma and coworkers used amphiphilic block copolymers (PPA1-3) synthesized by ring opening metathesis polymerization (ROMP), which incorporate biphenyl and peptide-based side-chains, to design responsive PPA-coated LC droplets (Figure 5.1C).⁶ The peptide sequences (GPLGLAGK and GPLGLAG-Ebes-G) were designed to be enzymatically processed by thermolysin, resulting in truncation of the peptide sequence to yield a pH-responsive carboxylate-containing product (Figure 5.1C). In order to discern proteolytically-driven changes in the LC ordering of PPA-decorated LC droplets, sodium dodecyl sulfate (SDS) was added and the aqueous solution was acidified to pH 3 post enzyme

treatment. Applying these conditions provoked LC droplets decorated by cleaved and uncleaved PPAs to adopt distinct configurations.

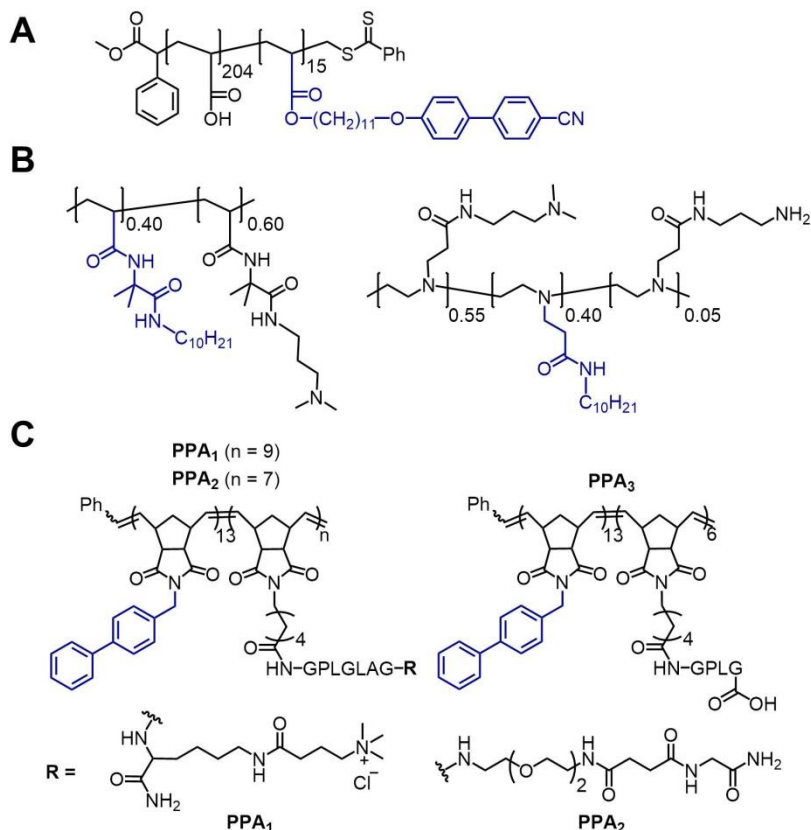


Figure 5.1 Examples of amphiphilic copolymers reported in previous studies. The mesogenic side chains used are (A) hendecaoxycyanobiphenyl (11OCB),^{3,8} (B) linear aliphatic tails,^{2,7} and (C) biphenyl.⁶

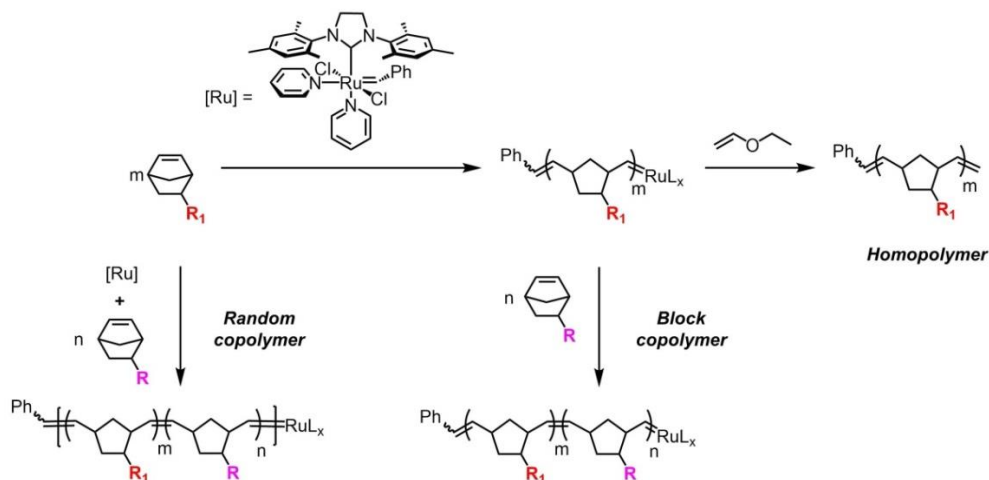
When collectively considered, these previous studies generate a number of questions related to the structure and architecture of the amphiphilic polymers and their specific interactions with LCs. First, we note that two classes of amphiphilic polymers; one with LC-like (Figure 1A) and one with surfactant-like (Figure 1B) side chains were able to anchor perpendicular (homeotropic anchoring) to LC surfaces, resulting in a radial configuration of the LC. Interestingly, however, LC-like polymers were shown to be more capable of

generating homeotropic LCs at a lower surface density of hydrophobic units (1 unit per 84.7 Å²) compared to aliphatic side-chain polymers (1 unit per 38 Å²). This suggests that amphiphilic polymers with LC-like side-chains are more effective than polymers with aliphatic side chains in inducing homeotropic anchoring. In contrast, the biphenyl side-chain used in the PPA shown in Figure 1C was unable to generate homeotropic anchoring of the LC. This inconsistency may stem from the short single methylene spacer connecting the mesogen to the rather rigid backbone of the polymer, which restricts perpendicular anchoring of the side chains to the LC interface.

By comparing the LC-like side-chain containing polymers (Figure 5.1A and 5.1C), we note three main differences. First, the length of the aliphatic chain linking the biphenyl gives rise to greater degrees of freedom of the LCP unit (C11 for ether-nitrile biphenyl and C1 for 4-phenylbenzyl, Figure 5.1A and 5.1C, respectively). Second, the functional group connectivity of the biphenyl, for example the ether functional group in Figure 5.1A, extends the rigidity of the mesogen⁹ compared to the benzyl group in Figure 5.1C; and third, the presence or absence of a nitrile terminal group on the biphenyl unit (Figure 5.1A and 5.1C, respectively). Next, by comparing these polymer architectures, we observe that the ratio of the hydrophobic: hydrophilic blocks are very different (15: 204 and 13: 9, Figure 5.1A and 5.1C, respectively). In addition, we note that these two polymers were synthesized using different methods (RAFT or ROMP, respectively), each of which generates distinct polymer backbone chemistry (and polymer flexibility) and may play an important role in polymer-LC interactions. Finally, amphiphilic copolymers in Figure 5.1A and 5.1B were synthesized as block and random copolymers, respectively. These two architectures are varied in the spatial density of mesogens along the polymer backbone, which also may dramatically affect polymer-LC interactions. To illustrate this point, a block copolymer oriented along a LC interface will display regions of hydrophobic-rich and hydrophobic-poor domains.

Comparatively, a random copolymer with a stochastic arrangement of hydrophobic and hydrophilic units along the polymer backbone has a homogeneous hydrophobic unit density along the LC interface.

In general, the impact of polymer composition and architecture on the interfacial ordering of polymers at LC interfaces is not understood. The work described in this chapter was initially motivated by the need to identify a set of design principles for amphiphilic copolymers that can be used to rationally tailor anchoring transitions at aqueous interfaces of LCs. To this end, we used ROMP as a synthetic method to enable the design of responsive polymers and the development of structure-property relationships for triggering ordering transitions in LC systems. Polymers of various architectures, such as homopolymers, block and random copolymers, can be readily prepared by this method using the bipyridyl Grubb's catalyst, which is known for its high-functional group tolerance and ability to incorporate peptides and other functionally complex molecules in a graft-through approach (Scheme 5.1).¹⁰ As a living polymerization technique, ROMP has the additional advantage of producing high molecular weight polymers with low dispersity, a feature that is generally more difficult to achieve with reversible deactivation radical polymerization (RDRP) methods such as RAFT and atom transfer radical polymerization (ATRP). Utilizing ROMP, we synthesized a library of polymers probing polymer composition as well as architecture on triggering LC ordering transitions.



Scheme 5.1 Synthesis of homopolymers, block and random copolymers using ROMP

First, we report a systematic study on the effect of mesogen side-chain structure on homopolymer anchoring at the LC/aqueous interface (Figure 5.2). From this survey, we identified a mesogen that is efficient at triggering homeotropic anchoring of LCs, and can be readily incorporated into copolymer structures that contain hydrophilic units. Second, we studied the effect of polymer architecture on LC ordering at the aqueous interface of polymer decorated LC droplets. Block and random copolymers bearing poly(ethylene glycol) (PEG) as the hydrophilic block and the optimized mesogen as the hydrophobic block, were prepared as model systems. Third, we study the effect of copolymer composition on LC ordering, specifically the presence of a nitrile functional groups on the biphenyl as well as functional group conjugation (ether or amide) to the polymer (Figure 5.2). Finally, by leveraging the design principles that emerge from the above studies, we report the design of copolymers incorporating a peptide hydrophilic unit that triggers ordering transitions in LC droplets when the peptide is processed by enzymatic hydrolysis.

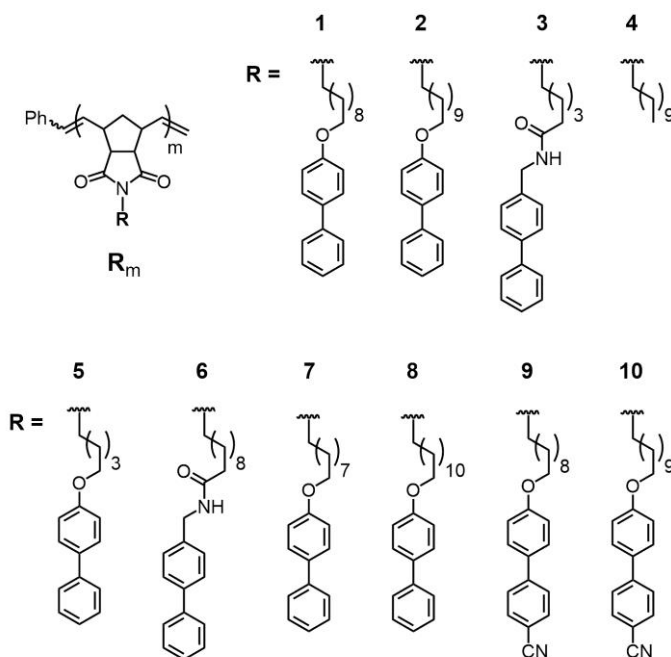


Figure 5.2 The catalogue of homopolymers utilized to determine the optimal mesogenic side-chain structure for triggering LC geometry changes at the liquid crystal interface.

5.2 Identifying LC configurations of polymer-decorated LC droplet emulsions by flow cytometry

In this work, we examine polymer-driven perturbations in the ordering of the LC within polymer-decorated LC droplets. In an aqueous environment, LCs form spherical droplets to minimize the interfacial area. The anchoring of LC molecules at the undecorated LC/aqueous interface is tangential, or planar.¹¹⁻¹³ Due to the spherical geometry of the droplet and a minimization of the elastic and surface anchoring energy at the interface of the droplet, the LC adopts a bipolar droplet configuration, with two diametrically opposite defects called boojums (Figure 5.3B). These droplets can be driven from a bipolar configuration to a radial configuration (with one point defect located at the center of the droplet) through a change in LC anchoring from planar to perpendicular or homeotropic (Figure 5.3A). The size at which

the droplet configuration is most sensitive is when the elastic energy and the anchoring energy are comparable, which is determined by setting the elastic energy, $E_k \propto KR$, equal to the anchoring energy, $E_w \propto WR^2$. This leads to a critical radius of $R = K \cdot W^{-1}$, where $K = 10^{-11} \text{ J}\cdot\text{m}^{-1}$ and $W = 10^{-5}\text{-}10^{-6} \text{ J}\cdot\text{m}^{-2}$ (weak anchoring), which are typical values for thermotropic LCs when the radius is between 1 and 10 μm . Droplets of this size may change configuration through a change in the LC anchoring strength by decorating the droplet interface with amphiphiles. Therefore, by choosing an amphiphile with a suitable mesogen, the hydrophobic moieties can interdigitate with the LC at the droplet interface, causing an anchoring change from planar to homeotropic.

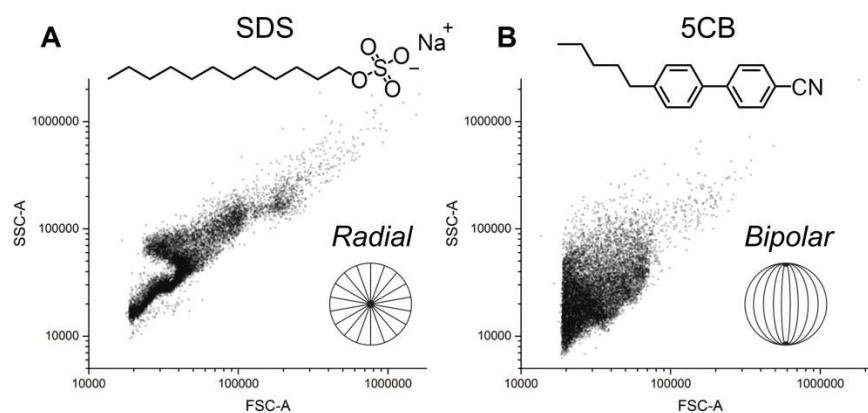


Figure 5.3 Liquid crystal droplets of 5CB exhibit different droplet configurations (detectable by flow cytometry scatter plots) in the (A) presence and (B) absence of surfactants, such as the single-tailed surfactant SDS. Perpendicular or homeotropic anchoring of SDS results in a change in the LC droplet geometry from (B) bipolar to (A) radial.

This change in anchoring propagates through the bulk of the LC droplet transforming the droplet from a bipolar configuration to a radial configuration (Figure 5.3). Furthermore, these two droplet configurations (bipolar and radial) are cylindrically and spherically symmetric, respectively. As such, we can readily measure the droplet configuration through the use of flow cytometry. A flow cytometer measures forward scattered light (related to the

droplet volume or size) and side scattered light (related to the internal complexity). For radial droplets, we observe an “S” shaped scatter plot (Figure 5.3A), due to the spherical symmetry of the droplet, while for bipolar droplets, we observe a more broad scatter plot (Figure 5.3B), due to the rotational freedom of the droplet and varying optical indices at the droplet interface.

5.3 Studying the effects of polymer side chain structure on polymer-LC interactions

To provide insight into mesogen side-chain structures that cause homeotropic anchoring of LCs, we first tested four designs based on the previously mentioned studies (Figure 5.1). Homopolymers with the desired mesogen were dispersed into the LC prior to emulsification in PBS. The side-chain functionalities of homopolymers, **1₁₈**, **2₁₈** and **3₂₁** all include biphenyl (Figure 5.4), a common rigid functional group in many mesogens such as 5CB; however the side chains differ in the design of the linker between the mesogen and backbone of the polymer. Homopolymers **1₁₈** and **2₁₈** differ by one carbon in the hydrocarbon linker length. Specifically, **1₁₈** and **2₁₈** have a C10 and C11 linear alkyl chain, respectively. Homopolymer **3₂₁** has an amide linking the biphenyl to the backbone along with a C5 linear alkyl spacer. Homopolymer **4₁₅** is a simple linear C11 hydrocarbon. The degree of polymerization (DP, $m \sim 20$) and molecular weights of homopolymers **1₁₈**, **2₁₈**, **3₂₁** and **4₁₅** are approximately similar (4–9 kDa), which enables a direct comparison of the hydrophobic side-chain structure of the homopolymers on the interactions with the LC droplet.

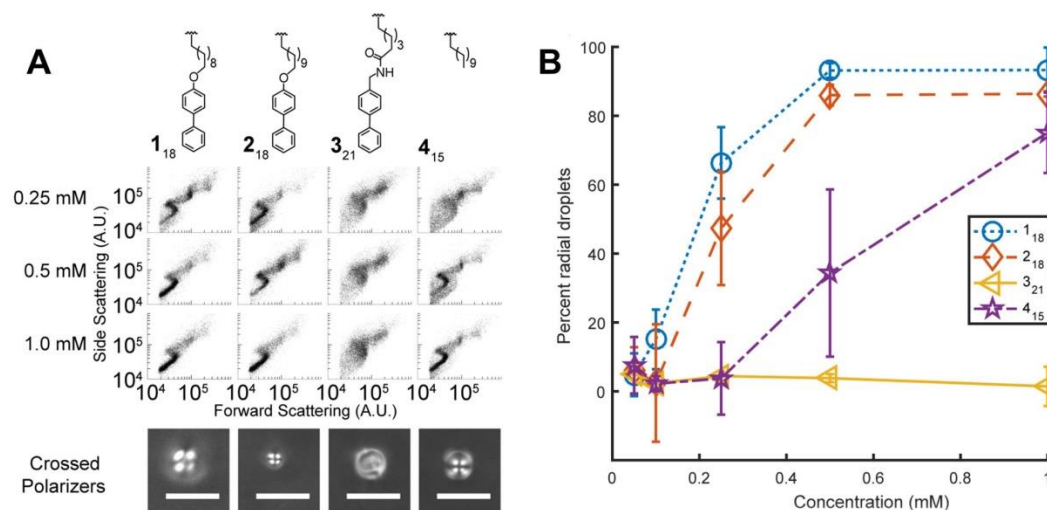


Figure 5.4 (A) Scatter plots generated from flow cytometry of LC droplets decorated with polymers 1-4 (Fig. 3.1-4) and crossed polarized microscopy images. (B) The percentage of radial droplets generated as a function of the polymer and polymer concentration, calculated from the scatter plots.

The percentage of radial droplets was dependent upon the polymer concentration (Figure 5.4A), likely due to a higher number density of hydrophobic side-chains at the LC droplet interface. We found that LC droplets decorated with **4**₁₅ required a higher homopolymer concentration than droplets decorated with **1**₁₈ or **2**₁₈ in order to transform the droplets to a radial configuration. The LC droplet configurations of droplets decorated with **1**₁₈ or **2**₁₈ was similar, so we speculate that either of these homopolymers, which differ by only one carbon in the alkyl linker, is sufficient for homeotropic anchoring. The LC droplet configuration was, however, sensitive to the structure of the hydrophobic side-chain. We observed that homopolymers **1**₁₈, **2**₁₈ and **4**₁₅ were able to generate radial droplets at the range of concentrations tested (0.25 to 1 mM); however, **3**₂₁ was unable to generate radial droplets (Figure 5.4A). Both flow cytometry scatter plots and optical micrographs collected under crossed polarizers verified these observations. Within the scope of substrates tested, it

remains unclear whether the short alkyl linker or the amide functional group prevents homeotropic anchoring (a point of discussion that is revisited later). Considering the surface area of an LC droplet and the assumption that all polymer chains adsorb to the droplet interface, we calculated that all homopolymers cause homeotropic anchoring at approximately the same side chain density. Specifically, we calculate an average surface area per hydrophobic unit of $\sim 30.6 \pm 7.4$, 35.3 ± 1.4 , 23.3 ± 2.3 and $54.8 \pm 21.8 \text{ \AA}^2$ for **1**₁₈, **2**₁₈ and **3**₂₁ and **4**₁₅ at 0.25 mM (moles of polymer with respect to 5CB volume), respectively. Comparison of these surface area values for the area per hydrophobic unit of the homopolymers (at 0.25 mM, $\sim 20\text{--}55 \text{ \AA}^2$), to the limiting area per classical single tail surfactants, such as SDS or CnTAB ($\sim 40\text{--}70 \text{ \AA}^2$); it is somewhat perplexing that the surfactant-like **4**₁₅ is unable to generate radial droplets at surface coverages comparable to those of small molecule surfactants.

To determine the underlying inability of homopolymer **3**₂₁ to generate radial droplets, we synthesized homopolymers **5**₂₀ and **6**₁₆ (Figure 5.2). For homopolymers **1**₁₈ and **5**₂₀ we observed that the length of the alkyl chain linking the biphenyl to the main chain affects the percentage of radial droplets generated (Figure 5.5). Specifically, **1**₁₈, bearing a C8 alkyl linker can generate approximately 25 % more radial droplets than **5**₂₀, which consists of a C5 alkyl linker. This observation is consistent with previous reports on the alkyl length dependence of surfactants on the anchoring of LC at the LC/aqueous interface.¹⁴ Further, these results indicate that the earlier ROMP-based copolymers bearing the short 4-phenylbenzyl side-chains would be unable to generate radial droplets under these conditions, as observed empirically.⁶

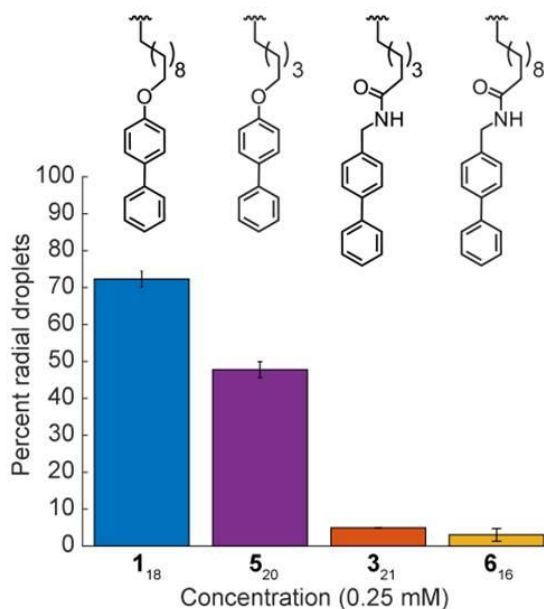


Figure 5.5 Percentage of radial configuration generated from LC droplets decorated with homopolymers **1₁₈**, **5₂₀**, **3₂₁**, and **6₁₆**.

By contrast, homopolymers **3₂₁** and **6₁₆** generate a small percentage of radial droplets (Figure 5.5). These results indicate that ether biphenyl mesogens are more effective at homeotropic anchoring and thereby generating radial droplets than the amide biphenyl mesogens. Several reasons could explain this phenomenon, one being the large lateral dipole moment of the amide, which is perpendicular to the longitudinal axis of the biphenyl side-chain. The dipole moment could perhaps bury itself in the dielectric medium (the LC), which would require the side-chain to lay parallel to the LC/aqueous interface. This side-chain ordering (planar to the LC interface), would be conducive to a bipolar, rather than a radial, droplet configuration. Indeed, the absence of a significant radial droplet population generated by homopolymers **3₂₁** and **6₁₆** suggests that the amide dipole is dominating the interactions of the polymer side-chains with the LC. This also illustrates the high sensitivity of the LC ordering to the structure of the hydrophobic side-chain. As such, when synthesizing

functional polymers, the hydrophobic side chain structure must be carefully considered to enable productive interactions with the LC.

Closer inspection of Figure 5.4 reveals a small difference in the percentage of droplets that assume a radial configuration in the presence of **1**₁₈ and **2**₁₈. Furthermore, the results of Figure 5.5 show an alkyl chain-length dependence on the LC droplet configuration. Since homopolymers **1**₁₈ and **2**₁₈ have side chains that differ in length by one carbon, we synthesized homopolymers **7**₁₆ and **8**₁₆ to determine if this difference can be attributed to an odd or even alkyl chain length (Figure 5.2). Within this library, homopolymers **7**₁₆, **1**₁₈, **2**₁₈, and **8**₁₆ have alkyl chain lengths of C9, C10, C11 and C12, respectively. At a concentration of 0.3 mM (moles of homopolymer with respect to 5CB volume), we observe a subtle difference in the ability of the homopolymers to generate radial droplets as a function of the alkyl chain length (Figure 5.6). When the linking aliphatic chain is C10, we observe a maximum percentage of droplets with a radial configuration compared to chain lengths of C5, C9, C11 or C12 (Figure 5.6). This results suggests that an even alkyl chain length is better than an odd alkyl chain length and specifically the hydrophobic side chain of **1**₁₈, with an alkyl chain length of C10, is more effective at triggering homeotropic anchoring compared to **7**₁₆, **2**₁₈, and **8**₁₆.

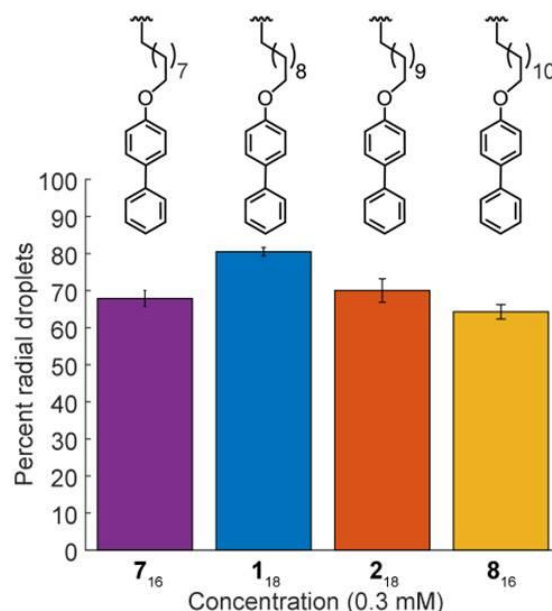


Figure 5.6 Percentage of radial configuration generated from LC droplets decorated with homopolymers 7_{16} , 1_{18} , 2_{18} , and 8_{16} .

Intrigued by the idea that subtle molecular changes in hydrophobic side chains can lead to drastic changes in the ordering of polymer-decorated LCs, we investigated the effect of the presence (9_{16} or 10_{19}) or absence (1_{18} or 2_{18}) of a nitrile terminal group on the ether-linked biphenyl side chain (Figure 5.2). Interestingly, we observed that side chains without a terminal nitrile functional group were able to generate a higher percentage of radial droplets than side chains bearing a nitrile group (Figure 5.7). This is a somewhat surprising result as we anticipated the presence of the nitrile group in the hydrophobic side chain would enhance the interactions with the nitrile-containing 5CB molecules due to dipole-dipole interactions. Nevertheless, from these collective studies, we have generated a set of design parameters for hydrophobic polymer side chains that are able to generate strong homeotropic anchoring at the LC interface. Based on these measurements, the side chain structure should incorporate a rigid mesogenic component, such as a biphenyl moiety. A single-tailed surfactant-like side

chain, as in the case of **4**₁₅, was unable to generate radial droplets at low concentrations. Moreover, incorporation of an amide or terminal nitrile group is not suitable, perhaps due to dipole-dipole interactions and as such, an ether biphenyl side chain is optimal. Lastly, the length of the hydrocarbon spacer connecting the rigid mesogenic component is vital for homeotropic anchoring of polymer decorated LCs; from these studies, a length of C10 was found to be best, inducing a higher percentage of droplets with radial configuration at lower concentrations (Figure 5.6). Based on these results, we conclude that the side chain used in **1**₁₈ is the optimal structure to trigger ordering transitions in the LC. In the next set of studies, we incorporated this mesogenic group into copolymers bearing hydrophilic moieties in order to probe the effect of copolymer composition and architecture on polymer-LC interactions.

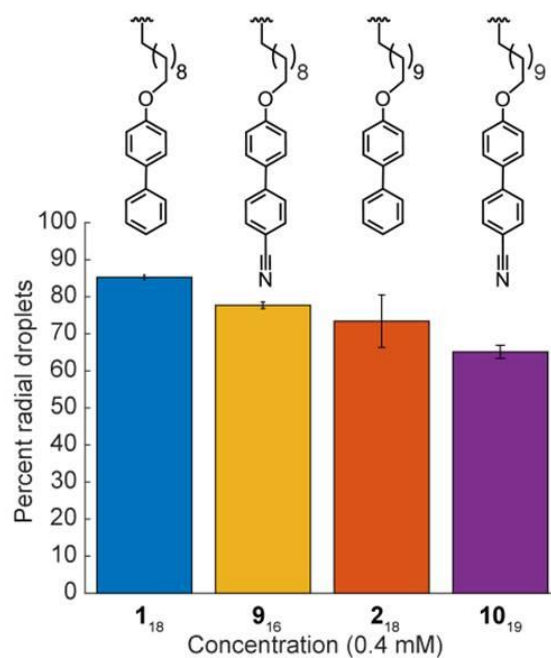


Figure 5.7 Percentage of radial configuration generated from LC droplets decorated with homopolymers **1**₁₈, **9**₁₆, **2**₁₈, and **10**₁₉.

5.4 Copolymer composition and architecture on LC ordering

Utilizing monomer **1**, the ether biphenyl rigid core identical to the hydrophobic side chain of **1**₁₈, we synthesized block and random copolymers consisting of poly(ethylene glycol) (12 repeat units), PEG12, as the hydrophilic unit (Figure 5.8, Table 5.1). Guided by the results described above, we used **1** as it was found to be effective at generating homeotropic anchoring of LCs. PEG12 was used simply as a model system.

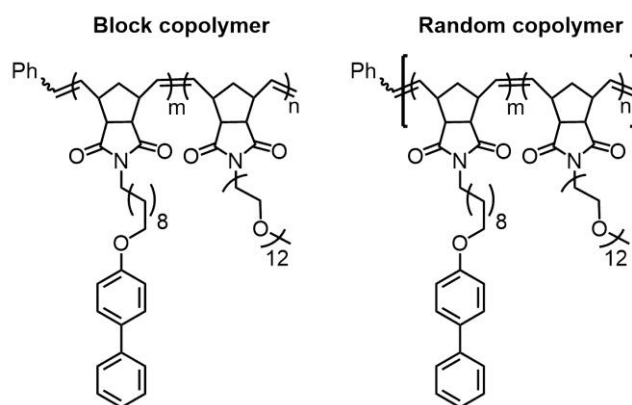


Figure 5.8 Chemical structures of copolymers synthesized by ROMP used in this study

We varied the the ratio of hydrophobic, m , to hydrophilic, n , units of random and block copolymers to compare the effect of copolymer architectures of similar compositions (Figure 5.8). For both copolymer architectures, we hypothesized that copolymers rich in mesogenic repeat units will generate radial droplets at low concentrations. First, we examined the effect of block copolymer composition on its ability to generate radial droplets. Based on previous work, we expected that even at high hydrophilic compositions, radial droplet configurations would predominantly form.³

Table 5.1 Copolymer library for examining copolymer-LC interactions

entry	IUPAC	M_n (Da) ^a	(M_w/M_n) ^b	DP (m) ^c	DP (n) ^d	wt fraction ^e
1	1₁₇-b-PEG12₂₉	27,680	1.02	17 (30)	29 (10)	0.29
2	1₃₀-b-PEG12₂₆	32,350	1.02	30 (27)	26 (13)	0.53
3	1₂₆-b-PEG12₁₆	22,970	1.01	26 (20)	16 (20)	0.43
4	1₄₇-b-PEG12₁₅	32,170	1.02	47 (32)	15 (8)	0.68
5	1₁₂-ran-PEG12₂₀	19,290	1.02	12 (13)	20 (27)	0.29
6	1₁₄-ran-PEG12₁₇	18,650	1.01	14 (20)	17 (20)	0.35
7	1₂₆-ran-PEG12₁₉	25,240	1.02	26 (27)	19 (13)	0.48
8	1₃₃-ran-PEG12₁₇	27,090	1.02	33 (32)	17 (8)	0.57

^a M_n denotes number-average molecular weight. ^b M_w denotes weight-average molecular weight. ^c DP_m denotes degree of polymerization of the first block, **1**; (m) denotes the theoretical DP of the first block. ^d DP_n denotes degree of polymerization of the second block, **PEG12**; (n) denotes the theoretical DP of the second block. ^e weight fraction of the hydrophobic block.

The block copolymers did not generate a substantial population of radial droplet configurations (Figure 5.9). The most hydrophobic composition (**1₄₇-b-PEG12₁₅**) generates a small number of radial droplets (~20%) at a polymer concentration of 1mM (Figure 5.9A). Comparing the surface area available per hydrophobic unit of the block copolymer (at 1 mM) and the homopolymer **1₁₈**, we find the surface density of hydrophobic repeat units to be somewhat comparable. For example, the hydrophobic surface densities of the block copolymer and the homopolymer were calculated as 3.0 Å² and 10.6 Å², respectively. This suggests that the hydrophobic units of the block copolymer are unable to interdigitate with the LC.

Random copolymers were synthesized (Figure 5.8) to test whether dispersing the mesogenic components within the hydrophilic units can lead to homeotropic anchoring and the generation of radial droplets. Intriguingly, random copolymers with a smaller hydrophobic weight (wt) fraction (**1₂₆-ran-PEG12₁₉** and **1₁₄-ran-PEG12₁₇** with 0.48 and 0.35 respectively) were able to generate radial droplets at 1 mM copolymer concentration (Figure 5.9B). The random copolymer with the lowest hydrophobic wt fraction (**1₁₂-b-PEG12₂₀**, 0.29

wt fraction) was unable to generate radial droplets. This suggests that the minimum hydrophobic wt fraction required to generate radial droplets is 0.35 for the random copolymer architecture. For 1 mM random copolymer (with respect to the volume of 5CB), with a hydrophobicity index of 0.35, we calculate the hydrophobic surface density as 16.9 \AA^2 . This is more comparable to the hydrophobic surface density calculated for homopolymer **1**₁₈, (10.6 \AA^2).

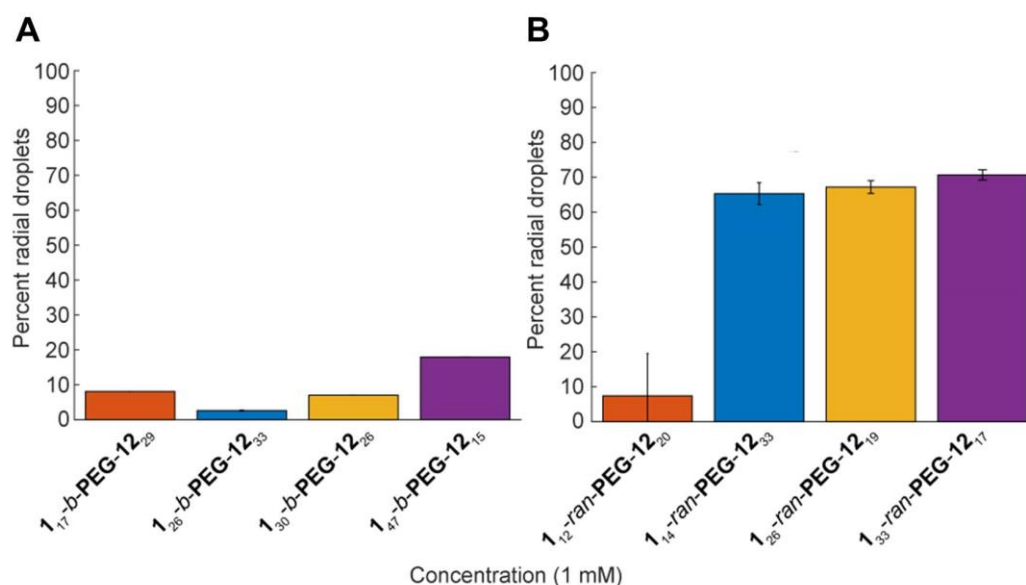


Figure 5.9 The percentage of radial droplets generated for (A) block copolymer-decorated LC droplets and (B) random copolymer-decorated LC droplets at 1 mM copolymer concentration. The block copolymer was unable to generate a significant amount of radial droplets even for copolymers of high mesogen content (~20 %). In contrast, random copolymers of varying mesogen content were able to generate a significant number of droplets (> 70 %) with radial configuration.

Comparing the block and random copolymer architectures with similar compositions at 1 mM, we observed that the random copolymer is suitable to generate radial droplet configurations. We then examined the effect of composition (using block and random copolymers of 0.53 and 0.57 hydrophobic mol percent, respectively) on a range of copolymer concentrations (Figure 5.10). Intriguingly, the random copolymer, **1**₃₃-ran-PEG12₁₇, was able

to generate radial droplets at low concentrations (0.1 mM). In contrast, the block copolymer of similar composition generated droplets with approximately 10 % radial configuration, even at the highest concentration tested (1 mM), similar to the previous measurements (Figure 5.9). These results demonstrate that random copolymers are able to trigger changes in the LC geometry more effectively than block copolymers.

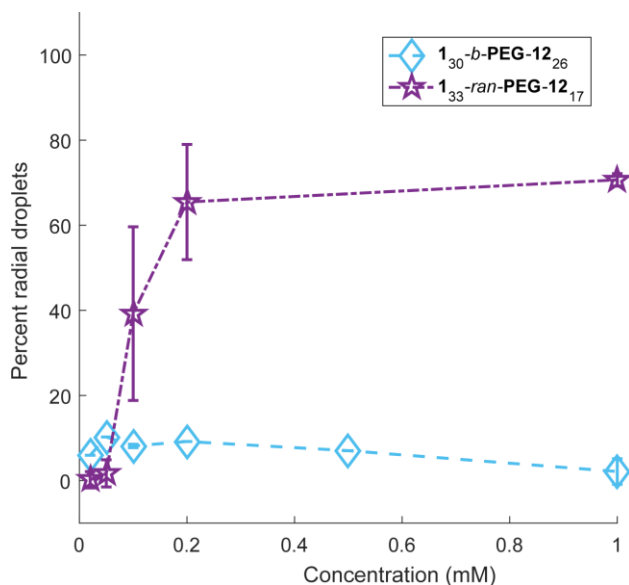


Figure 5.10 Comparison of the random and block copolymer architectures with a similar hydrophobic index (ratio of hydrophobic to hydrophilic). The random copolymer is able to generate radial droplets at a much lower concentration (with respect to the 5CB volume) than the block copolymer of similar hydrophobic index.

5.5 The organization of copolymers at the air–water interface

Both the random and block copolymers possess sufficiently high numbers of hydrophobic repeat units (mesogens) to be able to trigger homeotropic anchoring of the LC, yet this is only observed with the random copolymer. The previous results suggest that the copolymers order at the interface of the LC droplet in a manner, which depends upon the copolymer architecture. Accordingly, we performed Langmuir isotherms to determine if differences in the organization of the random and block copolymers at the aqueous interface

could be detected (Figure 5.11). To perform these experiments, 0.5 mg/mL of copolymer in chloroform was spread on an aqueous trough to produce a copolymer film at the aqueous/air interface. For the block copolymer (Figure 5.11A), we observed multiple features such as an initial rise in the pressure, a plateau, and finally a steep rise at small surface areas at the so-called “brush” region.¹⁵ Upon completion of barrier compression (25 cm²/min), the pressure dropped slowly. Furthermore, there was hysteresis in the expansion isotherm (-25 cm²/min) upon expansion. A second compression of the copolymers **1₃₀-*b*-PEG12₂₆** and **1₄₇-*b*-PEG12₁₅** was performed (Figure 5.13). The second compression isotherms exhibited a lower pressure when compared to the first isotherm until the “brush” region was reached (at a similar area per molecule) wherein the pressures from the first and second compression isotherms overlapped. We did not observe the isotherm to depend on the rate of the compression (Figure 5.14).

Lee and coworkers were able to observe homeotropic anchoring with their block copolymers (Figure 5.1A) using a Langmuir-Schaefer transfer with a polymer density of 1271 Å² per copolymer, which corresponds to a surface area of ~84.7 Å² per hydrophobic unit. For the copolymers reported here, this would correspond to the “brush” region of the isotherm (Figure 5.11A). This hydrophobic surface density is much larger than that calculated for the ROMP polymer systems (3.0 Å² per hydrophobic unit) yet homeotropic anchoring was not observed for the ROMP copolymers. These differences in the hydrophobic surface densities of the copolymers and the inability to obtain homeotropic anchoring suggest that the ROMP copolymer backbone has a large effect on the organization of the copolymer at the LC/aqueous interface. Furthermore, when the isotherms were normalized by the number of mesogens in the block copolymer, we observed a ranking of the isotherms based on the area of the initial rise in the pressure. For example, the copolymer consisting of the largest number of mesogen units also exhibited the largest area per mesogen with the initial rise in pressure.

For the random copolymers (Figure 5.11B), only one single rise in the surface pressure was observed. The area where this initial rise occurs, $\sim 1500\text{-}3000 \text{ \AA}^2$ per molecule, is smaller than that for most of the block copolymers ($\sim 5000\text{-}10000 \text{ \AA}^2$ per molecule) with the exception of **1₄₇-b-PEG12₁₅**. Nevertheless, when these isotherms were normalized by the number of mesogens, we observed a ranking similar to that of the block copolymers.

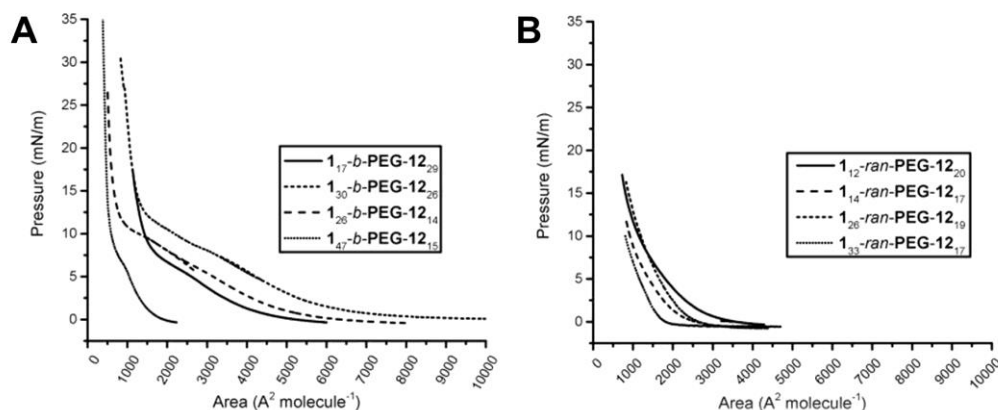


Figure 5.11 Langmuir surface pressure-area isotherms of (A) block and (B) random copolymers. Upon compression, the block copolymers exhibit an initial rise followed by a plateau region and finally a very steep rise. The random polymers do not exhibit these features and we observed the surface pressure to rise as the area decreases.

The previous studies provide evidence that a random copolymer architecture is able to organize at the LC interface in such a manner as to enable homeotropic anchoring, whereas a block copolymer architecture is incapable of doing so. We were encouraged to apply these findings to produce a responsive system, consisting of a random copolymer bearing a peptide moiety as the hydrophilic unit.

5.6 Enzyme-responsive copolymer-decorated LC droplets

By applying the optimized design parameters described in the previous sections, our goal was to produce a random copolymer that was capable of amplifying a targeted

biomolecular event to the micron scale through interactions of the copolymer with LC droplets. Our previous results showed that the mesogenic side chain **1** (Figure 5.2) is the optimal hydrophobic structure to generate homeotropic anchoring. Furthermore, the copolymer architecture and composition experiments indicated that a random copolymer with a hydrophobic wt fraction ≥ 0.35 would yield radial droplets. As such, we were motivated to use these principles to improve the original ROMP-based design reported by Ma and coworkers,⁶ by amplifying proteolytic cleavage events of a copolymer bearing peptides that are recognized by the enzyme, thermolysin. To determine if unprocessed (uncleaved) and enzymatically processed (cleaved) copolymers could give rise to dissimilar configurations of LC droplets, we synthesized an uncleaved and an authentically cleaved peptide polymer amphiphile (PPA) to simulate these structures (Figure 5.12). A random copolymer structure was utilized as this was determined to be the optimal architecture. For the uncleaved and cleaved peptide sequences, we used GPLGLAGK (containing a C-terminal amide), and GPLG (containing a C-terminal carboxylate), respectively. The resulting PPAs consisted of 0.65 and 0.68 hydrophobic wt fraction, respectively.

First, we decorated LC droplets with the uncleaved and cleaved PPAs using a copolymer concentration of 1 mM. Using optical microscopy (under crossed polarizers), the number of droplets with a radial configuration were counted and compared to the total number of droplets in order to determine the percentage of radial droplets. A small majority of LC droplets decorated with the uncleaved PPA exhibited a radial configuration (~55%). LC droplets decorated with the cleaved PPA exhibited a significantly lower percentage of radial droplets (~20%). This result suggests that when the uncleaved PPA is enzymatically processed by thermolysin, the PPA structural change is amplified *via* the LC to produce an optically detectable change in droplet configuration. Ongoing work is now aimed at characterizing and detecting the *in situ* enzyme cleavage of peptide-containing copolymers.

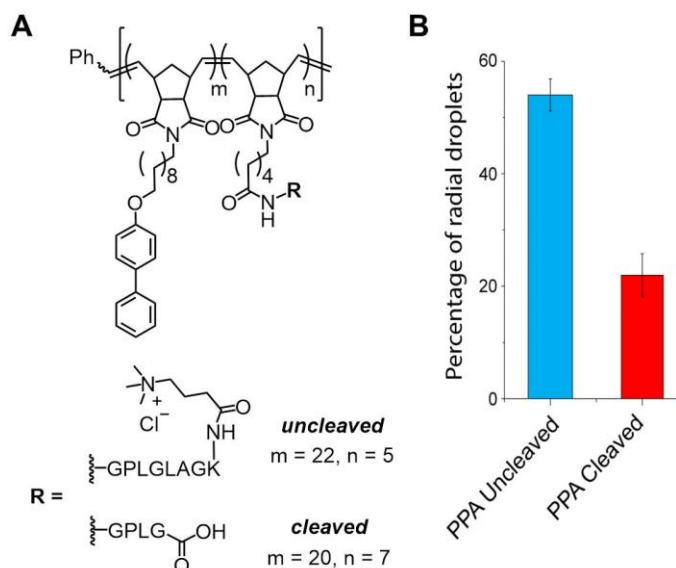


Figure 5.12 Peptide polymer amphiphiles (PPAs), synthesized as random copolymers, which incorporate either cleaved or uncleaved peptides to simulate copolymer structures prior to and after thermolysin cleavage. (A) Chemical structures of PPAs. The uncleaved and cleaved PPA consist of 0.65 and 0.68 wt. fraction hydrophobic side chain, respectively. (B) The percentage of LC droplets with a radial configuration from 5CB decorated with either uncleaved or cleaved PPAs (1 mM).

5.7 Conclusion and future outlook

Herein, we have described a systematic study to identify a set of rational design principles for amphiphilic polymers derived by ROMP that can trigger responses in LC systems. The ability to tailor not only the selectivity of the response but also the rate of the response by incorporating a variable number of reactive side chains and without compromising polymer-LC interactions, is an immense challenge. First, we investigated the effect of the hydrophobic side chain on homopolymer anchoring at the LC/aqueous interface. We identified an optimal structure that proved efficient at triggering homeotropic anchoring of LCs. Incorporating this optimized mesogen in either block or random copolymers, we found a clear difference in the ability of copolymers of different architectures to generate

radial droplets. Specifically, block copolymers were unable to generate a significant population of radial droplets even for the hydrophobic-rich compositions ($< 20\%$ for 0.68 hydrophobic wt fraction) and at high concentrations (1 mM). Conversely, the random copolymer was able to generate radial droplets for both hydrophobic-rich and poor compositions (0.35 wt fraction). The inability of the ROMP block copolymers to generate radial droplets is interesting when compared to block copolymers synthesized by RAFT polymerization, which were able to generate a radial configuration despite having a small wt fraction of hydrophobic units (0.07).⁴ In this work, Lee proposed that the polymer backbone along with hydrophobic side chains was able to penetrate the LC, while the hydrophilic block dissolved in the continuous phase. One key difference between the two types of copolymers is the backbone chemistry, which appears to have a significant impact on polymer organization at the LC/aqueous interface. The ROMP backbone, for example, is bulky and rigid, which restricts the rotational motion of the copolymer and may limit its ability to insert the backbone and hydrophobic side chains into the LC. Nevertheless, this behavior does not appear to be dependent upon the density of hydrophobic units at the interface of the droplets, which suggests that ROMP copolymers order differently depending on the polymer architecture. This finding was corroborated by Langmuir isotherms of block and random copolymers, which reorganize differently in response to isotherm compression.

Finally, in employing these design principles, we investigated random copolymer-decorated LC droplets, comprised of peptide polymer amphiphiles (PPAs) that trigger ordering transitions in the LC when the peptide side chain is processed by the enzyme thermolysin. We observed a greater percentage of radial droplets for the uncleaved PPA-decorated LC droplets than for the cleaved PPA decorated droplets. Further experiments will focus on *in situ* cleavage of the PPAs and the observation of biomolecular event-triggered LC ordering transitions. The ability to vary the number of hydrophilic units within the random

copolymer and still generate radial droplets should not be understated. Ultimately, we may find that the ROMP architecture is not practical for integrating with the LC for future applications. Alternate strategies may need to be considered in this regard, such as reducing the polyolefin backbone *via* common methods such as Pd-catalyzed hydrogenation to instill greater polymer flexibility or employing different polymerization methods. Despite these shortcomings, ROMP affords the ability to incorporate complex functionality with ease and high reproducibility, which makes it a method that is ideally suited, at present, for the design of bioactive systems for technological applications.

5.8 Acknowledgements

Chapter 5 contains material that is currently being prepared for submission for publication: "Design of Triggerable Amphiphiles with Mesogenic Side-Chains for Multi-Scale Responses with Liquid Crystals," Joel Pendery, Lisa Adamiak, Jiawei Sun, Nathan C. Gianneschi, and Nicholas L. Abbott. The dissertation author was the co-first author on this pending manuscript.

5.9 Methods

5.9.1 Materials

Reagents were purchased from Sigma-Aldrich, Fisher Scientific, TCI, and Acros and were used without further purification unless otherwise specified. Sealed ampules of CDCl₃ or DMF-d₇ (Cambridge Isotopes) for monitoring polymerization reactions were used without further modification. Reactions were monitored with analytical TLC (glass plate 60 F254, Merck). Column chromatography was performed using silica gel 60 (230 - 400 mesh, 40 – 63 μm). N-(hexanoic acid)-*cis*-5-norbornene-*exo*-dicarboximide was prepared as previously described.¹⁶ (H₂IMes)(pyr)₂Cl₂Ru=CHPh was prepared from (H₂IMes)(PCy₃)Cl₂Ru=CHPh

according to a literature procedure.¹⁰ Peptides were synthesized by standard solid phase peptide chemistry on rink amide resin (100-200 mesh, Aapptec) using an APPTTEC Focus XC automated synthesizer following previously published procedures.⁶ *cis*-5-Norbornene-*exo*-2,3-dicarboxylic anhydride, 4-phenylphenol, 4-phenylbenzylamine, 4'-Hydroxy-4-biphenylcarbonitrile, decylamine, and undecylamine were purchased from commercial sources and used without further purification.

5.9.2 General Methods

NMR spectra were recorded on a Varian Mercury 400 MHz, Bruker AVA 300 MHz, and a Varian VX 500 MHz in DMF-d₇, CD₂Cl₂, or CDCl₃ and referenced to the residual protons. HR and EI-MS (electron impact mass spectrometry) data were obtained on an Agilent 6230 HR-ESI-TOF MS and a Thermo Trace Plus GC-MS (70 eV) at the Molecular Mass Spectrometry Facility at the UCSD Chemistry and Biochemistry Department. For EI-MS, the molecular fragments are listed as the mass and charge ratio (*m/z*), followed by the intensities as a percentage value relative to the intensity of the base peak (100%). The molecular ion obtains the abbreviation [M⁺]. All Polymerizations were conducted in J Young NMR tubes (5 mm diameter) for monitoring via ¹H-NMR or in vials in a glove box under dinitrogen atmosphere at room temperature. Polymer dispersities and molecular weights were determined by size-exclusion chromatography (Phenomenex Phenogel 5u 10, 1K-75K, 300 x 7.80 mm in series with a Phenomex Phenogel 5u 10, 10K-1000K, 300 x 7.80 mm (0.05 M LiBr in DMF)) using a Shimadzu LC-AT-VP pump equipped with a multi-angle light scattering detector (DAWN-HELIOS: Wyatt Technology), a refractive index detector (Hitachi L-2490) and a UV-Vis detector (Shimadzu SPD-10AVP) normalized to a 30,000 MW polystyrene standard (Flow rate: 0.75 mL/min). RP-HPLC analyses were performed on a Jupiter Proteo90A phenomenex column (150 x 4.60 mm) using a Hitachi-Elite LaChrom L-

2130 pump equipped with a UV-Vis detector (Hitachi-Elite LaChrome L-2420) using a binary gradient (Buffer A: 0.1% TFA in water; Buffer B: 0.1% TFA in acetonitrile; Flow rate: 1 mL/min). Peptides were purified using a Jupiter Proteo90A Phenomenex column (2050 x 25.0 mm) on a Waters DeltaPrep 300 system using a binary gradient (Buffers A and B; Flow rate: 22 mL/min). For enzyme-treatment of PPA-coated LC microdroplets with thermolysin, see chapter 4 methods.

5.9.3 Characterization of LC droplets with optical microscopy

LC droplets were imaged using an Olympus IX71 inverted microscope with either a 60x objective or 100x oil immersion objective. Bright-field and polarized light micrographs of the LC droplets were collected with a Hamamatsu 1394 ORCAER CCD camera connected to a computer and controlled through SimplePCI imaging software. LC droplet characterization was limited to only LC droplets that were diffusing (translating and/or rotating).

5.9.4 Surface-pressure area isotherm measurements

For description of methods used for Langmuir isotherm experiments, see chapter 4 methods.

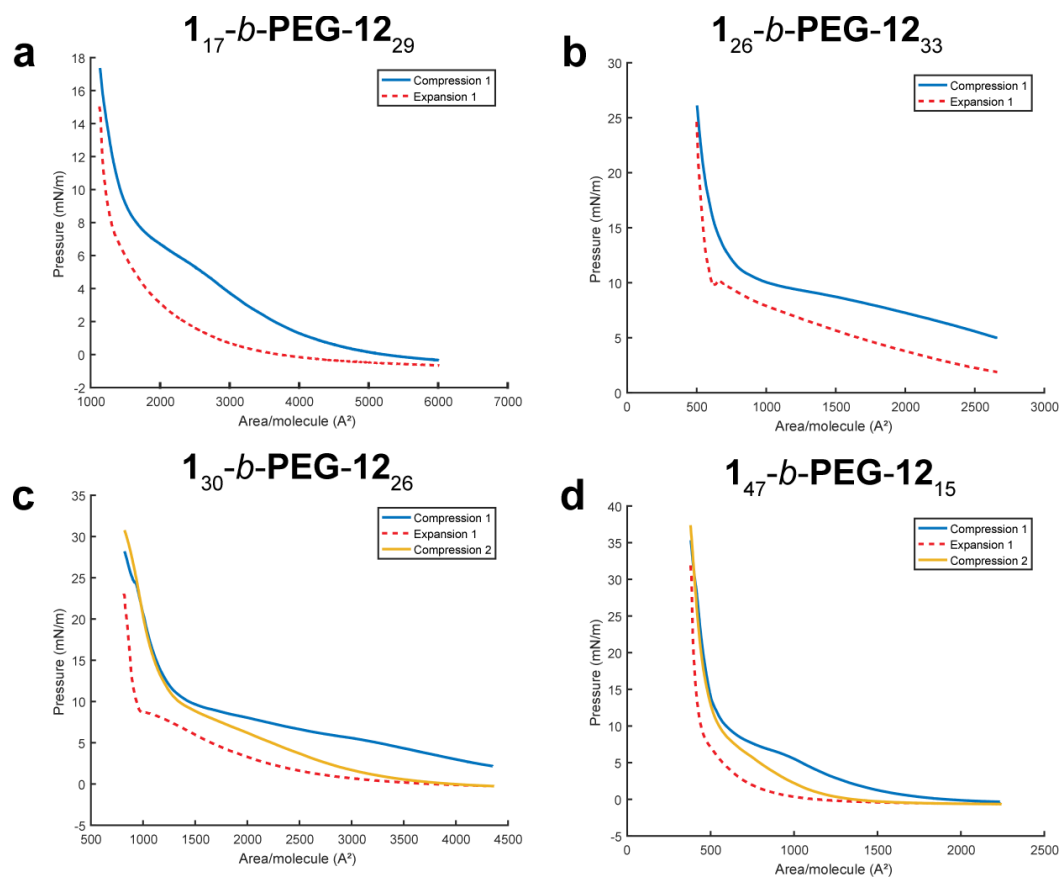


Figure 5.13 Langmuir isotherms for block copolymer polymers (A) 1_{17} -*b*-PEG12 $_{29}$, (B) 1_{26} -*b*-PEG12 $_{33}$, (C) 1_{30} -*b*-PEG12 $_{26}$ and (D) 1_{47} -*b*-PEG12 $_{15}$ exhibit hysteresis. Upon expansion, at high pressures the isotherm drops rapidly before leveling off and approaching zero. A second compression was performed for (C) and (D), which shows a deviation of the pressure of the isotherm from the first compression until the “brush” region is observed and then the pressures match again.

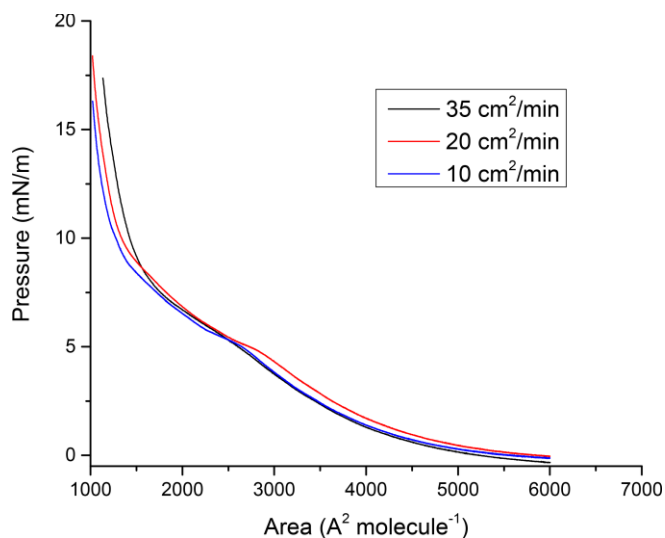


Figure 5.14 Langmuir isotherms for **1₁₇-b-PEG12₂₉** at various compression rates. All features were observed (initial rise, “plateau” and “brush” regions) and there were no major deviations of the isotherm as a function of barrier speed.

5.9.5 Representative homopolymer procedure

Grubbs’ modified second generation catalyst ($\text{H}_2\text{IMes})(\text{pyr})_2\text{Cl}_2\text{Ru}=\text{CHPh}$ (1 equiv) was dissolved in anhydrous CDCl_3 and added to **1** (20 equiv) in CDCl_3 to a final volume of 450 μL in a J Young NMR tube. The tube was inverted several times to ensure mixing. A ^1H NMR spectrum was recorded to confirm complete monomer consumption after 30 min. The homopolymer was terminated with 150 μL EVE and an aliquot (15 μL) was removed to characterize the polymer molecular weight and dispersity (\bar{D} or M_w/M_n) via SEC-MALS. The homopolymer was precipitated using cold Et_2O and centrifuged at 3000 rpm for 7 min. The Et_2O was decanted and the pellet was triturated two times with DMF and cold Et_2O , followed by centrifugation. The remaining pellet was washed several times with Et_2O and dried in vacuo or dissolved in water with a minimal amount of ACN and lyophilized to afford a white solid.

5.9.6 Representative block copolymer procedure

Grubbs' modified second generation catalyst (1 equiv) was dissolved in anhydrous CDCl₃ and added to **1** (20 equiv) in CDCl₃ to a final volume of 400 μL. After 1 h, an aliquot (15 μL) of the homopolymer was removed from the glove box and terminated with EVE (20 μL) for SEC-MALS analysis (first block). **PEG12** or peptide monomer (100 μL, 20 equiv) in CDCl₃ or DMF, respectively, was added to the solution. The copolymer was terminated with EVE (150 μL) after 2 h and analyzed by SEC-MALS. Purification was carried out as described in the homopolymer procedure.

5.9.7 Representative random copolymer procedure with PEG12 monomer

Grubbs' modified second generation catalyst (1 equiv) was dissolved in anhydrous CDCl₃ and added to a solution containing **1** (20 equiv) and **PEG12** (20 equiv) in CDCl₃ to a final volume of 400 μL. After 1 h, a ¹H NMR spectrum was recorded to confirm complete monomer consumption. The random copolymer was terminated with EVE (150 μL), followed by SEC-MALS analysis. Purification was carried out as described in the homopolymer procedure.

5.9.8 Representative random copolymer procedure using peptide monomer

Grubbs' modified second generation catalyst (1 equiv) was dissolved in anhydrous DMF-d₇ and added to a solution containing peptide (250 μL, 10 equiv) in DMF-d₇. An aliquot from a solution of **1** (12 μL, 1.7 equiv) in CDCl₃ was added to the reaction every five minutes over the course of an hour to reach a final volume of 450 μL. After 2 h, a ¹H NMR spectrum was recorded to confirm the complete consumption of both monomers and to estimate monomer ratios from the relative integration of biphenyl proton resonances and polymer backbone olefin protons. The random copolymer was terminated with EVE (150

μL), followed by SEC-MALS analysis. Purification was carried out as described in the homopolymer procedure.

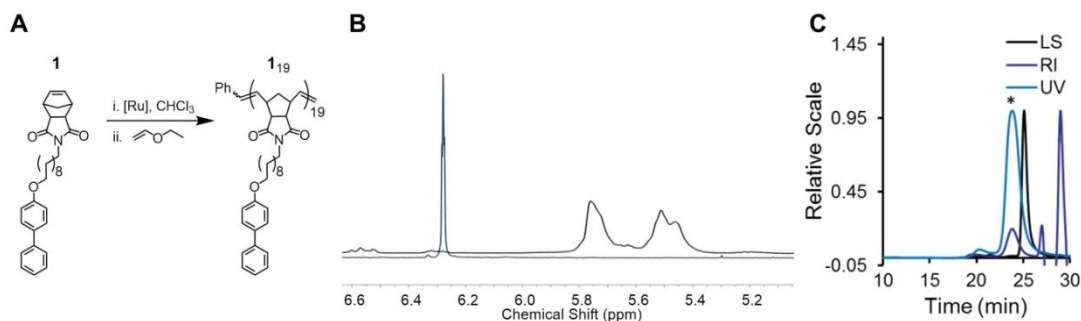


Figure 5.15 Polymerization and characterization of **1₁₉**. (A) Polymerization of monomer **1** to afford homopolymer **1₁₉**. (B) $^1\text{H-NMR}$ of **1** to confirm complete polymerization (M:I = 20:1). Spectra of the monomer and polymer depict olefin resonances and are shown in blue and black, respectively. (C) SEC-MALS data of polymer **1₁₉**; $M_n = 8,868$ g/mol, $M_w/M_n = 1.151$, ($dn/dc = 0.179$). The peak analyzed is indicated by (*).

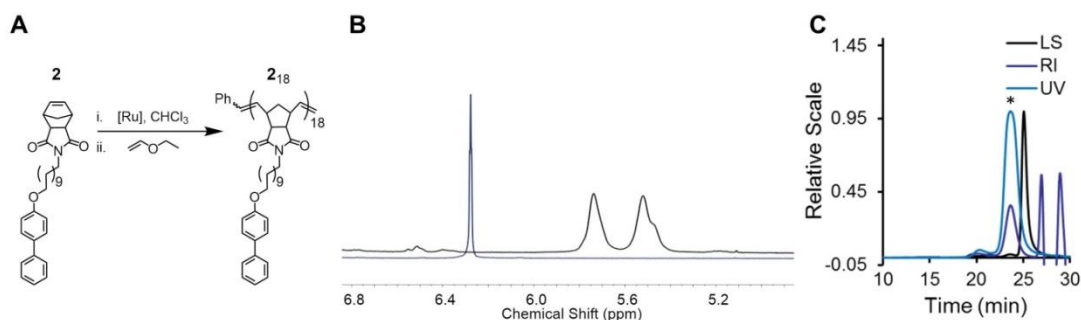


Figure 5.16 Polymerization and characterization of **2₁₈**. (A) Polymerization of monomer **2** to afford homopolymer **2₁₈**. (B) $^1\text{H-NMR}$ of **2** to confirm complete polymerization (M:I = 20:1). Spectra of the monomer and polymer depict olefin resonances and are shown in blue and black, respectively. (C) SEC-MALS data of polymer **2₁₈**; $M_n = 8,525$ g/mol, $M_w/M_n = 1.040$, ($dn/dc = 0.179$). The peak analyzed is indicated by (*).

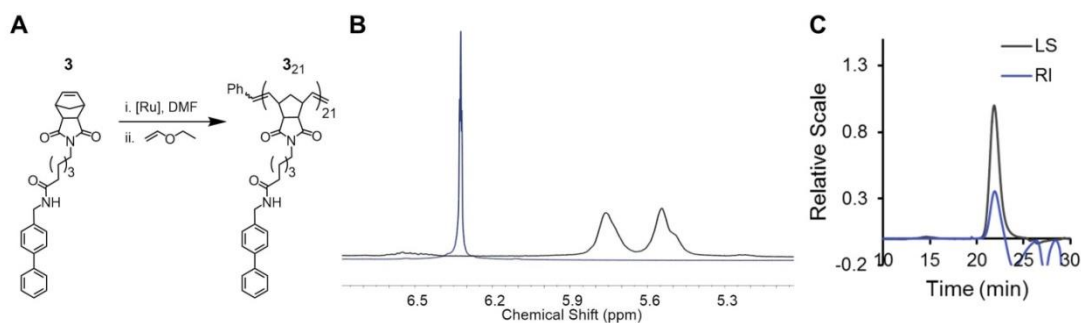


Figure 5.17 Polymerization and characterization of **3₂₁**. (A) Polymerization of monomer **3** to afford homopolymer **3₂₁**. (B) ¹H-NMR of **3** to confirm complete polymerization (M:I = 20:1). Spectra of the monomer and polymer depict olefin resonances and are shown in blue and black, respectively. (C) SEC-MALS data of polymer **3₂₁**; Mn = 9,426 g/mol, Mw/Mn = 1.010, (dn/dc = 0.179).

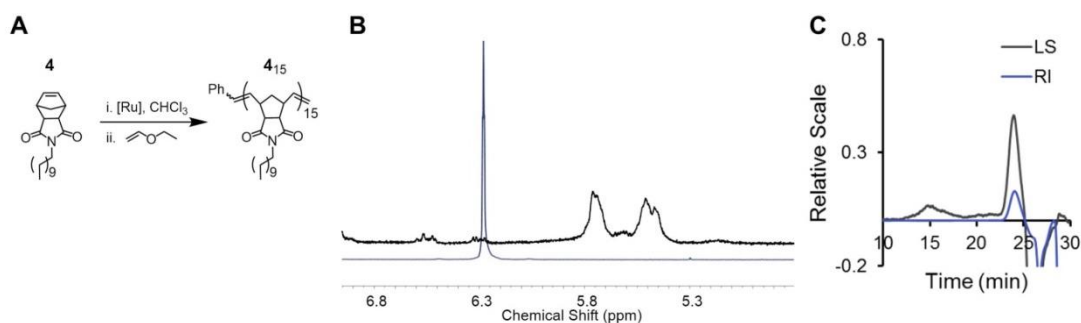


Figure 5.18 Polymerization and characterization of **4₁₅**. (A) Polymerization of monomer **4** to afford homopolymer **4₁₅**. (B) ¹H-NMR of **4** to confirm complete polymerization (M:I = 20:1). Spectra of the monomer and polymer depict olefin resonances and are shown in blue and black, respectively. (C) SEC-MALS data of polymer **4₁₅**; Mn = 4,726 g/mol, Mw/Mn = 1.437, (dn/dc = 0.179).

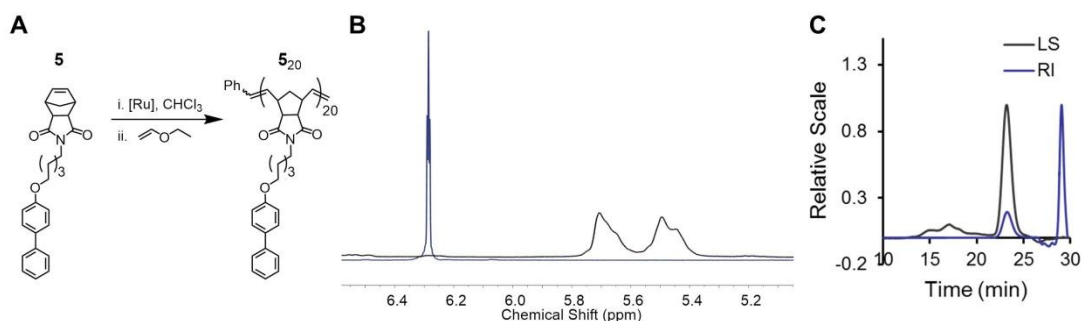


Figure 5.19 Polymerization and characterization of **5₂₀**. (A) Polymerization of monomer **5** to afford homopolymer **5₂₀**. (B) ¹H-NMR of **5** to confirm complete polymerization (M:I = 20:1). Spectra of the monomer and polymer depict olefin resonances and are shown in blue and black, respectively. (C) SEC-MALS data of polymer **5₂₀**; Mn = 7,880 g/mol, Mw/Mn = 1.035, (dn/dc = 0.179).

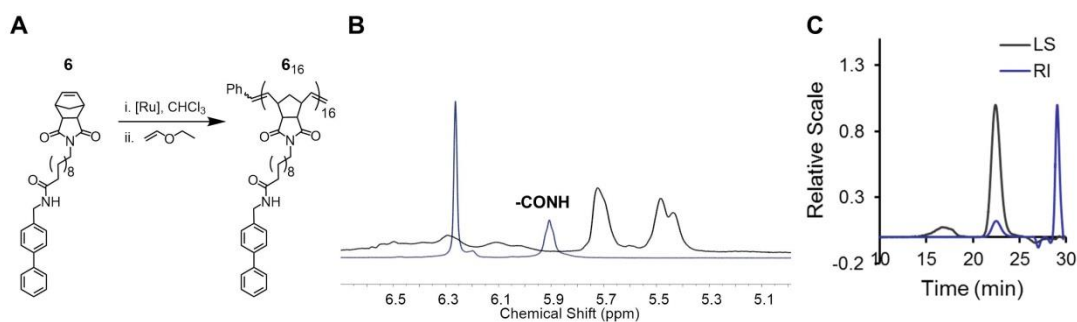


Figure 5.20 Polymerization and characterization of **6₁₆**. (A) Polymerization of monomer **6** to afford homopolymer **6₁₆**. (B) ¹H-NMR of **6** to confirm complete polymerization (M:I = 20:1). Spectra of the monomer and polymer depict olefin resonances and are shown in blue and black, respectively. The amide resonance in the monomer spectrum is indicated (-CONH). (C) SEC-MALS data of polymer **6₁₆**; Mn = 8,011 g/mol, Mw/Mn = 1.063, (dn/dc = 0.179).

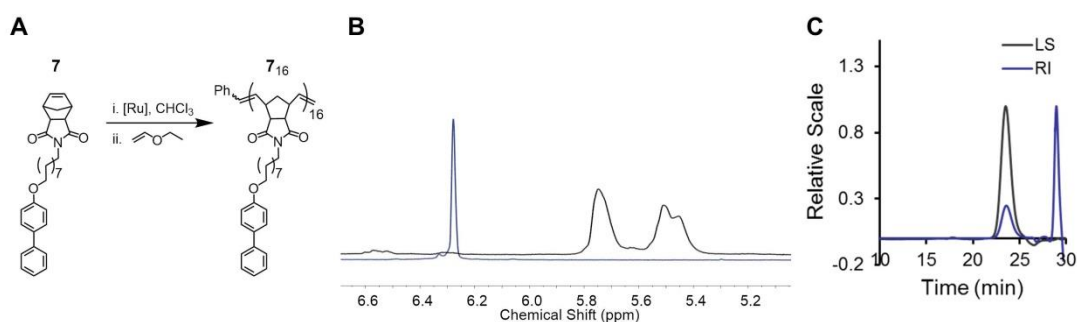


Figure 5.21 P Polymerization and characterization of **7₁₆**. (A) Polymerization of monomer **7** to afford homopolymer **7₁₆**. (B) ¹H-NMR of **7** to confirm complete polymerization (M:I = 20:1). Spectra of the monomer and polymer depict olefin resonances and are shown in blue and black, respectively. (C) SEC-MALS data of polymer **7₁₆**; Mn = 7,142 g/mol, Mw/Mn = 1.024, (dn/dc = 0.179).

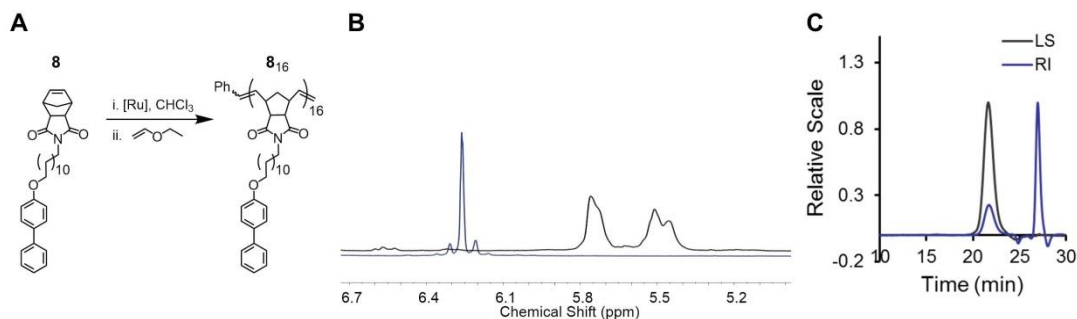


Figure 5.22 Polymerization and characterization of **8₁₆**. (A) Polymerization of monomer **8** to afford homopolymer **8₁₆**. (B) ¹H-NMR of **8** to confirm complete polymerization (M:I = 20:1). Spectra of the monomer and polymer depict olefin resonances and are shown in blue and black, respectively. (C) SEC-MALS data of polymer **8₁₆**; Mn = 8,139 g/mol, Mw/Mn = 1.017, (dn/dc = 0.179).

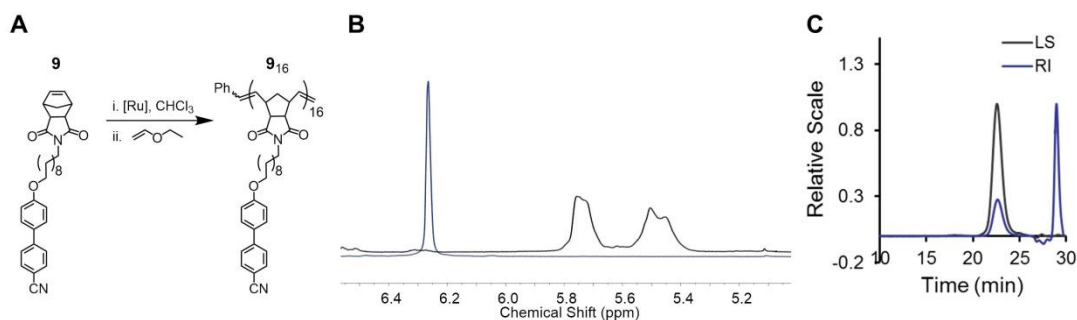


Figure 5.23 P Polymerization and characterization of **9₁₆**. (A) Polymerization of monomer **9** to afford homopolymer **9₁₆**. (B) ¹H-NMR of **9** to confirm complete polymerization (M:I = 20:1). Spectra of the monomer and polymer depict olefin resonances and are shown in blue and black, respectively. (C) SEC-MALS data of polymer **9₁₆**; Mn = 8,077 g/mol, Mw/Mn = 1.017, (dn/dc = 0.179).

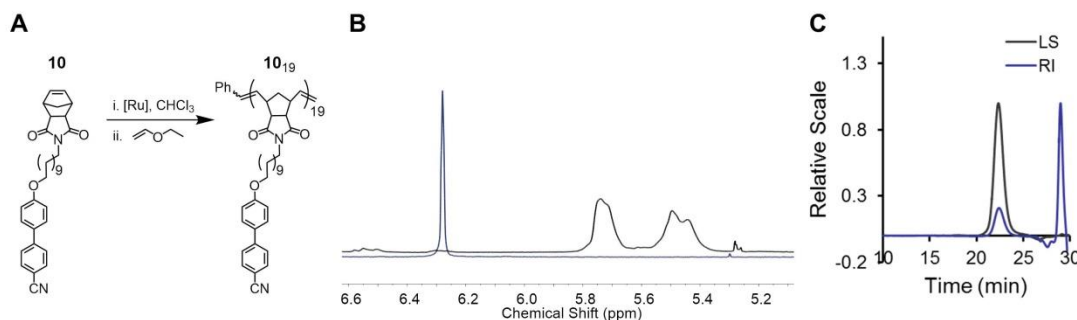


Figure 5.24 Polymerization and characterization of **10₁₉**. (A) Polymerization of monomer **10** to afford homopolymer **10₁₉**. (B) ¹H-NMR of **10** to confirm complete polymerization (M:I = 20:1). Spectra of the monomer and polymer depict olefin resonances and are shown in blue and black, respectively. (C) SEC-MALS data of polymer **10₁₉**; Mn = 9,746 g/mol, Mw/Mn = 1.021, (dn/dc = 0.179).

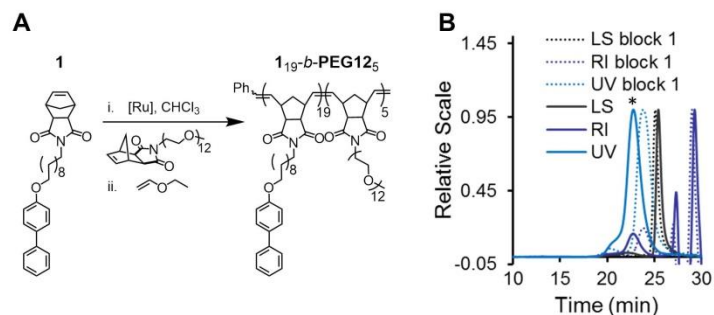


Figure 5.25 Polymerization and characterization of **1₁₉-b-PEG12₅**. (A) Polymerization of monomers **1** and PEG12 to afford block copolymer **1₁₉-b-PEG12₅**. (B) ¹H-NMR of **1₁₉-b-PEG12₅** to confirm complete polymerization (**1**:PEG12:I = 15:10:1). (C) SEC-MALS data of copolymer **1₁₉-b-PEG12₅**; Mn = 12,660 g/mol, Mn/Mw = 1.196, (dn/dc = 0.1375); Block 1: Mn = 8,868 g/mol, Mw/Mn = 1.151, (dn/dc = 0.179). The copolymer peak analyzed is indicated by (*).

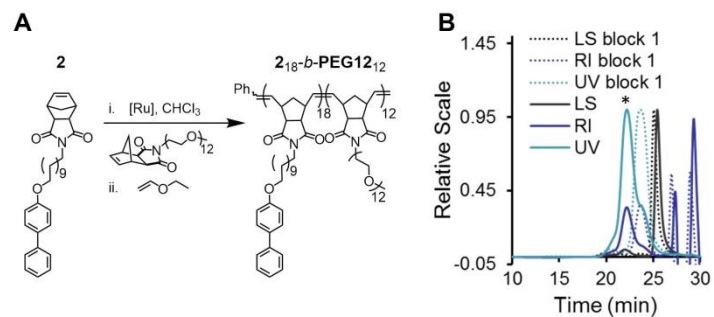


Figure 5.26 Polymerization and characterization of **2₁₈-b-PEG12₁₂**. (A) Polymerization of monomers **2** and PEG12 to afford block copolymer **2₁₈-b-PEG12₁₂**. (B) ¹H-NMR of **2₁₈-b-PEG12₁₂** to confirm complete polymerization (**2**:PEG12:I = 15:10:1). (C) SEC-MALS data of copolymer **2₁₈-b-PEG12₁₂**; Mn = 16,660 g/mol, Mw/Mn = 1.082, (dn/dc = 0.1375); Block 1: Mn = 8,525 g/mol, Mn/Mw = 1.040, (dn/dc = 0.179). The copolymer peak analyzed is indicated by (*).

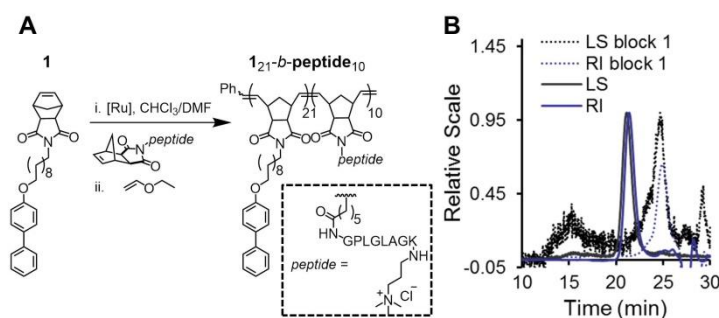


Figure 5.27 Polymerization and characterization of **1₂₁-b-peptide₁₀**. (A) Polymerization of monomers **1** and peptide to afford block copolymer **1₂₁-b-peptide₁₀**. (B) ¹H-NMR of **1₂₁-b-peptide₁₀** to confirm complete polymerization (**1**:peptide:I = 15:15:1). (C) SEC-MALS data of copolymer **1₂₁-b-peptide₁₀**; Mn = 20,250 g/mol, Mw/Mn = 1.169, (dn/dc = 0.179). Block 1: Mn = 11,720 g/mol, Mn/Mw = 1.276, (dn/dc = 0.179).

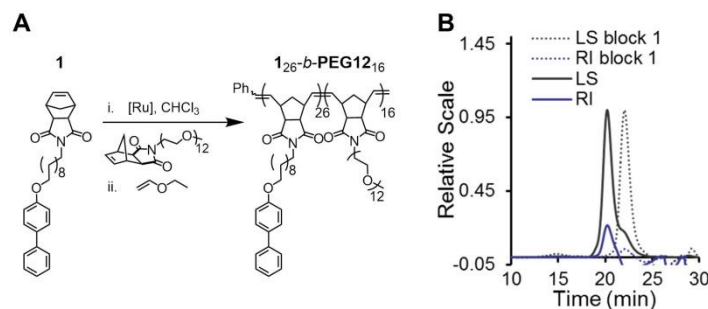


Figure 5.28 Polymerization and characterization of **1₂₆-b-PEG12₁₆**. (A) Polymerization of monomers **1** and **PEG12** to afford block copolymer **1₂₆-b-PEG12₁₆**. (B) ¹H-NMR of **1₂₆-b-PEG12₁₆** to confirm complete polymerization (**1**:**PEG12**:I = 20:20:1). (C) SEC-MALS data of copolymer **1₂₆-b-PEG12₁₆**; Mn = 22,970 g/mol, Mn/Mw = 1.011, (dn/dc = 0.1375); Block 1: Mn = 12,090 g/mol, Mw/Mn = 1.021, (dn/dc = 0.179).

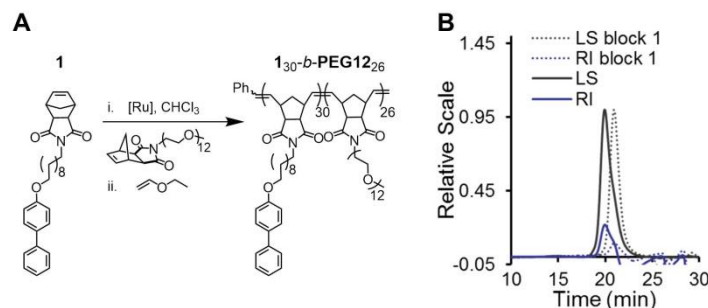


Figure 5.29 Polymerization and characterization of **1₃₀-b-PEG12₂₆**. (A) Polymerization of monomers **1** and **PEG12** to afford block copolymer **1₃₀-b-PEG12₂₆**. (B) ¹H-NMR of **1₃₀-b-PEG12₂₆** to confirm complete polymerization (**1**:**PEG12**:I = 27:13:1). (C) SEC-MALS data of copolymer **1₃₀-b-PEG12₂₆**; Mn = 32,350 g/mol, Mn/Mw = 1.022, (dn/dc = 0.1375); Block 1: Mn = 13,990 g/mol, Mn/Mw = 1.073, (dn/dc = 0.179).

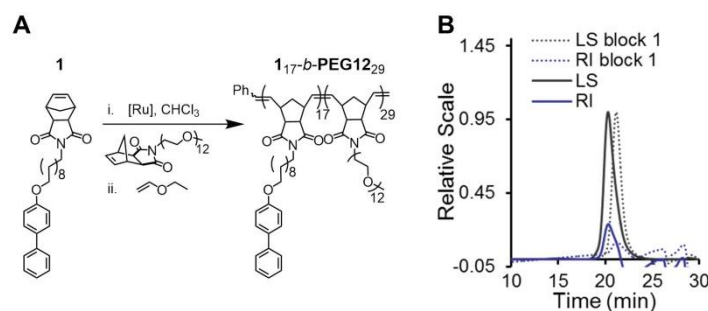


Figure 5.30 Polymerization and characterization of **1₁₇-b-PEG12₂₉**. (A) Polymerization of monomers **1** and **PEG12** to afford block copolymer **1₁₇-b-PEG12₂₉**. (B) ¹H-NMR of **1₁₇-b-PEG12₂₉** confirms complete polymerization (**1**:**PEG12**:I = 30:10:1). (C) SEC-MALS data of copolymer **1₁₇-b-PEG12₂₉**; Mn = 27,680 g/mol, Mn/Mw = 1.018, (dn/dc = 0.1375); Block 1: Mn = 7,860 g/mol, Mn/Mw = 1.131, (dn/dc = 0.179).

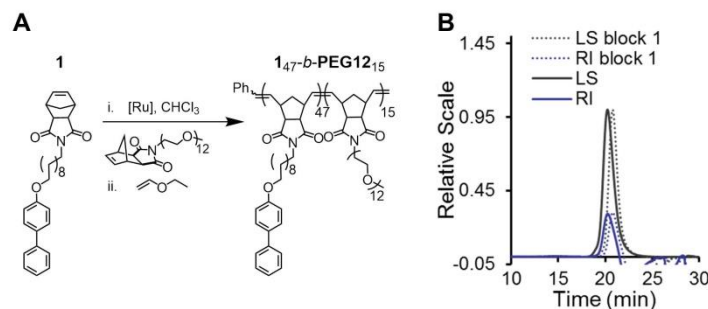


Figure 5.31 Polymerization and characterization of **1_{47-b}-PEG12₁₅**. (A) Polymerization of monomers **1** and **PEG12** to afford block copolymer **1_{47-b}-PEG12₁₅**. (B) ¹H-NMR of **1_{47-b}-PEG12₁₅** to confirm complete polymerization (**1:PEG12:I** = 32:8:1). (C) SEC-MALS data of copolymer **1_{47-b}-PEG12₁₅**; Mn = 32,170 g/mol, Mn/Mw = 1.016, (dn/dc = 0.1375); Block 1: Mn = 22,020 g/mol, Mw/Mn = 1.009, (dn/dc = 0.179).

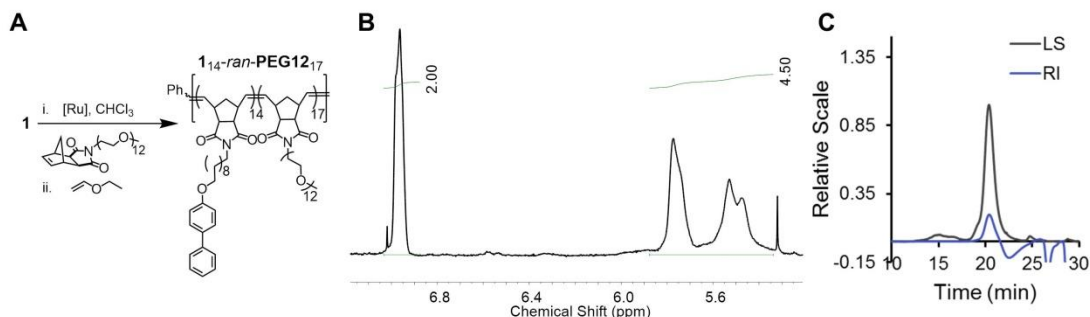


Figure 5.32 Polymerization and characterization of **1_{14-ran}-PEG12₁₇**. (A) Polymerization of monomers **1** and **PEG12** to afford random copolymer **1_{14-ran}-PEG12₁₇**. (B) ¹H-NMR of **1_{14-ran}-PEG12₁₇** to confirm complete polymerization (**1:PEG12:I** = 20:20:1). Monomer ratios are estimated from the relative integration of biphenyl proton resonances and polymer backbone olefin protons. (C) SEC-MALS data of copolymer **1_{14-ran}-PEG12₁₇**; Mn = 18,650 g/mol, Mw/Mn = 1.009, (dn/dc = 0.1375).

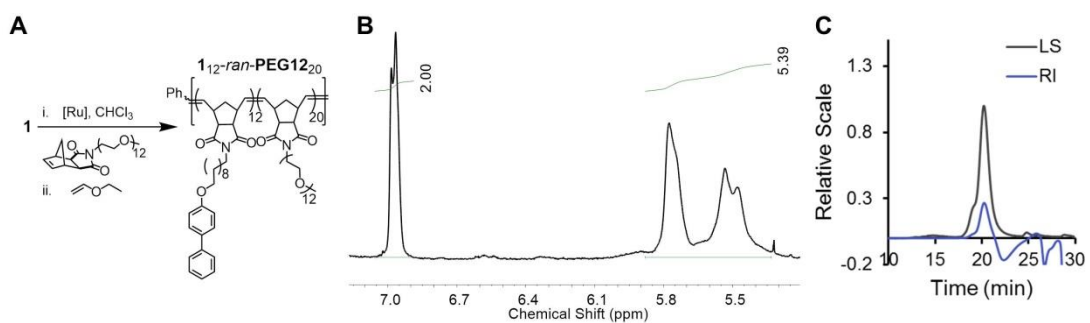


Figure 5.33 Polymerization and characterization of **1_{12-ran}-PEG12₂₀**. (A) Polymerization of monomers **1** and **PEG12** to afford random copolymer **1_{12-ran}-PEG12₂₀**. (B) ¹H-NMR of **1_{12-ran}-PEG12₂₀** to confirm complete polymerization (**1:PEG12:I** = 13:27:1). Monomer ratios are estimated from the relative integration of biphenyl proton resonances and polymer backbone olefin protons. (C) SEC-MALS data of copolymer **1_{12-ran}-PEG12₂₀**; Mn = 19,290 g/mol, Mw/Mn = 1.024, (dn/dc = 0.1375).

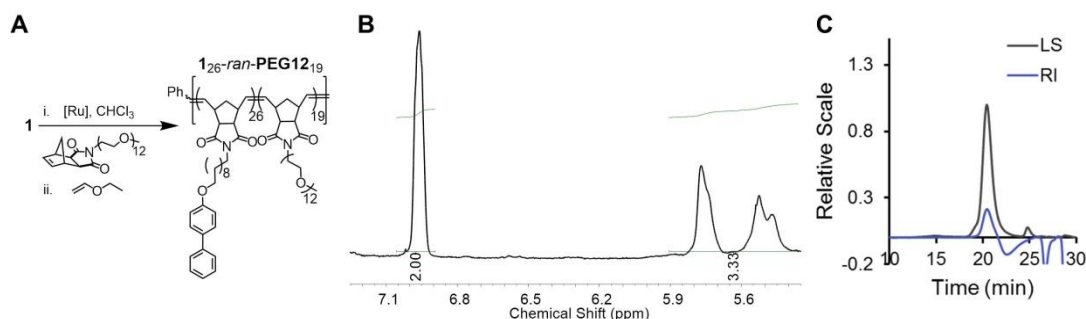


Figure 5.34 Polymerization and characterization of **1₂₆-ran-PEG12₁₉**. (A) Polymerization of monomers **1** and **PEG12** to afford random copolymer **1₂₆-ran-PEG12₁₉**. (B) ¹H-NMR of **1₂₆-ran-PEG12₁₉** to confirm complete polymerization (**1:PEG12:I** = 27:13:1). Monomer ratios are estimated from the relative integration of biphenyl proton resonances and polymer backbone olefin protons. (C) SEC-MALS data of copolymer **1₂₆-ran-PEG12₁₉**; Mn = 25,240 g/mol, Mw/Mn = 1.019, (dn/dc = 0.1375).

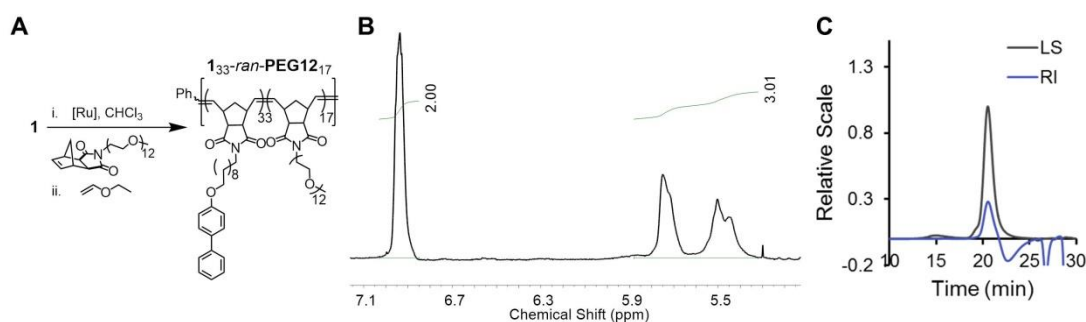


Figure 5.35 Polymerization and characterization of **1₃₃-ran-PEG12₁₇**. (A) Polymerization of monomers **1** and **PEG12** to afford random copolymer **1₃₃-ran-PEG12₁₇**. (B) ¹H-NMR of **1₃₃-ran-PEG12₁₇** to confirm complete polymerization (**1:PEG12:I** = 32:8:1). Monomer ratios are estimated from the relative integration of biphenyl proton resonances and polymer backbone olefin protons. (C) SEC-MALS data of copolymer **1₃₃-ran-PEG12₁₇**; Mn = 27,090 g/mol, Mw/Mn = 1.019, (dn/dc = 0.1375).

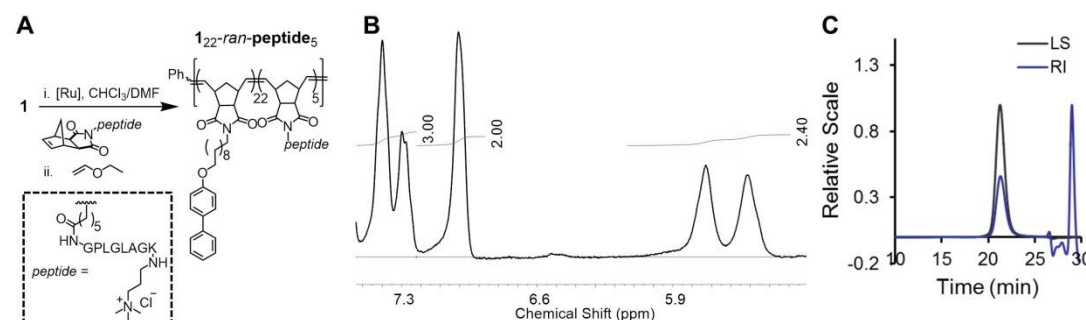


Figure 5.36 Polymerization and characterization of **1₂₂-ran-peptide₅**. (A) Polymerization of monomers **1** and peptide to afford random copolymer **1₂₂-ran-peptide₅**. (B) ¹H-NMR of **1₂₂-ran-peptide₅** to confirm complete polymerization (**1:peptide:I** = 20:10:1). Monomer ratios are estimated from the relative integration of biphenyl proton resonances and polymer backbone olefin protons. (C) SEC-MALS data of copolymer **1₂₂-ran-peptide₅**; Mn = 15,800 g/mol, Mw/Mn = 1.015, (dn/dc = 0.179).

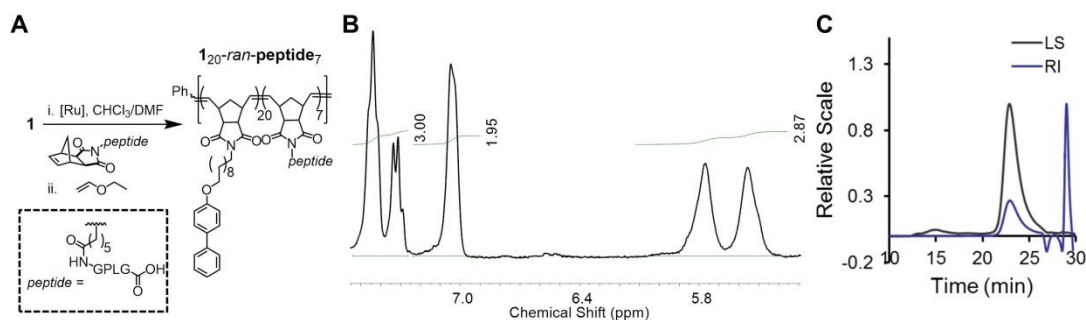
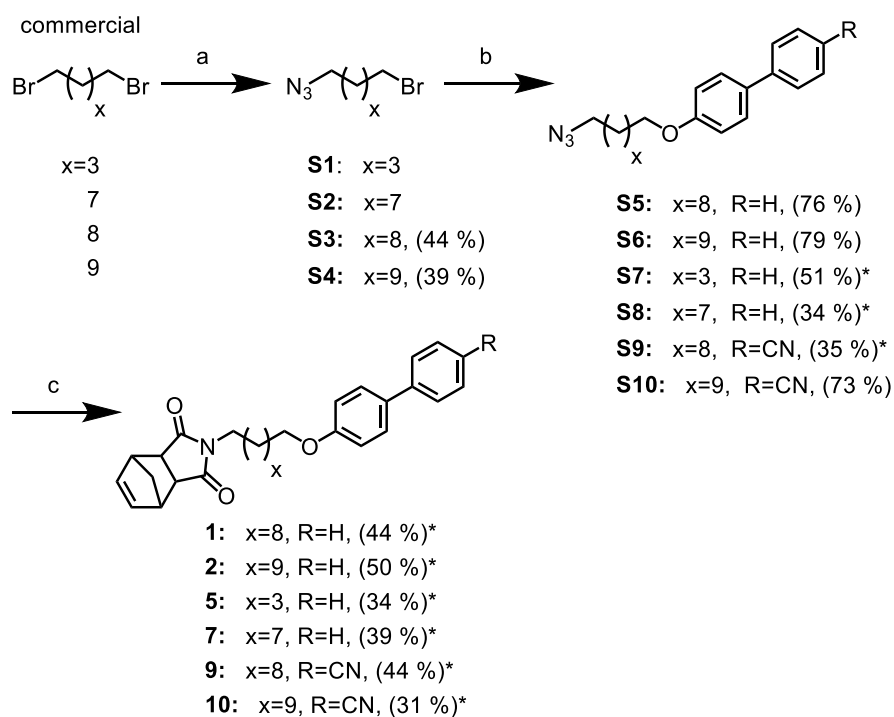
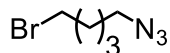


Figure 5.37 Polymerization and characterization of **1₂₀-ran-peptide₇**. (A) Polymerization of monomers **1** and **peptide** to afford random copolymer **1₂₀-ran-peptide₇**. (B) ¹H-NMR of **1₂₀-ran-peptide₇** to confirm complete polymerization (**1:peptide**:I = 20:10:1). Monomer ratios are estimated from the relative integration of biphenyl proton resonances and polymer backbone olefin protons. (C) SEC-MALS data of copolymer **1₂₀-ran-peptide₇**; Mn = 13,680 g/mol, Mw/Mn = 1.006, (dn/dc = 0.179).

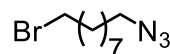


(a) NaN₃, DMSO, rt. (b) 4-phenylphenol or 4'-Hydroxy-4-biphenylcarbonitrile, K₂CO₃, Acetone, 56 °C. (c) i) 10% Pd/C, H₂, 4:1 THF/MeOH, rt; ii) *cis*-5-Norbornene-*exo*-2,3-dicarboxylic anhydride, TEA, Toluene, 110 °C. *denotes over two steps.

Scheme 5.2 Synthesis of norbornene monomers **1**, **2**, **5**, **7**, **9**, and **10**



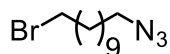
1-azido-5-bromopentane (S1). A round-bottom flask was charged with 1,5-dibromopentane (2.0 g, 8.7 mmol) and sodium azide (0.57 g, 8.7 mmol). To the solid mixture was added DMSO (35 mL). The solution was stirred vigorously at room temperature for 20 h. The solution was diluted with water (30 mL) and was allowed to cool. The aqueous phase was extracted with ether (3 x 30 mL) and the combined organic phase was washed with water (2 x 20 mL), dried over MgSO₄, filtered, and concentrated under reduced pressure. The reaction mixture was run through a silica plug (SiO₂, 3:1 hexanes:EtOAc, R_f = 0.69) to afford the crude product (1.53 g) as a pale yellow oil that was used without further purification. The analytical data of S1 were in agreement with those reported previously.¹⁷



1-azido-9-bromononane (S2). A round-bottom flask was charged with 1,9-dibromononane (2.0 g, 6.99 mmol) and sodium azide (0.46 g, 6.99 mmol). To the solid mixture was added DMSO (35 mL). The solution was stirred vigorously at room temperature for 9 h. The solution was diluted with water (30 mL) and was allowed to cool. The aqueous phase was extracted with ether (3 x 30 mL) and the combined organic phase was washed with water (2 x 20 mL), dried over MgSO₄, filtered, and concentrated under reduced pressure to afford the crude product (2.33 g) as a pale yellow oil that was used without further purification. The analytical data of S2 were in agreement with those reported previously.¹⁸

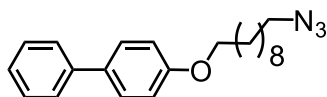


1-azido-10-bromodecane (S3). A round-bottom flask was charged with 1,10-dibromodecane (2.5 g, 8.33 mmol) and sodium azide (0.54 g, 8.33 mmol). To the solid mixture was added DMSO (40 mL). The solution was stirred vigorously at room temperature for 15 h. The solution was diluted with water (40 mL) and was allowed to cool. The aqueous phase was extracted with ether (3 x 30 mL) and the combined organic phase was washed with water (2 x 20 mL), dried over MgSO₄, filtered, and concentrated under reduced pressure. The reaction mixture was purified by flash chromatography (SiO₂, hexanes, R_f = 0.34) to afford the desired product (0.98 g, 44%) as a pale yellow oil: ¹H NMR (400 MHz, CDCl₃) δ 3.41 (t, J = 6.9 Hz, 2H), 3.26 (t, J = 6.9 Hz, 2H), 1.95 – 1.77 (m, 2H), 1.70 – 1.51 (m, 2H), 1.49 – 1.23 (m, 12H). ¹³C NMR (126 MHz, CDCl₃) δ 51.58, 34.25, 32.91, 29.48, 29.44, 29.23, 28.95, 28.84, 28.26, 26.81. MS calcd: 261.08; EI-MS (70 eV), m/z (%): 70 (100) [C₂H₄N₃⁺], 55 (48) [C₃H₅N], 84 (23) [C₃H₆N₃⁺], 98 (6) [C₄H₈N₃⁺], 120 (3) [C₃H₆Br⁺], 135 (6) [C₄H₈Br⁺], 232 (3) [M⁺ - N₂, C₁₀H₁₉BrN].

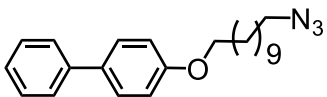


1-azido-11-bromoundecane (S4). A round-bottom flask was charged with 1,11-dibromoundecane (2.0 g, 6.37 mmol) and sodium azide (0.42 g, 6.37 mmol). To the solid mixture was added DMSO (35 mL). The solution was stirred vigorously at room temperature for 8 h. The solution was diluted with water (30 mL) and was allowed to cool. The aqueous phase was extracted with ether (3 x 30 mL) and the combined organic phase was washed with water (2 x 20 mL), dried over MgSO₄, filtered, and concentrated under reduced pressure. The reaction mixture was purified by flash chromatography (SiO₂, hexanes, R_f = 0.43) to afford the desired product (0.69 g, 39%) as a colorless oil: ¹H NMR (400 MHz, CD₂Cl₂) δ 3.42 (t, J = 6.9 Hz, 2H), 3.25 (t, J = 6.9 Hz, 2H), 1.91 – 1.78 (m, 2H), 1.65 – 1.50 (m, 2H), 1.46 – 1.18

(m, 14H). ¹³C NMR (126 MHz, CDCl₃) δ 51.60, 34.28, 32.94, 29.56, 29.54, 29.53, 29.27, 28.96, 28.88, 28.29, 26.84. MS calcd: 275.10; EI-MS (70 eV), m/z (%): 70 (100) [C₂H₄N₃⁺], 55 (50) [C₃H₅N], 84 (25) [C₃H₆N₃⁺], 98 (8) [C₄H₈N₃⁺], 135 (7) [C₄H₈Br⁺], 166 (2) [M⁺ - Br, C₁₁H₂₀N⁺].

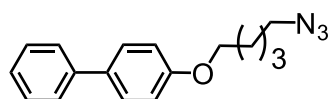


4-((10-azidodecyl)oxy)-biphenyl (S5). A round-bottom flask was charged with **S2** (0.46 g, 1.82 mmol), 4-phenylphenol (0.36 g, 2.18 mmol), and K₂CO₃ (1.21 g, 9.09 mmol). To the solid mixture was added acetone (40 mL) and the flask was heated to reflux for 21 h. The mixture was then allowed to cool to room temperature and concentrated. The residue was diluted with CHCl₃ (40 mL) and washed with water (3 x 20 mL). The organic layer was dried over MgSO₄, filtered, and concentrated under reduced pressure. The mixture was purified by flash chromatography (SiO₂, 20% DCM in hexanes, R_f = 0.44) to afford the desired product (0.47 g, 76%) as a white solid: ¹H NMR (400 MHz, CD₂Cl₂) δ 7.59 – 7.48 (m, 4H), 7.45 – 7.37 (m, 2H), 7.33 – 7.27 (m, 1H), 7.01 – 6.92 (m, 2H), 3.99 (t, J = 6.6 Hz, 2H), 3.26 (t, J = 7.0 Hz, 2H), 1.85 – 1.75 (m, 2H), 1.66 – 1.55 (m, 2H), 1.52 – 1.42 (m, 2H), 1.42 – 1.27 (m, 10H). ¹³C NMR (126 MHz, CDCl₃) δ 158.79, 140.97, 133.62, 128.83, 128.23, 126.82, 126.72, 114.84, 68.14, 51.60, 29.59, 29.55, 29.49, 29.41, 29.28, 28.97, 26.84, 26.18.

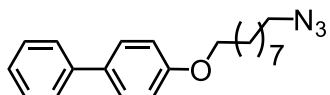


4-((11-azidoundecyl)oxy)-biphenyl (S6). A round-bottom flask was charged with **S4** (0.30 g, 1.09 mmol), 4-phenylphenol (0.22 g, 1.30 mmol), and K₂CO₃ (0.753 g, 5.45 mmol). To the solid mixture was added acetone (20 mL) and the flask was heated to reflux for 24 h. The

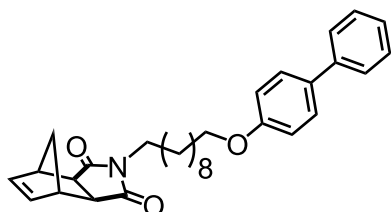
mixture was then allowed to cool to room temperature and concentrated. The residue was diluted with CHCl_3 (40 mL) and washed with water (2 x 20 mL). The organic layer was dried over MgSO_4 , filtered, and concentrated under reduced pressure. The mixture was purified by flash chromatography (SiO_2 , 20% DCM in hexanes, $R_f = 0.43$) to afford the desired product (0.31 g, 79%) as a white solid: $^1\text{H NMR}$ (400 MHz, CD_2Cl_2) δ 7.64 – 7.47 (m, 4H), 7.44 – 7.38 (m, 2H), 7.35 – 7.24 (m, 1H), 6.99 – 6.93 (m, 2H), 4.00 (t, $J = 6.6$ Hz, 2H), 3.25 (t, $J = 7.0$ Hz, 2H), 1.84 – 1.74 (m, 2H), 1.65 – 1.54 (m, 2H), 1.51 – 1.43 (m, 2H), 1.42 – 1.26 (m, 12H). $^{13}\text{C NMR}$ (126 MHz, CDCl_3) δ 158.81, 140.99, 133.63, 128.84, 128.24, 126.84, 126.73, 114.85, 68.17, 51.62, 29.68, 29.61, 29.52, 29.42, 29.30, 28.98, 26.85, 26.19.



4-((5-azidopentyl)oxy)-biphenyl (S7). A round-bottom flask was charged with **S1** (1.53 g, 7.97 mmol), 4-phenylphenol (2.71 g, 15.9 mmol), and K_2CO_3 (5.51 g, 39.8 mmol). To the solid mixture was added acetone (40 mL) and the flask was heated to reflux for 15 h. The mixture was then allowed to cool to room temperature and concentrated. The residue was diluted with CHCl_3 (40 mL) and washed with water (3 x 20 mL). The organic layer was dried over MgSO_4 , filtered, and concentrated under reduced pressure. The mixture was purified by flash chromatography (SiO_2 , 20% DCM in hexanes, $R_f = 0.32$) to afford the desired product (1.14 g, 51% over two steps) as a pale yellow oil: $^1\text{H NMR}$ (400 MHz, CDCl_3) δ 7.60 – 7.46 (m, 4H), 7.45 – 7.36 (m, 2H), 7.28 – 7.33 (m, 1H), 7.02 – 6.92 (m, 2H), 4.02 (t, $J = 6.3$ Hz, 2H), 3.32 (t, $J = 6.8$ Hz, 2H), 1.91 – 1.79 (m, 2H), 1.76 – 1.64 (m, 2H), 1.64 – 1.55 (m, 2H). $^{13}\text{C NMR}$ (126 MHz, CDCl_3) δ 158.63, 140.93, 133.81, 128.85, 128.28, 126.84, 126.77, 114.83, 67.74, 51.49, 28.98, 28.81, 23.55.

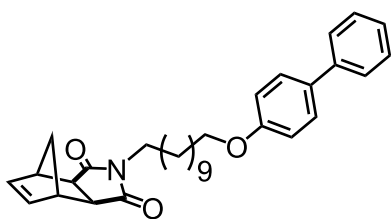


4-((9-azidononyloxy)-biphenyl) (S8). A round-bottom flask was charged with **S2** (1.74 g, 7.01 mmol), 4-phenylphenol (2.38 g, 13.9 mmol), and K_2CO_3 (4.74 g, 35.0 mmol). To the solid mixture was added acetone (25 mL) and the flask was heated to reflux for 21 h. The mixture was then allowed to cool to room temperature and concentrated. The residue was diluted with $CHCl_3$ (40 mL) and washed with water (3 x 20 mL). The organic layer was dried over $MgSO_4$, filtered, and concentrated under reduced pressure. The mixture was purified by flash chromatography (SiO_2 , 20% DCM in hexanes, $R_f = 0.29$) to afford the desired product (0.80 g, 34% over two steps) as a white solid: 1H NMR (400 MHz, $CDCl_3$) δ 7.58 – 7.48 (m, 4H), 7.44 – 7.37 (m, 2H), 7.30 (t, $J = 7.0$ Hz, 1H), 7.00 – 6.93 (m, 2H), 4.00 (t, $J = 6.5$ Hz, 2H), 3.23 – 3.29 (m, 2H), 1.85 – 1.76 (m, 2H), 1.65 – 1.57 (m, 2H), 1.53 – 1.43 (m, 2H), 1.42 – 1.29 (m, 8H). ^{13}C NMR (126 MHz, $CDCl_3$) δ 158.79, 140.98, 133.65, 128.84, 128.24, 126.84, 126.73, 114.85, 68.13, 51.60, 29.55, 29.42, 29.41, 29.24, 28.97, 26.84, 26.17.



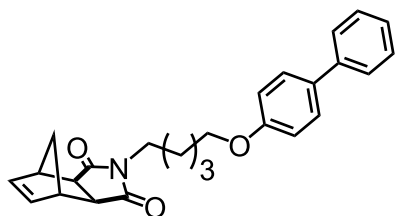
***N*-(4-decyloxy-biphenyl)-*cis*-5-norbornene-*exo*-dicarboximide (1).** To a solution of **S5** (0.39 g, 1.10 mmol) in 4:1 THF:MeOH (15 mL) was added 10% Pd/C (5 mol% of **S5**). The flask was evacuated and backfilled with H_2 (3 x) using a hydrogen balloon and the reaction was stirred at rt for 4 h. The reaction mixture was filtered through celite and washed using EtOAc. The filtrate was concentrated to give a white solid that was used in the next step without purification. A round-bottom flask was charged with the hydrogenated **S5** product

(0.36 g, 1.1 mmol), and *cis*-5-norbornene-*exo*-2,3-dicarboxylic anhydride (0.152 g, 0.93 mmol). To the solid mixture was added toluene (20 mL). Et₃N (15.5 μL, 0.11 mmol) was added. The flask was heated to reflux for 18 h. The mixture was then allowed to cool to room temperature and concentrated. The reaction mixture was diluted with CHCl₃ (40 mL) and washed with 1 M aqueous HCl (2 x 20 mL). The organic layer was washed with saturated aqueous NaCl (20 mL), dried over MgSO₄, filtered, and concentrated under reduced pressure. Purification by flash chromatography (SiO₂, 5:1 hexanes:EtOAc, R_f = 0.29) gave the desired product (0.19 g, 44% over two steps) as a white solid: ¹H-NMR (400 MHz, CDCl₃) δ 7.59 – 7.48 (m, 4H), 7.45 – 7.37 (m, 2H), 7.33 – 7.27 (m, 1H), 7.00 – 6.93 (m, 2H), 6.28 (t, J = 1.9 Hz, 2H), 3.99 (t, J = 6.6 Hz, 2H), 3.49 – 3.42 (m, 2H), 3.25 – 3.30 (m, 2H), 2.67 (d, J = 1.3 Hz, 2H), 1.85 – 1.74 (m, 2H), 1.60 – 1.40 (m, 4H), 1.40 – 1.16 (m, 12H). ¹³C NMR (126 MHz, CDCl₃) δ 178.29, 158.80, 141.00, 137.95, 133.60, 128.83, 128.23, 126.84, 126.71, 114.85, 68.16, 47.93, 45.29, 42.85, 38.89, 29.60, 29.52, 29.48, 29.42, 29.26, 27.91, 27.09, 26.18. HRMS (ESI) calcd for [C₃₁H₃₇NO₃Na]⁺ : 494.2666, found: 494.2666 [M + Na]⁺



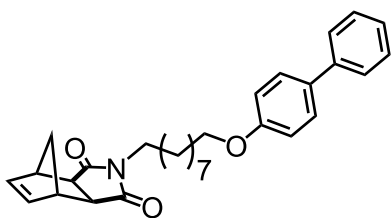
***N*-(4-undecyloxy-biphenyl)-*cis*-5-norbornene-*exo*-dicarboximide (2).** To a solution of **S6** (0.18 g, 0.492 mmol) in 4:1 THF:MeOH (15 mL) was added 10% Pd/C (5 mol% of **S6**). The flask was evacuated and backfilled with H₂ (3 x) using a hydrogen balloon and the reaction was stirred at rt for 21 h. The reaction mixture was filtered through celite and washed using EtOAc. The filtrate was concentrated to give a white solid that was used in the next step

without purification. A round-bottom flask was charged with the hydrogenated **S6** product (0.13 g, 0.38 mmol), and *cis*-5-norbornene-*exo*-2,3-dicarboxylic anhydride (0.052 g, 0.32 mmol). To the solid mixture was added toluene (15 mL). Et₃N (6.4 μL, 0.05 mmol) was added. The flask was heated to reflux for 18 h. The mixture was then allowed to cool to room temperature and concentrated. The reaction mixture was diluted with CHCl₃ (20 mL) and washed with 1 M aqueous HCl (2 x 15 mL). The organic layer was washed with saturated aqueous NaCl (15 mL), dried over MgSO₄, filtered, and concentrated under reduced pressure. Purification by flash chromatography (SiO₂, 4:1 hexanes:EtOAc, R_f = 0.39) gave the desired product (0.12 g, 50% over two steps) as a waxy pale yellow solid: ¹H NMR (400 MHz, CDCl₃) δ 7.60 – 7.47 (m, 4H), 7.46 – 7.36 (m, 2H), 7.34 – 7.26 (m, 1H), 7.02 – 6.91 (m, 2H), 6.28 (t, J = 1.8 Hz, 2H), 3.99 (t, J = 6.6 Hz, 2H), 3.45 (dd, J = 8.4, 6.6 Hz, 2H), 3.28 (dd, J = 9.9, 7.9 Hz, 2H), 2.66 (d, J = 1.1 Hz, 2H), 1.86 – 1.74 (m, 2H), 1.58 – 1.41 (m, 4H), 1.40 – 1.19 (m, 14H). ¹³C NMR (126 MHz, CDCl₃) δ 178.17, 158.69, 140.87, 137.83, 133.47, 128.70, 128.10, 126.71, 126.59, 114.73, 68.05, 47.80, 45.16, 42.73, 38.78, 29.53, 29.48, 29.45, 29.40, 29.30, 29.15, 27.80, 26.97, 26.07. HRMS (ESI) calcd for [C₃₂H₃₉NO₃Na]⁺: 508.2822, found: 508.2823 [M + Na]⁺



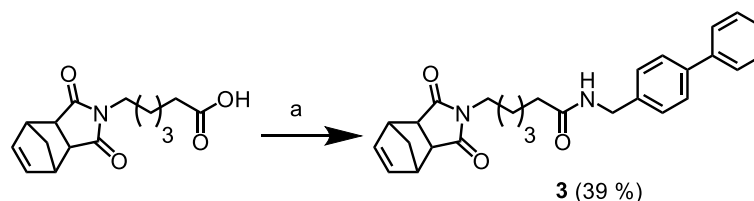
***N*-(4-pentyloxy-biphenyl)-*cis*-5-norbornene-*exo*-dicarboximide (5).** To a solution of **S7** (0.81 g, 2.89 mmol) in 4:1 THF:MeOH (35 mL) was added 10% Pd/C (5 mol% of **S10**). The flask was evacuated and backfilled with H₂ (3 x) using a hydrogen balloon and the reaction was stirred at rt for 17 h. The reaction mixture was filtered through celite and washed using

EtOAc. The filtrate was concentrated to give a white solid that was used in the next step without purification. A round-bottom flask was charged with the hydrogenated **S7** product (0.74 g, 2.89 mmol), and cis-5-norbornene-exo-2,3-dicarboxylic anhydride (0.39 g, 2.41 mmol). To the solid mixture was added toluene (50 mL). Et₃N (40.3 μL, 0.29 mmol) was added. The flask was heated to reflux for 18 h. The mixture was then allowed to cool to room temperature and concentrated. The reaction mixture was diluted with CHCl₃ (40 mL) and washed with 1 M aqueous HCl (2 x 20 mL). The organic layer was washed with saturated aqueous NaCl (20 mL), dried over MgSO₄, filtered, and concentrated under reduced pressure. The residue was purified by flash chromatography (SiO₂, 3:1, hexanes:EtOAc, R_f = 0.26) to afford the desired product (0.33 g, 34% over two steps) as a white waxy solid ¹H NMR (400 MHz, CDCl₃) δ 7.60 – 7.48 (m, 4H), 7.45 – 7.36 (m, 2H), 7.34 – 7.27 (m, 1H), 6.97 – 6.93 (m, 2H), 6.29 (t, J = 1.8 Hz, 2H), 3.99 (t, J = 6.3 Hz, 2H), 3.54 – 3.48 (m, 2H), 3.30 – 3.26 (m, 2H), 2.68 (d, J = 1.3 Hz, 2H), 1.88 – 1.78 (m, 2H), 1.71 – 1.61 (m, 2H), 1.56 – 1.45 (m, 3H), 1.26 – 1.22 (m, 1H). ¹³C NMR (126 MHz, CDCl₃) δ 178.24, 158.62, 140.94, 137.94, 133.70, 128.82, 128.23, 126.82, 126.72, 114.80, 67.64, 47.93, 45.27, 42.87, 38.67, 28.90, 27.65, 23.66. HRMS (ESI) calcd for [C₂₆H₂₇NO₃Na]⁺: 424.1883, found: 424.1884 [M + Na]⁺



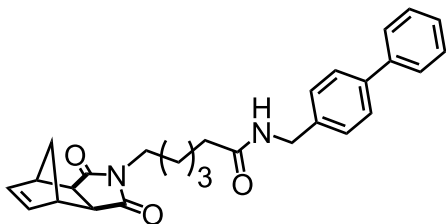
N-(4-nonyloxy-biphenyl)-cis-5-norbornene-exo-dicarboximide (7). To a solution of **S8** (0.58 g, 1.72 mmol) in 4:1 THF:MeOH (20 mL) was added 10% Pd/C (5 mol% of **S7**). The flask was evacuated and backfilled with H₂ (3 x) using a hydrogen balloon and the reaction

was stirred at rt for 4 h. The reaction mixture was filtered through celite and washed using EtOAc. The filtrate was concentrated to give a white solid that was used in the next step without purification. A round-bottom flask was charged with the hydrogenated **S8** product (0.44 g, 1.4 mmol), and cis-5-norbornene-exo-2,3-dicarboxylic anhydride (0.19 g, 1.1 mmol). To the solid mixture was added toluene (40 mL). Et₃N (20 μL, 0.14 mmol) was added. The flask was heated to reflux for 4 h. The mixture was then allowed to cool to room temperature and concentrated. The reaction mixture was diluted with CHCl₃ (40 mL) and washed with 1 M aqueous HCl (2 x 20 mL). The organic layer was washed with saturated aqueous NaCl (20 mL), dried over MgSO₄, filtered, and concentrated under reduced pressure. The residue was purified by flash chromatography (SiO₂, 5:1 hexanes:EtOAc, R_f = 0.21) to afford the desired product (0.21 g, 39% over two steps) as a white crystalline solid: ¹H NMR (400 MHz, CDCl₃) δ 7.60 – 7.47 (m, 4H), 7.45 – 7.36 (m, 2H), 7.33 – 7.27 (m, 1H), 7.00 – 6.91 (m, 2H), 6.24 – 6.31 (m, 2H), 3.99 (t, J = 6.6 Hz, 2H), 3.46 (t, J = 7.6 Hz, 2H), 3.31 – 3.23 (m, 2H), 2.71 – 2.63 (m, 2H), 1.86 – 1.73 (m, 2H), 1.61 – 1.40 (m, 4H), 1.39 – 1.17 (m, 10H). ¹³C NMR (126 MHz, CDCl₃) δ 178.28, 158.79, 140.99, 137.95, 133.61, 128.83, 128.23, 126.84, 126.71, 114.85, 68.14, 47.93, 45.29, 42.85, 38.87, 29.51, 29.42, 29.40, 29.21, 27.90, 27.07, 26.14. HRMS (ESI) calcd for [C₃₀H₃₅NO₃Na]⁺: 480.2509, found: 480.2507 [M + Na]⁺

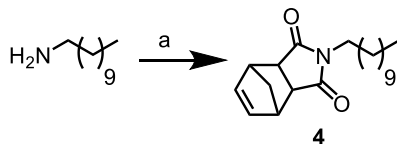


(a) 4-phenylbenzylamine, EDC, HOBT, DMF, 0 °C to rt.

Scheme 5.3 Synthesis of norbornene monomer **3**

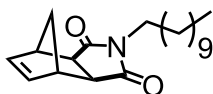


***N*-(4-phenylbenzyl-4-hexanamide)-*cis*-5-norbornene-*exo*-dicarboximide (3).** To a solution of *N*-(hexanoic acid)-*cis*-5-norbornene-*exo*-dicarboximide (1.0 g, 3.61 mmol), EDC (0.84 g, 5.41 mmol), HOBt (0.73 g, 5.41 mmol) in DMF (30 mL) at 0 °C was added 4-phenylbenzylamine (0.99 g, 5.41 mmol). The ice bath was removed and the reaction mixture was stirred at room temperature overnight. DMF was removed in vacuo and the residue was diluted with CHCl₃ (40 mL) and washed with 1 M aqueous HCl (2 x 20 mL). The organic layer was washed with saturated aqueous NaCl (20 mL), dried over MgSO₄, filtered, and concentrated under reduced pressure. The residue was purified by flash chromatography (SiO₂, 2:1 EtOAc:hexanes, R_f = 0.33) to afford the desired product (0.62 g, 39%) as a white waxy solid: ¹H NMR (400 MHz, CDCl₃) δ 7.62 – 7.50 (m, 4H), 7.48 – 7.39 (m, 2H), 7.39 – 7.30 (m, 3H), 6.26 (t, J = 1.9 Hz, 2H), 5.82 (t, J = 5.7 Hz, 1H), 4.48 (d, J = 5.7 Hz, 2H), 3.46 (t, J = 7.4 Hz, 2H), 3.27 – 3.23 (m, 2H), 2.64 (d, J = 1.6 Hz, 2H), 2.23 (t, J = 7.5 Hz 2H), 1.77 – 1.63 (m, 2H), 1.63 – 1.53 (m, 2H), 1.53 – 1.46 (m, 1H), 1.42 – 1.29 (m, 2H), 1.20 (dt, J = 9.9, 1.6 Hz, 1H). ¹³C NMR (126 MHz, CDCl₃) δ 178.18, 172.67, 140.69, 140.44, 137.84, 137.51, 128.86, 128.32, 127.46, 127.42, 127.10, 47.84, 45.19, 43.29, 42.80, 38.44, 36.44, 27.53, 26.59, 25.17. HRMS (ESI) calcd for [C₂₈H₃₀N₂O₃Na]⁺: 465.2149, found: 465.2146 [M + Na]⁺

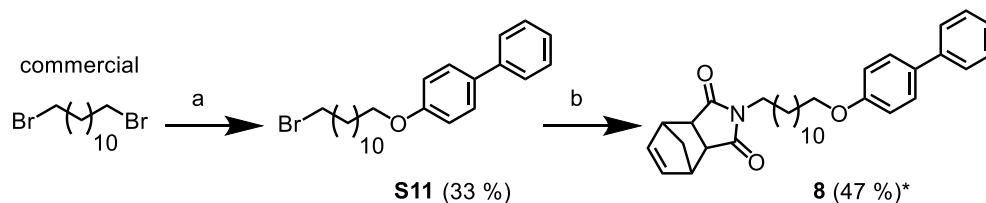


(a) *cis*-5-Norbornene-*exo*-2,3-dicarboxylic anhydride, TEA, Toluene, 110 °C.

Scheme 5.4 Synthesis of norbornene monomer **4**

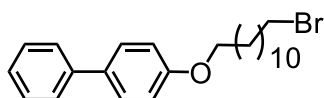


***N*-(undecyl)-*cis*-5-norbornene-*exo*-dicarboximide (4).** A round-bottom flask was charged with undecan-1-amine (0.47 g, 2.74 mmol), and *cis*-5-norbornene-*exo*-2,3-dicarboxylic anhydride (0.3 g, 1.83 mmol). To the solid mixture was added toluene (20 mL). Et₃N (31 μL, 0.22 mmol) was added. The flask was heated to reflux overnight. The mixture was then allowed to cool to room temperature and concentrated. The residue was diluted with CHCl₃ (40 mL) and washed with 1 M aqueous HCl (2 x 20 mL). The organic layer was washed with saturated aqueous NaCl (20 mL), dried over MgSO₄, filtered, and concentrated under reduced pressure. The residue was then purified by flash chromatography (SiO₂, 3:1 hexanes:EtOAc, R_f = 0.49) to afford the desired product as a pale yellow oil that was used without further purification: ¹H NMR (400 MHz, CDCl₃) δ 6.28 (t, J = 1.8 Hz, 2H), 3.48 – 3.42 (m, 2H), 3.30 – 3.23 (m, 2H), 2.67 (d, J = 1.1 Hz, 2H), 1.64 – 1.44 (m, 4H), 1.33 – 1.19 (m, 16H), 0.93 – 0.81 (m, 3H). HRMS (ESI) calcd for [C₂₀H₃₂NO₂]⁺: 318.2428, found: 318.2429 [M + H]⁺

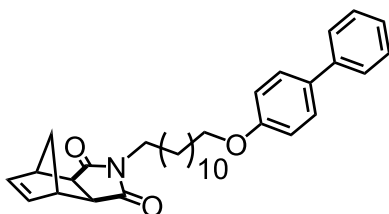


(a) 4-phenylphenol, K_2CO_3 , Acetone, 56 °C. (b) i) NH_3 (g), MeOH, 0 °C to 65 °C;
 ii) *cis*-5-Norbornene-*exo*-2,3-dicarboxylic anhydride, TEA, Toluene, 110 °C.
 *denotes over two steps.

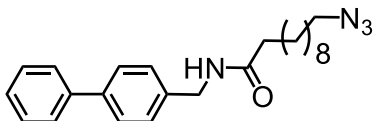
Scheme 5.5 Synthesis of norbornene monomer **8**



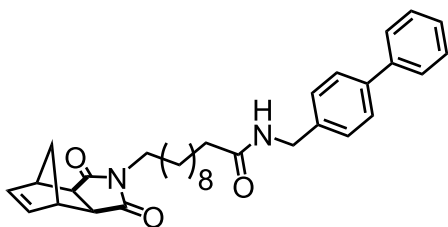
4-((12-bromododecyl)oxy)-biphenyl (S11). A round-bottom flask was charged with 1,12-dibromododecane (2.0 g, 6.10 mmol), 4-phenylphenol (1.24 g, 7.31 mmol), and K_2CO_3 (4.21 g, 30.5 mmol). To the solid mixture was added acetone (100 mL) and the flask was heated to reflux for 18 h. The mixture was then allowed to cool to room temperature and concentrated. The residue was diluted with CH_2Cl_2 (50 mL) and washed with water (3 x 30 mL). The organic layer was dried over $MgSO_4$, filtered, and concentrated under reduced pressure. The crude solid was recrystallized using DCM to afford the desired product (0.84 g, 33%) as a silvery white solid: 1H NMR (400 MHz, CD_2Cl_2) δ 7.60 – 7.49 (m, 4H), 7.46 – 7.37 (m, 2H), 7.33 – 7.26 (m, 1H), 7.01 – 6.91 (m, 2H), 3.99 (t, $J = 6.6$ Hz, 2H), 3.42 (t, $J = 6.8$ Hz, 2H), 1.92 – 1.72 (m, 4H), 1.52 – 1.24 (m, 16H). ESI-MS calcd: 416.17, found: 417.18 [$M + H$] $^+$; ^{13}C NMR (126 MHz, $CDCl_3$) δ 158.80, 140.98, 133.62, 128.84, 128.23, 126.83, 126.73, 114.85, 68.18, 34.31, 32.97, 29.70, 29.68, 29.67, 29.58, 29.54, 29.42, 28.91, 28.32, 26.20.



***N*-(4-dodecyloxy-biphenyl)-*cis*-5-norbornene-*exo*-dicarboximide (8).** A pressure vial containing a solution of **S11** (0.30 g, 0.719 mmol) in MeOH (4 mL) at 0 °C was sparged with NH₃ gas for 5 min. The vial was removed from the ice bath, capped, and heated to reflux for 17 h. The vial was allowed to cool to room temperature and opened at 0 °C. The reaction mixture was dried in vacuo and was used in the next step without purification. A round-bottom flask was charged with the hydrogenated S11 product (0.25 g, 0.72 mmol), and *cis*-5-norbornene-*exo*-2,3-dicarboxylic anhydride (0.098 g, 0.59 mmol). To the solid mixture was added toluene (20 mL). Et₃N (12 μL, 0.086 mmol) was added. The flask was heated to reflux for 18 h. The mixture was then allowed to cool to room temperature and concentrated. The reaction mixture was diluted with CHCl₃ (20 mL) and washed with 1 M aqueous HCl (2 x 15 mL). The organic layer was washed with saturated aqueous NaCl (15 mL), dried over MgSO₄, filtered, and concentrated under reduced pressure. The residue was purified by flash chromatography (SiO₂, 3:1 hexanes:EtOAc, R_f = 0.37) to afford the desired product (0.17 g, 47% over two steps) as a white solid: ¹H NMR (400 MHz, CDCl₃) δ 7.58 – 7.48 (m, 4H), 7.41 (t, J = 7.7 Hz, 2H), 7.33 – 7.27 (m, 1H), 7.01 – 6.92 (m, 2H), 6.28 (t, J = 1.9 Hz, 2H), 3.99 (t, J = 6.6 Hz, 2H), 3.51 – 3.39 (m, 2H), 3.30 – 3.24 (m, 2H), 2.67 (m, 2H), 1.87 – 1.74 (m, 2H), 1.62 – 1.41 (m, 4H), 1.40 – 1.19 (m, 16H). ¹³C NMR (126 MHz, CDCl₃) δ 178.28, 158.81, 140.99, 137.95, 133.59, 128.82, 128.22, 126.83, 126.71, 114.85, 68.18, 47.92, 45.28, 42.85, 38.90, 29.86, 29.70, 29.67, 29.58, 29.54, 29.42, 29.28, 27.92, 27.10, 26.19. HRMS (ESI) calcd for [C₃₃H₄₁NO₃Na]⁺: 522.2979, found: 522.2978 [M + Na]⁺



***N*-(4-phenylbenzyl)-11-azidoundecanamide (S13).** To a solution of **S12** (0.70 g, 3.08 mmol), EDC (0.59 g, 3.08 mmol), HOBt (0.47 g, 3.08 mmol) in DCM (35 mL) at 0 °C was added 4-phenylbenzylamine (0.56 g, 3.08 mmol). The ice bath was removed and the reaction mixture was stirred at room temperature overnight. DCM was removed in vacuo and the residue was purified by flash chromatography (SiO₂, DCM, R_f = 0.27) to afford the desired product (0.83 g, 69%) as a white waxy solid: ¹H NMR (300 MHz, CDCl₃) δ 7.62 – 7.52 (m, 4H), 7.48 – 7.40 (m, 2H), 7.39 – 7.30 (m, 3H), 5.57 (t, J = 5.9 Hz, 1H), 4.48 (d, J = 6.0 Hz, 2H), 3.24 (t, J = 6.9 Hz, 2H), 2.23 (t, J = 7.6 Hz, 2H), 1.78 – 1.50 (m, 4H), 1.45 – 1.16 (m, 12H). ¹³C NMR (126 MHz, CDCl₃) δ 173.12, 140.76, 140.58, 137.56, 128.92, 128.40, 127.54, 127.49, 127.17, 51.57, 43.37, 36.94, 29.53, 29.48, 29.43, 29.42, 29.24, 28.94, 26.81, 25.88.



***N*-(4-phenylbenzyl)-4-undecanamide)-*cis*-5-norbornene-*exo*-dicarboximide (6).** To a solution of **S13** (0.57 g, 1.45 mmol) in 4:1 THF:MeOH (20 mL) was added 10% Pd/C (5 mol% of **S13**). The flask was evacuated and backfilled with H₂ (3 x) using a hydrogen balloon and the reaction was stirred at rt for 19 h. The reaction mixture was filtered through celite and washed using EtOAc. The filtrate was concentrated to give a white solid that was used in the next step without purification. A round-bottom flask was charged with the hydrogenated **S13** product (0.38 g, 1.0 mmol), and *cis*-5-norbornene-*exo*-2,3-dicarboxylic

anhydride (0.14 g, 0.86 mmol). To the solid mixture was added toluene (40 mL). Et₃N (14 μL, 0.10 mmol) was added. The flask was heated to reflux for 18 h. The mixture was then allowed to cool to room temperature and concentrated. The residue was purified by flash chromatography (SiO₂, 10% EtOAc in DCM, R_f = 0.34) to afford the desired product (0.28 g, 63% over two steps) as a white waxy solid: ¹H NMR (400 MHz, CDCl₃) δ 7.62 – 7.49 (m, 4H), 7.47 – 7.39 (m, 2H), 7.38 – 7.30 (m, 3H), 6.28 (t, J = 1.9 Hz, 2H), 5.81 (t, J = 5.9 Hz, 1H), 4.47 (dd, J = 12.3, 5.1 Hz, 2H), 3.42 (dd, J = 14.8, 7.2 Hz, 2H), 3.29 – 3.22 (m, 2H), 2.67 – 2.62 (m, 2H), 2.22 (t, J = 7.6 Hz, 2H), 1.72 – 1.61 (m, 2H), 1.57 – 1.45 (m, 2H), 1.37 – 1.16 (m, 14H). ¹³C NMR (126 MHz, CDCl₃) δ 178.28, 173.15, 140.78, 140.59, 137.94, 137.59, 128.93, 128.42, 127.56, 127.49, 127.18, 47.91, 45.27, 43.39, 42.84, 38.85, 36.96, 29.42, 29.38, 29.35, 29.16, 27.84, 27.01, 25.88. HRMS (ESI) calcd for [C₃₃H₄₀N₂O₃Na]⁺: 535.2931, found: 535.2931 [M + Na]⁺

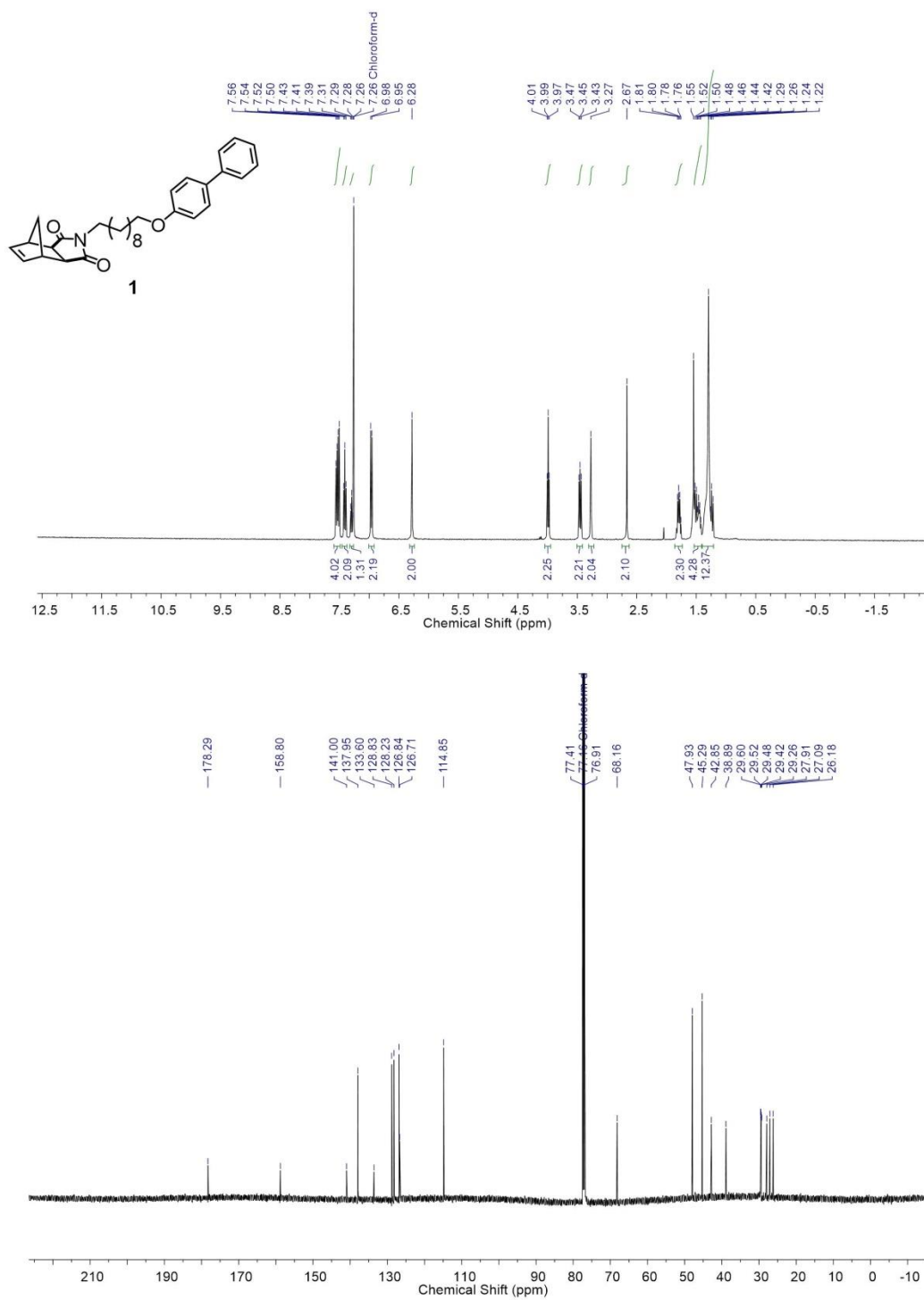


Figure 5.38 ¹H-NMR and ¹³C-NMR spectra of **1**

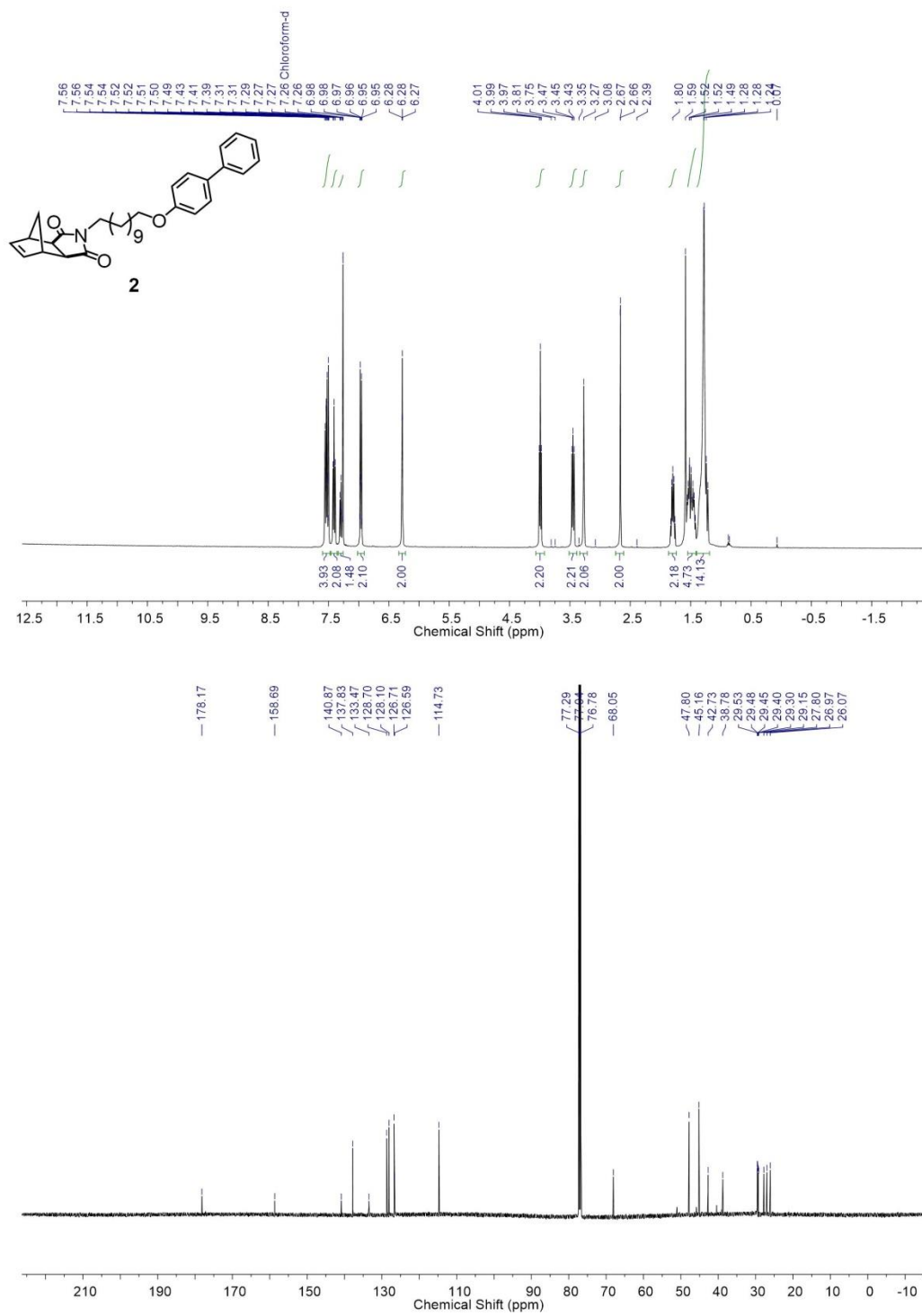


Figure 5.39 ¹H-NMR and ¹³C-NMR spectra of **2**

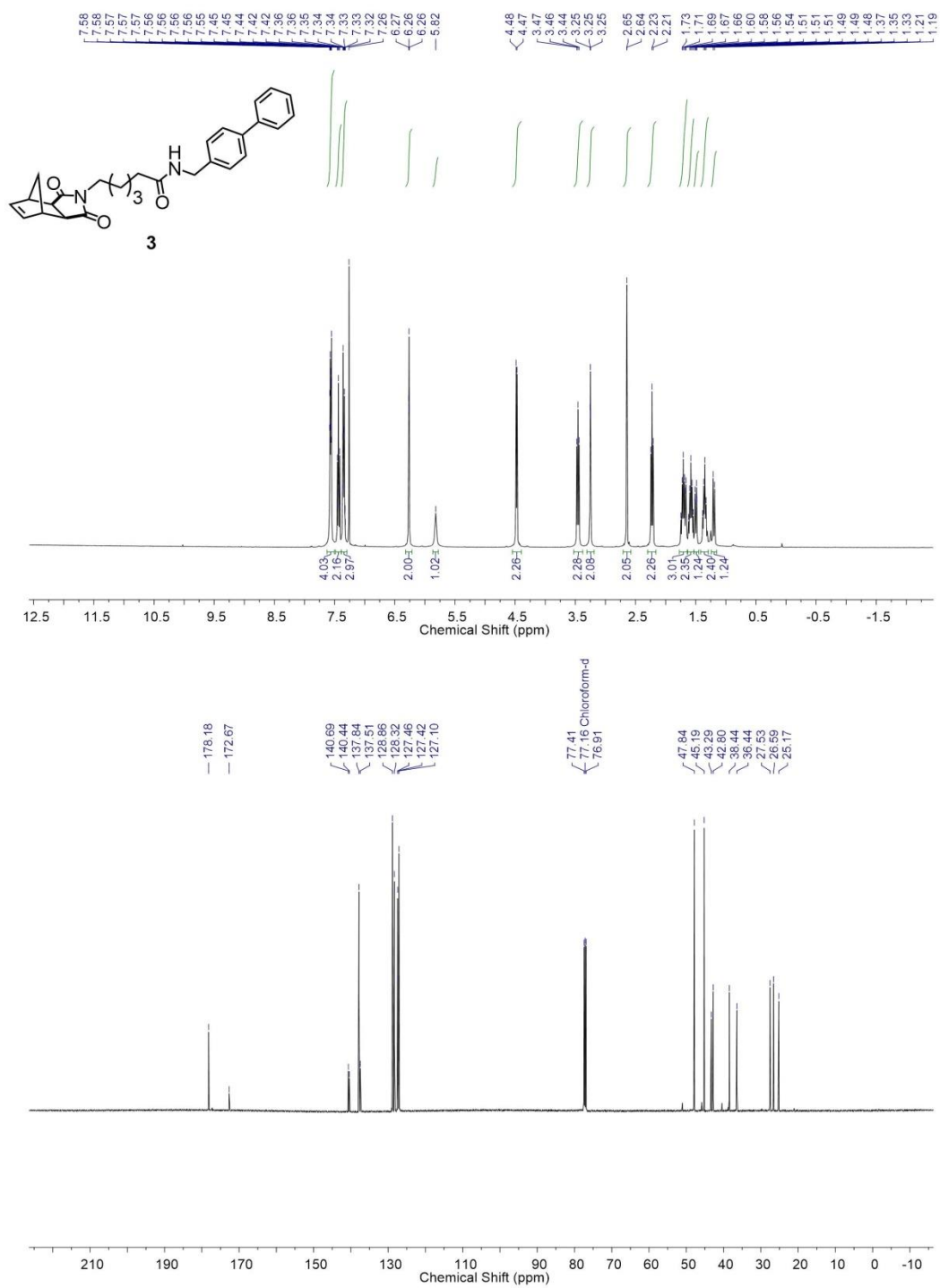


Figure 5.40 ¹H-NMR and ¹³C-NMR spectra of **3**

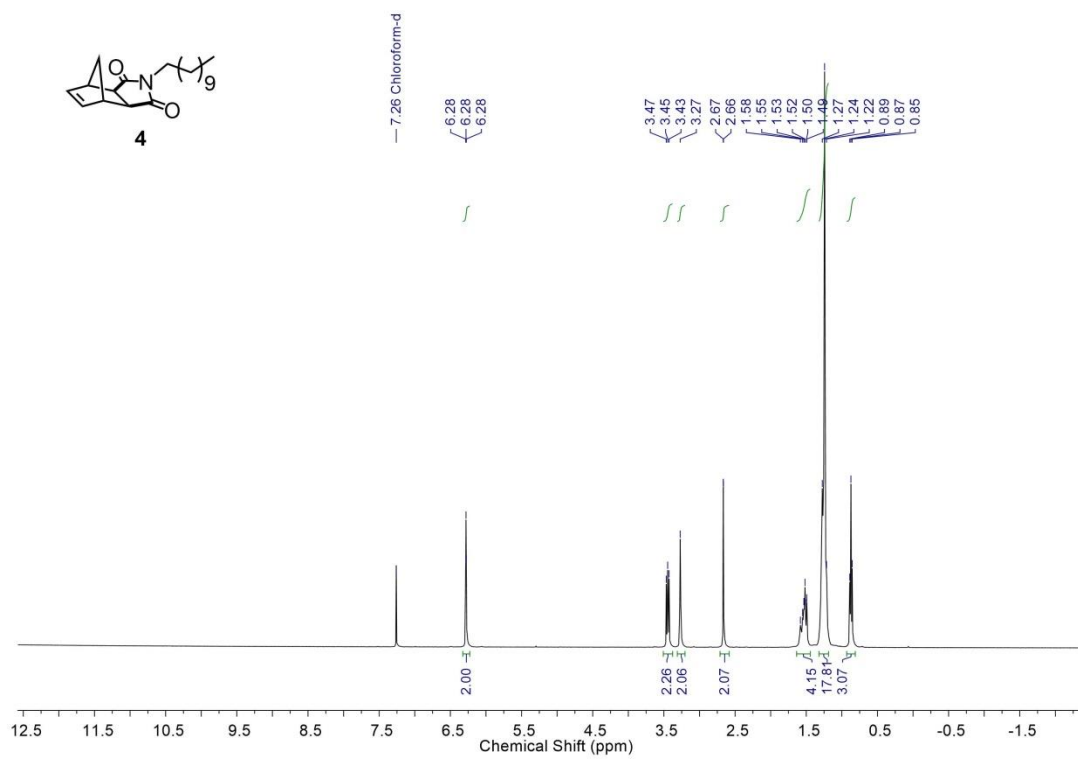


Figure 5.41 ¹H-NMR spectrum of **4**

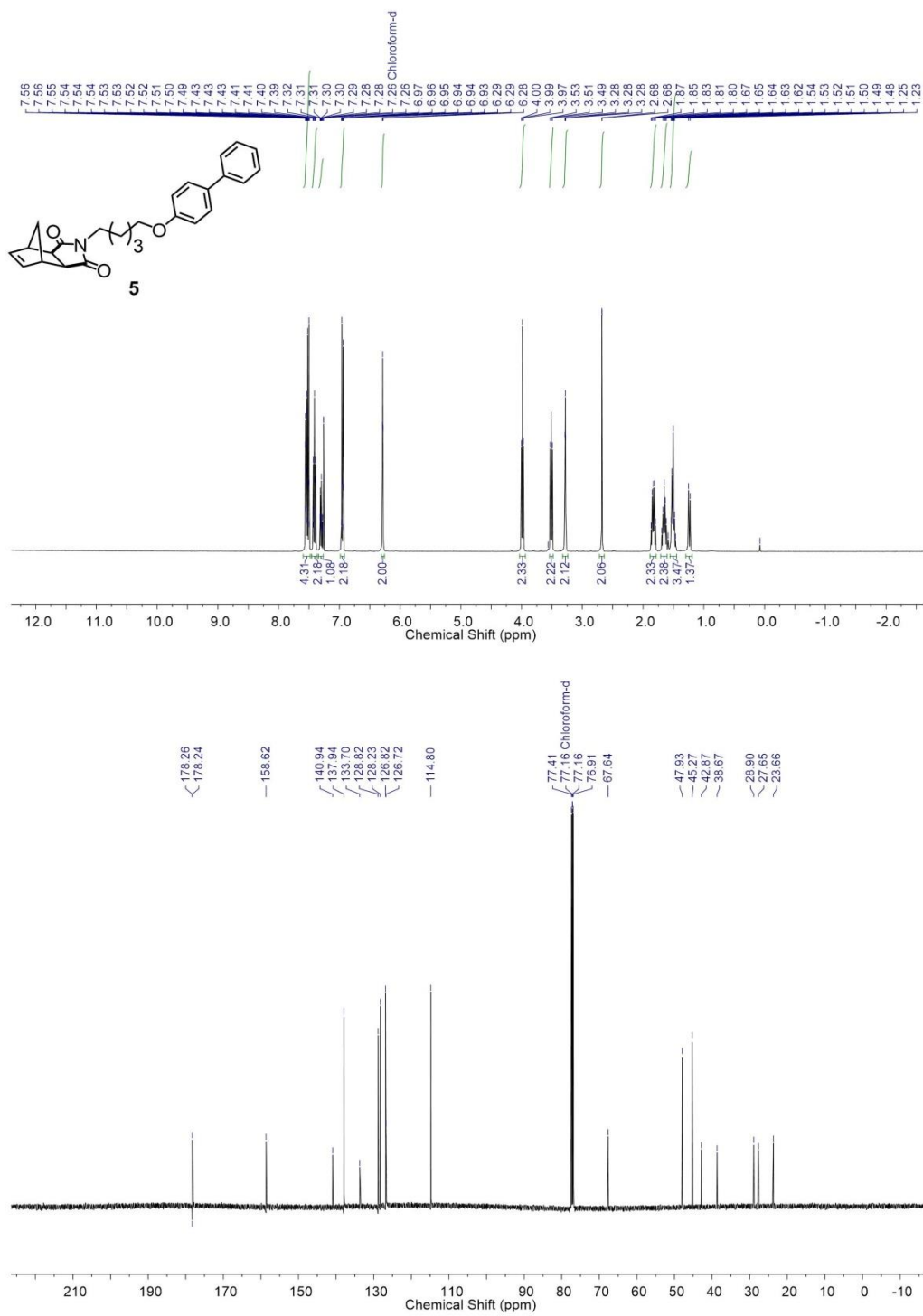


Figure 5.42 ¹H-NMR and ¹³C-NMR spectra of **5**

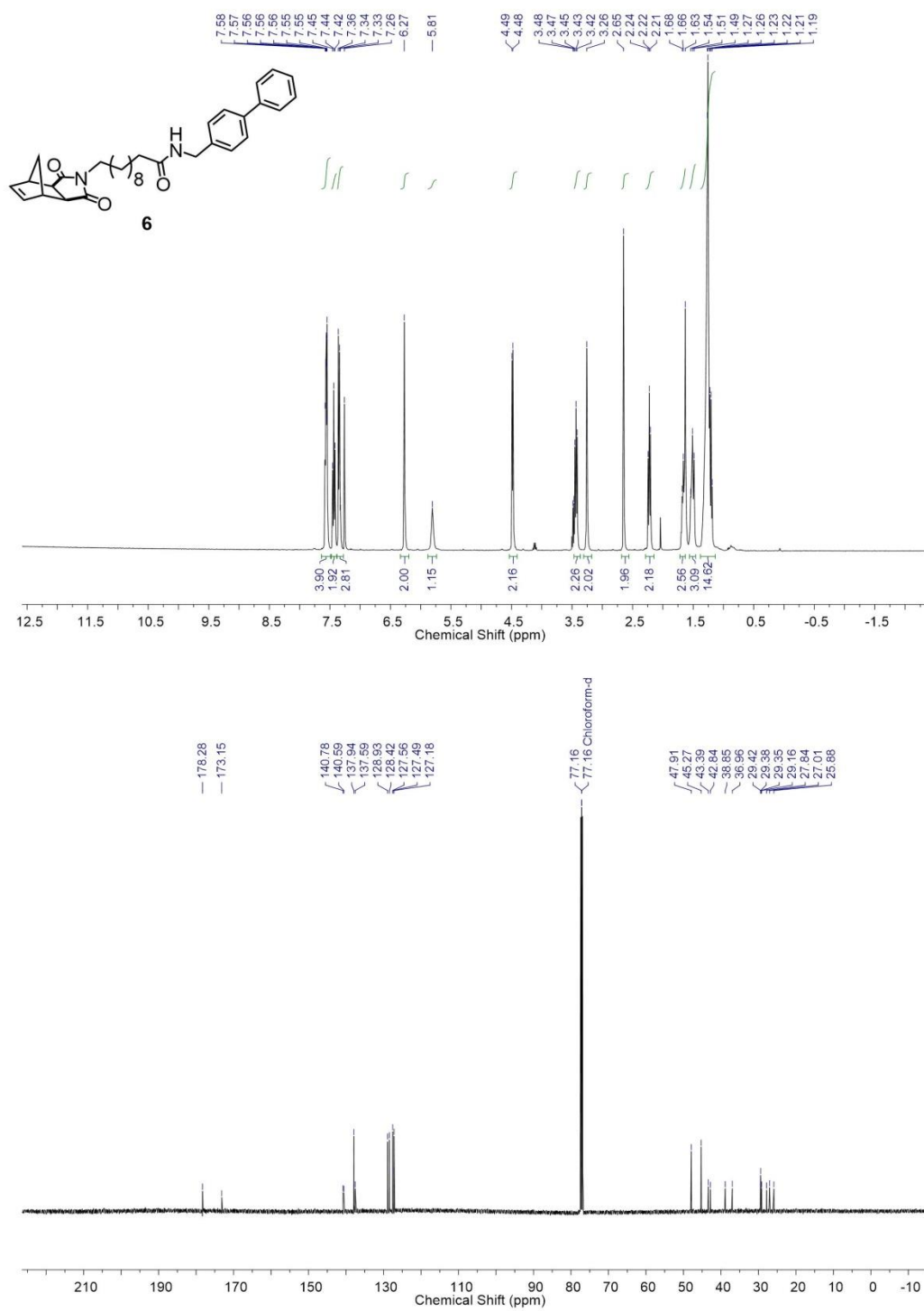


Figure 5.43 ¹H-NMR and ¹³C-NMR spectra of **6**

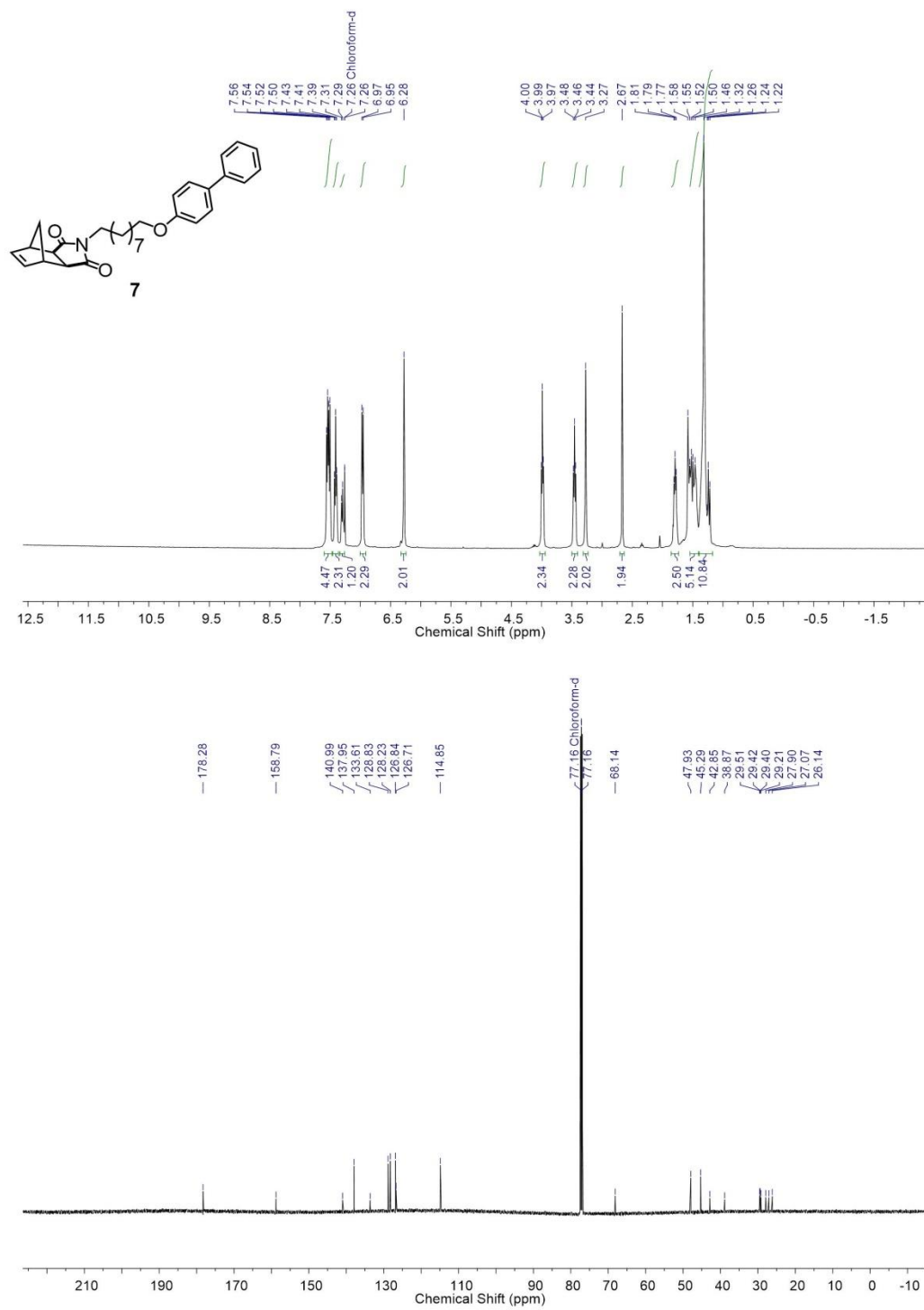


Figure 5.44 ¹H-NMR and ¹³C-NMR spectra of 7

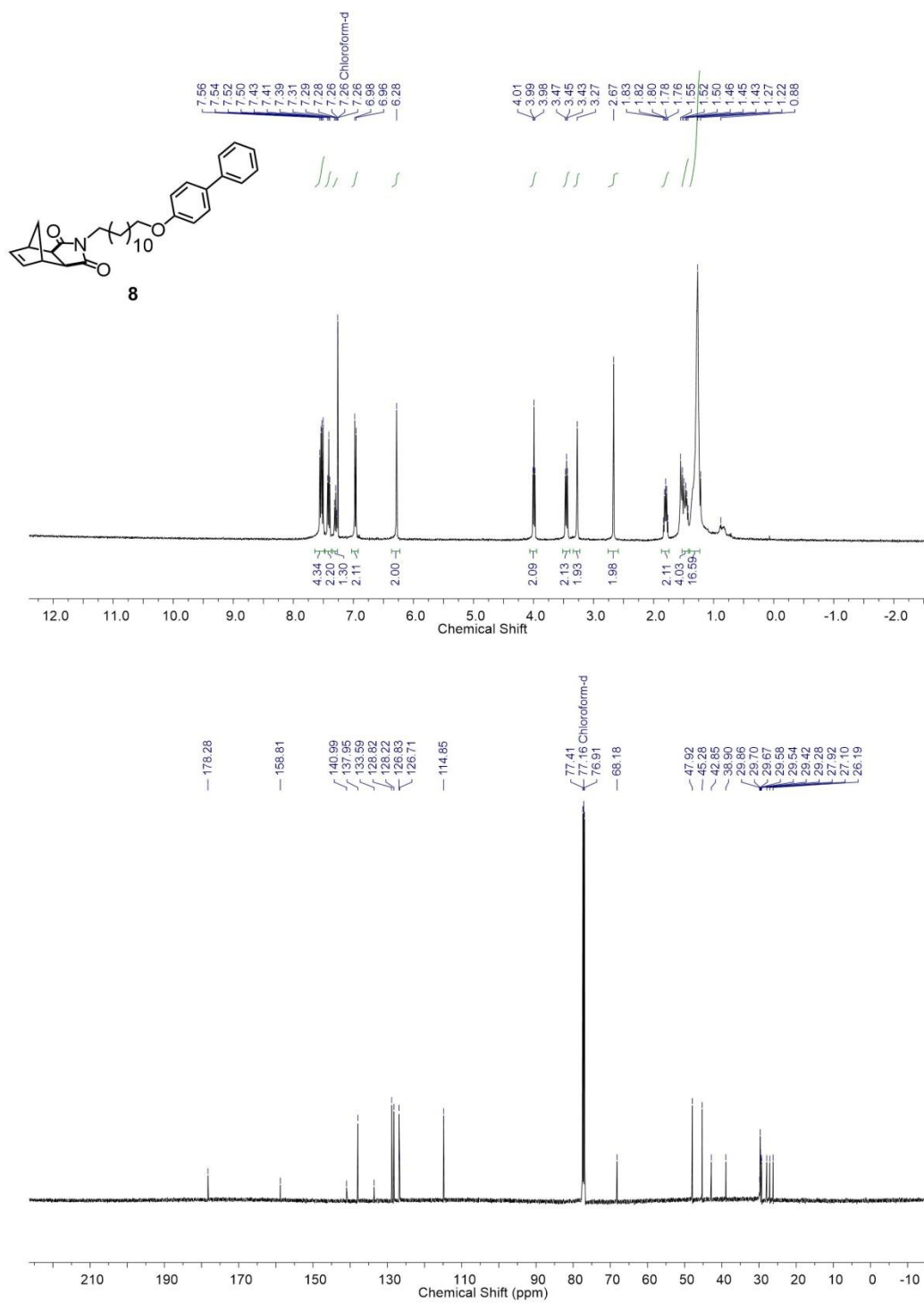


Figure 5.45 ¹H-NMR and ¹³C-NMR spectra of **8**

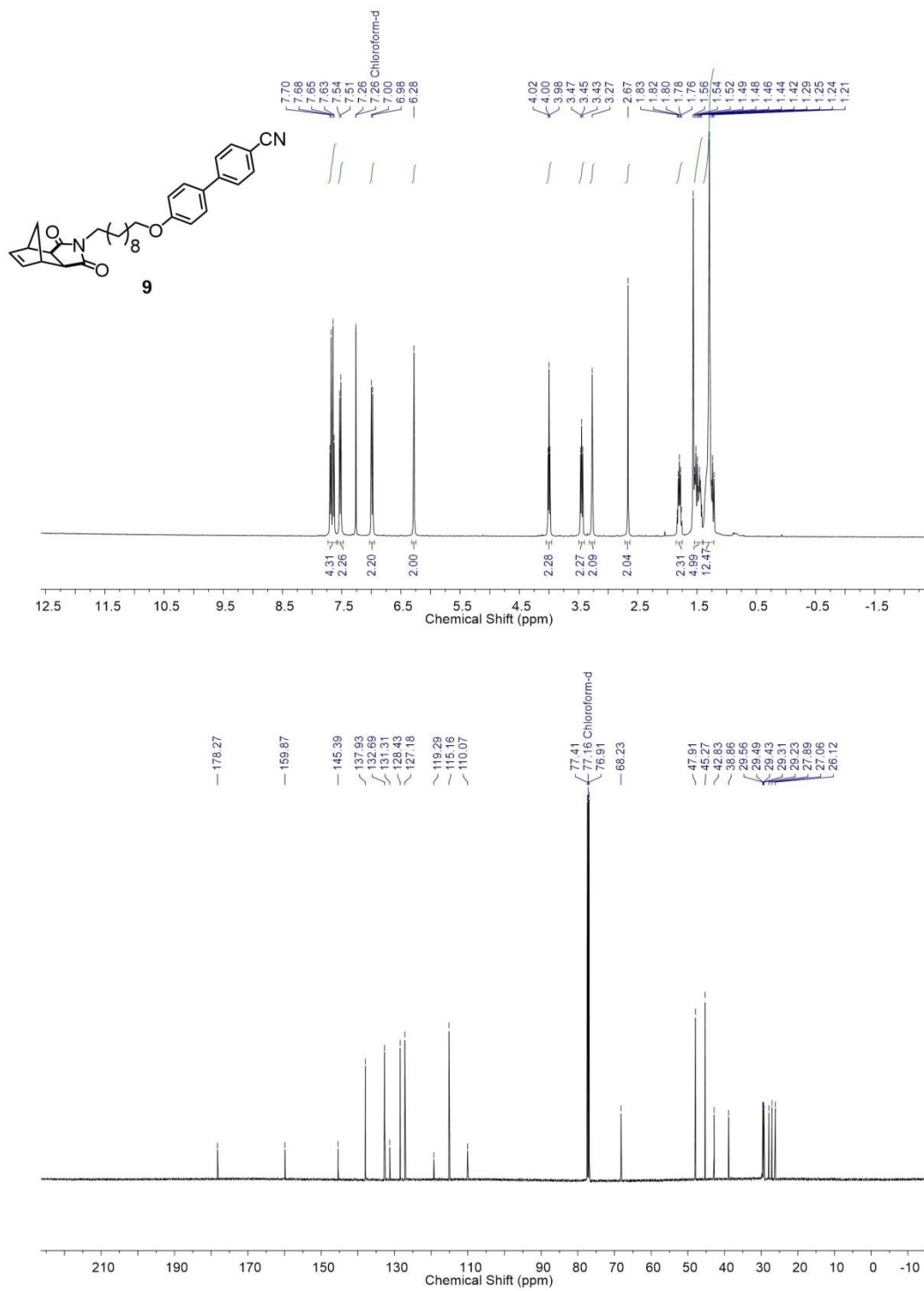


Figure 5.46 ¹H-NMR and ¹³C-NMR spectra of **9**

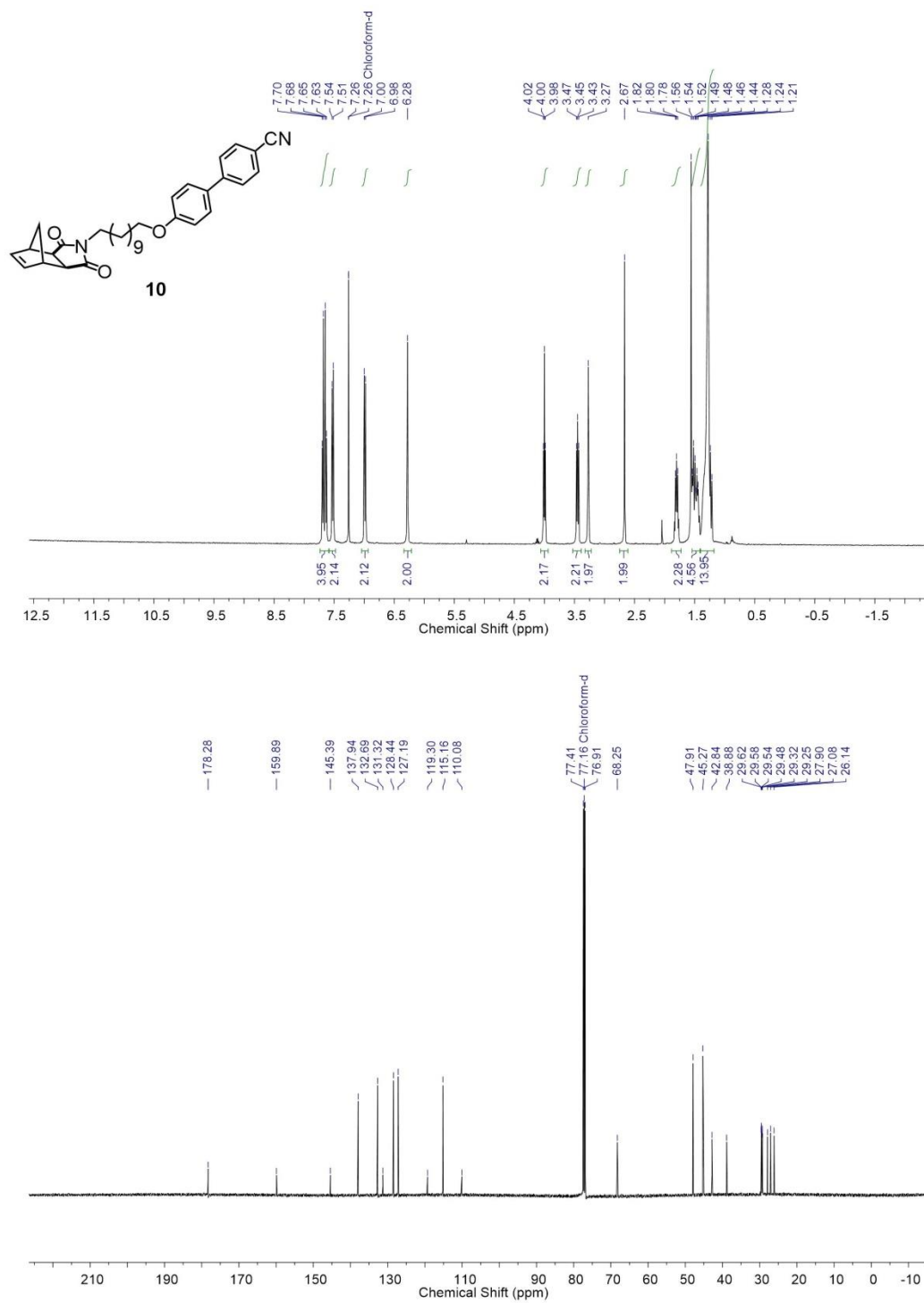


Figure 5.47 ¹H-NMR and ¹³C-NMR spectra of **10**

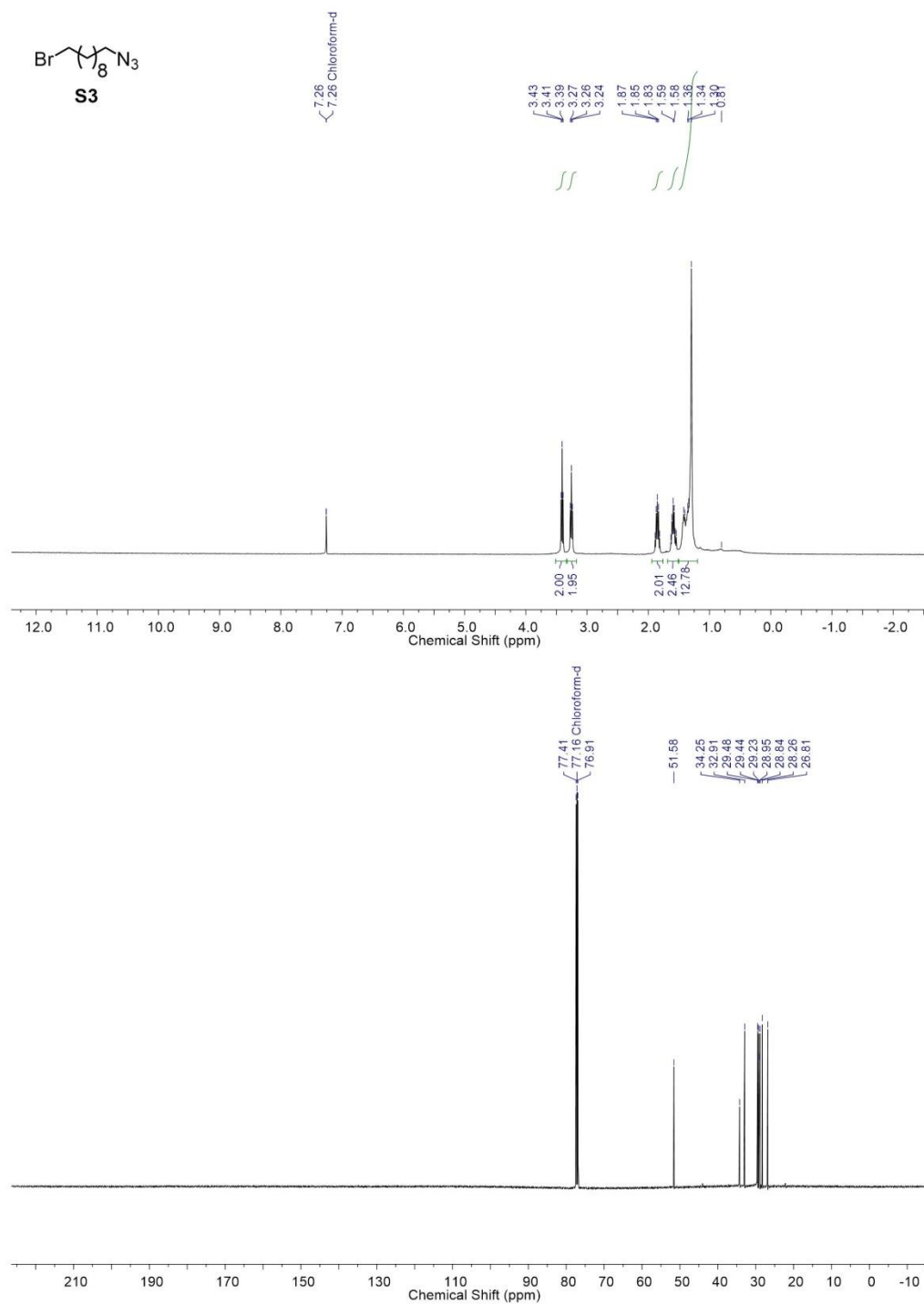


Figure 5.48 ^1H -NMR and ^{13}C -NMR spectra of **S3**

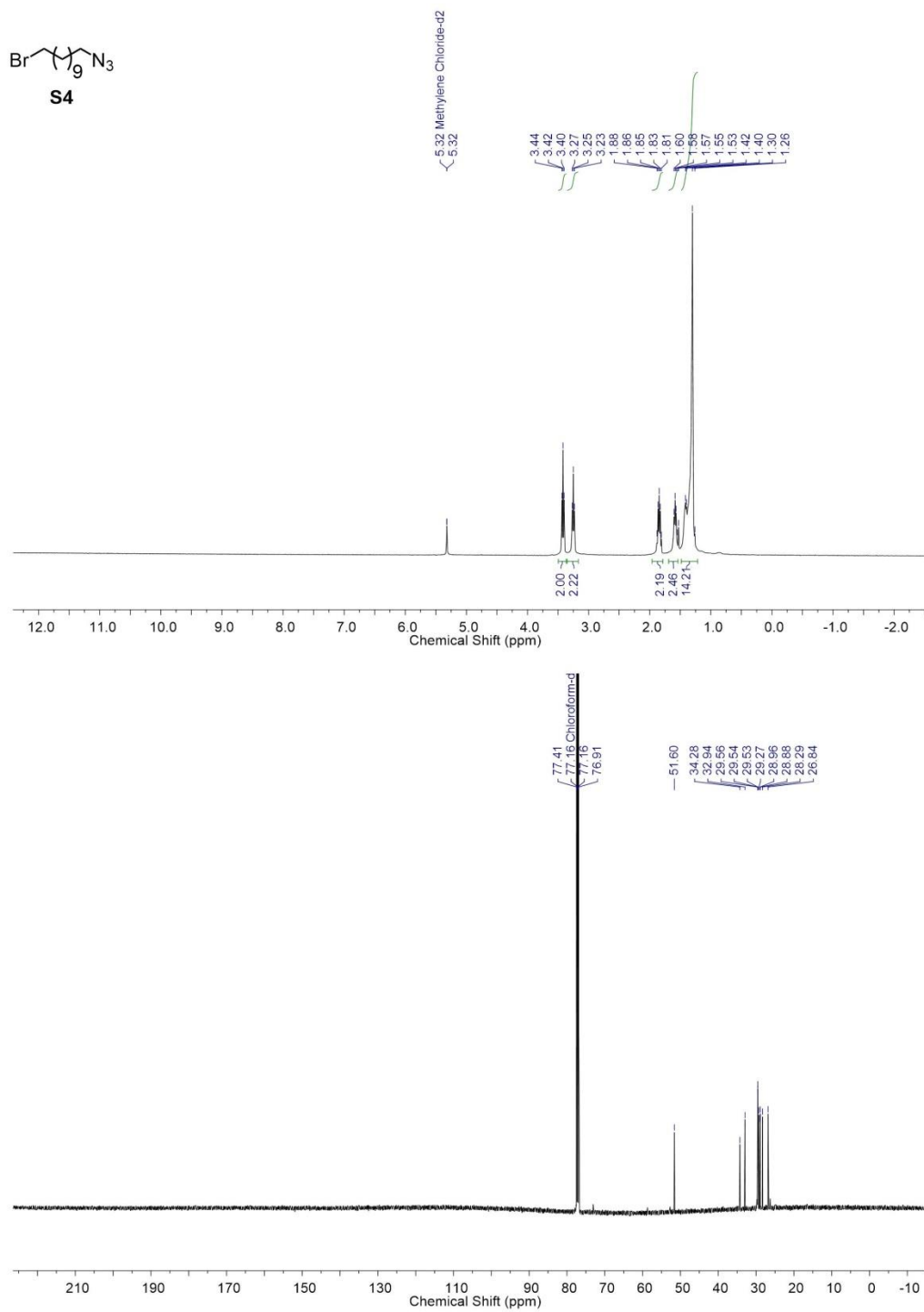


Figure 5.49 ¹H-NMR and ¹³C-NMR spectra of **S4**

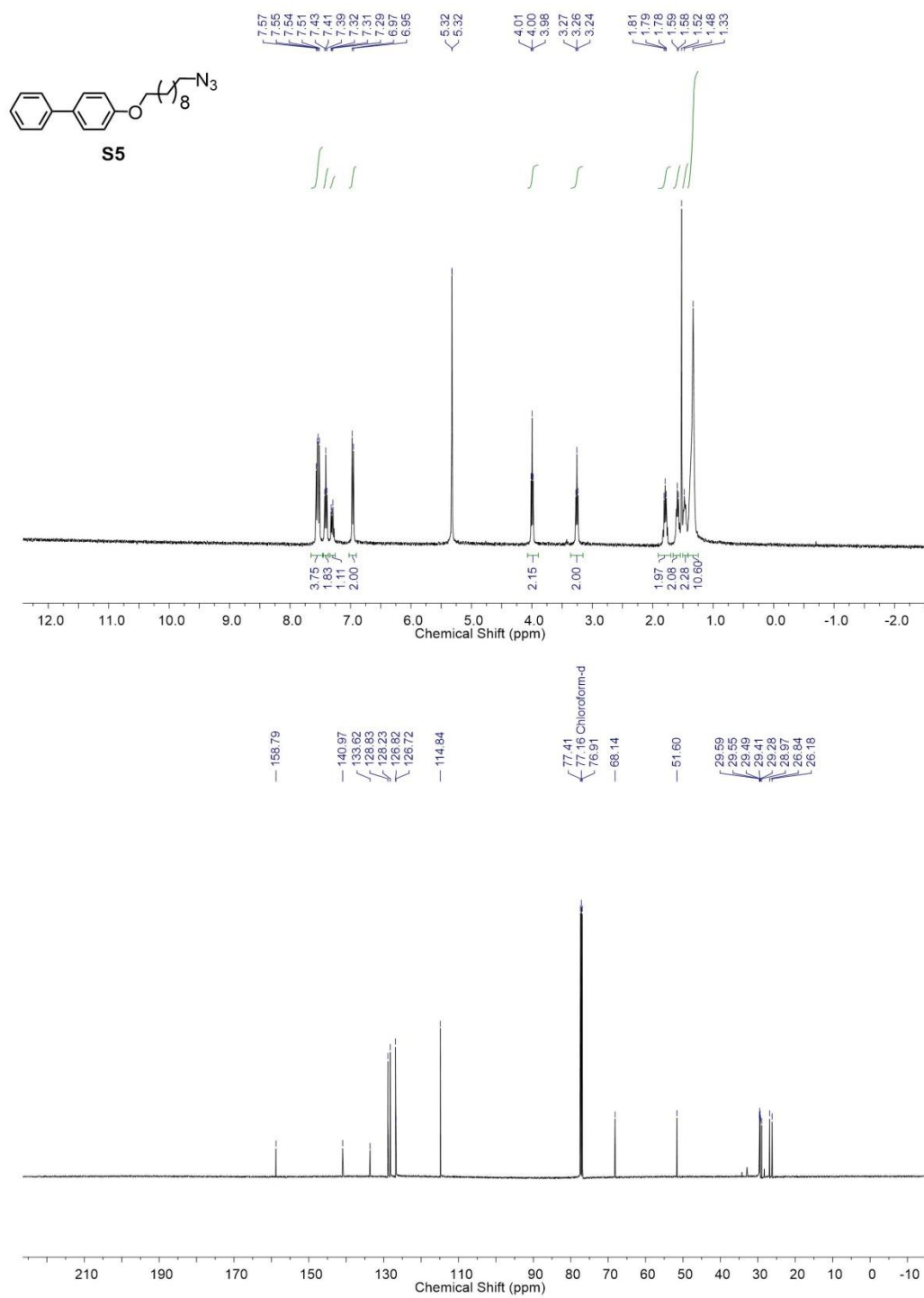


Figure 5.50 ¹H-NMR and ¹³C-NMR spectra of S5

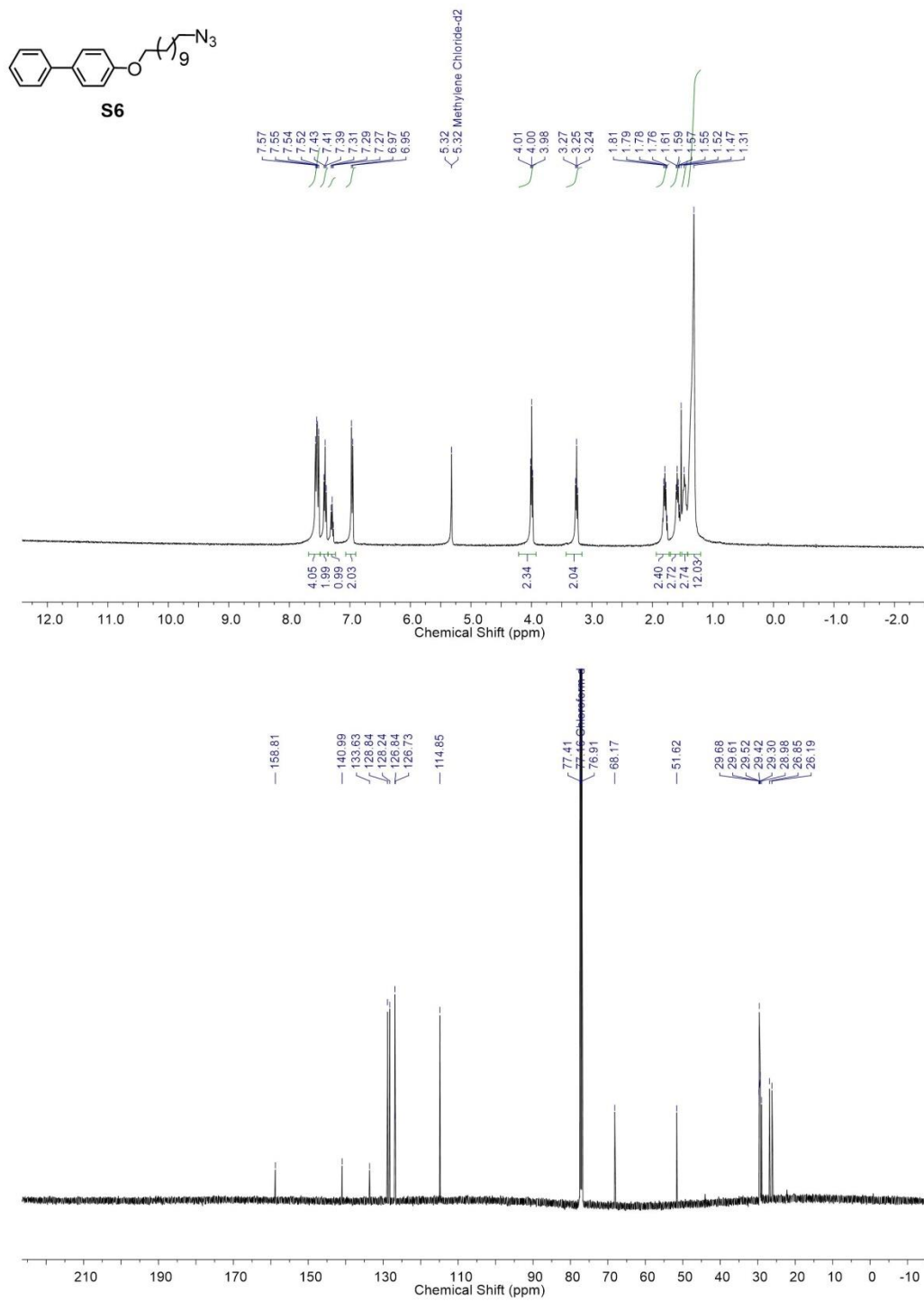


Figure 5.51 $^1\text{H-NMR}$ and $^{13}\text{C-NMR}$ spectra of **S6**

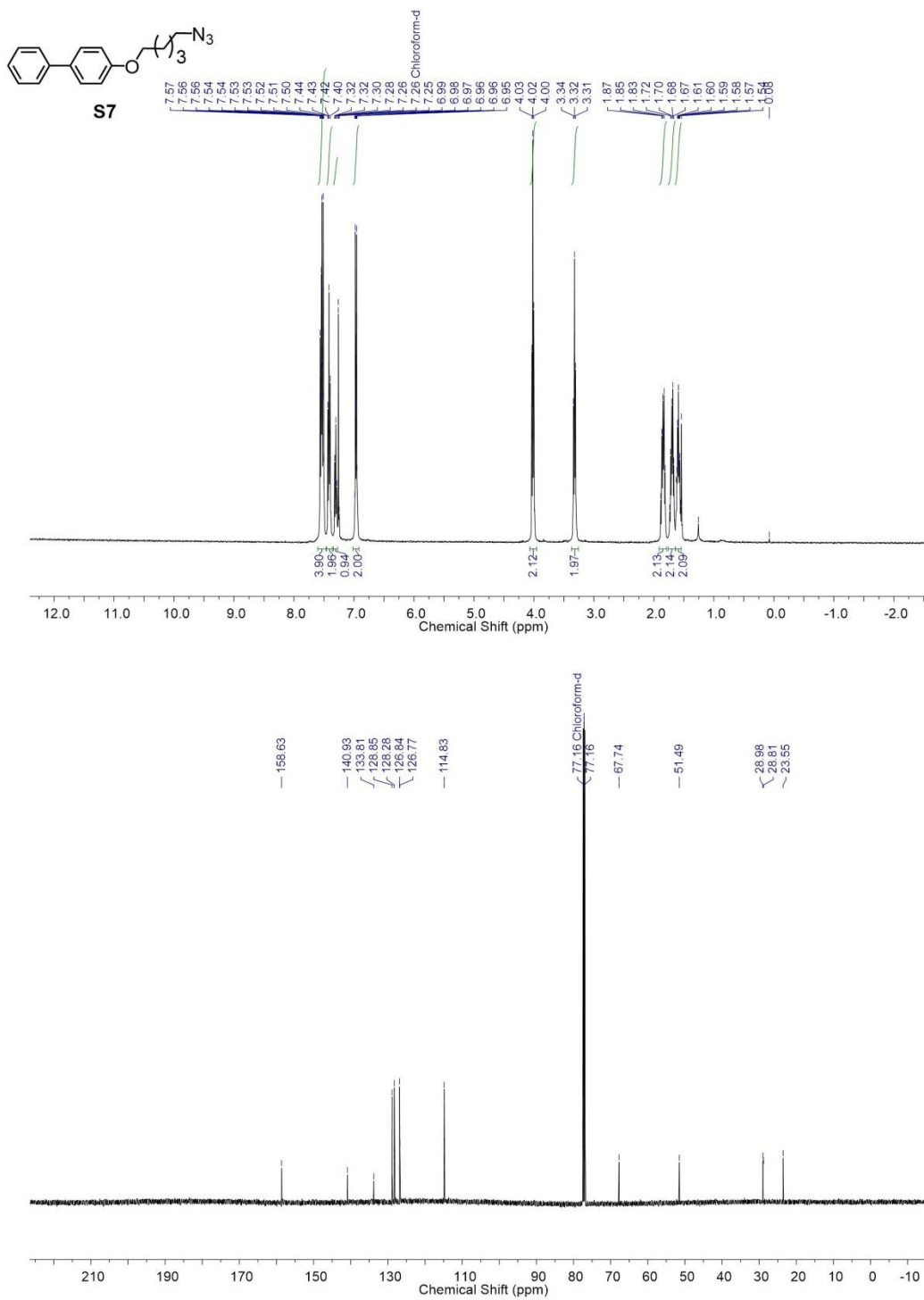


Figure 5.52 ¹H-NMR and ¹³C-NMR spectra of **S7**

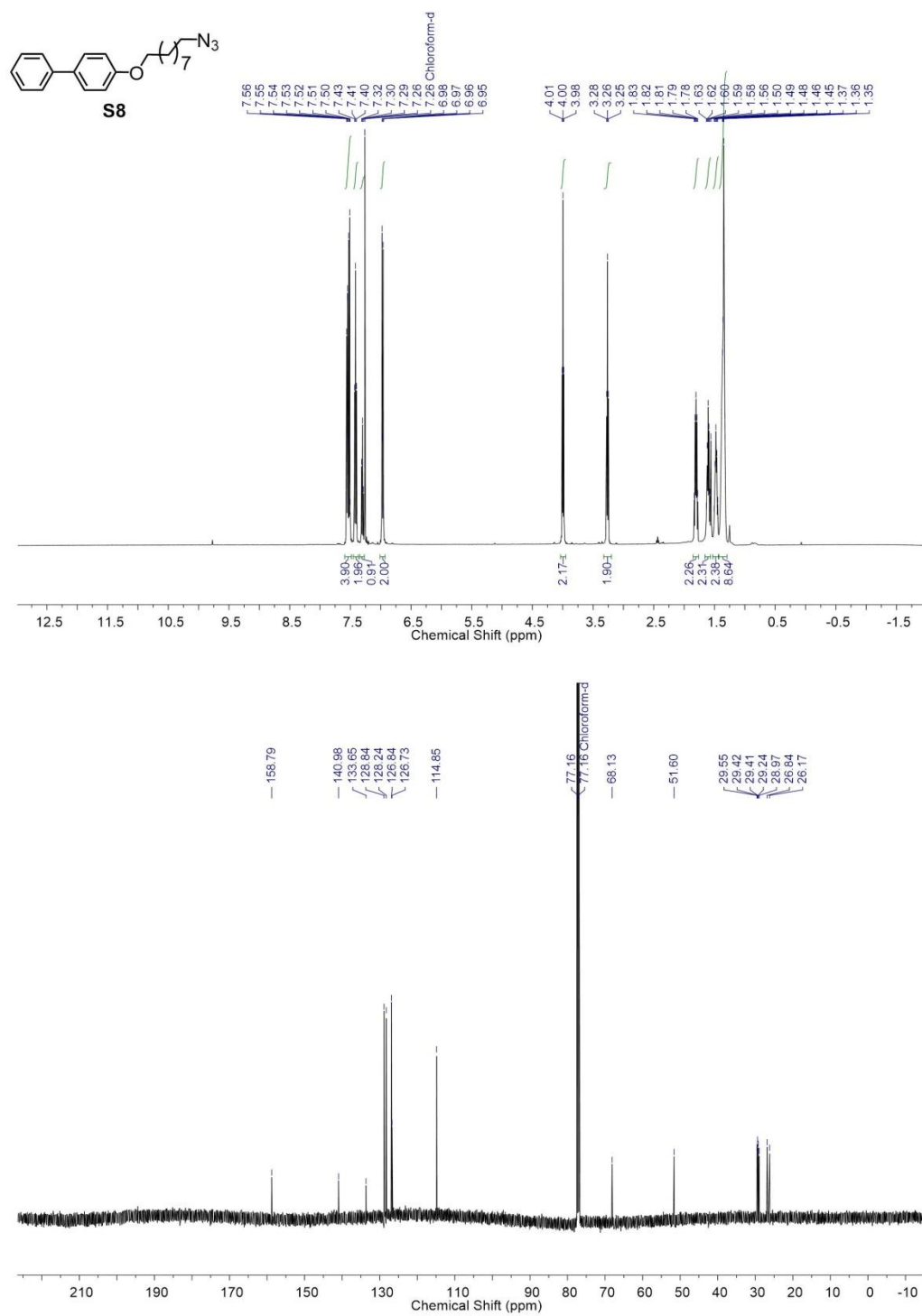


Figure 5.53 ¹H-NMR and ¹³C-NMR spectra of S8

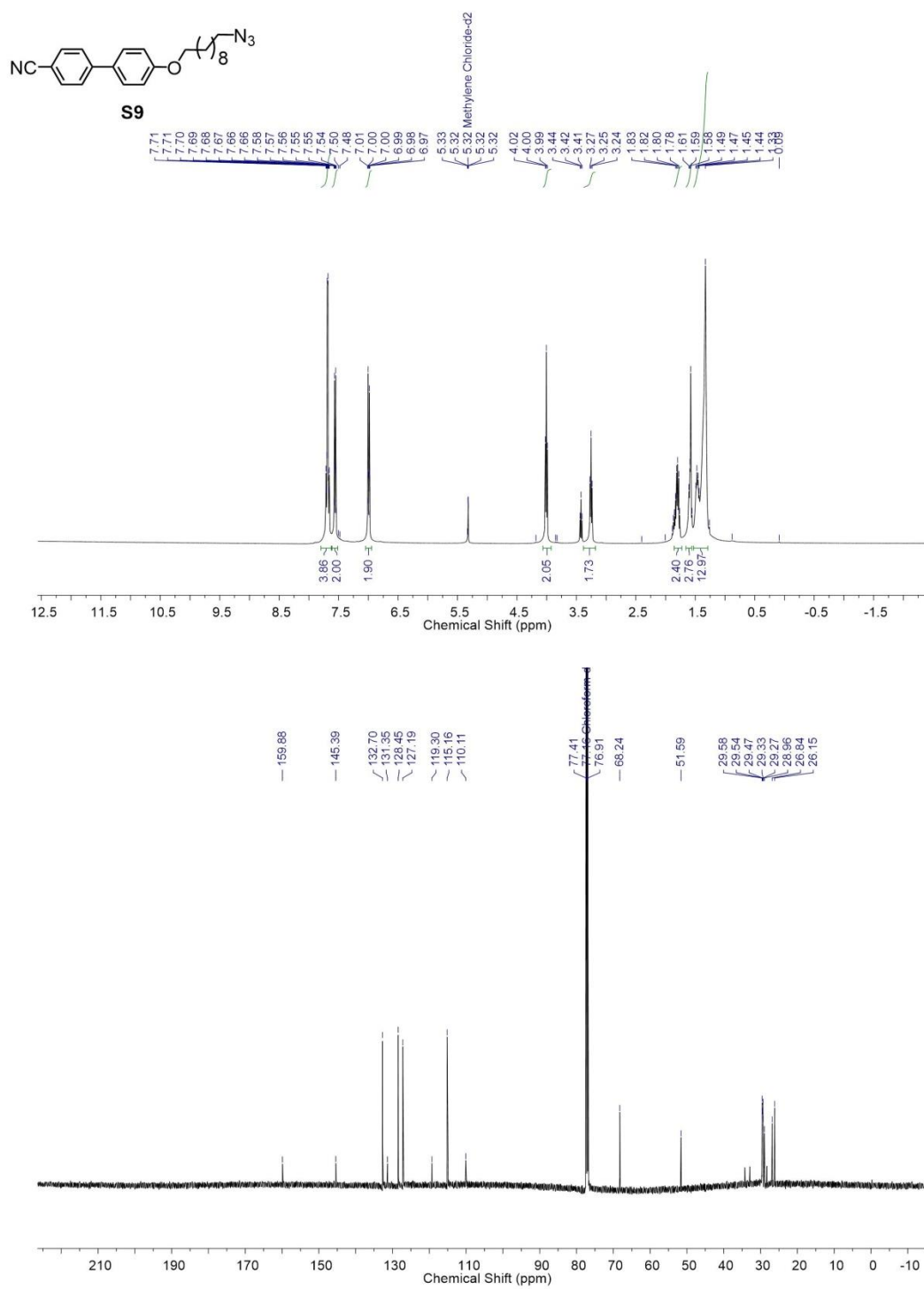


Figure 5.54 ¹H-NMR and ¹³C-NMR spectra of **S9**

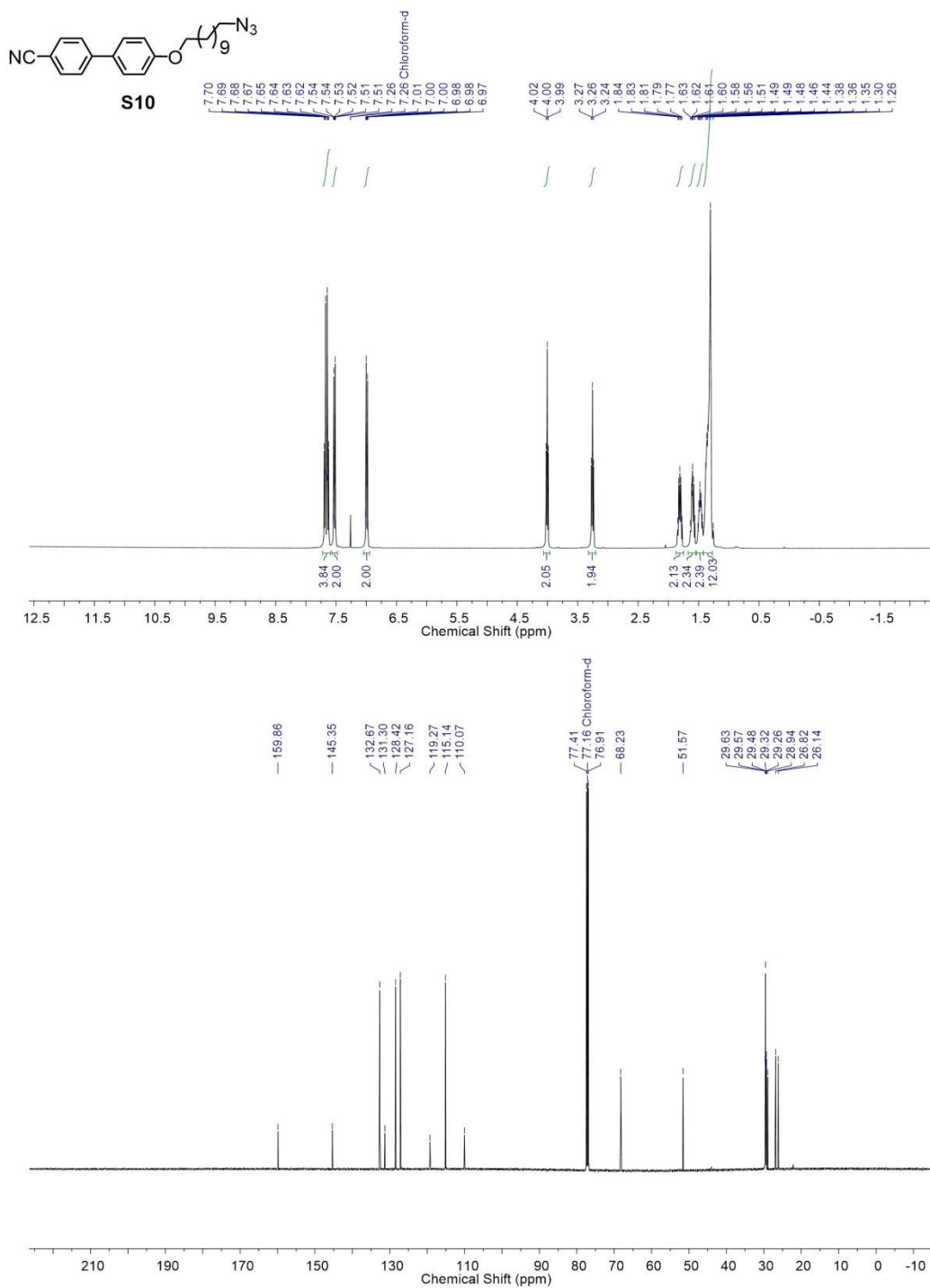


Figure 5.55 $^1\text{H-NMR}$ and $^{13}\text{C-NMR}$ spectra of **S10**

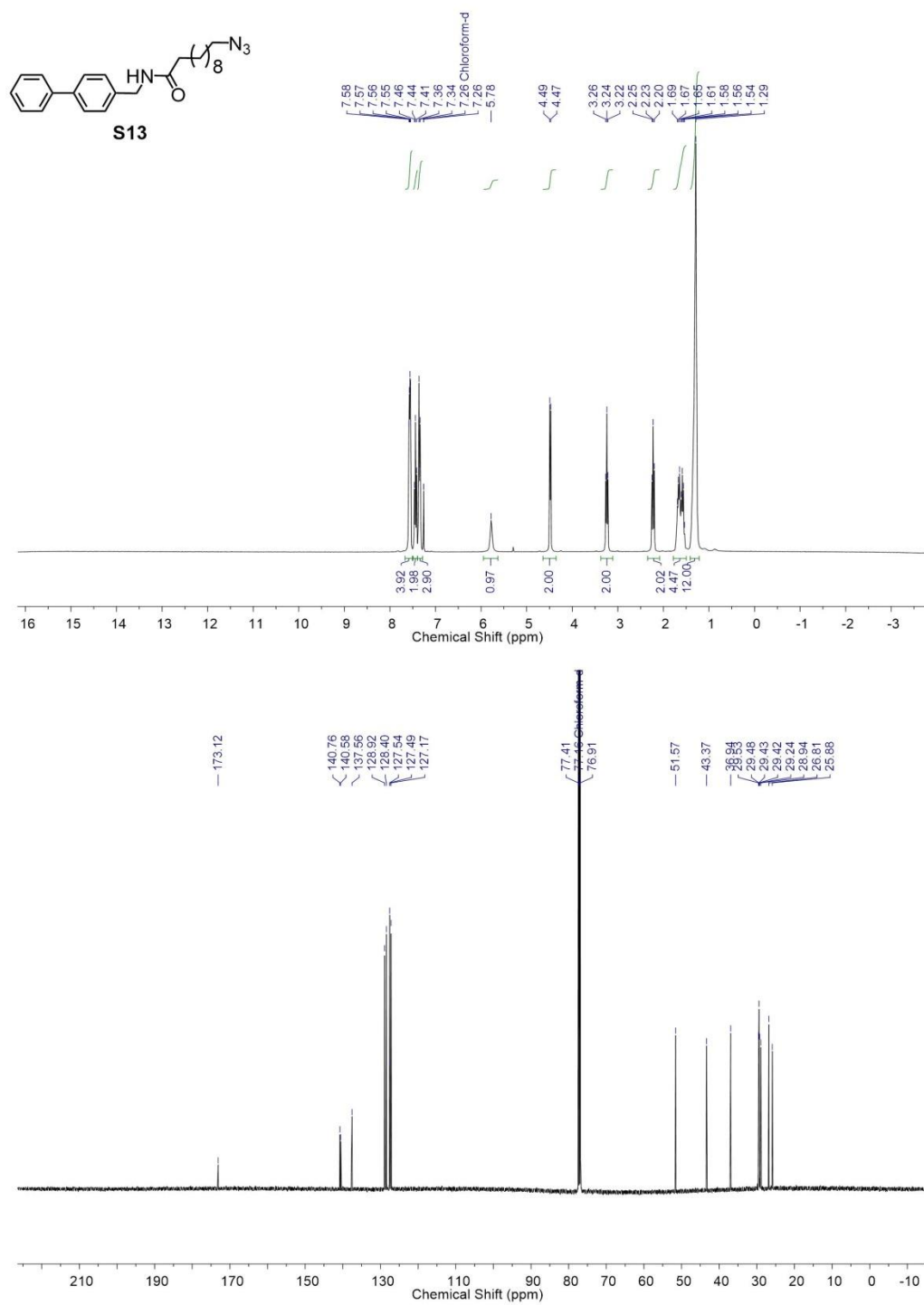


Figure 5.57 $^1\text{H-NMR}$ and $^{13}\text{C-NMR}$ spectra of **S13**

5.10 References

- (1) Khan, W.; Seo, J.-M.; Park, S.-Y. *Soft Matter* **2011**, 7 (2), 780.
- (2) Kinsinger, M. I.; Sun, B.; Abbott, N. L.; Lynn, D. M. *Adv. Mater.* **2007**, 19 (23), 4208.
- (3) Khan, W.; Park, S.-Y. *Lab Chip* **2012**, 12 (21), 4553.
- (4) Lee, D.-Y.; Seo, J.-M.; Khan, W.; Kornfield, J. A.; Kurji, Z.; Park, S.-Y. *Soft Matter* **2010**, 6 (9), 1964.
- (5) Kinsinger, M. I.; Buck, M. E.; Campos, F.; Lynn, D. M.; Abbott, N. L. *Langmuir* **2008**, 24 (23), 13231.
- (6) Ma, C. D.; Adamiak, L.; Miller, D. S.; Wang, X.; Gianneschi, N. C.; Abbott, N. L. *Small* **2015**, 11 (43), 5747.
- (7) Kinsinger, M. I.; Buck, M. E.; Abbott, N. L.; Lynn, D. M. *Langmuir* **2010**, 26 (12), 10234.
- (8) Khan, W.; Choi, J. H.; Kim, G. M.; Park, S.-Y. *Lab Chip* **2011**, 11 (20), 3493.
- (9) Collings, P. J.; Hird, M. *Introduction to liquid crystals chemistry and physics*; Taylor & Francis, 1997.
- (10) Sanford, M. S.; Love, J. A.; Grubbs, R. H. *Organometallics* **2001**, 20 (25), 5314.
- (11) Carlton, R. J.; Hunter, J. T.; Miller, D. S.; Abbasi, R.; Mushenheim, P. C.; Tan, L. N.; Abbott, N. L. *Liq. Cryst. Rev.* **2013**, 1 (1), 29.
- (12) Bukusoglu, E.; Bedolla Pantoja, M.; Mushenheim, P. C.; Wang, X.; Abbott, N. L. *Annu. Rev. Chem. Biomol. Eng.* **2016**, 7 (1), 163.
- (13) Lowe, A. M.; Abbott, N. L. *Chem. Mater.* **2012**, 24 (5), 746.
- (14) Brake, J.M.; Mezera, A.D.; Abbott, N. L. *Langmuir* **2003**, 19 (16), 6436.
- (15) Gonçalves da Silva, A. M.; Filipe, E. J. M. *Langmuir* **1996**, 12 (26), 6547.
- (16) Patel, P. R.; Kiser, R. C.; Lu, Y. Y.; Fong, E.; Ho, W. C.; Tirrell, D. A.; Grubbs, R. H. *Biomacromolecules* **2012**, 13 (8), 2546.
- (17) Caldarelli, S. A.; El Fangour, S.; Wein, S.; Tran van Ba, C.; Périgaud, C.; Pellet, A.; Vial, H. J.; Peyrottes, S. *J. Med. Chem.* **2013**, 56 (2), 496.
- (18) Decroocq, C.; Rodríguez-Lucena, D.; Russo, V.; Mena Barragán, T.; Ortiz Mellet, C.; Compain, P. *Chem. - A Eur. J.* **2011**, 17 (49), 13825.

- (19) Neumann, L. N.; Baker, M. B.; Leenders, C. M. A.; Voets, I. K.; Lafleur, R. P. M.; Palmans, A. R. A.; Meijer, E. W. *Org. Biomol. Chem.* **2015**, *13* (28), 7711.